Thermofluid Optimisation of Additive Manufacturing High Heat Flux Components for Fusion

Author:
Daniel Padrão

Supervisors:
Dr. Ian Maskery
Prof. Christopher Tuck
Dr. David Hancock

Internal Assessor:
Dr. Mirco Magnini

External Assessor:
Dr. Wessel Wits

Submitted to the University of Nottingham
for the degree of

Doctor of Philosophy

December 2023

Abstract

The divertor is a key component in magnetic confinement fusion as it reduces plasma contamination and protects the inner walls by removing heat and plasma exhaust. Divertors in DEMO (a planned demonstration fusion power plant) are needed to experience peak heat fluxes of up to 70 MW m^{-2} and neutron doses of 6-7 displacements per atom per full power year for long periods of time with little to no maintenance. Divertor targets experiencing heat fluxes and neutron irradiation doses of this magnitude can melt and suffer from mechanical failures or defects, such as embrittlement. However, novel divertor target structures can overcome this issue by having an optimised geometry which enhances heat transfer, ensuring that the divertor remains within an operational temperature regime where the aforementioned problems are minimised.

Additive manufacturing has been identified as a technology that can have significant potential applications in the nuclear fusion sector, particularly for high heat flux components, due to the freedom in geometric complexity offered. Additively manufactured cellular structures could exhibit improved thermal performances in heat transfer devices as they have high surface-to-volume ratios and enclosed channels, which are conducive for convective heat transfer applications. While interest in studying cellular structures for heat transfer applications has grown in recent years, further research benchmarking their performance against conventional structures, such as pin or fin arrays and circular channels, is necessary. The effect that their design variables, such as volume fraction, have on their thermal and hydraulic performance also needs to be determined.

Here, five cellular structures were examined numerically to determine the impact that different geometrical properties have on their hydraulic and thermal performance. Computational fluid dynamics was used to create useful predictive models for pressure drop and volumetric heat transfer coefficients over a range of flow rates and volume fractions. These can henceforth be used by heat transfer engineers to design appropriate heat sinks. The thermal performance of cellular structures was found to be heavily dependent on internal geometry, with structures capable of distributing thermal energy across the entire fluid volume having greater volumetric heat transfer coefficients than those with only localised areas of high heat transfer and low levels of fluid mixing.

Building on this work, a range of additively manufactured cellular structures were investigated as candidates for novel divertor target structures. Computational fluid dynamic results were verified experimentally using UKAEA's HIVE, a high heat flux testing facility. It was found that the divertor may be significantly improved by the inclusion of cellular structures, as the examined structures were able to remove $11-28\%$ more energy from the heated surface than a conventional circular channel. The examined structures exhibited greater pressure drops, however.

This investigation has determined that cellular structures show great promise for high heat flux applications in the nuclear fusion sector. Further research is needed to determine whether the enhanced cooling exhibited by the examined cellular structures can offset the additional energy associated with pumping fluids through larger pressure gradients, however. Additionally, the future of additively manufactured fusion components is dependent on the processability of fusion relevant metals. The developed predictive models for the hydraulic and thermal performance of the examined cellular structures can be used in conjunction with other rules, such as the Gibson-Ashby scaling laws for stiffness, to design multifunctional components. The accuracy of the models can be improved by examining additional geometrical properties, such as cell aspect ratio and surface area. Fluid flow dynamics and thermal transport within different cellular structures need to be further investigated and understood such that heat sinks can be designed from first principles.

Contents

Declarations

I declare that this thesis, entitled *Thermofluid Optimisation of Additive Manufacturing High Heat Flux Components for Fusion*, and the work presented in it are my own, except where explicitly stated in the text. It has been submitted to the University of Nottingham in support of my application for the degree of Doctor of Philosophy. It has not been submitted to any other academic institution. All work took place under the supervision of Dr. Ian Maskery, Prof. Christopher Tuck and Dr. David Hancock between October 2019 and June 2023.

Daniel Padrão

December 2023

Publications

Journal Papers

D. Padrão, D. Hancock, J. Paterson, F. Schoofs, C. Tuck and I. Maskery, "New structure-performance relationships for surface-based lattice heat sinks". In: *Applied Thermal Engineering* 236 (2024), pp. 121572

I. Maskery, L.A. Parry, D. Padrão, R. Hague and I. Ashcroft, "FLatt Pack: A research-focused lattice design program". In: *Additive Manufacturing* 49 (2022), pp. 102510

Conferences Presented

Daniel Padrão, Solid Freeform Fabrication Symposium 2022, *Surface-based lattice structures as candidates for heat exchangers*

Daniel Padrão, Solid Freeform Fabrication Symposium 2021, *Numerical fluid dynamics of surface-based cellular structures*

Acknowledgements

I'm extremely grateful to both the University of Nottingham and the EPSRC Energy Programme for their financial support, without which this Ph.D. would not have been possible. I would also like to express my gratitude to the University of Nottingham for providing the *Conference, travel and training fund*, which subsidised both of the conferences that I attended.

I am deeply indebted to my supervisors Dr. Ian Maskery, Prof. Christopher Tuck and Dr. David Hancock, who have all supported me throughout this research project and allowed me to grow in the process. Special note must be made to Dr. Ian Maskery for taking such an active and personal role here. I could not imagine doing this project without your involvement, thank you. I would also be remiss in not recognising Dr. Frank Schoofs, who supervised me for a significant period of this project.

I would like to express my appreciation to both Dr. Mirco Magnini and Dr. Wessel Wits for agreeing to be my internal and external assessors, respectively, and all of the work that has entailed. I hope that this thesis is worthy of your time.

I'm extremely grateful to the Centre for Additive Manufacturing at the University of Nottingham for supporting me and providing opportunities to develop my professional skills. I would like to extend my gratitude to Mirela Axinte, for organising many events and helping with innumerous admin, Mark Hardy, for all of the support and advice provided when printing parts, and Dr. Luke Parry, for involving me with your work and taking great interest in mine.

This project would not have been possible without the United Kingdom Atomic Energy Authority, which provided the main research question relevant to the nuclear fusion sector and gave me access to their facilities at the Culham Centre for Fusion Energy. I am also grateful to both Stephen Cosser and Josh Whitley, without which I would not have been able to use HIVE, and to James Paterson, for being an ever-present figure.

Many thanks to the Materials team at the University of Nottingham. Without their facilities and the training they provided, I would not have been able to post-process my printed parts. Special thanks to the technical team at the Precision Manufacturing Centre at the University of Nottingham for machining my printed parts. I am also grateful for access to the University of Nottingham's Augusta HPC service.

I'd like to recognise all of the friends that I made throughout my time here as a Ph.D. student, particularly in the Centre for Additive Manufacturing. Special thanks to Kristian Plender, who has been a part of this journey from the very beginning (and has always loved a good night out), and to both Diego Della Crociata and Alasdair Bulloch, who I only met after the multiple lockdowns but have been ever-present since. I'd also like to acknowledge our YES20 team and thank

both Dr. Richard Sélo and Dr. Annalisa Ferrante, I will always cherish the bonds that we formed.

I'd like to thank the University of Nottingham Taekwondo Club for being a constant throughout my university and doctoral studies, keeping me fit and developing my indomitable spirit. Special mentions to Bradley Hopkins, who has been a great friend and I could not imagine the club without you, and to Gary Skinner, Colin West and Dr. Wenqi Li for the innumerous hours spent coaching me. I'd also like to recognise the friendships that I (somehow) managed to sustain from my pre-Ph.D. life. Many thanks to my friends Tobias Long, who has been a true friend for almost a decade now, Jack Mitchell, someone I trust and spent many afternoons gaming with, and Ray Bellis, who has been a great friend and someone I can rely on.

Lastly, MANY thanks to my close family. Thank you to my mum, Ana, and dad, Manuel, for raising me into the person I am today. I never would have gotten this far without your influence. Thank you to my younger brother, Leandro, for being someone that I have been able to confide in. I am also incredibly grateful to my girlfriend, Paris, who has been my rock and been with me through thick and thin. Thank you to all of you.

List of Figures

List of Tables

Abbreviations

AM	Additive manufacturing.
AMAZE	Additive Manufacturing Aiming Towards Zero Waste & Efficient Production of High-Tech Metal Products.
CAD	Computer-aided design.
CFD	Computational fluid dynamics.
D-T	Deuterium-tritium.
DBTT	Ductile-brittle transition temperature.
DEMO	DEMOnstration power plant.
DNS	Direct numerical simulation.
FEA	Finite element analysis.
FLatt Pack	Functional Lattice Package.
GAMG	Generalised geometric-algebraic multi-grid.
HEMJ	Helium-cooled multi-jet.
HIVE	Heating by Induction to Verify Extremes.
HPJC	High pressure jet cascade.
IPW	I-graph and wrapped package-graph.
IR	Infrared.
JET	Joint European Torus.
LEAP	Leading Edge Aviation Propulsion.
LES	Large-eddy simulation.
LPBF	Laser powder bed fusion.
MAST	Mega Ampere Spherical Tokamak.
MPI	Message Passing Interface.
OpenFOAM	Open-source Field Operation And Manipulation.
PBiCGStab	Stabilized preconditioned (bi-)conjugate gradient.
PCG	Preconditioned (bi-)conjugate gradient.
PFU	Plasma-facing unit.
RANS	Reynolds-averaged Navier-Stokes.
SIMPLE	Semi-Implicit Method for Pressure Linked Equations.

STEP Spherical Tokamak for Energy Production.

TPMS Triply periodic minimal surface.

UKAEA United Kingdom Atomic Energy Authority.

WPDIV Work package divertor.

Nomenclature

Atoms and molecules

${}^{1}_{0}\mathrm{n}$	Neutron
${}^{2}_{1}\mathrm{H}$	Deuterium
${}^{3}_{1}\mathrm{H}$	Tritium
${}^{4}_{2}\mathrm{He}$	Helium
Cr	Chromium
Cu	Copper
CuCrZr	Copper-Chromium-Zirconium
$\mathrm{H_2O}$	Water
Mo	Molybdenum
Ta	Tantalum
V	Vanadium
W	Tungsten
$\mathrm{W_{AM}}$	Additively manufactured tungsten
$\mathrm{W_f}$	Fiber-reinforced tungsten
$\mathrm{W_p}$	Particle-reinforced tungsten

Computational fluid dynamics theory exclusive terms

α_{eff}	Effective thermal diffusivity [$\mathrm{m^2\ s^{-1}}$]
α_{U}	Under-relaxation factor
β	k-ω-SST turbulence model coefficient
β^*	k-ω-SST turbulence model coefficient
$\boldsymbol{\epsilon}^n$	Iteration error
$\boldsymbol{\Phi}$	Heat flux vector [$\mathrm{W\ m^{-2}}$]

$\boldsymbol{\phi}$	Vector containing the nodal variable values
$\boldsymbol{\rho}$	Residuals
$\boldsymbol{\tau}$	Stress tensor [Pa]
$\boldsymbol{A}$	Square sparse coefficient matrix
$\boldsymbol{b}$	Body forces [N]
$\boldsymbol{C}$	Matrix coefficients from the discretisation of the momentum equation
$\boldsymbol{f}$	Convection or diffusion flux vector
$\boldsymbol{H}(\boldsymbol{u})$	Function of the fluid velocity vector
$\boldsymbol{I}$	Identity matrix
$\boldsymbol{R}$	Reynolds stress tensor [$m^2\ s^{-2}$]
$\boldsymbol{R}_{\text{dev}}$	Deivatoric Reynolds stress tensor [$m^2\ s^{-2}$]
$\boldsymbol{u}$	Fluid velocity vector [$m\ s^{-1}$]
Γ	Diffusion constant [$m^2\ s^{-1}$]
γ	Linear interpolation factor
ν_{eff}	Effective kinematic viscosity [$m^2\ s^{-1}$]
ν_{t}	Turbulent kinematic viscosity [$m^2\ s^{-1}$]
ν_{w}	Near-wall kinematic viscosity [$m^2\ s^{-1}$]
ω_{t}	Turbulent specific dissipation rate [$m^2\ s^{-3}$]
ϕ	Arbitrary field variable
ζ	k-ω-SST turbulence model coefficient
a_1	k-ω-SST turbulence model coefficient
b_1	k-ω-SST turbulence model coefficient
$CD_{k\omega}$	k-ω-SST turbulence model auxiliary relation
D_ω	k-ω-SST turbulence model effective diffusivity for the turbulent specific dissipation rate
D_k	k-ω-SST turbulence model effective diffusivity for the turbulent kinetic energy
E_{num}	Specific total system energy [$J\ kg^{-1}$]
e_{num}	Specific internal energy [$J\ kg^{-1}$]
F_1	k-ω-SST turbulence model auxiliary relation

F_2	k-ω-SST turbulence model auxiliary relation
G	k-ω-SST turbulence model turbulent kinetic energy production rate
H	Height [m]
h_e	Enthalpy [J]
k_t	turbulent kinetic energy [J]
k_C	Von Kármán constant
K_num	Specific kinetic energy [J kg^{-1}]
n	Distance of the first mesh element node from the wall [m].
n^+	Dimensionless distance of the first mesh element node from the wall.
P_rgh	Pressure excluding the hydrostatic contribution [Pa]
R_P	Wall roughness parameter
S_ω	k-ω-SST turbulence model source term for the turbulent specific dissipation rate
S_e	Energy source or sink term [J m^{-3} s^{-1}]
S_k	k-ω-SST turbulence model source term for the turbulent kinetic energy
u^+	Dimensionless fluid velocity at the first mesh element node from the wall.
u_w	Near-wall fluid velocity [m s^{-1}]

OpenFOAM field variables

alphat	Turbulent thermal diffusivity
k	Turbulent kinetic energy
nut	Turbulent viscosity
omega	Turbulent specific dissipation rate
p_rgh	Pressure excluding the hydrostatic contribution
p	Pressure when using a conjugate heat transfer solver
rho	Density
T	Temperature
U	Fluid velocity

Material and fluid properties

α	Thermal diffusivity [m^2 s^{-1}]
μ	Dynamic viscosity [kg m^{-1} s^{-1}]

ν Kinematic viscosity [$m^2\ s^{-1}$]

ρ Density [$kg\ m^{-3}$]

σ_0 Material constant for the starting stress for dislocation movement [Pa]

σ_y Yield stress [MPa]

c_p Specific heat capacity [$J\ kg^{-1}\ K^{-1}$]

d Average grain diameter [m]

k Thermal conductivity [$W\ m^{-1}\ K^{-1}$]

k_y Strengthening coefficient [$N\ m^{-\frac{3}{2}}$]

Geometrical terms

Δr Channel radii range [m]

$\Delta\tau$ Tortuosity range

γ Volume fraction

τ Tortuosity

τ_{IQR} Tortuosity interquartile range

θ TPMS-based lattice solid-void boundary shift

A_ν Specific surface area [$m^2\ m^{-3}$]

A_t Tile surface area [m^2]

$A_{w,s}$ Wetted surface area [m^2]

D_h Hydraulic diameter [m]

f Defines whether a TPMS-based structure is a network or matrix lattice

$k_{x,y,z}$ TPMS-based lattice periodicity in the x, y or z direction [m^{-1}]

$L_{x,y,z}$ TPMS-based lattice absolute size in the x, y or z direction [m]

$N_{x,y,z}$ Number of cell repetitions in the x, y or z direction

r Channel radius [m]

r_{max} Maximum channel radius [m]

r_{min} Minimum channel radius [m]

V_T Total volume [m^3]

V_w Wetted volume [m^3]

Hydraulic performance terms

ΔP_{exp} HIVE experimental pressure drop [Pa]

$\Delta P_{\text{num,fD}}$ HIVE numerical model pressure drop with a fully-developed inlet velocity profile [Pa]

$\Delta P_{\text{num,K}_\text{S}}$ HIVE numerical model pressure drop with a wall sand-grain roughness greater than 0 [Pa]

$\Delta P_{\text{num,S}}$ HIVE numerical model pressure drop with a wall sand-grain roughness of 0 [Pa]

$\Delta P_{\text{num,uni}}$ HIVE numerical model pressure drop with a uniform inlet fluid velocity profile [Pa]

ΔP_{num} HIVE numerical model pressure drop [Pa]

$\dot{V}$ Volumetric fluid flow rate [$\text{m}^3\ \text{s}^{-1}$]

A_T Total cross-sectional area [m^2]

f_D Darcy friction factor

K Darcian permeability constant [m^2]

K_1 Forchheimer permeability constant [m^2]

K_2 Inertial permeability constant [m]

P Pressure [Pa]

Re Reynolds number

u_eff Effective fluid velocity [$\text{m}\ \text{s}^{-1}$]

u_in Fluid inlet velocity [$\text{m}\ \text{s}^{-1}$]

u_l Local average fluid velocity [$\text{m}\ \text{s}^{-1}$]

u_max Maximum fluid velocity [$\text{m}\ \text{s}^{-1}$]

u_s Superficial fluid velocity [$\text{m}\ \text{s}^{-1}$]

u_i Fluid velocity on the mesh element i [$\text{m}\ \text{s}^{-1}$]

Thermal performance terms

ΔE Percentage change in thermal energy for a given temperature change [-]

ΔE_t Percentage change in thermal energy on the tile surface [-]

ΔT Change in temperature [K]

ΔT_LMTD Logarithmic mean temperature difference [K]

E Change in thermal energy for a given temperature change [J]

h Heat transfer coefficient [$\text{W}\ \text{m}^{-2}\ \text{K}^{-1}$]

h_l Local wall heat transfer coefficient [$\text{W}\ \text{m}^{-2}\ \text{K}^{-1}$]

$h_{\mathrm{m,vol}}$	Volumetric heat transfer coefficient [W m^{-3} K^{-1}]
h_{m}	Global mean heat transfer coefficient [W m^{-2} K^{-1}]
m	Mass [kg]
Nu	Nusselt number
Nu_{vol}	Volumetric Nusselt number
Q_{eff}	Effective incident power [W]
Q_{IC}	Induction coil power [W]
T	Temperature [K]
$T_{\mathrm{f,in}}$	Fluid inlet temperature [K]
$T_{\mathrm{f,out}}$	Fluid outlet temperature [K]
T_{h}	Heater temperature [K]
T_{rtp}	Initial temperature [K]
$T_{\mathrm{t,max}}$	Maximum tile surface temperature [K]
$T_{\mathrm{t,m}}$	Mean tile surface temperature [K]

General terms

$\boldsymbol{g}$	Standard acceleration due to gravity (9.81 m s^{-2})
$\frac{\epsilon}{D_{\mathrm{h}}}$	Wall relative roughness
τ_{w}	Wall shear stress [Pa]
D_{s}	Layer thickness [m]
E_{v}	Volumetric energy density [J m^{-3}]
Gr	Grashof number
h_{s}	Hatch distance [m]
K_{S}	Sand-grain roughness [m]
$K_{\mathrm{S}}{}^{+}$	Dimensionless sand-grain roughness
Q_{l}	Laser power [W]
R_{a}	Arithmetic average roughness [m]
r_i	Radial distance from the centre of the channel to the mesh element i [m]
t	Time [s]
U	Isosurface
u^*	Shear velocity [m s^{-1}]
u_{sv}	Scan velocity [m s^{-1}]

Chapter 1

Introduction

1.1 Motivation

Energy sources which are carbon-free and sustainable are crucial in combatting climate change and its impact on our planet. As global annual electricity demands are expected to increase substantially throughout this century (potentially reaching 10 TW from 2050−2100 [1]), a predictable baseload electricity supply will be needed to replace fossil fuels and accommodate the variation in energy generation from renewable sources (such as in wind and solar energy). The European Union has recognised the potential of nuclear fusion as a long-term, predictable and clean energy source. Nuclear fusion should aim to generate an average of 1 TW of electric power over the course of the 22$^{\text{nd}}$ century to make relevant global contributions [1].

In 2012, the European Fusion Development Agreement (succeeded by EUROfusion in 2014) created a 'technical roadmap' [2] with the aim of achieving commercialised fusion electricity. This was necessary because a long-term perspective is mandatory for Europe to keep its place as a world leader in fusion research. This plan covered the potential challenges that could affect controlled fusion development and also the planned construction of many facilities, such as the experimental fusion reactors ITER (latin for *the way*) and DEMOnstration power plant (DEMO). These facilities will aid in understanding and overcoming current and future engineering problems, such that a fully-scaled fusion power plant can be constructed successfully.

Major advances in fusion development lead to a revised roadmap in 2018 [1]. One of the major challenges identified in both roadmaps was that the ITER divertor would not be able to withstand the conditions expected to be found in DEMO. The divertor is an integral component of magnetic confinement fusion reactors (i.e., tokamaks) as it removes heat and helium ash from the system, minimises plasma contamination and protects the inner walls from thermal loads. The divertor therefore experiences much larger peak heat fluxes than other tokamak components where it is predicted to experience peak heat fluxes of up to 70 MW m^{-2} and neutron doses of 6-7 dpa fpy^{-1} in DEMO for two years with little to no maintenance [1, 3]. In 2014, the work package divertor (WPDIV) project was launched to deliver a holistic conceptual design solution and the core technologies for the DEMO divertor [3, 4]. The baseline DEMO divertor design was finalised in 2020 with the completion of the WPDIV pre-concept design phase [5]. Further maturation of the high heat flux technology will be a focus of the concept design phase [5], showcasing that there is still scope to improve the heat exhaust system within DEMO and, therefore, future fusion reactors. Further divertor improvements will likely be necessary for a fully-scaled nuclear fusion power plant.

Additive manufacturing (AM) has been identified as having significant potential applications in the design and construction of divertor targets. Parts produced via AM are made layer-by-layer, allowing them to have complex structures which cannot be manufactured using conventional, subtractive manufacturing methods [6]. While AM has commonly been used for lightweighting components [6, 7], it can also be used in the design of heat sinks to improve thermal performance. Triply periodic minimal surface (TPMS) based lattice structures can promote increased heat transfer and convection due to their enclosed channels, high surface-to-volume ratios and solid-fluid contact areas [8–11]. AM divertor targets, featuring complex TPMS-based lattice structures, therefore have the potential to improve the thermal performance of the divertor.

1.2 The research gap

A major challenge identified by the nuclear fusion industry, as reactors and facilities scale up, is that the divertor component will not be able to withstand the conditions expected to be found in such reactors [1]. TPMS-based lattice structures, manufacturable by AM, can potentially improve the thermal performance of the divertor. There are, however, insufficient studies on both the convective heat transfer properties and the performance of TPMS-based lattice structures compared to conventional structures, such as circular channels and fin arrays [12]. In addition, the effects of TPMS-based lattice structure design variables have received limited research [13].

1.3 Aim and objectives

The aims of this thesis were to (i) determine the impact of different geometrical properties on the hydraulic and thermal performance of TPMS-based lattice heat sinks and (ii) establish whether divertor target-like manifolds exhibit greater performance with the inclusion of TPMS-based lattice structures in fusion relevant conditions.

Numerical models were generated using Open-source Field Operation And Manipulation (OpenFOAM) v1812 [14], an open-source computational fluid dynamics (CFD) C++ solver, to simulate the fluid dynamics and conjugate heat transfer of the examined TPMS-based lattice structures. Heating by Induction to Verify Extremes (HIVE), a high heat flux testing facility operated by the United Kingdom Atomic Energy Authority (UKAEA), was used for physical testing and to validate the numerical models at fusion relevant conditions.

The following objectives, summarised in figure 1.1, were set to achieve these aims:

1. Determine the impact that volume fraction and fluid velocity have on the hydraulic and thermal performance of TPMS-based lattice heat sinks. This is given in chapter 5.
2. Establish structure-performance relationships for TPMS-based lattices structures by characterising their hydraulic and thermal performance, shown in chapter 5.
3. Ascertain the impact of tortuosity and channel radius on the hydraulic and thermal performance of TPMS-based lattice structures. This is discussed in chapter 6.
4. Determine the impact that fusion relevant conditions have on the hydraulic and thermal performance of divertor target-like manifolds, both experimentally and numerically. This is examined in chapter 7.

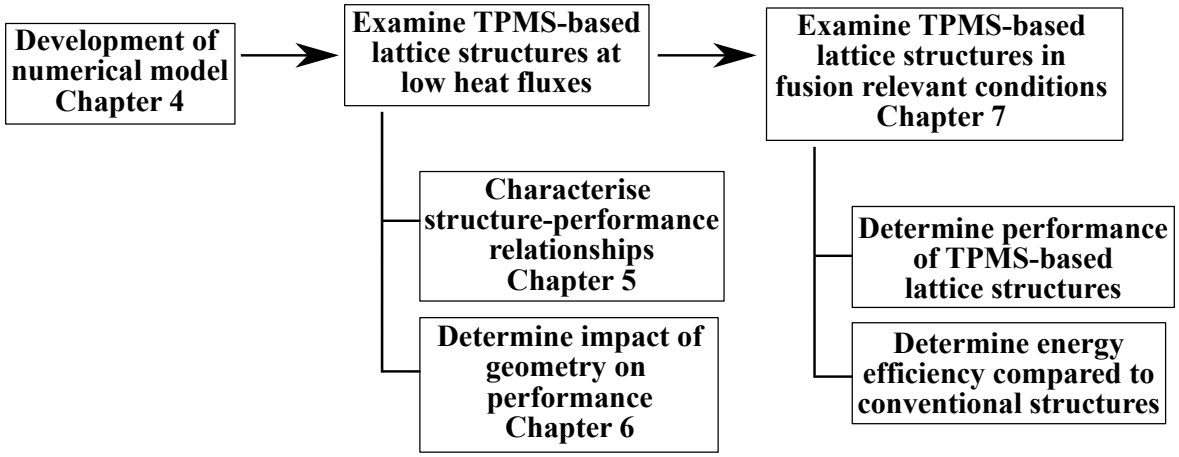

Figure 1.1: General work flow for this project.

5. Increase heat transfer within divertor target-like structures with the inclusion of TPMS-based lattice structures. This is discussed in chapter 7.

1.4 Outline

Chapters 2 and 3 discusses the literature relevant to AM and nuclear fusion, respectively. Chapter 4 discusses basic fluid dynamics principles and gives the general methodology used throughout this research project for the CFD of TPMS-based lattice structures. The hydraulic and thermal performance, characterised in terms of their principal design properties, are given in chapter 5, whereas the impact that different geometrical parameters have on the hydraulic and thermal performance of TPMS-based lattice structures are examined in chapter 6. Chapter 7 discusses the performance of the examined TPMS-based lattice structures in fusion relevant conditions. Finally, concluding remarks and a collection of proposals for future projects are given in chapters 8 and 9, respectively.

Chapter 2

Additive Manufacturing

2.1 Background

Additive manufacturing (AM) began as a tool to quickly prototype models with polymeric material to visualise them more effectively than traditional drawings or renders, without having to commit to costly and time-consuming manufacturing. This was known as *rapid prototyping*. As the technology improved however, these parts were no longer restricted to being prototypes and could instead be used as the final product. Some of these improvements include [6]:

1. The introduction of a wider range of materials, such as metals and composites.
2. Materials developed specifically for AM processes.
3. Improvements in computational technology.
4. The expansion of different AM processes suitable for different applications.
5. Improvements in hardware. The use of solid-state lasers in laser powder bed fusion (LPBF) has improved part quality, for example.

The term used to describe this technology became inadequate as its use deviated further from prototyping and new terminology was adopted to better express the basic principals of the technology [6]. The current adopted term is *additive manufacturing* and is defined by ISO/ASTM as the "process of joining materials to make parts from 3D model data, usually layer upon layer" [15]. This is the complete opposite of traditional (subtractive) manufacturing methods, where material is machined away until the part has the desired geometry.

An advantage of AM is that near-net shape parts can be built using only the raw materials required to build it, leading to less material wastage. AM can also manufacture complex internal geometries, such as tortuous channels and open cellular structures, which are not possible with subtractive manufacturing methods due to tool access restrictions. Figure 2.1 gives an example of an AM TPMS-based lattice structure. AM parts can be highly customisable and their topology can be optimised for specific applications, such as lightweighting and thermal management, due to the freedom offered in geometric design. The high customisability also allows AM to fill certain industry niches, such as parts which need to be tailored for end-users or highly specialised parts which can not be manufactured on a large-scale [6]. This is particularly the case for medical applications [16], where each patient requires a unique solution. Some of the common uses of AM here are the production of artificial tissues and organs [17], personalised implants

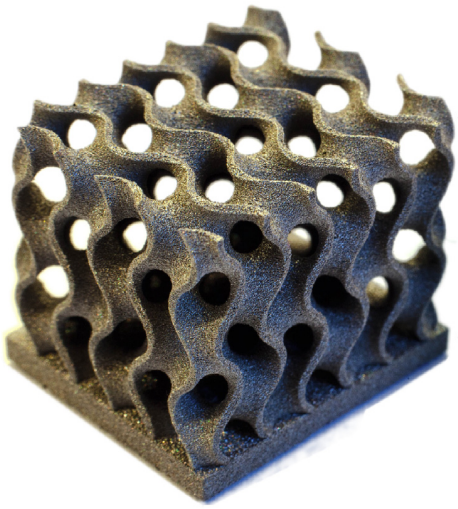

Figure 2.1: Example of an additively manufactured tungsten gyroid lattice produced by laser powder bed fusion [22].

[18] and orthodontic appliances [19]. Metal AM parts have also been used across a wide range of industries. One such example is the aerospace industry [20], where the GE Leading Edge Aviation Propulsion (LEAP) fuel nozzle has been a notable commercial success [21].

Each AM process has a different method for building parts and comes with their own inherent advantages and disadvantages. The next section will give an in-depth explanation on the LPBF process and why it was used in this research project.

2.2 Laser powder bed fusion

LPBF is an important AM process as it can produce near fully-dense metal parts with complex structures. It also has the potential of providing greater financial and environmental sustainability compared to traditional manufacturing methods as unused powder can be recycled [6].

LPBF processes share similar methodologies, depicted in figure 2.2, with only slight variations. The building process begins by distributing a layer of powder across the build plate with the aid of a roller or scraper. A laser then induces fusion between the powder particles by scanning the relevant sections. Once one layer has been scanned, the build plate is lowered by one powder layer thickness and the whole process repeats itself until the part has been fully built [6].

There are multiple different powder binding mechanisms within LPBF, but the focus here is on full-melting as this is the most applicable mechanism for metals. In this case, the entire region subjected to the thermal energy is melted to a depth exceeding the layer thickness, known as the melt pool. This allows for partial re-melting of the previously solidified layers, as shown in figure 2.3. Melt pool formation and characteristics are fundamentally determined by the energy absorbed by the powder bed [6]. A simplified model using volumetric energy density, E_{v}, allows for an analytical approach to optimise machine performance for a given material. This was shown by Caiazzo *et al* [24], where it was found that the volumetric energy density had a significant statistical impact on the features, such as surface roughness, of LPBF-produced

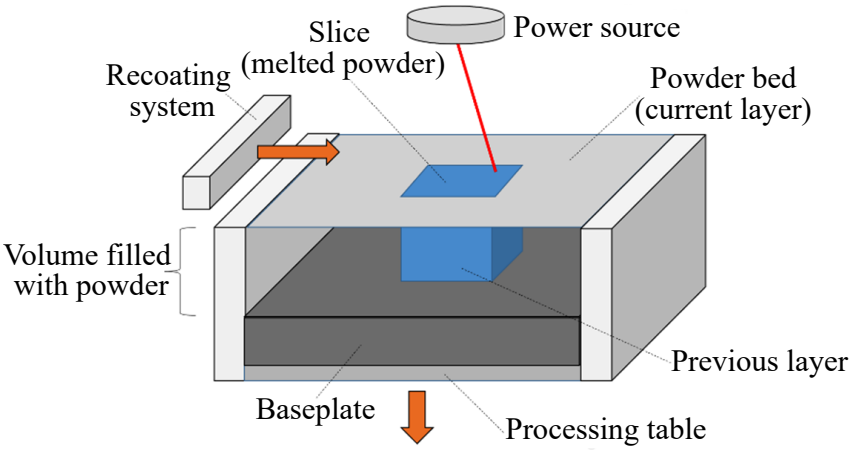

Figure 2.2: General schematic for a laser powder bed fusion machine. Modified from [23].

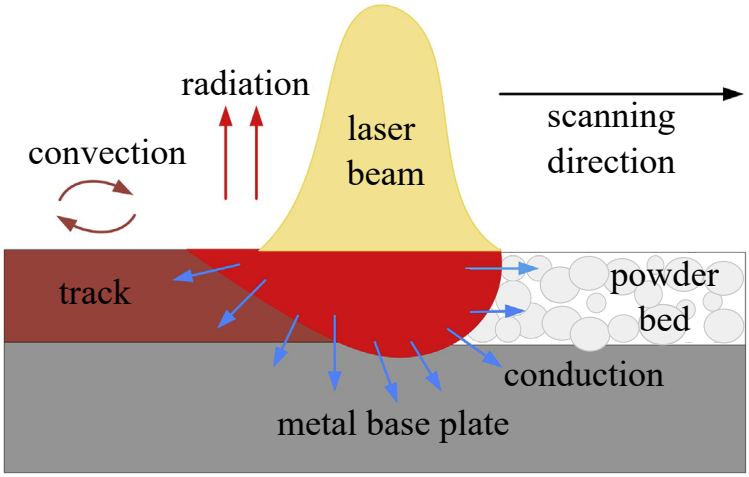

Figure 2.3: Heat transfer from the melt pool to the surrounding area. Modified from [26].

Inconel-718 parts. The volumetric energy density is calculated by [24, 25]

$$E_{\mathrm{v}} = \frac{Q_{\mathrm{l}}}{u_{\mathrm{sv}}\, h_{\mathrm{s}}\, D_{\mathrm{s}}}\,, \tag{2.1}$$

where Q_{l} is laser power, u_{sv} is scan velocity, h_{s} is hatch distance and D_{s} is layer thickness. It is apparent from equation 2.1 that many variables that play a role in the energy absorbed by the powder bed (powder absorptivity, heat of fusion, laser diameter, etc.) are not included [27]. Users must therefore not make the mistake that this model fully represents the physics of this process.

Parts built from LPBF have fine microstructures compared to traditionally manufactured parts due to the high thermal gradients and solidification rates present during manufacturing. The microstructure is important because it has a large impact on thermomechanical properties such as yield strength, conductivity and ductility. Dislocations within the microstructure of the material cause shear strains that can lead to cracking and failure, but the presence of grains and grain boundaries can dampen this effect. This is because dislocations in one grain cannot propagate to the next grain. An increase in grain number therefore leads to a stronger part

because the dislocations travels a shorter distance before being impeded by another grain [28, 29]. This is quantified by the Hall-Petch relationship,

$$\sigma_{\mathrm{y}} = \sigma_0 + \frac{k_{\mathrm{y}}}{\sqrt{d}}, \tag{2.2}$$

where σ_{y} is the yield stress, σ_0 is a material constant for the starting stress for dislocation movement, k_{y} is the strengthening coefficient and d is the average grain diameter. This relationship is invalid for ultrafine-grained materials, however [30].

Whilst cast parts have equiaxed grain structures, LPBF parts typically feature both elongated and equiaxed grain structures, as shown in figure 2.4. The microstructure of LPBF parts is dependent on the temperature gradient at the solid-liquid interface of the melt pool and the growth rate of the solidifying front [31], as shown in figure 2.5. The ratio of these two parameters gives the morphology of the grains and their product gives the size of the microstructure [32, 33]. LPBF process parameters, such as laser power and absorptivity, impact the above parameters and therefore play a large role in the formation of the microstructure [34–36]. The microstructure can also be altered via recrystallisation and grain growth. This can be achieved through post-manufacture heat treatments, such as annealing [35].

Despite the advantages of using LPBF, there are limitations associated with this process. Hollow structures cannot be manufactured because it would be impossible to remove the trapped powder within. There are also difficulties associated with manufacturing overhangs due to the metal powders' low density, where the powder is not able to support the overhang [6], and thermal conductivity, which leads to severe local heating [38]. Support structures therefore need to be included to mitigate part deformation if the manufactured part is not self-supporting. This reduces the sustainability of LPBF as some of the material needs to be used for supports, which is then disposed of [6]. Unmelted powder cannot be infinitely recycled due to powder particle degradation from exposure to elevated temperatures. The degraded powder particles can agglomerate, which impacts the flowability of the powder, and risk contamination from gas pick-up, which leads to part defects [39]. Weld fume and spatter are also produced during this process and can have adverse effects on the part. Weld fumes are airborne powder particles which can cloud the laser beam and decrease the energy absorbed by the powder. Weld spatter is melted material ejected from the melt pool and can be caused by a number of different mechanisms, as discussed

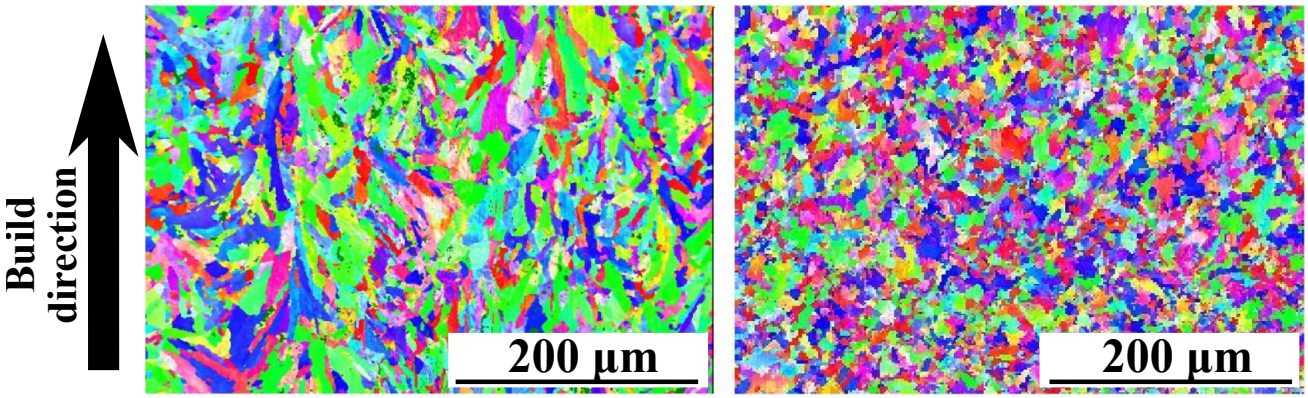

Figure 2.4: Electron backscattered diffraction images of the microstructure of a laser powder bed fusion part. Elongated grains were observed in the build direction (left) and equiaxed grains were observed in the transverse direction (right). Modified from [37].

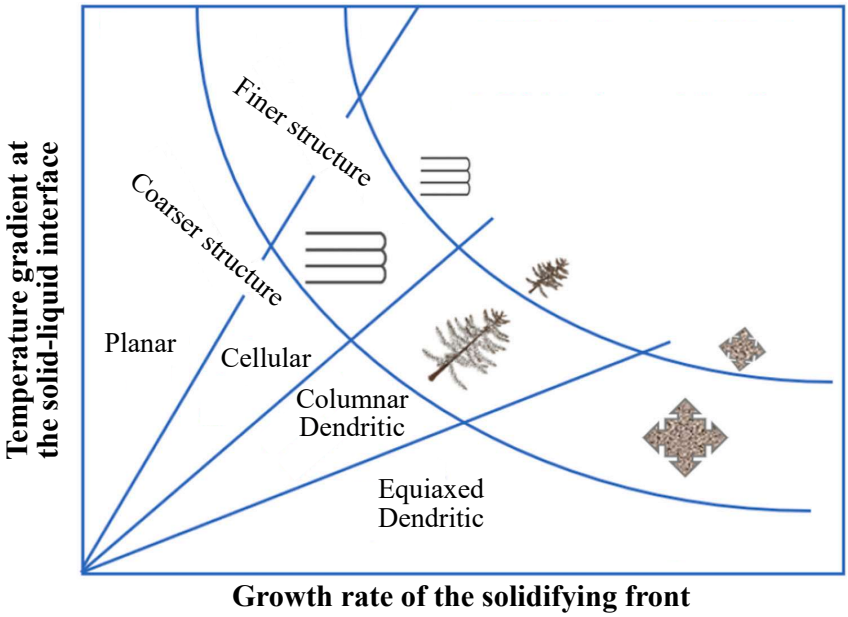

Figure 2.5: Dependency of the morphology and size of a laser powder bed fusion part microstructure on the temperature gradient at the solid-liquid interface and the growth rate of the solidifying front. Modified from [33].

by Wang *et al* [40]. Spatter can also undergo oxidation and changes in chemical composition during in-flight cooling, contaminating the powder bed with different microstructures and particle sizes [40]. This has a large effect on surface roughness and porosity. Fortunately, the fumes and spatter can be mostly removed from the system via an inert gas flow within the chamber [26, 41].

Manufactured parts can suffer from a number of different defects; the most common being porosity, residual stresses, geometric defects and surface defects [23]. Porosity strongly impacts fatigue performances and crack growth characteristics of a part. The parameters with the greatest impact on porosity are powder-related parameters and the energy absorbed by the powder bed. Anisotropic residual stresses between layers are caused by the high temperature gradients present as the powder melts and re-solidifies rapidly. This can lead to part cracking and delamination when the residual stress exceeds its ultimate tensile strength. Geometric and dimensional deviations from computer-aided design (CAD) models have been reported in LPBF parts. This includes part shrinkage (typically 3-4% [6]), part growth and warping. High surface roughness is generally considered as a defect because they adversely affect fatigue performance. They can be beneficial in heat sinks however, as they disrupt viscous fluid flow in the near-wall region, which improves heat transfer. Many of these part defect effects can be reduced during the post-processing phase, though this proves to be more difficult for TPMS-based lattice structures. Grasso and Colosimo [23] provide a thorough review of the possible part defects and their impacts.

Despite these issues, LPBF was the chosen AM process for this research project because it is able to produce fine and complex metal structures with a relatively high surface roughness and resolution. Additionally, many lattices are self-supporting and the only supports required are between the powder bed and the bottom of the part. While high residual stresses are present in LPBF parts, these can be reduced to an acceptable level using post-processing techniques.

2.3 Cellular structures

Foams, honeycombs and lattices are a subcategory of cellular structures, which are structures made of an interconnected network of plates, struts or unit cells [42] and are typically periodic. Cellular structures have unique and useful properties [43] due to their geometries. While they are more commonly used for lightweighting [6, 7], there is interest in using them for cooling applications [8–10], such as heat exchangers and heat sinks, due to their high surface-to-volume ratios and solid-fluid contact areas.

Cellular structures cannot generally be manufactured conventionally due to their complex geometries, though foams can be made through gas injection moulding [7]. Many AM processes can be used to manufacture cellular structures however, and the study of cellular structures has therefore experienced a resurgence with the growth of AM [6].

A key challenge in designing cellular structures for specific applications is choosing the appropriate design variables; such as material, cell type and volume fraction. These variables are important in determining the thermomechanical properties of a lattice, but the exact relationships between the properties and design variables are generally poorly understood. Research regarding the influence of design variables on the thermal properties of cellular structures has garnered more interest lately. For example, Bracconi *et al* [44] found that the ratio between node and strut diameter has a strong influence on the effective heat conduction performance of open-cell foams.

Lattices have received significant attention in the literature [6, 45] and can be divided into two groups, surface-based and strut-based lattices, which are depicted in figure 2.6. The former offer several potential advantages over the latter as they have enclosed channels (ideal for fluid flow), higher surface areas and are typically stronger for a given weight [11]. Surface-based lattice structures therefore offer unique advantages for fluid flow and heat transfer applications, in addition to other niche areas such as intervertebral devices [46].

There also exists a subset of surface-based lattice structures known as TPMS-based lattices, which are structures which have minimal surfaces (i.e., zero mean curvature). TPMS-based

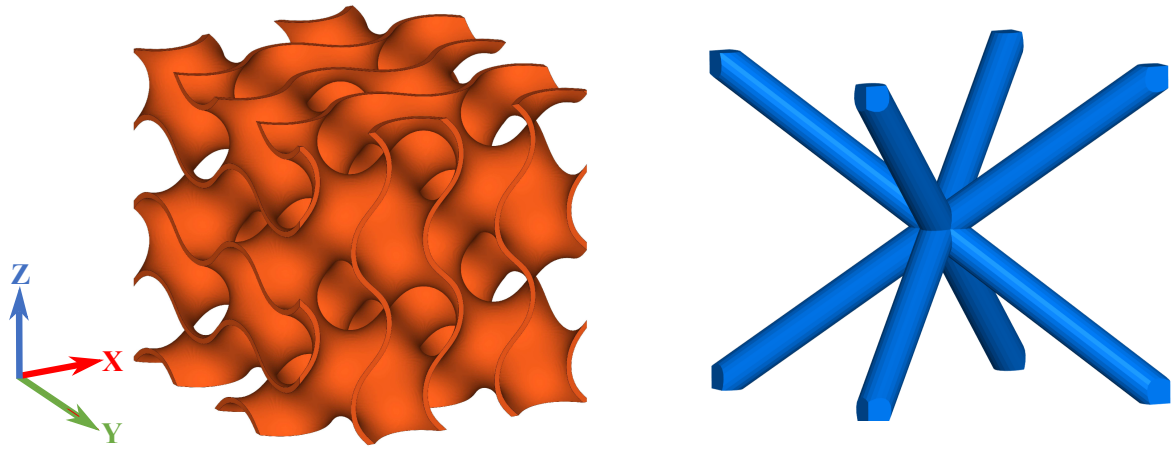

Figure 2.6: Example of a surface-based gyroid matrix lattice structure (left) and a strut-based body-centered cubic lattice structure (right). Modified from [47].

lattices are generated by finding the isosurface from their surface equations. Minimal surfaces can be approximated using Fourier series expansions of trigonometric terms, where the inclusion of more terms brings the approximated surface closer to the TPMS [48, 49]. The surface approximation for a gyroid lattice (G) is given below

$$U_{\mathrm{G}} = \big(\sin(k_x x)\cos(k_y y) + \sin(k_y y)\cos(k_z z) + \sin(k_z z)\cos(k_x x)\big)^f - \theta^f \,, \tag{2.3}$$

where U is the isosurface, $k_{x,y,z} = 2\pi\,(N_{x,y,z}/L_{x,y,z})$ is the lattice periodicity, $N_{x,y,z}$ is the number of cell repetitions and $L_{\mathrm{x,y,z}}$ is the absolute size. The lattice space is divided into two separate regions by the $U = 0$ isosurface; a solid region where $U \leq 0$ and an empty region where $U > 0$. This is shown in figure 2.7. The position of the solid-void boundary is shifted by θ, which changes the volume fraction of the TPMS-based lattice. By correlating the volume fraction and θ for different cell types, lattice structures with predefined volume fractions can be generated [50].

TPMS-based lattice structures can be further subdivided into 'network' and 'matrix' phases by setting the variable f to either 1 or 2, respectively, in equation 2.3. Network phase lattices consist of two continuous regions, one solid and one void, while matrix phase lattices have three continuous regions, two void regions with equivalent geometries and one solid region separating them. Matrix phase lattices posses greater surface-to-volume ratios than their network phase counterparts [51].

Two dimensional honeycomb lattices based on TPMS-based lattice structures can be approximated from the relevant TPMS equation by omitting the terms in the direction where the geometry of the honeycomb lattice is invariant [47]. The isosurface equation for a honeycomb gyroid lattice (HG) invariant in the z-direction is therefore given as

$$U_{\mathrm{HG}} = \big(\sin(k_x x)\cos(k_y y) + \sin(k_y y) + \cos(k_x x)\big)^f - \theta^f \,. \tag{2.4}$$

These structures typically consist of one continuous solid region and multiple unconnected voids.

Strut-based lattice structures (e.g., body-centred cubic cell types) are generally constructed by forming three dimensional intersections from rigid struts and repeating them periodically. Changing the volume fraction of this structure requires varying the thickness of the individual struts.

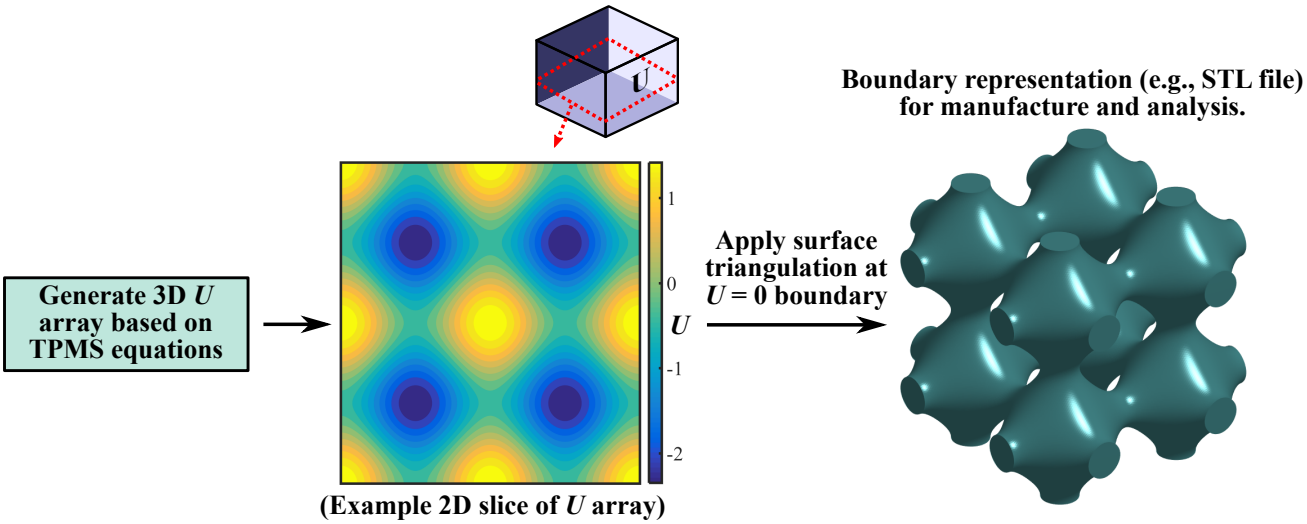

Figure 2.7: How surface-based lattice structures are designed from the U isosurface. Modified from [47].

This makes generating strut-based lattice structures with a predetermined volume fraction difficult when compared to TPMS-based lattices, which can be graded more easily through direct manipulation of their underlying equations [50].

The geometry of strut-based lattice structures can be approximated using TPMS equations. This results in a surface-based lattice with geometries similar to strut-based lattices, where the volume fraction can be controlled in the same manner as a conventional TPMS-based lattice. In this case, the intersection between the struts become smooth curves instead of sharp corners, reducing stress concentrations when the structure is subject to a load [50]. Figure 2.8 provides visual examples of the matrix, network, honeycomb and strut surface-based lattice structures.

2.4 Additively manufactured heat transfer devices

Common heat transfer devices in industry include heat sinks [52, 53] and heat exchangers [54]. Heat sinks typically employ circular channels or extended surfaces, such as fin arrays, depicted in figure 2.9, where heat is dissipated by a fluid. Heat exchangers are similar but generally transfer heat between different fluid mediums. The fluids can either be in direct contact with each other or separated by a wall. The latter case is depicted in figure 2.10.

Improving the performance of heat transfer devices has been a major goal for researchers in

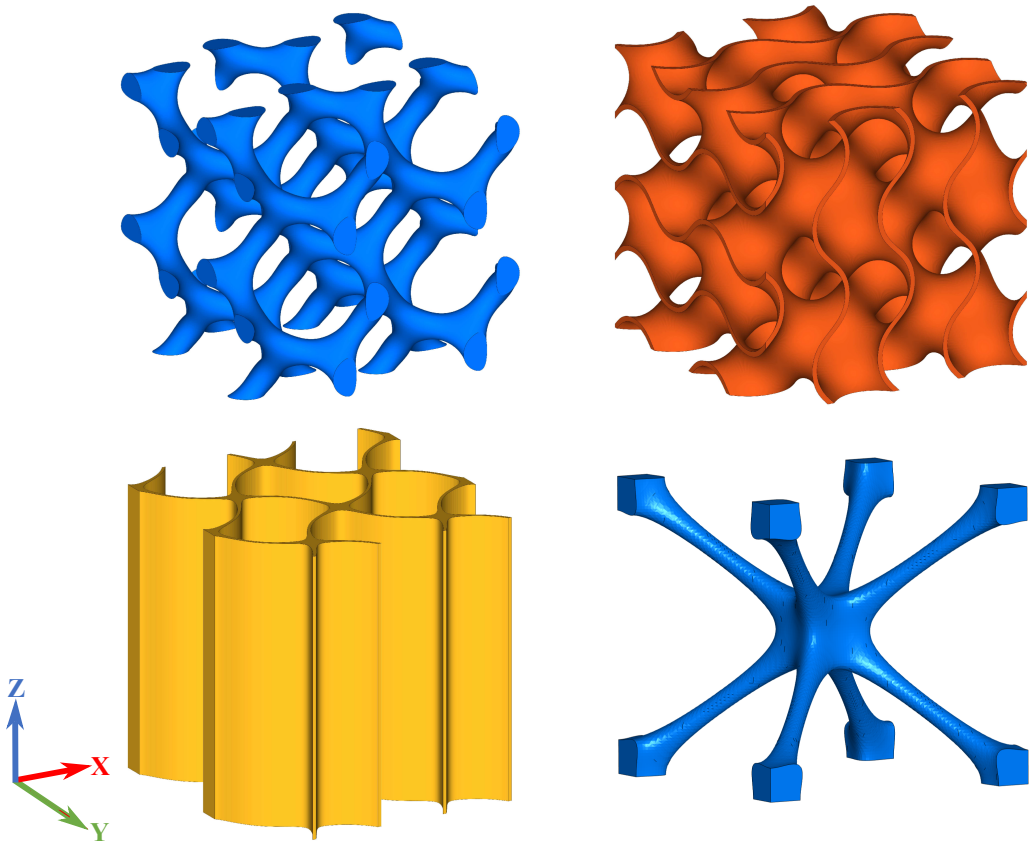

Figure 2.8: Examples of different surface-based lattice structure forms, such as the gyroid network (top left), gyroid matrix (top right), gyroid honeycomb (bottom left) and body-centered cubic strut (bottom right) lattices. Modified from [47].

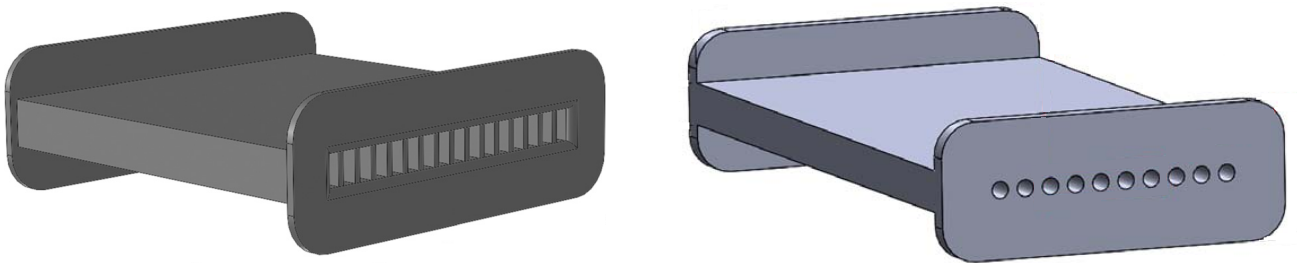

Figure 2.9: CAD models for an additively manufactured fin array heat sink by Stimpson *et al* [55] (left) and an additively manufactured circular channel heat sink by Wildgoose *et al* [56] (right).

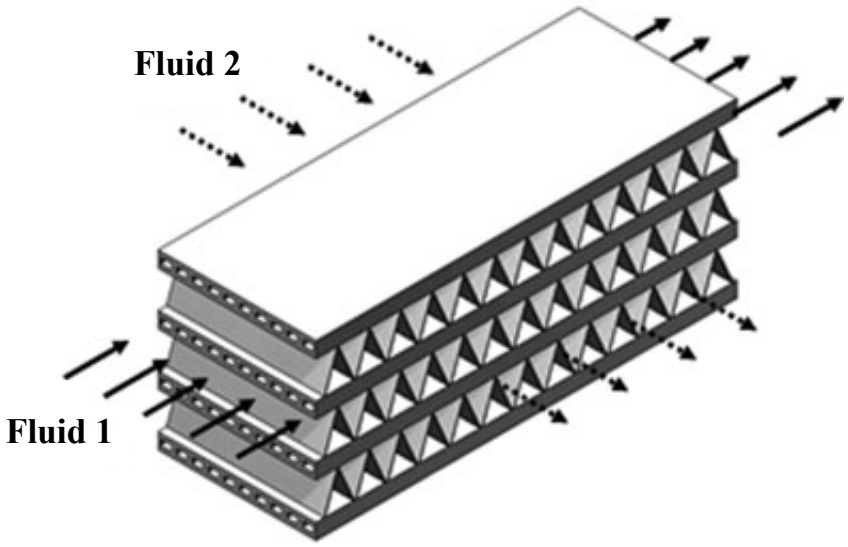

Figure 2.10: Example heat exchanger design, where two different fluid mediums are separated by a wall. Modified from [57].

recent decades due to increasing power demands across different industries, such as the nuclear fusion and automotive sectors [53, 58], and the miniaturisation of electronic components [52]. The need to dissipate growing quantities of heat from small volumes has therefore become important. LPBF has been identified as a manufacturing method that can improve heat transfer device performance [58]. This is because it can manufacture extended surfaces (increasing surface area), complex geometrical features (promoting fluid mixing) and small structures.

The thermal and hydraulic performance of LPBF heat sinks and exchangers are dependent on the manufacturing process. Stimpson *et al* [55] showed that LPBF fin arrays with arithmetic average roughnesses, R_a, between 9.5−13.8 μm exhibited higher pressure drops than their smooth counterparts due to increased surface roughness (associated with the LPBF process) when Reynolds numbers, Re, of approximately 100−50,000 were used. The friction factor, a parameter which relates pressure drop due to friction along a channel, also increased with decreasing hydraulic diameter due to the higher roughness-to-hydraulic diameter ratio. Kirsch and Thole [59] found that the surface roughness and pin shape of LPBF pin arrays (with arithmetic average roughnesses of approximately 0.074−0.1 mm) are linked to the pin density, which thereby informs the heat sink performance, when examined using Reynolds numbers of 400−20,000. While the friction factor of smooth pin arrays is generally independent of the pin streamwise spacing (distance between

pins in the fluid flow direction), differences in the friction factor between two LPBF pin arrays with equal pin spanwise spacing (distance between pins in the fluid flow normal direction) but different streamwise spacings were observed and attributed to the different surface roughnesses. It was also found that LPBF pin arrays heated by constant temperature copper block on the end walls exhibited greater heat transfer than equivalent smooth pin arrays when the pin spanwise spacing was small. This was because the surface roughness increased the strength of the pin wake interactions, which is an important heat transfer mechanism in pin arrays. Build direction also has a large impact on the surface roughness and hence thermal performance of LPBF parts. Wildgoose *et al* [56] showed that build angles, visually depicted in figure 2.11, smaller than 60° impacted the channel shape and increased the surface roughness of circular channels. Friction factor could therefore be minimised by ensuring that the build angle remains between 60° and 90°. It was also found that heat transfer in these structures for Reynolds numbers ranging from 5,000−50,00 peaked for build angles between 30° and 45°, likely due to the increased surface roughness and non-circular shape.

TPMS-based lattice structures manufacturable by LPBF could potentially improve heat transfer device performance for a given design space due to their unique geometrical features (discussed in section 2.3). Jafari and Wits [58] reviewed the development of LPBF heat sinks, heat exchangers and heat pipes. While many different geometries were discussed within the context of these devices, such as strut-based lattices and fin arrays, TPMS-based lattice structures were not mentioned. Additionally, research on AM heat sinks has generally been dedicated towards foams [60–63], strut-based lattices [64–69] and conventional pin or fin arrays and circular channels [55, 56, 59, 69]. TPMS-based lattice structures have historically not received widespread attention for heat transfer applications across the AM and heat exchange communities, as noted by Tang *et al* [12]. Yeranee and Rao [13] have also argued that the effects of TPMS-based lattice structure design variables, such as volume fraction, have received limited research.

Interest in examining the effect of TPMS-based lattice structures for heat exchange applications

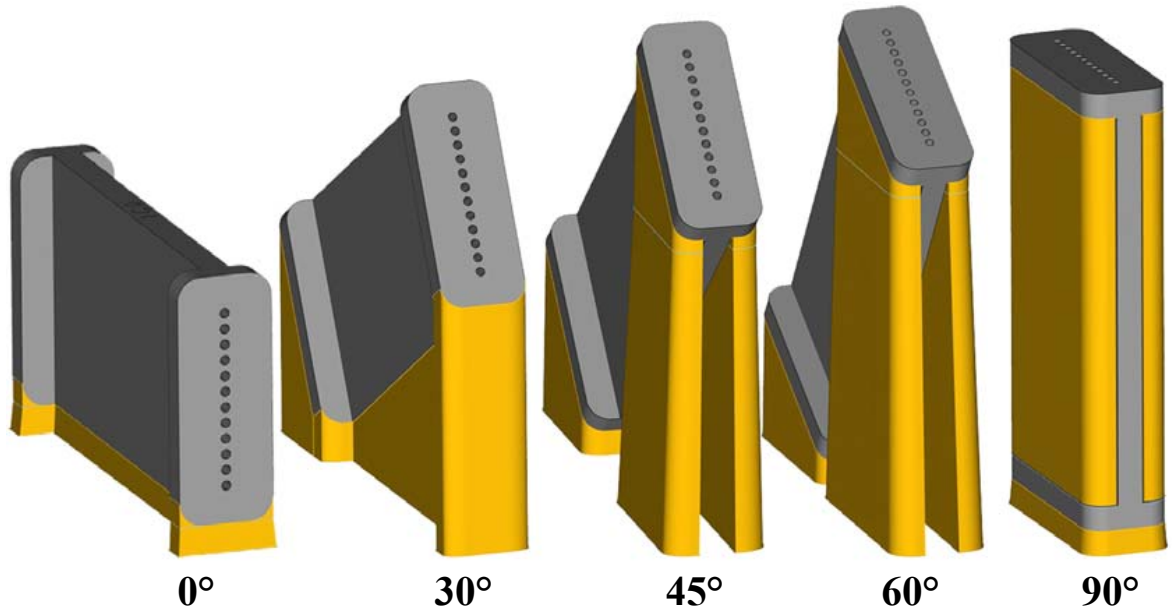

Figure 2.11: Depiction of build angles for LPBF parts produced by Wildgoose *et al* [56]. Support structures are shown in yellow. Modified from [56].

has grown in recent years, however. This includes injection mold cooling [70], latent heat thermal energy storage systems [71–73] and heat sinks and exchangers [12, 13, 74–81]. Pulvirenti *et al* [74] conducted a numerical study into the gyroid matrix lattice for Reynolds numbers between 3.6 and 21.6, inlet fluid temperatures of 20 °C and constant solid temperatures of 25 °C, 50 °C and 75 °C. The lattice structure was found to be characterised by local volumetric heat transfer coefficients similar to those of other periodic structures, such as the Kelvin geometry [62, 63]. Different TPMS-based lattice cell types exhibit different heat transfer capabilities due to their geometrical differences. This was shown independently by Al-Ketan *et al* [75], where the heat transfer coefficient for the diamond matrix cell type was 32% larger than the gyroid matrix cell type for Reynolds numbers of 4,080−65,000 and input powers of 50−500 W, and Cheng *et al* [76], where the gyroid matrix cell type exhibited greater volumetric heat transfer coefficients than the primitive matrix cell type for Reynolds numbers of 11.23−67.51, a fluid inlet temperature of 45 °C and an initial solid temperature of 150 °C. Attarzadeh *et al* [77] found that the design parameters of an individual TPMS-based lattice cell type affects the thermal performance of the lattice, as it was shown that diamond matrix lattices with smaller wall thicknesses exhibited greater heat transfer coefficients for Reynolds numbers of 25−125, inlet fluid temperatures of 273 K and the structure being heated from above by 313 K. This method was dependent on the surface area of the examined lattice structures however, which inflated the results for structures with greater surface area (i.e., structures with smaller wall thicknesses). Care must therefore be taken when examining structures with different surface areas. Attarzadeh *et al* [81] also found that both the fluid properties (such as density and viscosity) and initial temperatures had a large impact on the thermal performance of an individual TPMS-based lattice cell type for Reynolds numbers less than 150 and using the same thermal parameters used by Attarzadeh *et al* [77].

The hydraulic performance of heat sinks is also important. Structures with low permeabilities (i.e., exhibit large pressure drops) require greater power consumption to drive the coolant, negatively impacting the efficiency of the heat sink [82–84]. Additionally, different geometries affect the hydraulic performance and, hence, the fluid dynamics. This has a significant impact on the thermal performance of the heat sink as convective cooling is typically the dominant heat transfer mechanism in fluids [85]. Santos *et al* [83] examined the permeability of a range of TPMS-based lattice structures for volumetric flow rates of 1−100 mL min^{-1} and found that their hydraulic performance was described by the Darcy-Forchheimer law, which relates pressure drop to fluid velocity. It was also shown that specific cell types were not inherently more permeable than other cell types. This is depicted in figure 2.12, where the primitive matrix cell type exhibited a lower Forchheimer permeability than the gyroid matrix cell type at low porosities (starting from a porosity of 50%) but a higher Forchheimer permeability at high porosities (up to a porosity of 80%).

The study of AM TPMS-based lattice structures in relation to conventional structures for heat exchange is important. This will indicate whether TPMS-based lattice structures warrant further research and if they are an improvement over current designs. Femmer *et al* [79] found that heat exchangers featuring primitive, diamond, gyroid and I-graph and wrapped package-graph (IPW) matrix lattice structures, using two coolants (at 50 °C and 5 °C) flowing with Reynolds numbers from approximately 1−15, exhibited greater Nusselt numbers (up to an order of magnitude) than a flat plate or a circular channel. The examined TPMS-based lattice structures also exhibited greater pressure drops than a circular channel. Tang *et al* [12] found similar results for heat sinks, with an initial temperature of 293.15 K, heated by a surface at 373.15 K on the bottom plane and cooled by a coolant flowing with Reynolds numbers of 135−3,500. The gyroid, diamond

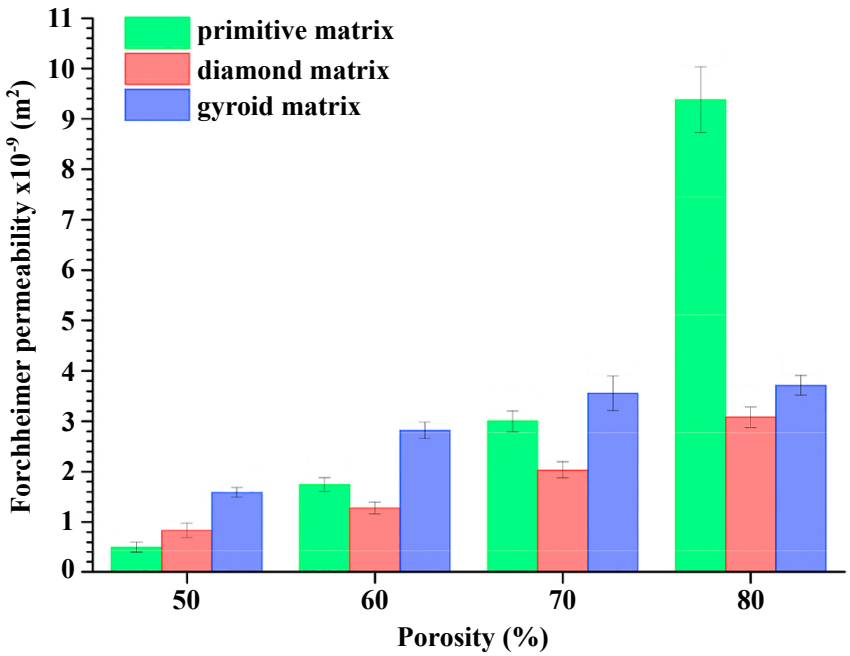

(a) Forchheimer permeabilities. Modified from Santos *et al* [83].

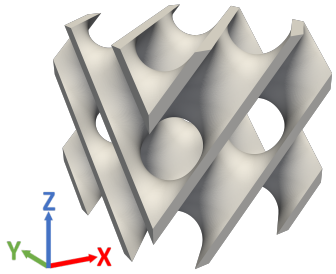

(b) Diamond matrix unit cell.

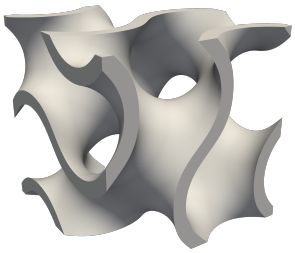

(c) Gyroid matrix unit cell.

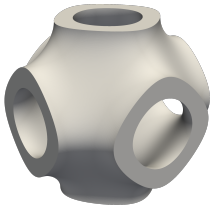

(d) Primitive matrix unit cell.

Figure 2.12: Forchheimer permeabilities calculated by Santos *et al* [83] for the depicted TPMS-based lattice cell types.

and IWP matrix lattice structures exhibited greater averaged heat transfer coefficients than the examined fin array. The diamond matrix lattice structure exhibited the greatest improvement in relation the fin array, with averaged heat transfer coefficients greater by 85−207%, and the IWP matrix lattice structure exhibited the smallest improvement, with averaged heat transfer coefficients greater by 16−55%. Tang *et al* [12] also identified that the differences in performance between TPMS-based lattice structures and conventional structures needs further research.

2.5 Summary

AM is a manufacturing method where material is joined, usually layer upon layer, from 3D model data [15]. This is in contrast to conventional manufacturing methods where material is machined away. AM has numerous advantages over conventional manufacturing methods, such as reduced material wastage, the ability to manufacture complex internal geometries and high component customisability (such that parts can be optimised for specific applications) [6]. LPBF, one of the many available AM processes, can produce fully-dense metal parts with fine, complex structures for different applications, such as for lightweighting or heat transfer [6]. The

use of metal AM parts has been increasing within different industries, with a noticeable example being the GE LEAP fuel nozzle [21] within the aerospace industry.

Cellular structures (structures which are typically periodic and are made of an interconnected network of plates, struts or unit cells [42]) have seen increased prominence within research alongside the growth of AM. This is because they generally cannot be manufactured due to their complex geometries [6]. There are many subcategories of cellular structures, such as TPMS-based lattice structures, which are surface-based lattice structures which have minimal surfaces (i.e., zero mean curvature). These structures have enclosed channels, high surface areas and strength for a given weight [11]. These features are advantageous for convection-based heat sink applications.

Whilst AM and LPBF parts have seen widespread research for heat transfer applications, Tang *et al* [12] stated that TPMS-based lattice structures have seen relatively little interest within the AM and heat transfer communities. The effects of TPMS-based lattice structure design variables have also received limited research according to Yeranee and Rao [13]. TPMS-based lattice structures show great promise for heat sink applications from the available research however, where Femmer *et al* [79] found that TPMS-based lattice heat exchangers exhibited greater Nusselt numbers than a plate or a circular channel but also exhibited greater pressure drops. Tang *et al* [12] found similar results for TPMS-based lattice heat sinks, which exhibited greater heat transfer coefficients than a fin array.

To fully realise the potential of TPMS-based lattice heat sinks, design guides for fluid flow and heat transfer, similar to the Gibson-Ashby scaling laws for stiffness or thermal conductivity [45], need to be established in terms of their principal geometrical and design variables. This work therefore aims to characterise the hydraulic and thermal performance of a selection of TPMS-based lattice structures in terms of their principal geometrical properties. These can be used to determine the effect of different geometrical properties on the hydraulic and thermal performance and to establish design guides.

If this research project is able to show that TPMS-based lattice structures are promising candidates for heat sink applications, through the characterisation of their hydraulic and thermal performance, then there will be greater interest in examining these structures and they may eventually see use within industrial components. This would also further propel the AM industry into multiple sectors which depend on heat transfer devices. Additionally, a design guide would aid engineers and lattice designers in designing TPMS-based lattice structures which minimise pressure drop whilst achieving a specified heat transfer coefficient without the need for expensive physical or numerical testing. This would be important for various applications which require enhanced cooling.

Chapter 3

Nuclear Fusion

3.1 Background

Nuclear fusion generates energy through the merger of two light nuclei to form products with a total mass that is less than the sum of its parts. This mass difference is converted into energy. A deuterium-tritium (D-T) fuel source is commonly used in fusion reactors, which undergoes the following reaction

$$ {}^{2}_{1}\mathrm{H} + {}^{3}_{1}\mathrm{H} \rightarrow {}^{4}_{2}\mathrm{He} + {}^{1}_{0}\mathrm{n}\,, \tag{3.1} $$

where ${}^{2}_{1}\mathrm{H}$ is deuterium, ${}^{3}_{1}\mathrm{H}$ is tritium, ${}^{4}_{2}\mathrm{He}$ is helium and ${}^{1}_{0}\mathrm{n}$ is a neutron. This reaction releases approximately 17.6 MeV, with the neutron having a kinetic energy of up to 14 MeV, and produces no greenhouse gasses. In addition, deuterium is naturally abundant in oceans and tritium can be produced via a reaction between lithium and a neutron. The global deuterium and lithium resources should theoretically be able to satisfy the world's energy demand for millions of years, providing a long-term energy solution [1].

To achieve nuclear fusion, atomic nuclei need to collide at sufficiently high speeds and energy to overcome the electromagnetic repulsion. The fuel source needs to be heated to approximately $2{\times}10^{8}$ K, at which point the atoms have ionised into plasma. In magnetic confinement fusion, this reaction is confined to the vacuum vessel of a tokamak through the use of toroidal and poloidal magnetic field coils. The plasma current and coils gives rise to strong helical magnetic fields, shown in figure 3.1 [1].

There are a number of significant challenges within nuclear fusion. The magnetic fields must be strong enough to confine the plasma away from the plasma-facing walls of the vacuum vessel, for example. This is because plasma-wall interactions can cause extensive damage to the walls. Despite the strong magnetic fields, plasma ions still collide with the walls, which releases heavier elements from the wall into the plasma, where they ionise, via sputtering. The heavy ions cool the plasma through radiation, preventing plasma ignition, and can be redeposited on to the surface of the wall, inducing morphological and compositional changes [87, 88]. Fuel particles can also be embedded on to the walls, which affects its structural properties and decreases the fuel density within the plasma. These are issues which severely impact core plasma performance [88].

The neutrons produced from the reaction in equation 3.1 activate the surrounding materials and cause irradiation damage, such as swelling and embrittlement, which has a negative impact on the thermal and mechanical properties of the components. This happens due to transmutation reactions within the material, which produces hydrogen and helium atoms and changes the

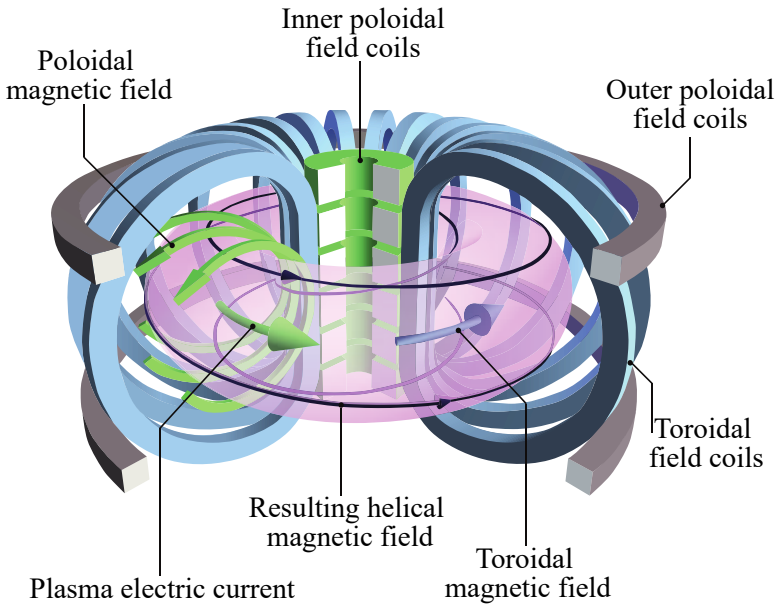

Figure 3.1: Representation of the magnetic fields inside a tokamak. Modified from [86].

composition of the metal or alloy. Therefore, materials with low activations that can resist high energy neutron irradiation are desired for the plasma-facing units (PFU) in a tokamak. [22, 89].

3.2 Facilities

EUROfusion designed a roadmap [1] which detailed the facilities that need to be built before a fully scaled nuclear fusion power plant is possible, shown in figure 3.2. There are also multiple governmental organisations and private companies worldwide which are working towards scaling up fusion technology and building their own tokamaks. A selection of these facilities are briefly discussed below to provide an idea of the advances required in fusion technology to develop a nuclear fusion power plant.

3.2.1 ITER

Construction of ITER began in 2010 in France and was initially expected to be completed by 2025 [1], though the earliest possible completion date is currently 2027. This is due to delays associated with the COVID-19 pandemic, regulatory issues and the Russian invasion of Ukraine [90]. ITER will have double the linear dimensions and 10 times the plasma volume of the Joint European Torus (JET), the world's largest and most powerful tokamak [91, 92]. ITER will use a D-T fuel mix, and beryllium and tungsten plasma-facing walls [1]. ITER aims to [1, 93]:

1. Generate 500 MW of fusion power from 50 MW of injected heating power for 400 s pulses. This corresponds to a fusion power gain (the ratio of fusion power produced to the power required to maintain plasma in a steady-state) greater than 10.

2. Achieve a D-T plasma that is sustained through internal heating, known as burning plasma. This is where the energy of the helium nuclei produced exceeds the plasma heating from external sources.

3. Demonstrate the feasibility of producing tritium within the vacuum vessel.

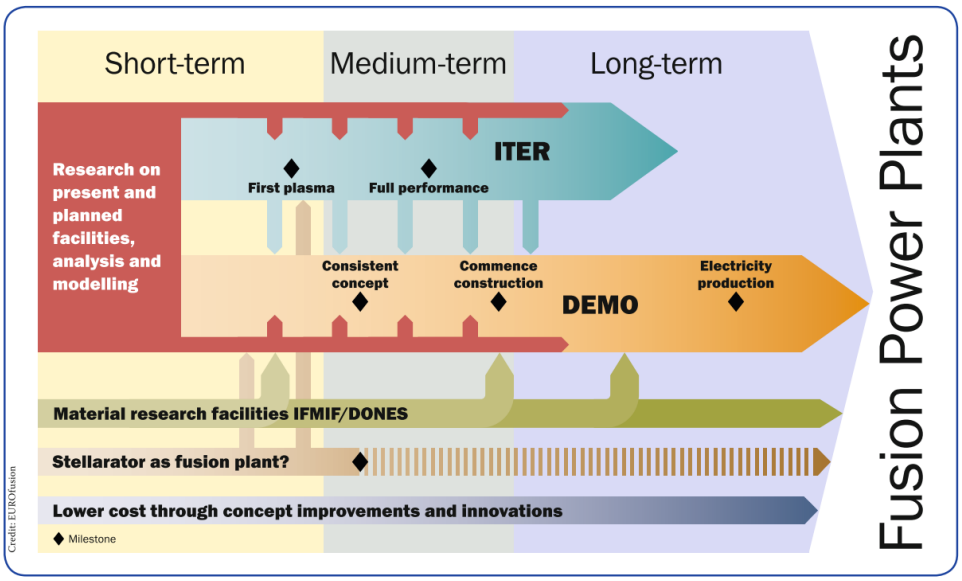

Figure 3.2: The European fusion roadmap. Arrows between elements show where research from one section contributes elsewhere [1].

4. Show the safety characteristics of a fusion reactor.
5. Bridge the gap between smaller-scale experimental fusion devices (e.g., JET) and DEMO.

3.2.2 DEMO

DEMO is a demonstration fusion power plant and will be the first tokamak-based fusion reactor in Europe that will supply fusion electricity to the grid. The main aims for DEMO are to achieve [1]:

1. $300 - 500$ MW of net fusion electricity and supply it to the grid.
2. Safety and environmental sustainability.
3. Tritium self-sufficiency.
4. A resolution to all the expected physical and engineering issues in fusion relevant technologies.
5. The basis for an assessment of the economic viability and feasibility of a commercial nuclear fusion power plant.

DEMO aims to bridge the gap between ITER and fully-scaled fusion power plants. In order to produce commercial fusion electricity during the second half of the 21st century, construction of DEMO needs to begin in the early 2040s. DEMO's design phase will therefore coincide with ITER's operational phase. Results from ITER will directly affect DEMO's design, shown in figure 3.3 [1].

3.2.3 MAST Upgrade

The original Mega Ampere Spherical Tokamak (MAST) facility, which operated from $2000 - 2013$, was designed by the UKAEA to explore the concept of a spherical tokamak [94]. Spherical tokamaks are of interest because they could potentially lead to cost-effective reactors as they may

be significantly smaller than conventional tokamaks. This is due to their smaller aspect ratio and different plasma shape, presented in figure 3.4.

MAST was rebuilt, as MAST Upgrade, to enable longer pulses, greater heating powers and stronger magnetic fields, where it commenced operation in 2020 [94]. The main goals for MAST Upgrade are to [95]:

1. Add to the ITER knowledge base to help resolve plasma physics questions and develop predictive models.
2. Test alternative divertor concepts, such as the Super-X divertor.
3. Explore the suitability of spherical tokamaks as future fusion devices.

3.2.4 STEP

Spherical Tokamak for Energy Production (STEP) is another UKAEA programme which will demonstrate the ability to generate net electricity from fusion energy and aims to [96]:

1. Build on the United Kingdom's global leadership in fusion.

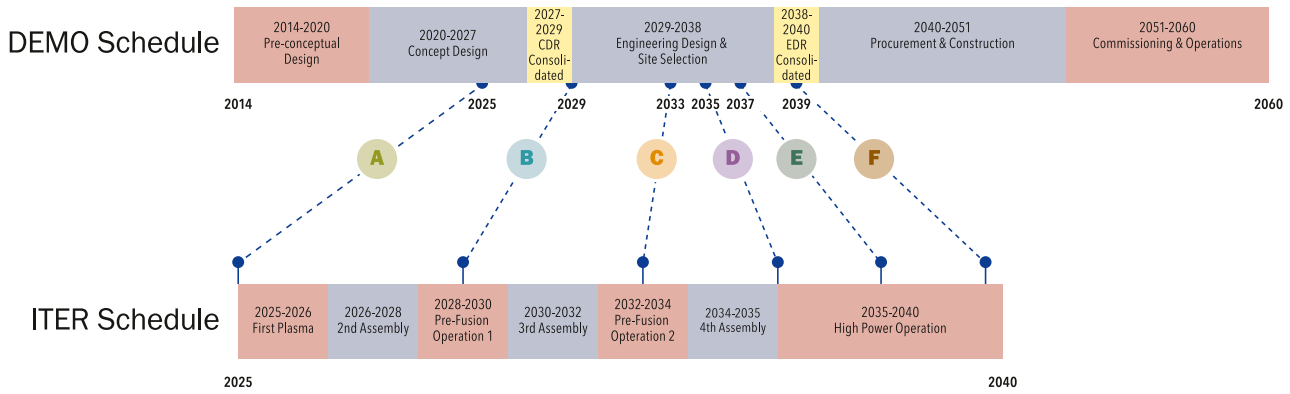

Figure 3.3: Concept design, construction and operation timelines for ITER and DEMO. Modified from [1].

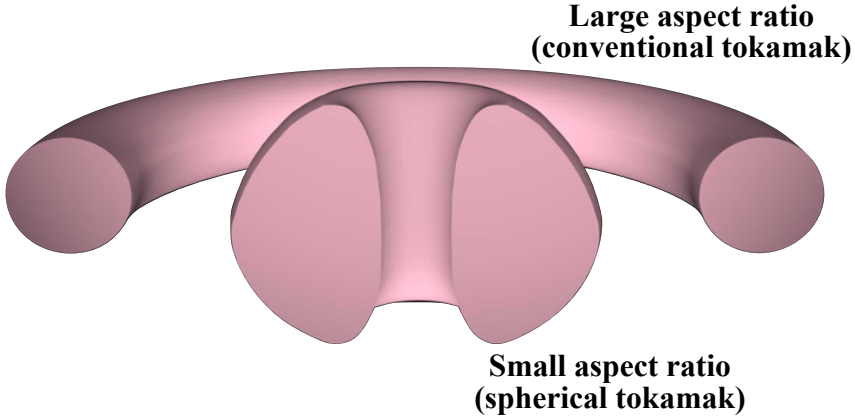

Figure 3.4: Representation of the plasma shape and size of a spherical and a conventional tokamak. Modified from [94].

2. Demonstrate the commercial viability of fusion.

3. Enable the development of world-leading fusion industry, which can be exported.

It will be a spherical tokamak, which is expected to reduce costs, and be connected to the National Grid. The first phase of this programme is to produce a concept design by 2024 [97].

3.2.5 Private sector

The private sector has gained significant funding and momentum within the last five years, with eight new companies being founded globally in 2021 and 2022. Private companies tend to have more ambitious timescales for device and pilot plant operation than their publicly-funded counterparts and many of them are aiming for the construction of their pilot plants to be complete between 2030 and the mid-2030s [90].

There is a more diverse approach to nuclear fusion within private sector than in the public sector [90]. The main innovation employed by Tokamak Energy (a spin-out from UKAEA [98]) for example, is the combination of spherical tokamaks and high temperature superconducting magnets which operate at $23.15 - 73.15$ K (typical superconducting magnets operate at 4.15 K) [99]. This leads to significant energy and cost savings [100]. Fusion energy processes other than magnetic confinement fusion are also used, such as inertial confinement fusion (by Marvel Fusion) and magneto-inertial fusion (by General Fusion) [90].

3.3 The divertor

As discussed in section 3.1, impurities within the plasma significantly impact core plasma performance. The removal of these impurities, and excess heat, is therefore critical for sustained nuclear fusion. The divertor, shown in figure 3.5(a), removes heat and helium ash from the tokamak, minimises plasma contamination and protects the walls from thermal loads. It is therefore an important component in maintaining core plasma performance and is situated at the bottom of the vacuum vessel [1].

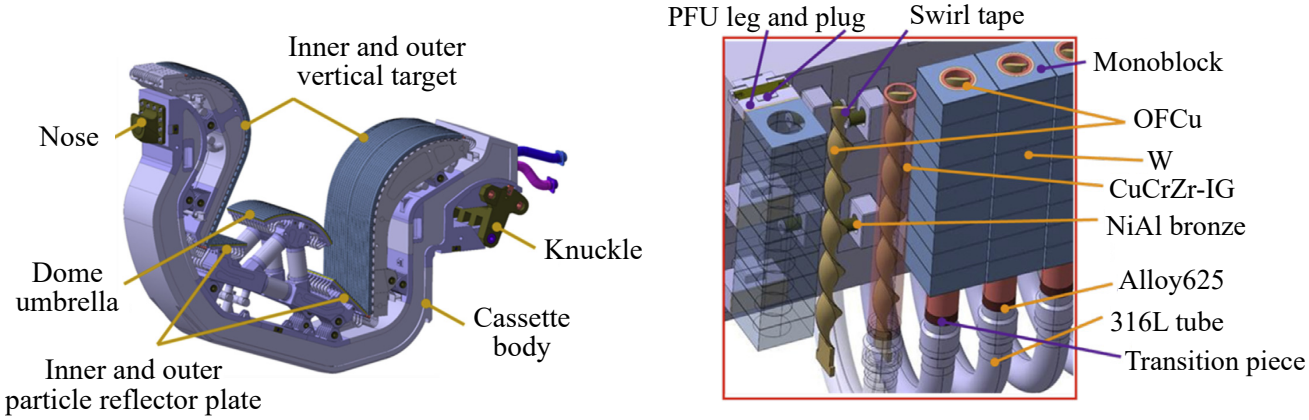

(a) One ITER divertor cassette.

(b) The vertical target of the ITER divertor.

Figure 3.5: Schematics of the ITER divertor. Modified from [101].

In modern magnetic confinement fusion reactors, plasma is contained through elongated, D-shaped, toroidal magnetic field lines, where the border of the confined region is known as the separatrix. The Scrape-Off Layer, a plasma region outside the separatrix characterised by open field lines, absorbs most of the plasma exhaust and transports it along the field lines to the divertor target plates, as depicted in figure 3.6. This maximises the divertors performance as the plasma exhaust is directed towards the PFU of the divertor targets and away from the walls, creating a concentrated heat load and build-up of contaminants on the vertical targets [102]. The areas where the exhaust collides and interacts with the PFUs are known as strike zones. Although this gives added protection to the walls of the vacuum vessel, it also means that the divertor is subject to greater heat fluxes than the walls. In ITER, it is expected that the strike zones will experience peak heat fluxes of approximately 10 MW m^{-2} during a steady-state phase and 40 MW m^{-2} during a transient phase [103]. Outside of these strike zones, the target should experience an average heat flux less than 5 MW m^{-2} [3].

The operating window of the divertor target depends on the material used. Considering the use of refractory metals, the lower temperature limit is determined by the ductile-brittle transition temperature (DBTT), which increases under neutron irradiation. The upper temperature limit is determined by recrystallisation (which increases the DBTT and decreases toughness and strength) and helium embrittlement effects [104, 105].

The divertor design must take peak heat fluxes and neutron irradiation doses into account and ensure that it can operate in all operational scenarios, not just in peak conditions. The optimal cooling condition must be determined through the following requirements [3]:

1. Loss of coolant accidents (e.g., from boiling) must be avoided at the maximum heat load.

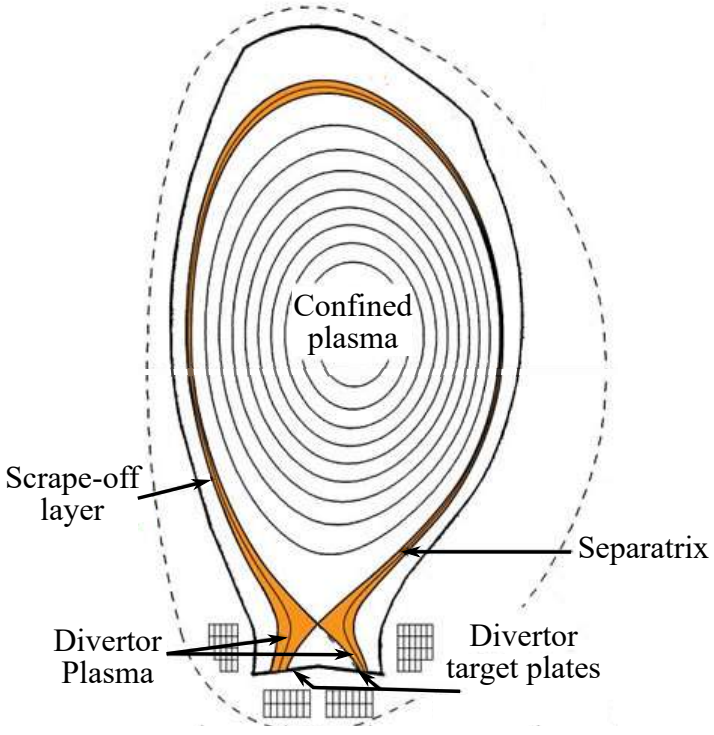

Figure 3.6: Cross-section of the JET tokamak depicting the magnetic field lines directing plasma exhaust towards the divertor targets. Modified from [102].

2. Structural material for the heat sink pipe must maintain sufficient ductility and strength to avoid structural failure at maximum neutron irradiation doses.

The ITER divertor, shown in figure 3.5(a), is made up of 54 individual cassettes, each measuring $0.8 \times 2.3 \times 3.5$ m [106]. The current ITER divertor target design can be seen in figure 3.5(b) and consists of $28 \times 28 \times 12$ mm tungsten (W) monoblocks (the plasma-facing armour) joined to a 12 mm inner diameter, 1.5 mm thick copper-chromium-zirconium alloy (CuCrZr) cooling pipe with a 1 mm thick copper (Cu) interlayer [101, 107]. As the plasma exhaust interacts with the PFUs, the armour heats up. This heat is then transferred to the coolant (water), which is pumped out of the vacuum vessel. The swirl tape within the pipe, observed in figure 3.5(b), promotes fluid flow behaviour which increases the heat transfer from the armour to the coolant [101].

The ITER divertor target has already been qualified for use in ITER, where it was demonstrated that a prototype PFU could survive 5,000 cycles at 10 MW m^{-2} and 300 cycles at 20 MW m^{-2} for ITER nominal hydraulic conditions (i.e., pressure of 3.9 MPa, temperature of 70 °C and velocity of 11 m s^{-1}). This fulfils the envisaged lifetime of ITER [107, 108].

The DEMO divertor targets are expected to experience peak heat fluxes of approximately 10 MW m^{-2} under steady-state operation and 20 MW m^{-2} during slow transient events [1, 5]. They are also expected to experience peak heat fluxes of up to 70 MW m^{-2} during short transient events [5]. Additionally, the neutron irradiation dose could increase by up to an order of magnitude [1, 4, 5]. This can cause transmutation reactions within the divertor material which leads to embrittlement and a decline in many of its properties, such as thermal conductivity [109, 110] and ductility [111]. The DEMO divertor is going to have to maintain its power exhaust capabilities and ensure structural reliability while under cumulative neutron doses of 13 dpa for 2 full power years (the envisaged lifetime of a DEMO divertor) [1]. Irradiation effects may be ignored if the temperature is high enough for thermal recovery and if the transmutation products play a negligible role, however. The divertor target will also experience fatigue damage from the pulsed fusion operations (5,000 heat flux pulses) which generate a cyclic variation of temperature and thermal stresses [4].

The ITER divertor will therefore not be able to remain within its operational region under the extreme conditions expected in DEMO [1, 3, 4]. Hence, a different design approach was adopted for the DEMO divertor [5]. A CAD model of the final baseline design can be seen in figure 3.7 and was validated in 2020. The DEMO divertor consists of 48 cassettes, where each cassette has dimensions of $1.2 \times 4.1 \times 2.2$ m. A noticeable difference between the ITER and DEMO divertor designs was the replacement of the dome umbrella with a shielding liner and reflector plates. This was to reduce costs and to protect the target and manifold pipes. The technology for the divertor targets were inherited from ITER, where the only design change was the reduction of the monoblock width to 23 mm, as they demonstrated excellent heat removal capacity and appear to fulfil both the thermo-hydraulic and structure-mechanical design requirements [5]. The DEMO divertor target is expected to operate under fluid pressures of 5 MPa and fluid temperatures of $280 - 320$ °C. Despite this, maturation of the high heat flux component technology remains a main focus throughout the concept design phase, which will run from $2021 - 2027$ [5].

The important sub-components of the target include the plasma-facing armour, mechanical support, substructure and coolant. The plasma-facing armour is a monoblock typically made from tungsten alloys due to its high melting and boiling points, high sputtering resistance, vacuum compatibility and resistance to neutron irradiation damage. The substructure must be joined

to the armour and be compatible with the coolant whilst containing pressure and allowing heat to transfer away from the armour effectively. Candidate coolants include water, heavy water, helium, supercritical CO_2, liquid metals and molten salts (hydrogen has been historically discounted for fusion applications due to embrittlement concerns). The mechanical support does not have a significant impact on the thermal performance of the target. The selection of substructure material and coolant therefore provides a great degree of innovation in improving the performance of the divertor [22, 101]. More information regarding fusion relevant materials for the substructure of the divertor is given in appendix A.

The performance of the divertor can also be improved by designing novel divertor target structures which promote greater heat transfer from the armour to the coolant. AM is therefore uniquely poised to have the largest impact in this area as parts with complex structures optimised for high heat flux applications can be manufactured [22]. Novel research to improve the performance of the divertor target is discussed in the following section.

3.4 Novel divertor target designs

The function and design of the divertor cassette module was the focus of section 3.3. This section will instead have a larger emphasis on the evolution of the design and performance of different divertor target concepts.

A conceptual design programme was launched in 2014 by EUROfusion. One of the main focuses was the development of the DEMO divertor design and technology, known as WPDIV [3, 4]. The WPDIV pre-concept design phase concluded in 2020, where the final DEMO divertor design was finalised and shown in figure 3.7 [5]. Throughout this programme, new targets were designed and tested. A selection of these are explored below.

You [4] reviewed two separate divertor target concepts for DEMO. The first being a baseline water-cooled ITER-like target which could accommodate slow transient events with heat flux

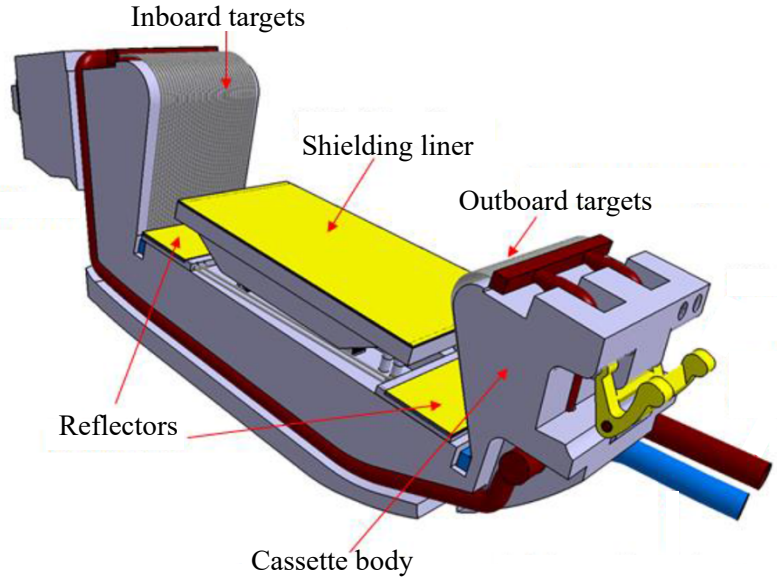

Figure 3.7: CAD model of the DEMO divertor cassette module. Modified from [5].

loads up to 20 MW m^{-2} and coolant temperatures less than 150 ℃. The maximum allowable steady-state heat flux at this coolant temperature is 10 MW m^{-2}. To allow for higher steady-state heat flux loads, significant research is needed to improve the high-temperature strength and corrosion resistance of water-cooled heat sinks. A dedicated structural design criteria for brittle and embrittled metals is also needed for low coolant temperatures.

The second divertor target concept You [4] reviewed was the helium-cooled multi-jet (HEMJ) impingement modular finger target, seen in figure 3.8(a), initially designed at the Karlsruher Institut für Technologie [114]. Here, a pressurized jet of hot helium was fed towards a thimble to cool the tungsten tile. The thimble needed to fulfil relevant structural design criteria for the envisaged operation temperature window. This concept was optimised for heat flux loads of 10 MW m^{-2} for unirradiated cases and for an optimistic assumption on the DBTT of the irradiated heat sink material. Large deviations from the optimised heat flux load can lead to embrittlement or softening of the target, however. You [4] concluded that if an innovative design concept with a sufficient operational margin for the divertor target is devised, then this concept could be a feasible DEMO divertor target. Due to issues raised with the manufacturability of the complex manifold system and many small pressure-loaded elements (the fingers), a pipe concept initially introduced by Reiser and Rieth [113] was instead proposed by Zhao *et al* [115]. This concept employs an array of round jets impinging on the concave surface of the cooling pipe, see figure 3.8(b), and was validated for a heat flux of 10 MW m^{-2}.

Another heat sink module, using a similar jet-impingement technology as the HEMJ finger target, was designed by Nicholas *et al* [116]. The general design structure was labelled as high pressure jet cascade (HPJC) and a baseline design, HPJC-1a, was examined. This water-based target design aims to reduce the mass flow rate required to obtain a set component temperature and increase the operational pressure to ensure higher fluid temperatures without the risk of a phase change. A high pressure cooling system with cascade jet impingement was therefore used in the design for this heat sink module, shown in figure 3.9. Numerical results showed that HPJC-1a was capable of handling divertor target steady-state heat flux magnitudes at DEMO relevant coolant inlet conditions whilst also having a reduced pumping power and mass flow rate when compared to ITER-like DEMO targets.

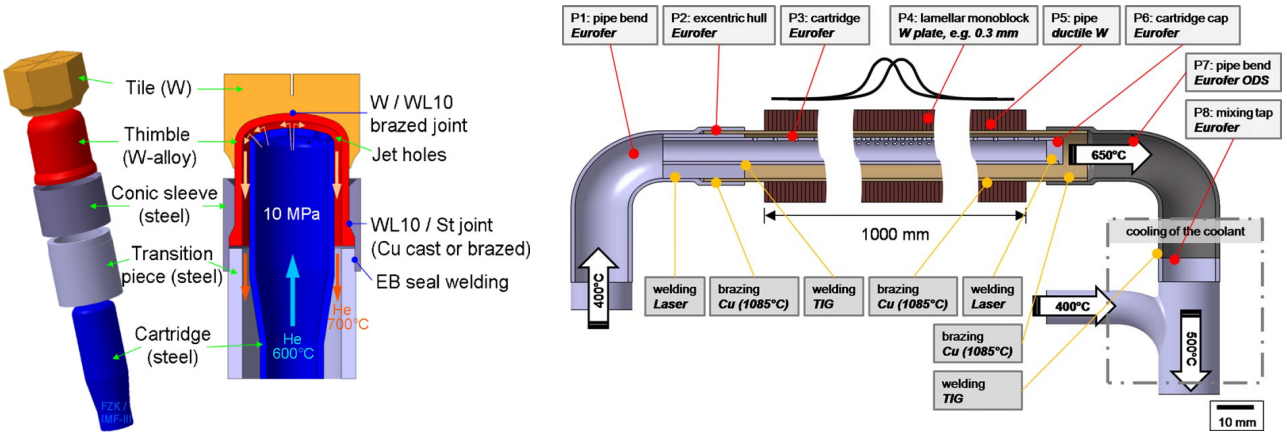

(a) Finger target concept [112]. **(b)** Pipe target concept [113].

Figure 3.8: HEMJ target concept design schematics.

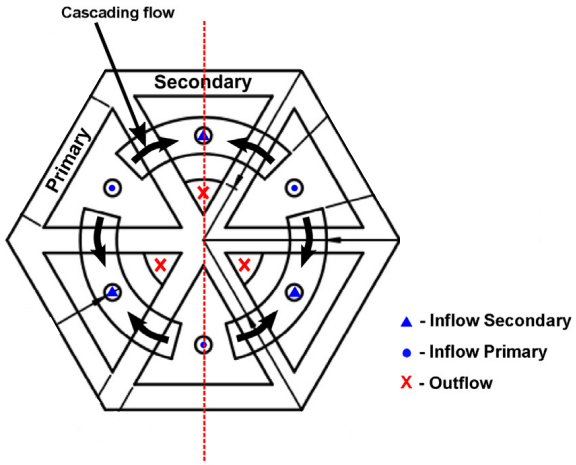

(a) Plan view of the HPJC-1a target design, indicating flow path.

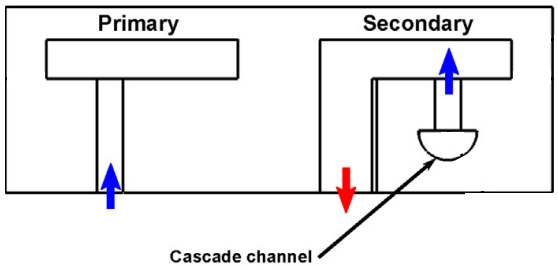

(b) Cross-section view along the dashed line in figure 3.9(a).

Figure 3.9: HPJC-1a divertor target design. Semi-circular cascade channels are shown with coolant inflow (blue) and outflow (red). Modified from [116].

Liquid metal divertors are also of interest as they may offer greater capabilities compared to the ITER-like design, such as improved robustness against transient loadings and a self-replenishing surface [3]. Rindt et al [117] designed a liquid metal divertor, see figure 3.10, which used water and tin (as opposed to lithium due to tritium retention issues). This concept was considered a significant improvement over the ITER-like designs. Many issues preclude the use of this design within DEMO however, such as the technology not being sufficiently ready and it forcing a complete overhaul of the DEMO fuel cycle [117].

Seven divertor target design mock-ups were developed in the first WPDIV R&D phase, using the ITER-like target as a reference to take advantage of its technological maturity. They were evaluated by means of non-destructive inspections and high heat flux fatigue testing [118]. A summary of the different concepts is provided in table 3.1.

The performance of these target design mock-ups were determined via their structural integrity after 500 loading cycles, where defect evolution and failure was judged by in-situ observations of surface temperature. It was found that three target design mock-ups survived 500 load cycles at 20 MW m^{-2} and a coolant temperature of 130 °C. These were the ITER-like, composite pipe and thin graded interlayer concepts [118].

The target concepts examined as part of WPDIV rely on conventional manufacturing technologies, in both design and construction, and are therefore limited by this. In the United Kingdom, parallel research on AM novel divertor designs began with the Additive Manufacturing Aiming Towards Zero Waste & Efficient Production of High-Tech Metal Products (AMAZE) programme in 2013 [119]. The key goal of this project was to build confidence in AM for end user decision makers within the project consortium and the wider EU industry. During its 4 years of activity, the project improved the AM of metals for nuclear fusion applications [119], which has opened the way for AM to become a key part of the industry going forward. AM divertor target geometries have since been developed and these are explored below.

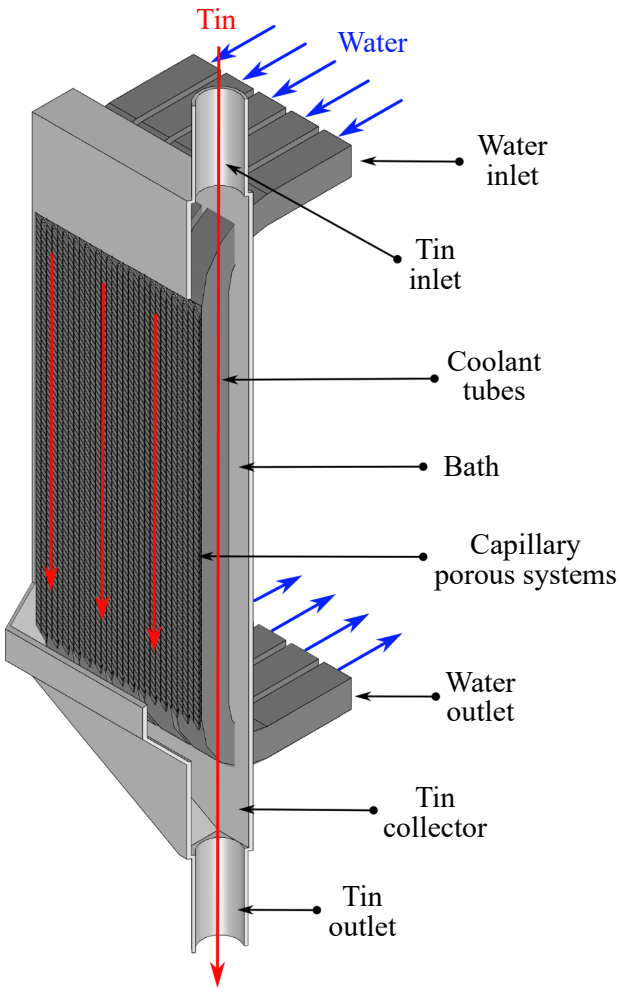

Figure 3.10: Liquid metal divertor concept. Modified from [117].

Hancock *et al* [53] introduced multiple concept-level divertor target geometries that displayed the potential advantages enabled by AM. These concepts aimed to improve the thermofluid performance and reduce stress (due to thermal expansion coefficient mismatch), manufacturing risks and the volume of structural and armour material needed.

The first concept introduced was based on the millipipe design from AMAZE, shown in figure 3.11(a). Instead of one singular large pipe being embedded in the monoblock, multiple small channels were used. This concept has a number of benefits compared to the ITER-like design, such as higher heat transfer coefficients and a reduction in peak wall temperature, maximum overall temperature, stress, weight and material used for an increasing number of small pipes [53].

The millipipe concept was then used as a basis for the rear feed-pipe concept, seen in figure 3.11(b). Using the DEMO baseline water parameters, empirical calculations of the pressure drop for this part connected in series showed that it increased by a small margin when compared to the ITER-reference twist-tape. When set up in a parallel configuration, each element only experienced a pressure drop of 0.014 MPa (whereas the ITER configuration experienced a pressure drop of 0.35 MPa m^{-1}, corresponding to 0.042 MPa). The thermomechanical results obtained by Hancock *et al* [53] via finite element analysis (FEA) are presented in table 3.2. These results show that the concept operates within the limit for yield stress for recrystallised

Concepts	Coolant	Armour	Interlayer	Heat sink	Design rationale
ITER-like	H_20	W block	Cu	CuCrZr pipe	Avoid deep cracking
Thermal break	H_20	W block	Porous Cu	CuCrZr pipe	Mitigate heat flux peaking, reduce thermal stress
Composite pipe	H_20	W block		W_f/Cu	Enhance strength, reduce thermal stress
Thin graded interlayer	H_20	W block	Graded W/Cu	CuCrZr pipe	Avoid thick Cu interlayer, enhance joining quality
W flat tile	H_20	W tile	Cu	CuCrZr block	Enhance toughness & flexibility in cooling concept
Composite block	H_20	W tile		W_p/Cu	Enhance toughness, reduce thermal stress
Pipe multi-jet	He	W block	Cu	W laminate pipe	Enhance efficiency by high operating temperature

Table 3.1: WPDIV divertor target design concepts [118].

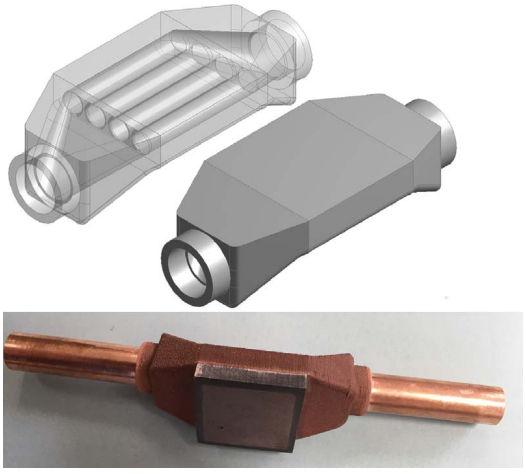

(a) AMAZE millipipe geometry (above) and mock-up (below).

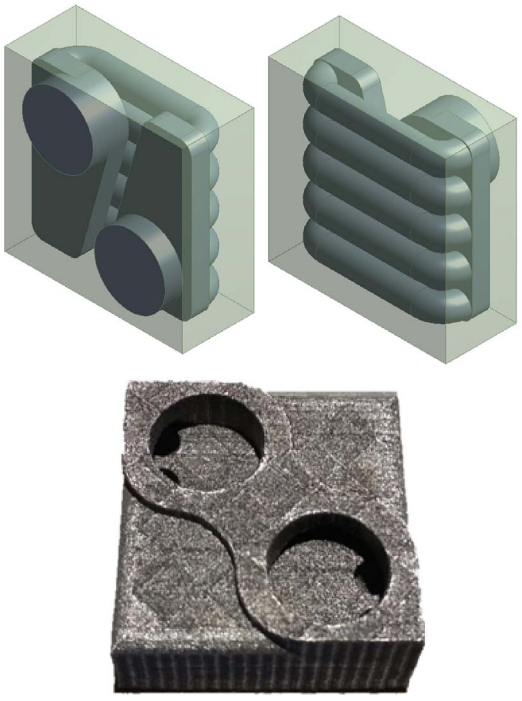

(b) Rear fed small-pipe geometry (above) and test build (below).

Figure 3.11: The additively manufactured manifold small pipe concept. Modified from [53].

Coolant parameters	Heat flux (MW m^{-2})	Stress (MPa)	Maximum body temperature (℃)	Maximum armour temperature (℃)
$T = 150$ ℃	5	224	470	633
$P = 4$ MPa	10	484	778	1162
$h = 0.1$ W mm^{-2} K^{-1}				
$T = 600$ ℃	5	250	899	1095
$P = 5$ MPa	10	441	1193	1620
$h = 0.1$ W mm^{-2} K^{-1}				

Table 3.2: Rear fed small pipe thermomechanical results where T is temperature, P is pressure and h_{wall} is the pipe heat transfer coefficient [53].

tantalum when the heat flux was 5 MW m^{-2}. At 10 MW m^{-2}, the peak stress is highly localised at the interface between the tungsten armour and tantalum heat sink. The higher temperature and higher power case could be rendered feasible if the armour thickness is reduced, but this would require a method to replace eroded material [53].

A secondary concept featuring an enclosed pin fin array, shown in figure 3.12, was also investigated by Hancock *et al* [53]. This concept was originally explored by the electronics industry, but research has shown high heat transfer capabilities with low pressure drops for fusion relevant heat fluxes [120]. Hancock *et al* [53] were not able to give a quantitative assessment of pressure drop for this design, due to its dependency on both pin geometry and coolant parameters, but were able to obtain thermomechanical results, given in table 3.3. A pessimistic heat transfer coefficient was chosen for the FEA model to showcase the effect that the increased surface area would have on the temperature and stress of the component. This showed that the stress in the structure remained below the yield at 5 MW m^{-2} and that the temperature of the armour and heat sink were within the operating region for a coolant temperature of 600 ℃.

Hancock *et al* [53] showed that these preliminary designs were able to operate within the elastic stress regime of the material at 5 MW m^{-2} but exceeded the yield stress at 10 MW m^{-2}. When a 600 ℃ coolant was used, both concepts were within the operating range for the 10 MW m^{-2} cases. The enclosed pin fin array has the potential to reduce flow velocity, pumping power, erosion and increase overall efficiency due to the high internal surface area and heat transfer coefficients; although further design development is needed to demonstrate this. The rear feed-pipe design displayed this empirically. It was therefore concluded that these concepts were worthy of further investigation.

It must be noted that the AM concept divertor geometries models examined by Hancock *et al* [53] do not model the coolant. Heat transfer due to the coolant is therefore calculated from a user-defined wall heat transfer coefficient and coolant properties. This does not capture the fluid dynamics, particularly at high Reynolds numbers where there is turbulence, or the wall surface roughness, which are typically greater for AM components than conventionally manufactured components. These effects increase heat transfer but adversely affect the pressure drop. Detailed fluid and thermal modelling is required to truly understand the performance of AM components in fusion relevant conditions.

Coolant parameters	Heat flux (MW m^{-2})	Stress (MPa)	Maximum body temperature (℃)	Maximum armour temperature (℃)
$T = 150$ ℃	5	262	342	421
$P = 4$ MPa	10	603	546	941
$h = 0.02$ W mm^{-2} K^{-1}				
$T = 600$ ℃	5	250	899	1095
$P = 5$ MPa	10	537	1029	1485
$h = 0.02$ W mm^{-2} K^{-1}				

Table 3.3: Enclosed pin fin array thermomechanical results summary where T is temperature, P is pressure and h_{wall} is the pipe heat transfer coefficient [53].

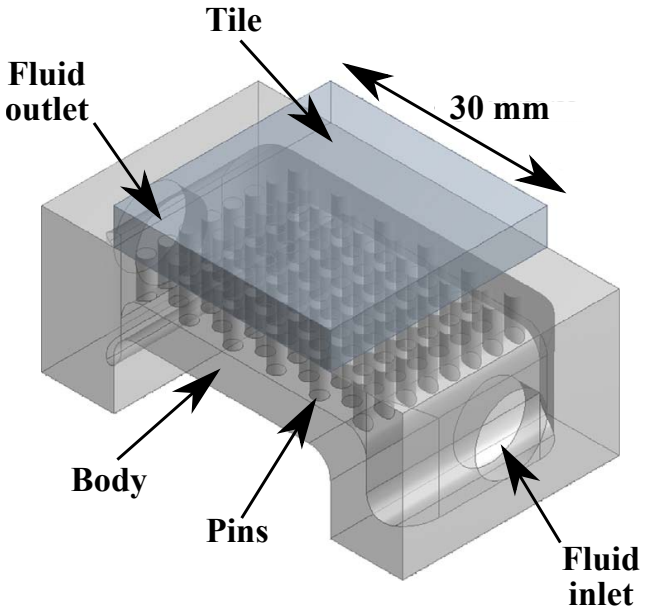

Figure 3.12: Additively manufactured enclosed pin fin array geometry. Modified from [53].

3.5 Summary

The divertor is a key component in a nuclear fusion tokamak reactor. Without it, the plasma-facing walls would be exposed to higher heat fluxes and neutron irradiation doses, leading to plasma contamination and wall-degradation. This leads to the divertor experiencing increased loads instead. Research showed that the ITER divertor will not be able to operate in the conditions found in DEMO for its envisaged lifetime [1].

The WPDIV was established to improve the designs of the divertor for DEMO relevant conditions. Despite this, the maturation of high heat flux components was identified as an area for further research [5] and, hence, new divertor target designs need to be developed to improve the performance of future divertors. AM was identified as a technology with significant potential for components in high heat flux applications due to the complex structures that can be manufactured. These parts can be further optimised for high heat flux applications. There is therefore a lot of interest in designing novel divertor target geometries using AM to take advantage of its

unique characteristics.

Novel divertor target concepts using AM have been designed and preliminary FEA results have shown that these concepts can operate within the operational temperature region whilst also improving certain aspects of the baseline divertor design [53, 121].

This work aims to further the development of AM divertor targets, as this is a novel area with different avenues to explore. Heavy emphasis is placed upon examining TPMS-based lattice structures, which have received minimal attention in the nuclear fusion industry, within divertor target-like designs. This is achieved by incorporating them in structures which represent the AMAZE geometries, such as those shown in figures 3.11(a) and 3.12, in place of their respective millipipe and pin fin array geometries. TPMS-based lattice structures are used because of their ability to act as natural heat sinks, due to their high surface-to-volume ratios, as discussed in chapter 2. Additionally, the inclusion of TPMS-based lattices within AM divertor target structures has not yet been explored extensively in the literature.

If this research project shows that AM TPMS-based lattice structures are promising for high heat flux applications compared to conventional heat sinks, the nuclear fusion industry will have another avenue to develop and design novel divertor targets to improve the performance of future reactors. Important strides will also be made in the AM industry as well, such as the formulation of design processes and characterisation of metal AM cellular structures for high heat flux applications. This will be determined predominately through CFD simulations.

Chapter 4

Modelling Flow in TPMS-based Lattice Structures

4.1 Overview

In this work, OpenFOAM v1812 [14], a computational fluid dynamics (CFD) finite volume software written in C++, was used to produce numerical models of TPMS-based cellular structures and structures representing the AMAZE geometry (shown in section 3.4). OpenFOAM was selected due to being open-source, having the potential to modify solvers for new applications and being able to compile, load and execute C++ code at run-time through the use of *codeStreams*. v1812 was selected as it was compatible with the University of Nottingham's High Performance Computing service, Augusta. The progress and development of the numerical model for this project is shown in figure 4.1.

CFD models were visualised in ParaView, which is an open-source, multiple-platform application for interactive and scientific visualisation. This software allows the user to manipulate, plot and extract data. ParaView is also fully scriptable, using Python, which offers users more flexibility and allows for batch post-processing or extraction of results.

The general method, technical details and physical principles used to set up the numerical models are discussed in this chapter. The computational method described here was used to

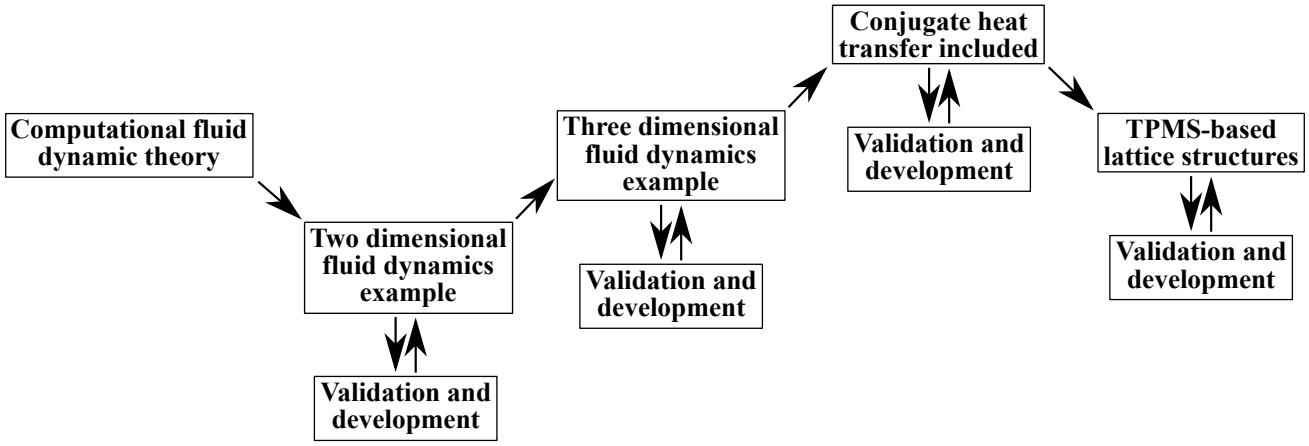

Figure 4.1: Progress and development of the numerical model.

achieve the objectives set out in section 1.3. Case and experiment dependent information, such as boundary conditions and medium properties, are explained in the relevant chapters. Background information regarding CFD can be found in appendix B.

4.2 Fluid dynamics

4.2.1 Fluid flow

The fluid dynamics of a system need to be fully understood to ensure that valid decisions are made regarding the numerical model. This section therefore aims to provide sufficient information to the reader prior to discussing the numerical models and method used here.

Fluid flow can be described as either laminar or turbulent. The boundary layers and velocity profiles for both laminar and turbulent flow are shown in figure 4.2. Laminar flow typically occurs at low fluid velocities and is characterised by high momentum diffusion and low momentum convection, where the fluid travels in smooth lamellae with no mixing between the different layers. Turbulent flow happens at higher fluid velocities and is characterised as [85]:

- Highly unsteady.
- Three-dimensional.
- Having a large amount of vorticity.
- Increased mixing of conserved quantities.
- Being a dissipative process.
- Containing coherent structures.
- Fluctuating on a broad range of length and time scales.

Fluid flow can be determined to be either laminar or turbulent by examining its Reynolds number, Re, which gives the ratio between the inertial and viscous forces of the fluid. Laminar flow exists for small Reynolds numbers, where viscous forces dominate, and turbulent flow exists for

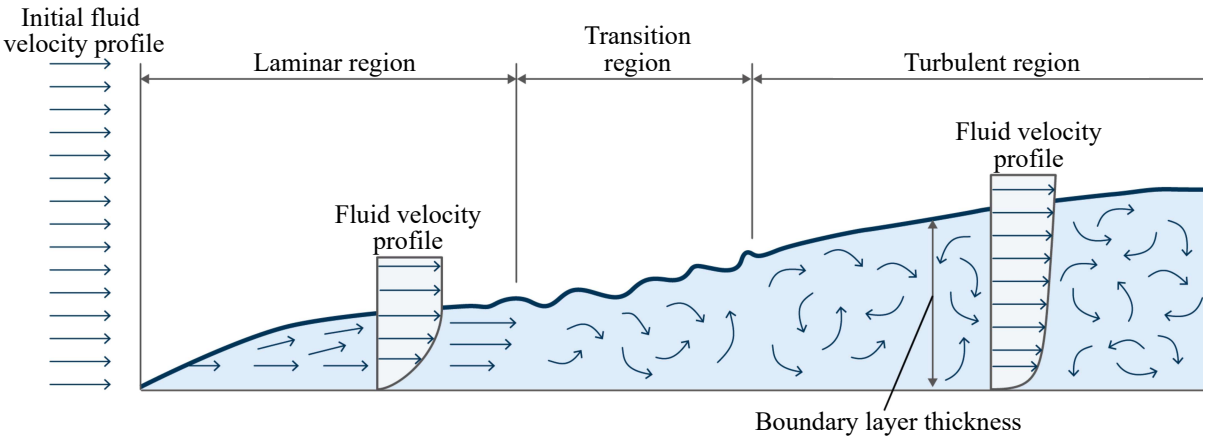

Figure 4.2: Fluid velocity profiles and boundary layers for laminar and turbulent flow over a flat plane. Modified from [122].

large Reynolds numbers, where inertial forces dominate. The transition region between laminar and turbulent flow occurs in the range $2,000 < Re < 40,000$ for circular channel flow [123] and $10 < Re < 2,000$ for porous structures [124].

Turbulence may be a desirable effect, depending on the application of the flow. For example, turbulence is useful in heat transfer as the increased mixing and vorticity can increase heat transfer by an order of magnitude [85]. Turbulence can also lead to increased friction forces and higher pressure drops, removing kinetic energy from the system. In engineering applications, such as for thermal management, this could necessitate greater pumping power than would otherwise be needed. Turbulence effects are negligible in the near-wall region however, as fluid flow is laminar due to the fluid's viscosity and skin friction. The region where this happens is defined as the viscous sublayer.

The dimensionless distance of the first mesh element node from the wall, n^+, is typically used in CFD to determine the region (e.g., the viscous sublayer) which the wall-adjacent mesh elements are located in. A coarse mesh in the near-wall region may mean that viscous sublayer effects are not being modelled correctly and this needs to be accounted for. More information regarding n^+ is provided in appendix B.5.

4.2.2 Heat transfer

Convection is the transfer of heat by the motion of fluid and is the heat transfer process most closely linked with fluid mechanics. Another prominent heat transfer process for fluids is conduction, where the collisions and diffusion of the fluid particles transfers heat across a system. For laminar fluid flow, the dominant heat transfer process is convection in the streamline direction and conduction in the perpendicular direction. For turbulent flow, heat transfer is driven by convection in both the streamline and perpendicular directions.

If temperature differences are small (e.g., less than 5 K in water) and the Reynolds number is high, then temperature behaves as a passive scalar (i.e., does not affect the fluid properties). If the fluid is instead driven by density differences, temperature must be taken into account.

There are also cases where conduction in a solid needs to be considered alongside convection in a fluid (e.g., within heat sinks). The transfer of energy between these two (or more) mediums is referred to as conjugate heat transfer.

4.3 General work flow

A flowchart depicting the general work flow to set up the numerical models in this work is shown in figure 4.3. To begin with, a case folder is set up with all of the relevant dictionaries to enable OpenFOAM to run. This includes a directory which houses the initial and boundary conditions for the field variables of each domain, typically named *0* or *0.orig*. Another directory, labelled *constant*, contains information regarding the physical properties of the domain and any STL files used in the finite volume meshing process. *Constant* will also contain the data pertaining to the mesh once it is generated. The final directory that is included is *system*, which specifies the numerical schemes and solvers and includes information regarding the generation of the mesh.

A script file can be used to automate the computational modelling process. Commands which generate the mesh, such as *blockMesh*, and modify the initial and boundary conditions are included. The numerical solver is run once the mesh has been generated. The outputted data can be post-processed and extracted (using ParaView) once the solver has finished running.

Additionally, the initial mesh can be decomposed in to multiple partitions, where each partition has its own Message Passing Interface (MPI) process (a message passing application which allows data to be shared between partitions). The interfaces of the partitioned meshes are coupled to the relevant interface of its adjacent partition via boundary conditions. The method of decomposition and number of partitions can also be specified. The benefit of decomposing a mesh is that multiple computational cores can be used to run the numerical solver, where one core is devoted to one partition, as opposed to using one core for the entire computational domain. This significantly improves computational efficiency through parallel processing.

Initial studies were also performed when modelling different fluid flow and heat transfer applications. These included mesh convergence (to ensure that a suitable mesh which would give accurate results was used), temporal convergence (to ensure that the numerical had converged to a steady state) and validation studies (to ensure that the numerical model behaves as expected for a physical system). These studies are discussed in greater detail, where relevant, in chapters 5 and 7.

4.4 Geometry and mesh generation

Figure 4.4 shows a flowchart describing the lattice and mesh generation process. TPMS-based lattices are generated via the Functional Lattice Package (FLatt Pack) software [47], a research-focused surface-based lattice design program, and saved using the STL file format. They are then imported into Materialise Magics to check and fix triangulated surface errors (e.g., overlapping triangles). The number of surface triangles are also reduced to optimise file size, whilst ensuring that the surface feature quality is not compromised through visual examination. The surface is then checked for errors and fixed again. The OpenFOAM command *surfaceCheck* is

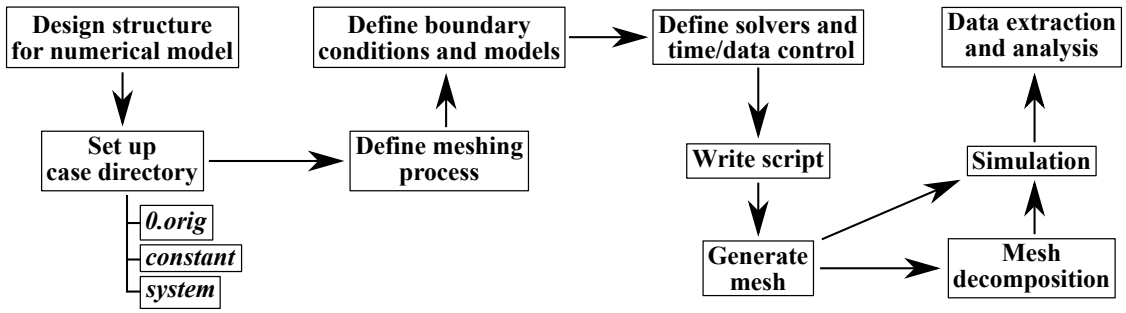

Figure 4.3: General work flow for an OpenFOAM model.

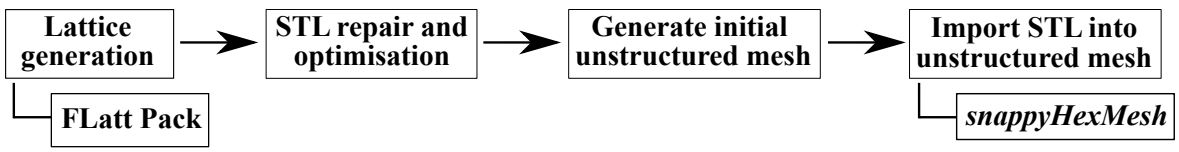

Figure 4.4: General work flow for lattice and mesh generation.

used to ensure that the geometric and topological quality of the structure is sufficient as low quality surfaces can lead to low quality meshes. The surface features (such as edges and corners) of the lattice geometry are then extracted and used later.

An initial unstructured mesh is first generated by specifying its properties (e.g., vertex locations, mesh resolution and boundary definitions). *SnappyHexMesh* is then used to import the lattice geometry into the mesh, where the *snappyHexMesh* process is shown in figure 4.5. This generates a three-dimensional mesh from triangulated surface geometries stored in either STL or OBJ file formats. A background mesh consisting solely of hexahedra elements must be present before it can be used. Once the triangulated surface has been imported into the mesh, elements must be split at the feature edges and surfaces using the extracted surface features (discussed above). Elements within specified regions can also be refined or removed entirely. The jagged castellated surface from the element splitting and removal process is then smoothed by a surface snapping procedure. Finally, prism layers can be introduced to the boundary surface to solve the boundary layer (more information regarding the use of prism layers is provided in section 4.6). Multiple regions and domains can also be specified using *snappyHexMesh*.

The final step in the meshing process is to check the quality of the mesh. When using *snappyHexMesh* with complex lattices, it is often found that not all the checks were passed successfully due to the complexity of the structures. As an example, highly skewed elements, which impact the interpolation of the element centred quantities to the face centre and affects convective and diffusive terms, may be present. This does not necessarily mean that the mesh will give poor results, however. CFD users therefore need to take special care to ensure that any poor-quality elements do not have a strong impact on the model.

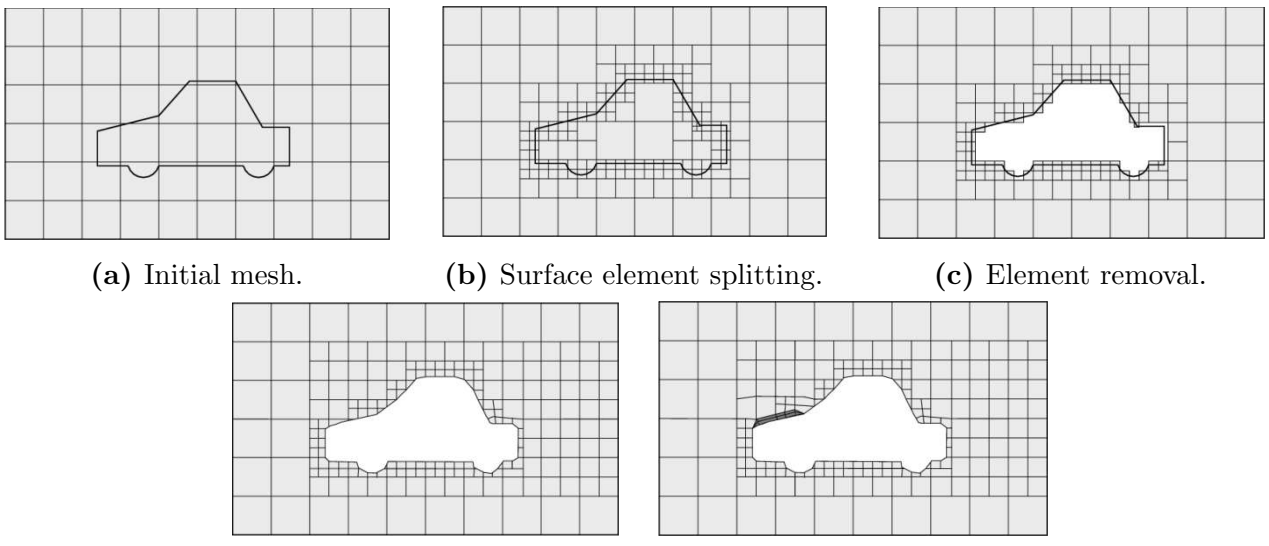

(a) Initial mesh. **(b)** Surface element splitting. **(c)** Element removal.

(d) Surface snapping. **(e)** Layer addition (shaded in dark grey).

Figure 4.5: Visual representation of the *snappyHexMesh* meshing process [125].

4.5 Numerical method

4.5.1 Mathematical model

Users must ensure that the equations solved in the numerical model are appropriate for the intended application. Throughout this research project, the flow of incompressible fluid through heat sink geometries was examined numerically to determine hydraulic and thermal performance metrics once equilibrium was reached. A solver which is suitable for steady-state conjugate heat transfer problems therefore needs to be selected, where steady-state simulations compute the time-independent solution of the model and are much faster than a transient simulation (which computes the time-dependent solution). It is important to note however, that it is not guaranteed that a fully developed solution exists when there is turbulence, and it is instead likely that the flow oscillates between two points.

For these reasons, the OpenFOAM *chtMultiRegionSimpleFoam* solver (a steady-state solver for buoyant, turbulent fluid flow and solid heat conduction with conjugate heat transfer between solid and fluid regions) was used. This solver follows a segregated solution strategy, where the equations for each variable in the system are solved sequentially and the solution from the previous equation is used in the subsequent equation.

Here, the equations for the fluid domain are solved first (for a given time step). This begins with momentum conservation, which solves for fluid velocity $\boldsymbol{u}$, and takes the form

$$\begin{aligned}\frac{\partial \rho \boldsymbol{u}}{\partial t} + \boldsymbol{\nabla} \cdot (\rho \boldsymbol{u}) + (\boldsymbol{u} \cdot \boldsymbol{\nabla}) \rho \boldsymbol{u} - \mu \nabla^2 \boldsymbol{u} \; = \\ \mu \boldsymbol{\nabla} \cdot \left((\boldsymbol{\nabla} \boldsymbol{u})^{\mathrm{T}} - \frac{2}{3} \mathrm{tr} \left((\boldsymbol{\nabla} \boldsymbol{u})^{\mathrm{T}} \right) \boldsymbol{I} \right) - \boldsymbol{g} H \boldsymbol{\nabla} \rho - \boldsymbol{\nabla} P_{\mathrm{rgh}} \,,\end{aligned} \tag{4.1}$$

where ρ is density, $\boldsymbol{u}$ is the fluid velocity vector, t is time, μ is the fluid dynamic viscosity, the superscript T denotes the transpose of a vector, $\mathrm{tr}(\boldsymbol{A})$ gives the trace of $\boldsymbol{A}$, $\boldsymbol{I}$ is the identity matrix, $\boldsymbol{g}$ is gravity, H is height and P_{rgh} is the fluid pressure excluding the hydrostatic contribution (defined as $\rho \boldsymbol{g} H$).

By using the following relationships

$$\boldsymbol{\nabla} \cdot \left((\boldsymbol{\nabla} \boldsymbol{u})^{\mathrm{T}} \right) = \boldsymbol{\nabla} (\boldsymbol{\nabla} \cdot \boldsymbol{u}) \,, \tag{4.2}$$

$$\mathrm{tr} \left((\boldsymbol{\nabla} \boldsymbol{u})^{\mathrm{T}} \right) = \boldsymbol{\nabla} \cdot \boldsymbol{u} \qquad \text{and} \tag{4.3}$$

$$\boldsymbol{\nabla} \cdot (\boldsymbol{\nabla} \cdot \boldsymbol{u}) \boldsymbol{I} = \boldsymbol{\nabla} (\boldsymbol{\nabla} \cdot \boldsymbol{u}) \,, \tag{4.4}$$

equation 4.1 can be simplified to

$$\frac{\partial \boldsymbol{u}}{\partial t} + (\boldsymbol{u} \cdot \boldsymbol{\nabla}) \boldsymbol{u} = \nu \nabla^2 \boldsymbol{u} - \frac{1}{\rho} \boldsymbol{\nabla} P_{\mathrm{rgh}} \tag{4.5}$$

for an incompressible fluid, where ν is the fluid kinematic viscosity.

The energy equation is then solved and can compute either the internal energy or enthalpy of the system (this choice is user-dependent). When ignoring radiative terms and solving for enthalpy, h_{e}, the energy equation takes the following form

$$\boldsymbol{\nabla} \cdot (\rho \boldsymbol{u} h) + \frac{1}{2} \boldsymbol{\nabla} \cdot (\rho \boldsymbol{u} \cdot (\boldsymbol{u} \cdot \boldsymbol{u})) = \nabla^2 (\alpha_{\mathrm{eff}} h_{\mathrm{e}}) + \rho \boldsymbol{u} \boldsymbol{g} \,, \tag{4.6}$$

where α_{eff} is the sum of thermal diffusivity and turbulent thermal diffusivity of the medium.

The final equation solved for in the fluid domain is the pressure equation, which takes the form

$$\nabla^2 \frac{P}{\boldsymbol{C}} = \boldsymbol{\nabla} \cdot \frac{\boldsymbol{H}(\boldsymbol{u})}{\boldsymbol{C}}, \tag{4.7}$$

where P is pressure, $\boldsymbol{C}$ are the matrix coefficients from the discretisation of the momentum equation and $\boldsymbol{H}(\boldsymbol{u})$ is a function of the fluid velocity vector and is defined as

$$\boldsymbol{C}\boldsymbol{u} - \boldsymbol{H}(\boldsymbol{u}) \equiv \frac{\partial \boldsymbol{u}}{\partial t} + (\boldsymbol{u} \cdot \boldsymbol{\nabla})\,\boldsymbol{u} - \nu \nabla^2 \boldsymbol{u} \tag{4.8}$$

for an incompressible fluid. This is the same as equation 4.5 with the pressure term neglected. The fluid velocity used in the pressure equation is that which was calculated from the momentum conservation equation above. Using the pressure term from the solved pressure equation, the fluid velocity vector is corrected by

$$\boldsymbol{u} := \frac{\boldsymbol{H}(\boldsymbol{u})}{\boldsymbol{C}} - \frac{1}{\boldsymbol{C}} \boldsymbol{\nabla} P. \tag{4.9}$$

With this, the fluid domain has been solved for a given time step.

The equations for the solid domain are then solved. This comprises solely of an energy equation, which takes the form

$$-\nabla^2 (\alpha h_{\text{e}}) = 0, \tag{4.10}$$

where α is the thermal diffusivity of the medium. This is similar to the energy equation for the fluid domain, shown in equation 4.6, with the velocity terms neglected. The above process is then repeated for each subsequent time step until convergence is reached.

The above mathematical model requires additional input from users to fully define the thermophysical model. These inputs control the thermophysical properties of the medium and the form of the above equations for each domain, and are found in the *thermophysicalProperties* dictionary. For both the fluid and solid domains in this work, it was specified that there was a constant isobaric specific heat capacity, heat of fusion and density, and that the energy equations (shown in equations 4.6 and 4.10) solve for enthalpy. It was additionally specified that dynamic viscosity and Prandtl number (a dimensionless quantity giving the ratio of momentum diffusivity to thermal diffusivity) was constant in the fluid domain and that thermal conductivity was constant in the solid domain.

Finally, the boundary conditions and internal fields for the various field variables are defined in their individual files. These files are labelled as U (fluid velocity), p (pressure), *p_rgh* (pressure excluding the hydrostatic contribution), *rho* (density) and T (temperature). The boundary conditions for pressure is typically set to *calculated* as it is calculated from

$$P = P_{\text{rgh}} + \rho \boldsymbol{g} H. \tag{4.11}$$

Information regarding the chosen boundary conditions for the numerical models used throughout this work are provided in their respective chapters (chapter $5 - 7$).

4.5.2 Turbulence models

Turbulent flow is more complex than laminar flow and the mathematical model described in section 4.5.1 needs amending such that (1) the equations can be solved and (2) are computationally efficient. This is achieved through the implementation of turbulence models.

The Reynolds-averaged Navier Stokes (RANS) is a method to numerically approximate fluid turbulence, where fluid velocity is decomposed into its mean, $\overline{\boldsymbol{u}}$, and fluctuating, $\boldsymbol{u}'$, components. This gives

$$\boldsymbol{u} = \overline{\boldsymbol{u}} + \boldsymbol{u}' \,, \tag{4.12}$$

where $\overline{\boldsymbol{u}'} = 0$. Applying equation 4.12 to equation 4.5, the simplified momentum conservation, gives the following equation

$$\frac{\partial \overline{\boldsymbol{u}}}{\partial t} + (\overline{\boldsymbol{u}} \cdot \boldsymbol{\nabla})\, \overline{\boldsymbol{u}} = \nu \nabla^2 \overline{\boldsymbol{u}} - \frac{1}{\rho} \boldsymbol{\nabla} \overline{P_{\mathrm{rgh}}} - \boldsymbol{\nabla} \cdot \boldsymbol{R} \,, \tag{4.13}$$

where $\overline{P_{\mathrm{rgh}}}$ is the mean pressure (excluding the hydrostatic contribution) and $\boldsymbol{R}$ is the Reynolds stress tensor, which is defined as the mean value of the Kronecker product of the fluctuating component of the fluid velocity. The Reynolds stress tensor can be divided into its isotropic and deviatoric anisotropic contributions,

$$\boldsymbol{R} = \overline{\boldsymbol{u}' \otimes \boldsymbol{u}'} = \frac{2}{3} k_{\mathrm{t}} \boldsymbol{I} + \overline{\boldsymbol{u}' \otimes \boldsymbol{u}'} - \frac{2}{3} k_{\mathrm{t}} \boldsymbol{I} \,, \tag{4.14}$$

where k_{t} is the turbulent kinetic energy. The first term is the isotropic contribution, which can be added to the mean pressure, and the remaining two terms are the deviatoric contribution. This transforms equation 4.13 into

$$\frac{\partial \overline{\boldsymbol{u}}}{\partial t} + (\overline{\boldsymbol{u}} \cdot \boldsymbol{\nabla})\, \overline{\boldsymbol{u}} = \nu \nabla^2 \overline{\boldsymbol{u}} - \frac{1}{\rho} \boldsymbol{\nabla} \overline{P_{\mathrm{rgh}}}' - \boldsymbol{\nabla} \cdot \boldsymbol{R}_{\mathrm{dev}} \,, \tag{4.15}$$

where

$$\boldsymbol{R}_{\mathrm{dev}} = \overline{\boldsymbol{u}' \otimes \boldsymbol{u}'} - \frac{2}{3} k_{\mathrm{t}} \boldsymbol{I} \qquad \text{and} \tag{4.16}$$

$$\overline{P_{\mathrm{rgh}}}' = \overline{P_{\mathrm{rgh}}} + \frac{2}{3} k_{\mathrm{t}} \,. \tag{4.17}$$

This method was used for the numerical models which exhibited high Reynolds numbers in this work as it is more computationally efficient than other method, such as direct numerical simulation (DNS) and large-eddy simulation (LES).

Turbulence models suitable for the chosen method must then be selected. For example, linear eddy viscosity turbulence models, such as the k-ω-SST turbulence model, are suitable for the RANS method. Here, the deviatoric anisotropic Reynolds stress tensor is considered proportional to the traceless mean rate of strain, which gives

$$\boldsymbol{R}_{\mathrm{dev}} = -\nu_{\mathrm{t}} \left(\boldsymbol{\nabla} \overline{\boldsymbol{u}} - (\boldsymbol{\nabla} \overline{\boldsymbol{u}})^{\mathrm{T}} \right) - \nu_{\mathrm{t}} \left(\frac{2}{3} \boldsymbol{\nabla} \cdot \overline{\boldsymbol{u}} \right) \boldsymbol{I} \,, \tag{4.18}$$

where ν_t is the turbulent kinematic viscosity. Equation 4.15 therefore becomes

$$\frac{\partial \overline{\boldsymbol{u}}}{\partial t} + (\overline{\boldsymbol{u}} \cdot \boldsymbol{\nabla})\,\overline{\boldsymbol{u}} = \nu_{\text{eff}} \nabla^2 \overline{\boldsymbol{u}} - \frac{1}{\rho} \boldsymbol{\nabla} \overline{P_{\text{rgh}}}', \tag{4.19}$$

where ν_{eff} is the sum of the kinematic viscosity and turbulent kinematic viscosity. The turbulent kinematic viscosity is then calculated by a turbulence model dependent equation. For example, the turbulent kinematic viscosity in the k-ω-SST turbulence model is given by

$$\nu_t = \frac{a_1 k_t}{\max\left(a_1 \omega_t, \frac{b_1 F_2}{2}\left(\boldsymbol{\nabla}\overline{\boldsymbol{u}} + (\boldsymbol{\nabla}\overline{\boldsymbol{u}})^{\mathrm{T}}\right)\right)}, \tag{4.20}$$

where the max function selects the largest of the two arguments, a_1 and b_1 are model coefficients, ω_t is the turbulent specific dissipation rate and F_2 is an auxiliary relation (which expresses unclosed terms as functions of the dependent variables). The turbulent kinetic energy and turbulent specific dissipation rate for incompressible fluids are found by solving

$$\frac{\partial k_t}{\partial t} + \overline{\boldsymbol{u}} \cdot \boldsymbol{\nabla} k_t = \boldsymbol{\nabla} \cdot (D_k \boldsymbol{\nabla} k_t) + G - \frac{2}{3} k_t (\boldsymbol{\nabla} \cdot \overline{\boldsymbol{u}}) - \beta^* \omega_t k_t + \frac{S_k}{\rho} \qquad \text{and} \tag{4.21}$$

$$\frac{\partial \omega_t}{\partial t} + \overline{\boldsymbol{u}} \cdot \boldsymbol{\nabla} \omega_t = \boldsymbol{\nabla} \cdot (D_\omega \boldsymbol{\nabla} \omega_t) + \frac{\zeta G}{\nu} - \frac{2}{3} \zeta \omega_t (\boldsymbol{\nabla} \cdot \overline{\boldsymbol{u}}) - \beta {\omega_t}^2 - (F_1 - 1)\, CD_{k\omega} + \frac{S_\omega}{\rho}, \tag{4.22}$$

where D_k and D_ω is the effective diffusivity for the turbulent kinetic energy and turbulent specific dissipation rate respectively, G is the turbulent kinetic energy production rate due to the anisotropic part of the Reynolds stress tensor, β^*, β and ζ are model coefficients, S_k and S_ω are source terms for the turbulent kinetic energy and turbulent specific dissipation rate respectively, and F_1 and $CD_{k\omega}$ are auxiliary relations.

The k-ω-SST turbulence model was used for the numerical models discussed in chapter 7 due to the presence of high Reynolds number. The reasoning behind this choice is given in chapter 7. DNS, where the equations in the mathematical model are solved without making any approximations (outside of discretisation), was used for the remaining numerical models presented in this work as they featured Reynolds numbers within the laminar region.

These choices are made in the *turbulenceProperties* dictionary by specifying either *laminar*, *RAS* (i.e., RANS) or *LES* in the *simulationType* subdictionary. Here, *laminar* denotes that a DNS approach was used (i.e., no turbulence model). The turbulence model then needs to be specified in the respective *RASModel* or *LESModel* sub-dictionary. The boundary conditions and internal fields for the turbulent field variables also need to be defined when a turbulence model is used, similar to section 4.5.1. For the k-ω-SST turbulence model, these include *alphat* (turbulent thermal diffusivity), *nut* (turbulent kinematic viscosity), k (turbulent kinetic energy) and *omega* (turbulent specific dissipation rate).

4.5.3 Pressure-velocity coupling algorithms and solution method

The pressure-velocity algorithm and the solution method is defined within the *fvSolution* dictionary for each domain. As discussed in section 4.5.1, momentum conservation is solved first, followed by the energy equation, and then the pressure equation (which provides a correction for the fluid velocity). This is repeated for the following iteration using the previously solved values, until either convergence or the maximum number of iterations is reached. This process is

given by a pressure-velocity coupling algorithm. The Semi-Implicit Method for Pressure Linked Equations (SIMPLE) algorithm was used throughout this work because it produces steady flow solutions. A flow chart of the SIMPLE algorithm for a fluid domain is shown in figure 4.6.

For any given iteration, the above equations are discretised and solved multiple times until either (1) convergence is reached, (2) the maximum number of iterations is reached or (3) the ratio of current to initial residual falls below a user-specified value. To distinguish these iterations with that for the entire model (the pseudo time steps), they are labelled as inner iterations. These discretised equations are solved using linear solvers. The preconditioned (bi-)conjugate gradient (PCG) linear solver was used for density and the stabilized preconditioned (bi-)conjugate gradient (PBiCGStab) linear solver was used to find the solutions for fluid velocity, enthalpy, turbulent kinetic energy and turbulent specific dissipation rate. The generalised geometric-algebraic multigrid (GAMG) linear solver was used to find the solution for pressure in the numerical models presented in chapters 5 and 6, whereas the PCG linear solver was used for the models presented in chapter 7 as the GAMG linear solver was found to not be stable during parallel processing.

The SIMPLE algorithm also makes use of under-relaxation factors. Under-relaxation factors, α_U, limit the amount by which a field variable can change from successive iterations by either changing the solution matrix and source or changing the field directly. This improves the stability of the computation as large changes in a field variable may slow or prevent convergence. Under-relaxation factors vary between $0 \leq \alpha_U \leq 1$, where under-relaxation increases in strength as $\alpha_U \to 0$ (i.e., there is no change in solution) and where there is no under-relaxation at $\alpha_U = 1$. Under-relaxation factors need to be chosen such that the computation remains stable, which

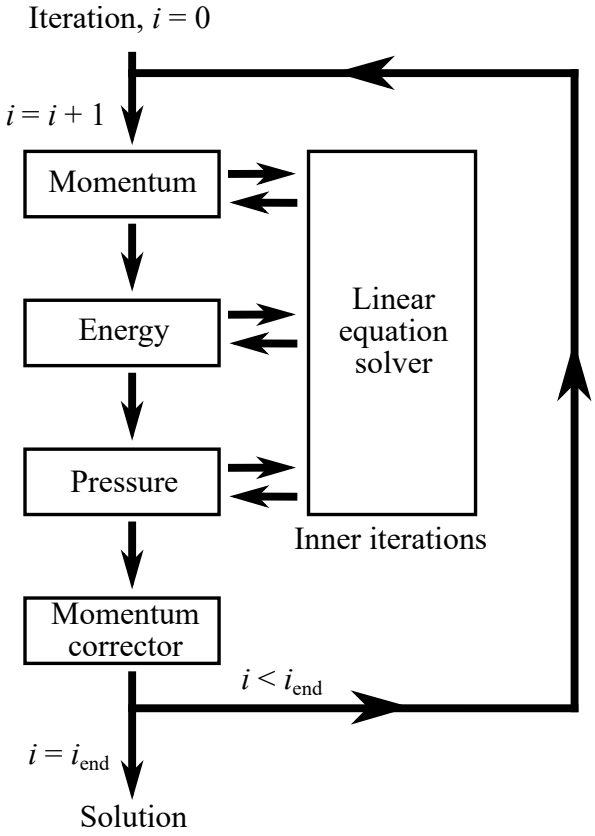

Figure 4.6: Flow chart of the SIMPLE algorithm for a single fluid domain.

happens at lower under-relaxation factors, while making the iterative process move quickly, which happens at higher under-relaxation factors. Under-relaxation values of $0.2 - 0.3$ were used for fluid velocity, turbulent kinetic energy and turbulent specific dissipation rate and values of 0.7 were used for pressure and enthalpy (under-relaxation was not used for density as the fluid was incompressible). This provided a stable model which ran at an acceptable speed.

4.5.4 Numerical schemes

The equations discussed in sections 4.5.1 and 4.5.2 need to be discretised. There are multiple discretisation methods which can be used to generate the set of linear equations, and these need to be specified for the various terms that appear in the mathematical model, such as derivatives. The methods used are given in the *fvSchemes* dictionary file as the finite volume method, which is a decomposition method for the numerical grid, was used.

The discretisation methods are given in table 4.1. The *steadyState* scheme was used for the time derivatives as steady fluid flow and heat transfer were being examined. The remaining numerical schemes were chosen by finding test cases for conjugate heat transfer problems within OpenFOAM to ensure that appropriate schemes were selected.

4.5.5 Time and data control

A database which controls the inputs and outputs for the model is set up. Outputted data is typically requested at set time intervals during the modelling stage and, hence, time is a crucial part of the database. This is controlled by the *controlDict* dictionary. Various parameters are needed to set up the database. These include time controls, which handles the start and end time of the simulation, time step controls, which handles the time steps in the simulation, and

Term	Numerical scheme	Description
$\frac{\partial}{\partial t}$	*steadyState*	Time derivatives are not solved
Interpolation scheme (interpolation of values from finite volume centre to face centre)	*linear*	Linear interpolation (second order, unbounded)
$\boldsymbol{\nabla}$	*Gauss linear*	Second order Gaussian integration with linear interpolation
$\boldsymbol{\nabla}$ (Surface normal gradient)	*corrected*	Explicit non-orthogonal correction
$\boldsymbol{\nabla}\cdot\left[\rho\nu_{\text{eff}}\left((\boldsymbol{\nabla}\boldsymbol{u})^{\text{T}}-\frac{2}{3}\text{tr}\left((\boldsymbol{\nabla}\boldsymbol{u})^{\text{T}}\right)\right)\right]$	*Gauss linear*	Second order Gaussian integration with linear interpolation
$\boldsymbol{\nabla}\cdot(\boldsymbol{u}, h_{\text{e}}, k_{\text{t}}, \omega_{\text{t}})$	*Gauss upwind*	Second order Gaussian integration with upwind differencing (first order, bounded)
∇^2	*Gauss linear corrected*	Second order Gaussian integration with linear interpolation and explicit non-orthogonal correction

Table 4.1: Numerical schemes used in the OpenFOAM models.

data writing controls, which handles how and when data is outputted and saved.

Run-time loadable functions, which take place during the simulation and have their own separate time and data control database, can also be specified. There are many different functions with a wide-range of applications which prove useful, such as outputting the components of a field variable vector at a user-specified probe point.

4.6 Problems modelling TPMS-based lattice structures

TPMS-based lattice structures exhibit more curvature than conventional channels and fin arrays and therefore require more mesh elements to capture the surface geometry accurately. The complex fluid dynamics present in TPMS-based lattice structures, which may not exist within channels or fin arrays, also require more mesh elements to model them accurately. This significantly impacted the computational cost and slowed down the simulation of the numerical models featuring TPMS-based lattice structures in this work as computational run time scales with the number of mesh elements.

TPMS-based lattice structures have small wall thicknesses and may not be meshed correctly. The mesh needs to be visually checked as holes may appear in the lattice walls if the mesh elements are not small enough to capture the geometry for example. Smaller mesh elements need to be used in these cases, but this has a large effect on the computational performance. Additionally, TPMS-based lattice structures may not be modelled accurately or efficiently due to the small number of mesh elements in the wall. The same is also true for TPMS-based lattice structures with high volume fractions, where the fluid channels have very small radii and may not be meshed properly. This affects the convergence of the numerical model and the accuracy of its results.

The fluid velocity gradient within the boundary layer is much larger in the fluid flow transverse direction than in the longitudinal direction. Prism elements, which are typically thin (i.e., have a high aspect ratio) as shown in figure 4.7, are generally used to resolve the fluid velocity boundary layer. They are arranged in layers, where each successive layer is thicker than the last (known as inflation), until the mesh structure transitions into an unstructured mesh. This transition should happen after the boundary layer is fully resolved by the prism elements. The layers inflate to reduce computational costs and to ensure that the volume of the prism element in the final layer (farthest from the wall boundary) is similar to the closest unstructured mesh element to improve model accuracy (a sudden change in element volume can lead to an error in the local gradient). Prism layers were not used throughout this research project when modelling TPMS-based lattice structures, however. This was because the high curvature of the TPMS-based lattice structures hindered the generation of the prism layers. A heavily refined unstructured mesh was used to resolve the boundary layer in these cases instead, but this significantly increased computational costs.

In comparison to conventional circular channels, the modelled TPMS-based lattice structures exhibit multiple tortuous channels. This can cause fluid flow phenomena, such as flow separation and vortices, which would not typically be present within circular channels. Hence, it was expected that n^+, the dimensionless distance of the first mesh element node from the wall, would vary along the walls of the modelled TPMS-based lattice structures. Prism layers generally

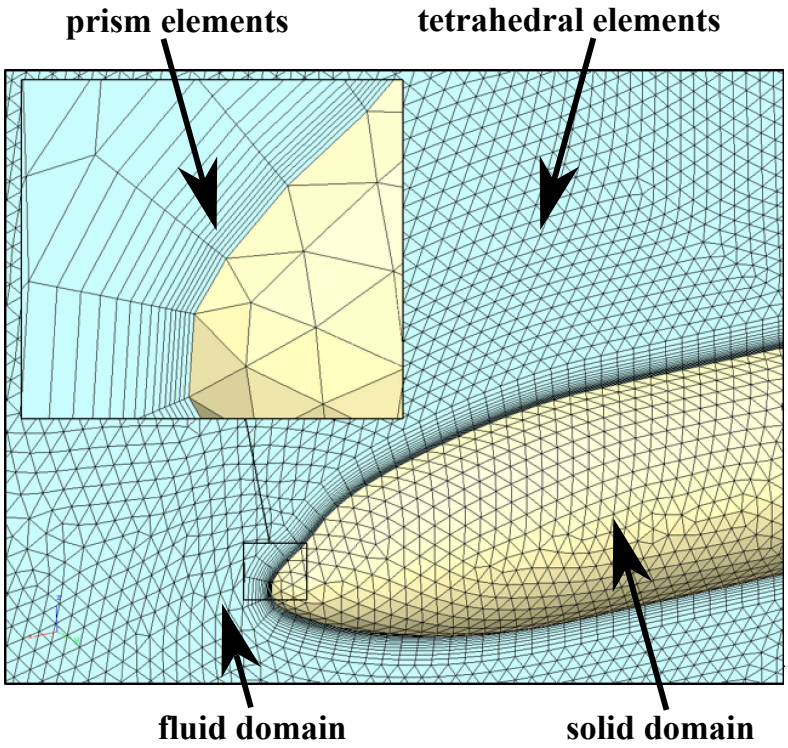

Figure 4.7: Example of inflating prism layers in the near-wall region, followed by an unstructured mesh. Modified from [126].

reduce n^+, due to their small size in the fluid flow transverse direction, and can be manipulated more easily (through parameters such as first layer thickness, total number of layers and growth ratio) than refinement regions to control n^+ throughout the modelled structure. The lack of prism layers generated for the modelled TPMS-based lattice structures therefore exacerbated the above issue as n^+ was more difficult to control. This lead to n^+ values which were both within and outside the viscous sublayer across the modelled TPMS-based lattice structures. An all-n^+ wall treatment, discussed in appendix B.5, was adopted to mitigate this issue. Generating appropriate prism layers in the near-wall region for TPMS-based lattice structures is therefore a priority for future development as this would substantially reduce computational costs and improve model accuracy.

Analytical relationships for the fluid flow and heat transfer through TPMS-based lattice structures do not exist. The TPMS-based lattice structure numerical models cannot be validated analytically and must instead be validated experimentally or shown to be robust through comparison with other numerical predictions. The validation of these models is therefore time-consuming and requires that the numerical model is similar to the performed experiment (e.g., all of the experimental parameters, such as fluid velocity profile, must be known) or to other numerical predictions. Another option is to first model structures for which analytical solutions exist, such as circular channels. This can provide initial validation and confidence in the numerical model, but cannot be used as proof that the model can accurately predict fluid flow in more complex structures.

Chapter 5

Structure-performance Relationships for TPMS-based Lattices

5.1 Introduction

As discussed in section 2.4, further work needs to be undertaken to find relationships between the performance of TPMS-based heat sinks and their geometrical properties. Without these relationships, engineers incorporating TPMS-based lattices into heat sink designs make uninformed decisions on the geometrical properties of the structure, such as cell type and volume fraction, and cannot design multifunctional heat sinks, such as heat sinks with increased heat transfer and mechanical properties (e.g., strength). This can lead to unoptimised heat sinks which do not meet the necessary performance requirements. This chapter is therefore focused on understanding the fluid dynamics within TPMS-based lattice structures and how this affects heat transfer at low Reynolds numbers and temperatures, where they are simpler to model and validate. Complex fusion-relevant fluid flow and temperature conditions are examined in chapter 7 using the knowledge gained from this simpler application.

Here, the hydraulic and thermal performance of several TPMS-based lattice geometries are examined numerically over a range of fluid flow velocities and volume fractions. The performance of these structures are characterised and explained by examining the fluid dynamics within them. Design guides for the hydraulic and thermal performance of the examined structures, in terms of their principal geometrical properties, are then established. These can be used by heat transfer engineers to design appropriate heat sinks incorporating TPMS-based lattice structures whilst eliminating the need for expensive and difficult physical testing and numerical modelling.

5.2 Method

5.2.1 Cellular structures

Five different lattice structures, generated using FLatt Pack, were chosen for this study and are shown in figure 5.1. These are the diamond, gyroid, lidinoid, primitive and split-p matrix phases

The contents of this chapter have been published in: D. Padrão, D. Hancock, J. Paterson, F. Schoofs, C. Tuck and I. Maskery, "New structure-performance relationships for surface-based lattice heat sinks". In: *Applied Thermal Engineering* 236 (2024), pp. 121572

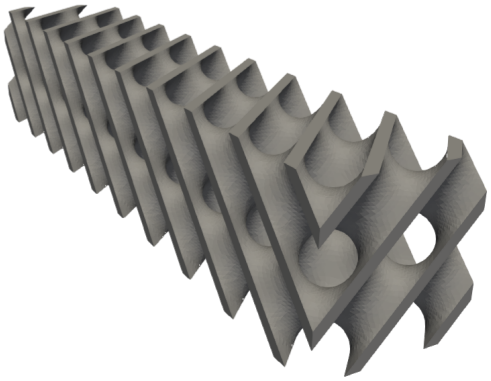

(a) Diamond matrix lattice.

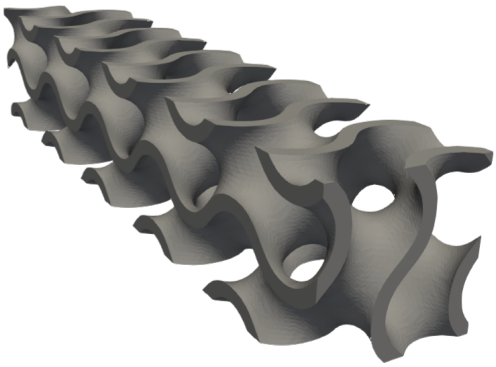

(b) Gyroid matrix lattice.

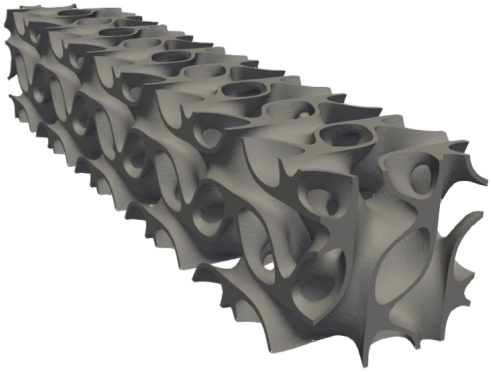

(c) Lidinoid matrix lattice.

(d) Primitive matrix lattice.

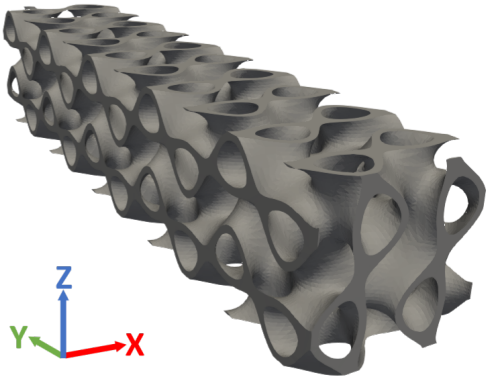

(e) Split-p matrix lattice.

Figure 5.1: Examples of the examined structures with a volume fraction of 0.25.

of the TPMS-based lattice structures, with volume fractions, γ, ranging from $0.15 - 0.4$. This gave lattice structures with hydraulic diameters of $2.2 - 7.3$ mm. Increasing volume fraction leads to thicker walls and therefore, smaller hydraulic diameters. The former three structures were chosen as they have received the most attention in the literature, while the remaining structures were chosen for their tortuous channels and relatively high surface areas, suggesting they may perform well as heat sinks. The matrix phases were used here because they possess greater surface areas per unit volume than the network phases [51].

The examined lattice structures had dimensions of $10 \times 50 \times 10$ mm and contained $1 \times 5 \times 1$ cells. These dimensions were chosen to provide sufficient surface to allow the fluid flow to fully

Volume fraction	Diamond matrix	Gyroid matrix	Lidinoid matrix	Primitive matrix	Split-p matrix
0.15	0.187	0.237	0.204	0.268	0.210
0.2	0.245	0.312	0.273	0.351	0.277
0.25	0.309	0.392	0.350	0.443	0.348
0.3	0.367	0.466	0.423	0.527	0.415
0.35	0.429	0.546	0.503	0.618	0.486
0.4	0.488	0.619	0.578	0.702	0.552

Table 5.1: Values for θ in equations 5.1–5.5 which give the desired volume fraction for the examined TPMS-based lattice structures.

develop and to examine the evolution of mixing arising from the periodicity of the structures. The structures examined here are comprised of a single unit cell in the direction normal to the inlet fluid flow. This was done to gain insight into the fluid dynamics within lattice cells, which can then be used to develop general structure-performance models for arbitrary lattice structures.

FLatt Pack generates TPMS-based lattice structures using surface equations, which were described in section 2.3. These are

$$\begin{aligned} U_{\mathrm{DM}} = &\big(\cos(k_x x)\cos(k_y y)\cos(k_z z)) + \sin(k_x x)\sin(k_y y)\sin(k_z z) + \\ &\sin(k_x x)\cos(k_y y)\sin(k_z z) + \cos(k_x x)\sin(k_y y)\sin(k_z z)\big)^2 - \theta^2\,, \end{aligned} \tag{5.1}$$

$$U_{\mathrm{GM}} = \big(\sin(k_x x)\cos(k_y y) + \sin(k_y y)\cos(k_z z) + \sin(k_z z)\cos(k_x x)\big)^2 - \theta^2\,, \tag{5.2}$$

$$\begin{aligned} U_{\mathrm{LM}} = &\big(\big(\sin(2k_x x)\cos(k_y y)\sin(k_z z) + \sin(2k_y y)\cos(k_z z)\sin(k_x x) + \\ &\sin(2k_z z)\cos(k_x x)\sin(k_y y)\big) - \big(\cos(2k_x x)\cos(2k_y y) + \\ &\cos(2k_y y)\cos(2k_z z) + \cos(2k_z z)\cos(2k_x x)\big)\big)^2 - \theta^2\,, \end{aligned} \tag{5.3}$$

$$U_{\mathrm{PM}} = \big(\cos(k_x x) + \cos(k_y y) + \cos(k_z z)\big)^2 - \theta^2\,, \tag{5.4}$$

$$\begin{aligned} U_{\mathrm{SPM}} = &\big(1.1\big(\sin(2k_x x)\cos(k_y y)\sin(k_z z) + \sin(2k_y y)\cos(k_z z)\sin(k_x x) + \\ &\sin(2k_z z)\cos(k_x x)\sin(k_y y)\big) - 0.2\big(\cos(2k_x x)\cos(2k_y y) + \\ &\cos(2k_y y)\cos(2k_z z) + \cos(2k_z z)\cos(2k_x x)\big) - \\ &0.4\big(\cos(2k_x x) + \cos(2k_y y) + \cos(2k_z z)\big)\big)^2 - \theta^2\,, \end{aligned} \tag{5.5}$$

for the diamond (DM), gyroid (GM), lidinoid (LM), primitive (PM) and split-p matrix (SPM) lattice structures, respectively. $k_{x,y,z}$ is dependent on the length and number of cells of the generated TPMS-based lattice structures, which are given in this section. θ gives the position of the solid-void boundary and can be correlated with the volume fraction as discussed in section 2.3. The values for θ used to give the desired volume fractions are provided in table 5.1.

5.2.2 Numerical method

The computational domain used in this study, shown in figure 5.2, comprised of a cuboid fluid domain of dimensions $10 \times 90 \times 10$ mm. The lattice structures were situated in the mesh such

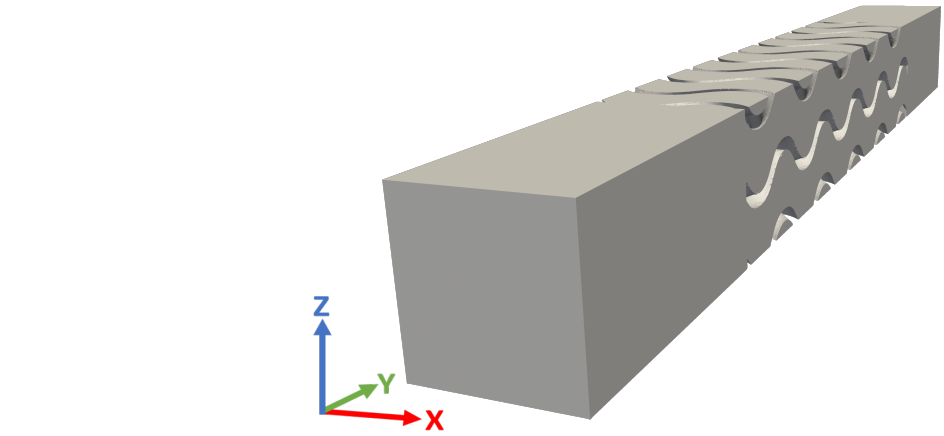

(a) Fluid domain.

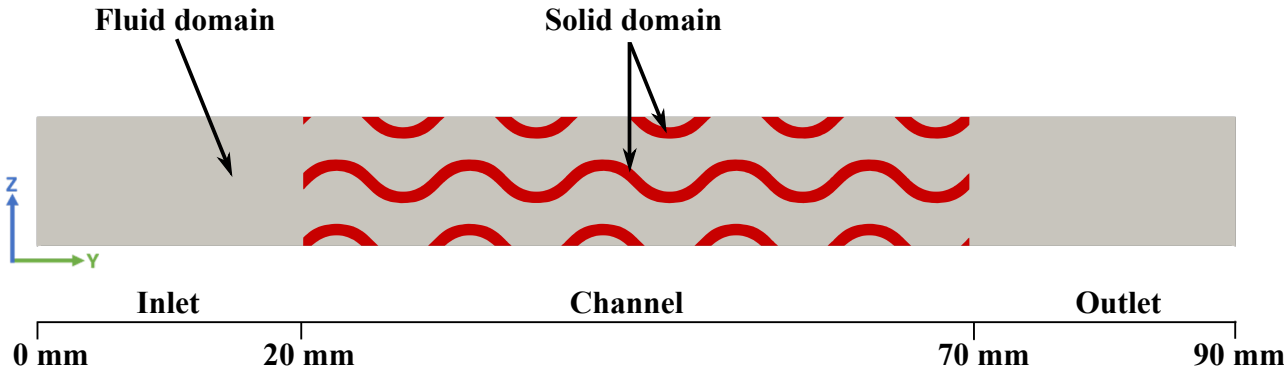

(b) Cross-sectional view with the fluid domain (grey) and solid domain (red).

Figure 5.2: Schematics for the computational domain of a gyroid matrix lattice structure with a volume fraction of 0.25.

that inlet and outlet pipes, 20 mm in length each, were present. This was sufficient for the flow to transition into the structures and to prevent the propagation of divergent results upstream from the outlet. A constant temperature of 323 K, also used in a study performed by Pulvirenti *et al* [74], was applied to the base of the solid and fluid domains in the channel section. Thermal energy was applied to the structures in only one direction to be more closely analogous to real applications and to examine the impact of a directional heat source. The properties of the computational domains are shown in table 5.2.

The fluid was modelled travelling in the y-direction with inlet superficial velocities, u_s, of $0.8\times10^{-3} - 6\times10^{-3}$ m s^{-1}, corresponding to Reynolds numbers of $3.2 - 62.5$ across the examined structures, and an inlet temperature of 293 K. This flow regime was examined to ensure that the performance of these structures can be meaningfully compared with other work in the literature, such as that of Pulvirenti *et al* [74], where a gyroid matrix lattice structure was examined for cooling applications, and Santos *et al* [83], where the hydraulic performance of various TPMS-based lattice structures were determined. The solid domain was modelled as Inconel-718 as it has seen extensive research for heat exchange applications in the aerospace industry [20]. The *chtMultiRegionSimpleFoam* solver was used here because it is adept at solving conjugate heat transfer problems for steady-state incompressible fluids.

Computational domain	Medium	Density (kg m^{-3})	Kinematic viscosity (m^2 s^{-1})	Specific heat capacity (J kg^{-1} K^{-1})	Thermal conductivity (W m^{-1} K^{-1})
Solid	Inconel-718	8,190		435	11.4
Fluid	Water (incompressible)	1,000	8.9×10^{-7}	4,180	0.532

Table 5.2: Material properties for the computational domains to determine structure-performance relationships of TPMS-based lattice structures.

	Boundary conditions			
Boundary	Velocity, u (m s^{-1})	Pressure, P (Pa)	Fluid temperature, T_f (K)	Lattice temperature, T_l (K)
Inlet	$u = u_{ref}$	Adjust ∇P to match flux with velocity	$T_f = 293$	
Outlet	$\nabla u = 0$	$P = 0$	$\nabla T_f = 0$	
Walls	$u = 0$	Adjust ∇P to match flux with velocity	$\nabla T_f = 0$	$\nabla T_l = 0$
Bottom wall in channel	$u = 0$	Adjust ∇P to match flux with velocity	$T_f = 323$	$T_l = 323$
Fluid-solid boundary	$u = 0$	Adjust ∇P to match flux with velocity	$T_f = T_{l,adj}$, $\nabla T_f = 0$	$T_l = T_{f,adj}$, $\nabla T_l = 0$

Table 5.3: Boundary conditions for the numerical model to determine structure-performance relationships of TPMS-based lattice structures. Here, the subscript 'ref' refers to a user-specified value and the subscript 'adj' refers to an adjacent face in a different domain.

The implemented boundary conditions can be seen in table 5.3. A $\nabla T_f = 0$ boundary condition was applied to the outlet fluid temperature to prevent errors propagating upstream and because the profile of the outlet temperature was not known. The above boundary conditions are well-established for finite volume modelling and have been used to accurately predict fluid flow and heat transfer [63, 77, 84].

The fluid-solid boundary was modelled as a smooth interface. This was chosen instead of a rough interface, which may be more reflective of AM components generally, in order to obtain useful structure-performance relationships across a range of manufacturing and materials scenarios.

To determine the validity of the smooth-wall approach for the examined structures, a short investigation into wall roughness for the examined range of superficial fluid velocity was performed. Wall roughness can be modelled by implementing a boundary condition for turbulent viscosity which modifies the wall roughness parameter by modelling a layer of sand particles on the walls. The morphology of the particles are controlled by a sand-grain roughness, K_S, and a roughness constant. The sand-grain roughness represents the particle diameter and the roughness constant represents the particle shape uniformity and particle spacing (a typical roughness constant of 0.5

gives uniform spherical particles). If the dimensionless sand-grain roughness, $K_S{}^+$, (which gives a dimensionless sand-grain roughness at the first element node from the wall) is less than 2.25, then the wall roughness parameter is not modified and the wall is modelled as hydrodynamically smooth. This is because the surface protrusions lie fully within the fluid boundary layer.

The dimensionless sand-grain roughness can be calculated from the sand-grain roughness by

$$K_S{}^+ = \frac{u^* K_S}{\nu_w} . \tag{5.6}$$

For the wall to be modelled as a rough interface, the sand-grain roughness must therefore fulfil the following condition,

$$K_S > \frac{2.25\,\nu_w}{u^*} . \tag{5.7}$$

Considering the case with the greatest superficial fluid velocity examined here (6×10^{-3} m s^{-1}), the sand-grain roughness would need to be greater than 5.2 mm for the wall to be modelled as a rough interface. This can be converted to an arithmetic average roughness, R_a, which is widely used in surface metrology, through the following correlation [127]

$$R_a = \frac{K_S}{5.863} . \tag{5.8}$$

The walls must therefore have an arithmetic average roughness greater than 890 µm for it to be modelled as a rough interface. Metal upward-facing surfaces, produced from a range of different AM materials and processes, typically have arithmetic average roughnesses on the order of magnitude of 10 µm [128–131]. This is significantly lower than the minimum arithmetic average roughness needed for the walls to be treated as a rough interface and, therefore, the smooth-wall approach is appropriate for this case.

5.2.3 Validation of the numerical model

A CFD mesh convergence study was performed to determine a suitable mesh element density for accurate fluid flow and conjugate heat transfer calculations. This was performed for a gyroid matrix lattice structure with a volume fraction of 0.4 at a volumetric flow rate of $6{\times}10^{-7}$ m^3 s^{-1}. The pressure drop and outlet fluid temperature were found to be well converged at around $1.8{\times}10^6$ elements, as shown in figure 5.3, for an unstructured mesh featuring refined polyhedral elements at the fluid-solid boundaries and hexahedral elements elsewhere. An example of this is shown in figure 5.4. The models for this work feature similar meshes, as shown in figure 5.5.

A convergence study was also performed for a gyroid matrix lattice structure with a volume fraction of 0.4 to determine whether a turbulence model was necessary to model the fluid accurately. This was done because the tortuous channels of the TPMS lattice structures may promote turbulence and, as discussed in the section 5.2.4, the examined flow range is in the laminar-turbulent transition region for a porous structure. The pressure drop for the RANS k-ϵ turbulence model agreed with the results from the DNS simulation, as shown in figure 5.6, so a turbulence model was not implemented for this study.

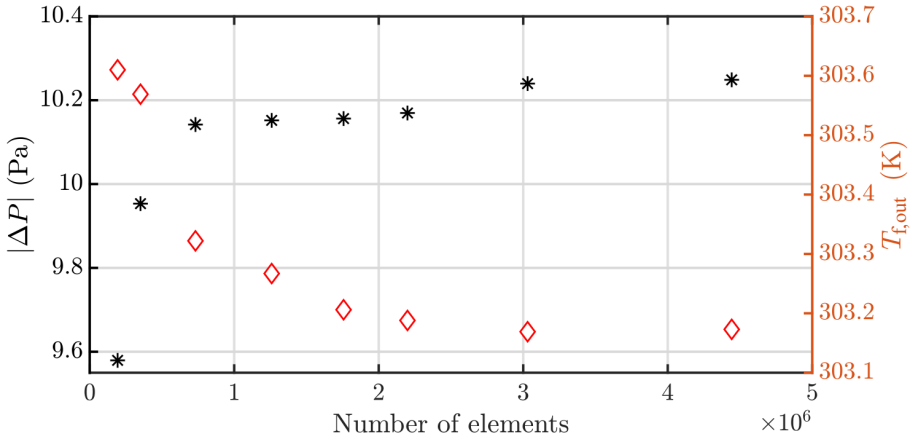

Figure 5.3: Pressure drop (black star) and outlet fluid temperature (red diamond) mesh convergence analysis for a gyroid matrix lattice (superficial fluid velocity $= 6 \times 10^{-3}$ m s^{-1}, volume fraction $= 0.4$).

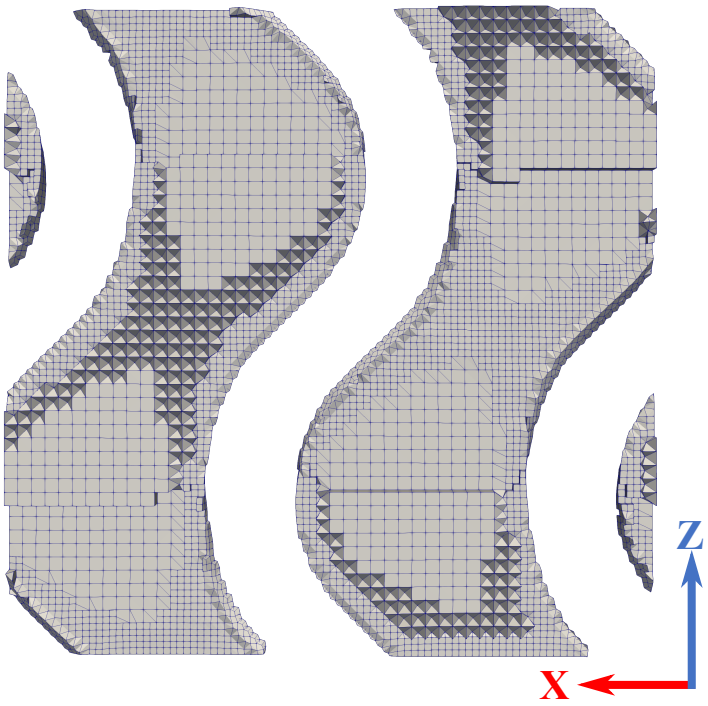

Figure 5.4: Cross-section of the fluid domain mesh for a gyroid matrix lattice with a volume fraction of 0.4 at a position $y = 0.045$ m after the inlet plane.

These models were first validated against the numerical results presented by Pulvirenti *et al* [74], where differences of 1.4% and 0.01% were obtained for the pressure drop and fluid exit temperature, respectively, for an equivalent gyroid matrix structure. For completeness, a simple circular channel, with a channel radius of 4.88×10^{-3} m and a length of 0.01 m, was also modelled, with fully-developed inlet flow, and validated against the Hagen-Poiseuille law [132], given by

$$\Delta P = \frac{8\mu L\dot{V}}{\pi r^4}, \tag{5.9}$$

where ΔP is pressure drop, μ is the dynamic viscosity of the fluid, L is the pipe length, $\dot{V}$ is the volumetric flow rate and r is the channel radius. This law gives the pressure drop due

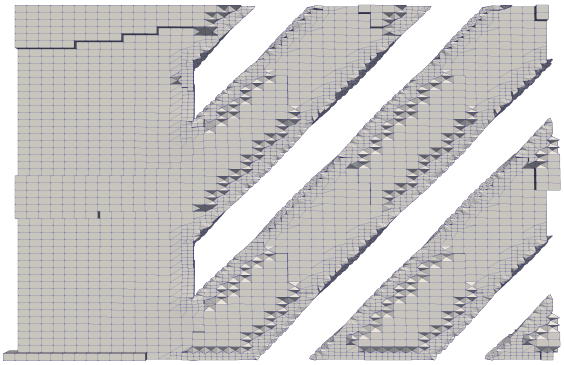

(a) Diamond matrix lattice.

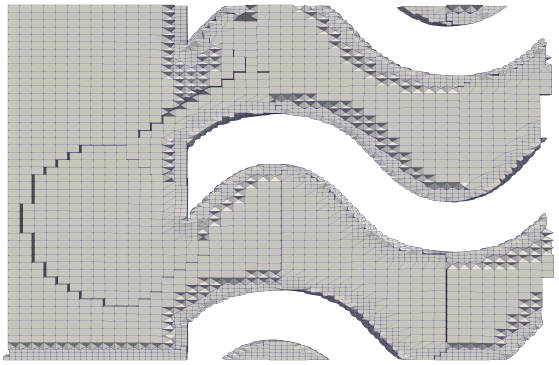

(b) Gyroid matrix lattice.

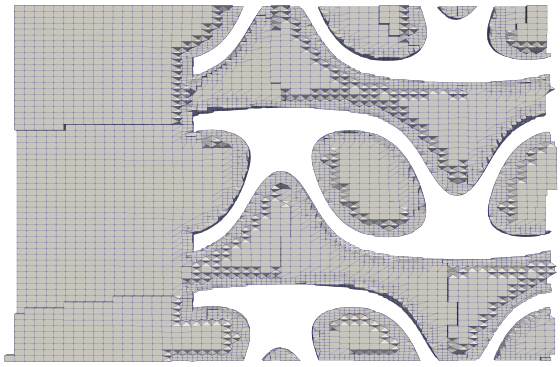

(c) Lidinoid matrix lattice.

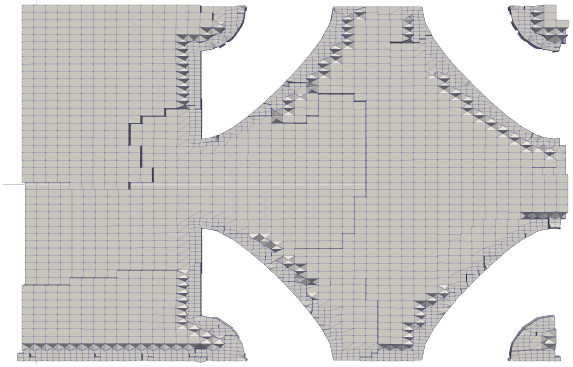

(d) Primitive matrix lattice.

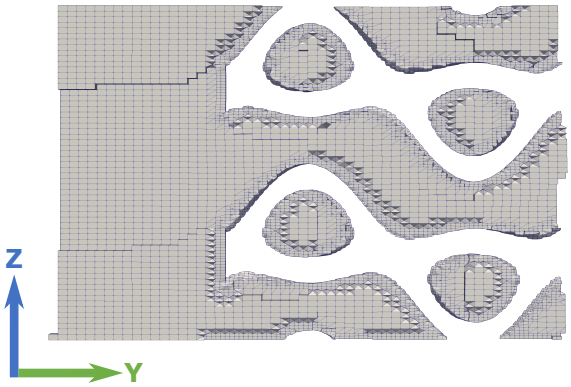

(e) Split-p matrix lattice.

Figure 5.5: Cross-section of the fluid domain mesh for the examined surface-based lattice structures with a volume fraction of 0.4 at a position x =0.025. The first unit cell and 5 mm of the inlet are displayed.

to viscous forces for incompressible and Newtonian fluids under laminar flow conditions in a circular channel. The numerical model agreed with equation 5.9, where the predicted pressure drops were within 1% of the analytical solution, shown in figure 5.7.

5.2.4 Theoretical background and method

Pressure drop across the test structures was examined to determine the hydraulic performance of each lattice cell type. The fluid dynamics and variation of fluid pressure within the structures

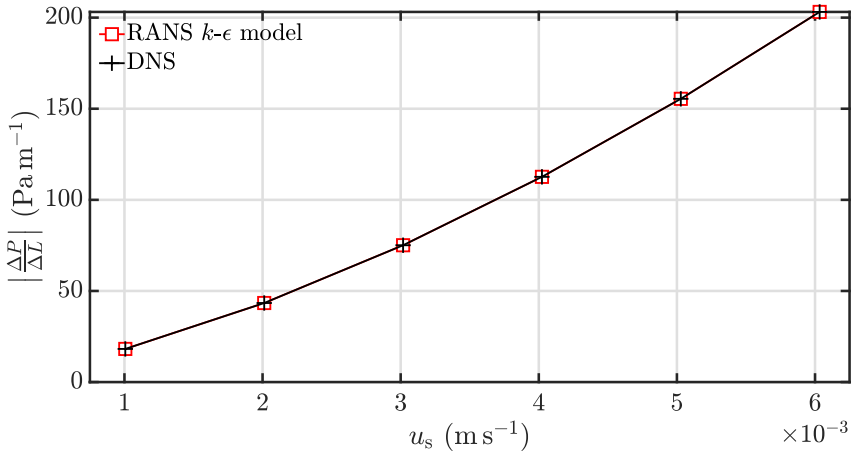

Figure 5.6: Comparison of pressure drop results from DNS and the RANS k-ϵ model for a gyroid matrix with a volume fraction of 0.4.

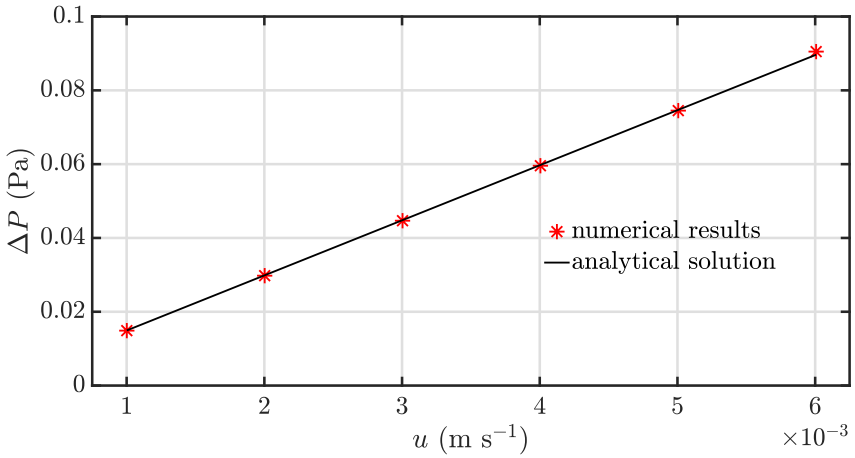

Figure 5.7: Comparison between numerical results and the analytical solution for a circular channel.

were also examined to understand the impact of different lattice geometries at equivalent volume fractions.

Darcy's law describes pressure drop across a porous medium for slow, viscous flow [83],

$$\left|\frac{\Delta P}{\Delta L}\right| = \frac{\mu}{K} u_\mathrm{s}\,, \tag{5.10}$$

where $\Delta P/\Delta L$ is the pressure drop per unit length, K is the Darcian permeability constant and u_s is the superficial fluid velocity. Superficial fluid velocity is defined as

$$u_\mathrm{s} = \frac{\dot{V}}{A_\mathrm{T}}\,, \tag{5.11}$$

where A_T is the total cross-sectional area of the fluid and solid domain. At high flow rates, the flow is no longer Darcian and a non-linear term, the Forchheimer term, is added to account for the inertial effects [82],

$$\left|\frac{\Delta P}{\Delta L}\right| = \frac{\mu}{K_1} u_\mathrm{s} + \frac{\rho}{K_2} {u_\mathrm{s}}^2\,, \tag{5.12}$$

where ρ is density and K_1 and K_2 are the Forchheimer and inertial permeability constants, respectively. These constants are generally associated with the geometry of the porous medium, where K and K_1 represent the viscous drag and K_2 is linked to the blockage of the internal geometry [82]. It is important to note that K and K_1 are not the same as transitioning from a Darcian to a Forchheimer flow regime implies changes to the viscous and inertial drags [82, 133]. It is vital to know which regime applies to the flow in a particular structure, in order to use the appropriate model. This was achieved by rearranging equation 5.12 to obtain

$$\left| \frac{\Delta P}{\Delta L \, u_\mathrm{s}} \right| = \frac{\mu}{K_1} + \frac{\rho}{K_2} u_\mathrm{s} \,, \tag{5.13}$$

which was then used to fit pressure drop data [82]; any part which is linearly proportional to superficial fluid velocity is Forchheimer flow.

Reynolds numbers are also quoted in this work as they provide more general descriptions of fluid flow and can be compared to other studies, which may use differential initial conditions and geometries. The Reynolds number for a porous structure was given by [61]

$$Re = \frac{u_\mathrm{s} \, D_\mathrm{h}}{\nu \, (1 - \gamma)} \,, \tag{5.14}$$

where D_h is the hydraulic diameter and ν is the kinematic viscosity. The transition region between laminar and turbulent flow for porous structures occurs in the range $10 < Re < 2,000$ [124].

The hydraulic diameter for the lattice structures was calculated using [61]

$$D_\mathrm{h} = 4 \frac{V_\mathrm{w}}{A_\mathrm{w,s}} \,, \tag{5.15}$$

where V_w is the fluid volume and $A_\mathrm{w,s}$ is the wetted surface area, which was extracted from the CAD representations of the lattice structures. Different lattice types therefore do not experience the same Reynolds numbers at equivalent inlet fluid flow rates and volume fractions as their hydraulic diameters are different.

Thermal performance was examined through mass flow rate weighted averages of heat transfer coefficients and Nusselt numbers. Two different heat transfer coefficients were used, one being a local wall heat transfer coefficient, h_l. This was calculated directly in OpenFOAM using the Reynolds analogy model [134, 135], which relates the wall shear stress to heat transfer by

$$h_\mathrm{l} = \frac{c_\mathrm{p} \tau_\mathrm{w}}{u_\mathrm{s}} \,, \tag{5.16}$$

where c_p is the specific heat capacity and τ_w is the wall shear stress. The local wall heat transfer coefficient can be used to determine points of high and low heat transfer within the examined structures as it is a local variable.

The global, mean heat transfer coefficient, h_m, was also examined. It was given by [66]

$$h_\mathrm{m} = \frac{\dot{m} c_\mathrm{p} \left(T_\mathrm{f,out} - T_\mathrm{f,in} \right)}{A_\mathrm{w,s} \Delta T_\mathrm{LMTD}} \,, \tag{5.17}$$

where $\dot{m}$ is the fluid mass flow rate and $T_{\mathrm{f,out}}$ and $T_{\mathrm{f,in}}$ are the fluid outlet and inlet temperatures, respectively. ΔT_{LMTD} is the logarithmic mean temperature difference, which is a typical engineering approach to rate heat sinks and heat exchangers. ΔT_{LMTD} was given by

$$\Delta T_{\mathrm{LMTD}} = \frac{T_{\mathrm{f,out}} - T_{\mathrm{f,in}}}{\ln\left(\frac{T_{\mathrm{h}} - T_{\mathrm{f,in}}}{T_{\mathrm{h}} - T_{\mathrm{f,out}}}\right)}\,, \tag{5.18}$$

where T_{h} is the heating temperature. This definition of logarithmic mean temperature difference has been used by Dixit *et al* [66], but an alternative definition uses the average channel surface temperature in place of heating temperature [55]. The heating temperature was used here because $T_{\mathrm{h}} - T_{\mathrm{f,in}}$ gives the initial temperature difference in the structures [72], whereas the surface temperature gives the heat transfer over the fluid-solid interface, the size of which varies significantly between lattice designs. It is also not representative of the large distribution of surface temperatures present in TPMS-based lattice structures, as observed by Al-Ketan *et al* [75].

In this study, the volumetric heat transfer coefficient, $h_{\mathrm{m,vol}}$, was used instead of the mean heat transfer coefficient as it is independent of surface area, which differs for different lattice structures at equivalent volume fraction. This was obtained from [62]

$$h_{\mathrm{m,vol}} = h_{\mathrm{m}} A_{\nu}\,, \tag{5.19}$$

where A_{ν} is the specific surface area, the ratio of wetted surface area to design space volume.

The Nusselt number, Nu, gives the ratio of convective to conductive heat transfer for a fluid and is an alternative way to express thermal performance. The volumetric Nusselt number, Nu_{vol}, was used in this study instead of the Nusselt number to be consistent with the use of the volumetric heat transfer coefficient above. This was defined as [62]

$$Nu_{\mathrm{vol}} = \frac{h_{\mathrm{m,vol}} {D_{\mathrm{h}}}^2}{k} = Nu\, A_{\nu}\, D_{\mathrm{h}}\,, \tag{5.20}$$

where k is the fluid thermal conductivity. This is a dimensionless quantity and can be used alongside Reynolds number to compare structures under different flow conditions.

5.3 Results

5.3.1 Hydraulic performance

Pressure drop per unit length for a range of volume fractions and flow rates are presented in figure 5.8. This was calculated by finding the difference between inlet and outlet average pressure and dividing it by the length of the examined structure. Figure 5.8 shows that the pressure drop per unit length increased non-linearly with both superficial fluid velocity and volume fraction, where the lidinoid matrix structure exhibited the greatest pressure drop across the examined ranges while the primitive matrix structure exhibited the lowest pressure drop in most cases. At low volume fractions, the gyroid matrix lattice exhibited greater pressure drop than the primitive matrix lattice. This behaviour switched as volume fraction increased, indicating that a particular lattice geometry may not be treated as inherently more efficient than others, with performance also being dependent on fluid flow conditions.

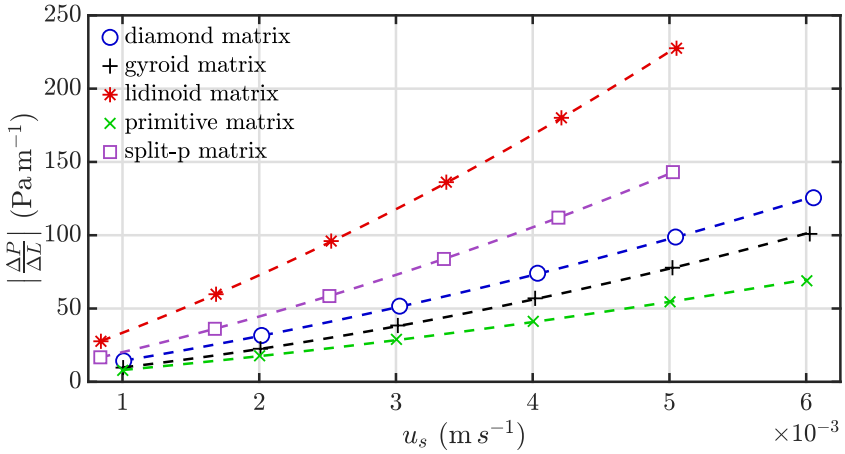

(a) Pressure drop for structures with a volume fraction of 0.25. The (−−) lines represent equation 5.12.

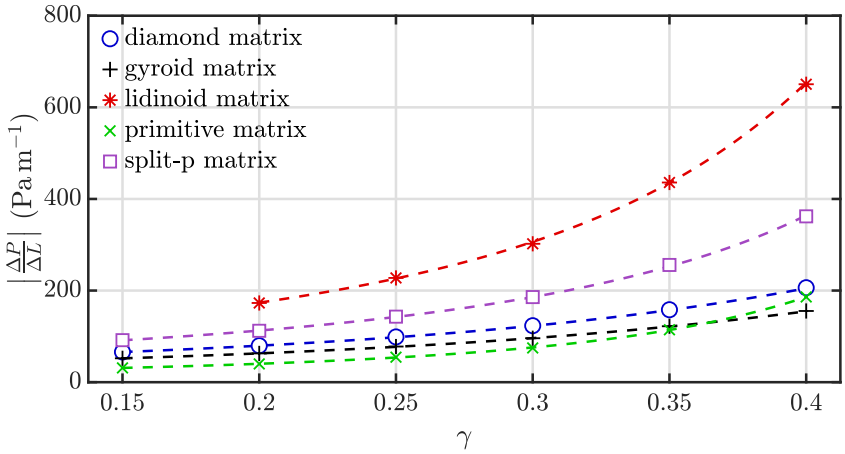

(b) Pressure drop for structures with a superficial fluid velocity of 5×10^{-3} m s^{-1}. The (−−) lines represent equation 5.23.

Figure 5.8: Pressure drop per unit length exhibited by the examined geometries.

Examining the evolution of pressure in figure 5.9, taken as a cross-sectional average, it was observed that pressure decreased linearly along the flow direction in the gyroid matrix, diamond matrix and lidinoid matrix lattices, despite the tortuous natures of the channel. This is not replicated in the primitive matrix or split-p matrix lattices, which instead exhibited discontinuous periodic pressure drops.

This can be explained by examining the flow within the structures, as shown in figure 5.10. Regarding the primitive matrix structure, the majority of the fluid passed through a central volume or 'channel'. As the channel diameter decreased at the cell boundary, some fluid was recirculated in the characteristic chambers of the primitive matrix lattice, appearing as eddies. The primitive matrix geometry therefore acts as a series of bottlenecks, providing sharp pressure drops within the structure. This was also observed in the split-p matrix structure, but to a lesser degree. Flow was not periodically impeded in the remaining structures because their internal geometry does not possess such large variations in channel diameter, minimising fluid recirculation. The dominant factor behind pressure drop for TPMS-based lattice structures is therefore the channel diameter, where smaller channels lead to larger pressure drops, shown in figure 5.11, and significant changes in the channel diameter lead to localised pressure drops.

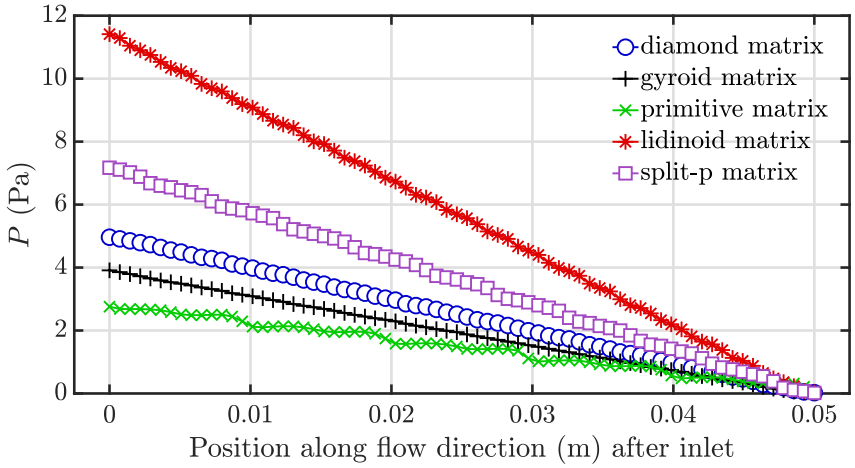

Figure 5.9: Evolution of pressure within the examined structures (superficial fluid velocity = 5×10^{-3} m s^{-1}, volume fraction = 0.25).

Before calculating the permeability constants, the flow regime must be determined. It was found that $\Delta P/(\Delta L\, u_s)$, shown in figure 5.12, increased linearly with superficial fluid velocity for each lattice over the range of examined volume fractions, indicating that the flow was entirely in the Forchheimer regime. Pressure drop per unit length was therefore fit with equation 5.12 to determine the permeability constants for each lattice structure, which are plotted in figure 5.13. K_2 were four orders of magnitude larger than K_1, with both constants decreasing as volume fraction increased. K_1 therefore has a larger impact on the pressure drop than K_2 for a given fluid velocity. Figure 5.13 shows that at low volume fractions, the primitive matrix lattice exhibited larger K_1 and K_2 than the gyroid matrix structure. This changed at a volume fraction of $\gamma = 0.310$ for K_1 and the approach of this change was observed at $\gamma = 0.4$ for K_2. The volume fraction at which the pressure drop intersects for the gyroid and primitive matrix structures in figure 5.8(b) will therefore be in the range of $0.310 - 0.4$, irrespective of fluid velocity. The lidinoid matrix structure also exhibited the lowest permeability constants.

For each examined lattice cell type, the equations

$$K_1 = A_1\gamma^2 + B_1\gamma + C_1\,, \tag{5.21}$$
$$K_2 = A_2\gamma^2 + B_2\gamma + C_2 \tag{5.22}$$

were used to relate K_1 and K_2 to the volume fraction, where $A_{1,2}$, $B_{1,2}$ and $C_{1,2}$ are fit parameters. The intention behind using these equations was to construct usable models to predict performance based on the design parameters. The form of these equations are arbitrary and it is reasonable to assume that the permeability constants vary with volume fraction, as it controls the pore size and shape.

Equation 5.12 can then be expressed as

$$\left|\frac{\Delta P}{\Delta L}\right| = \frac{\mu\, u_s}{A_1\gamma^2 + B_1\gamma + C_1} + \frac{\rho\, {u_s}^2}{A_2\gamma^2 + B_2\gamma + C_2}\,, \tag{5.23}$$

which can be used to predict the pressure drop per unit length exhibited for the examined lattice structures over a range of volume fractions and superficial fluid velocities. Equation 5.23

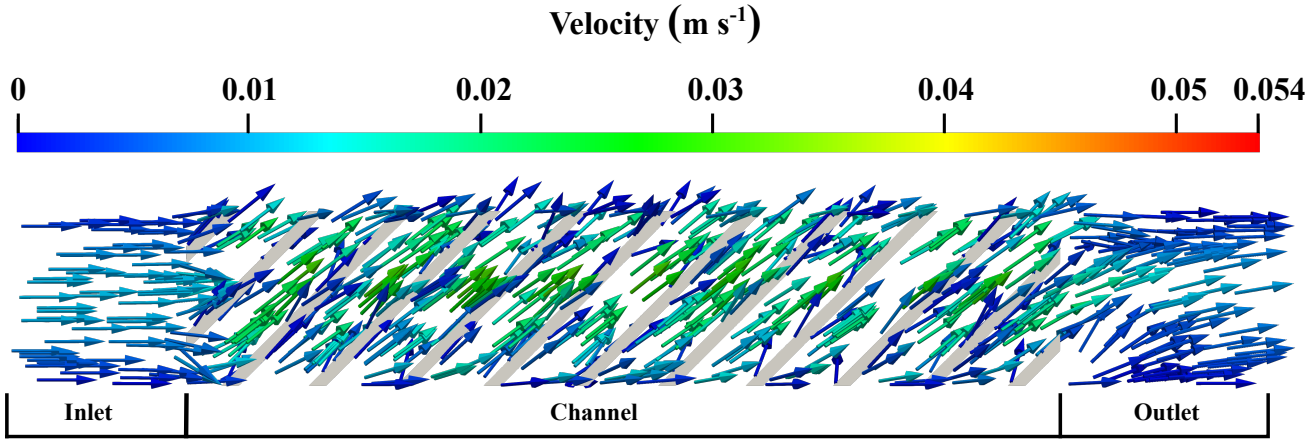

(a) Diamond matrix lattice.

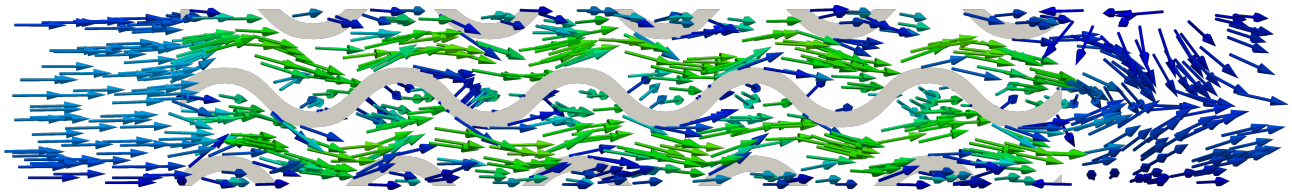

(b) Gyroid matrix lattice.

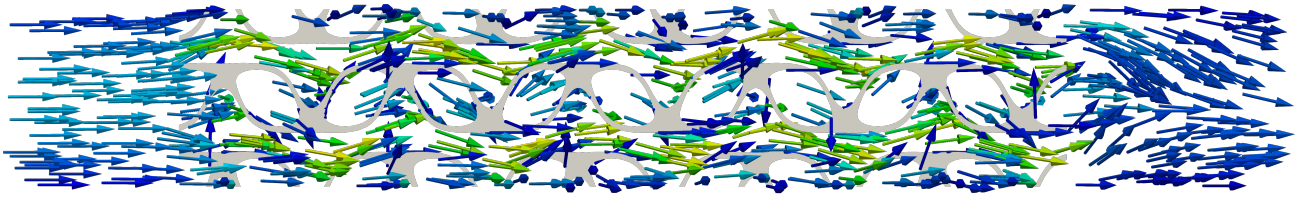

(c) Lidinoid matrix lattice.

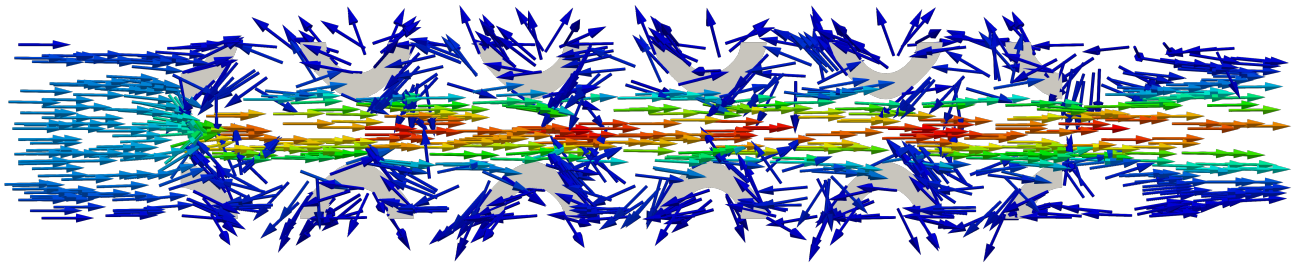

(d) Primitive matrix lattice.

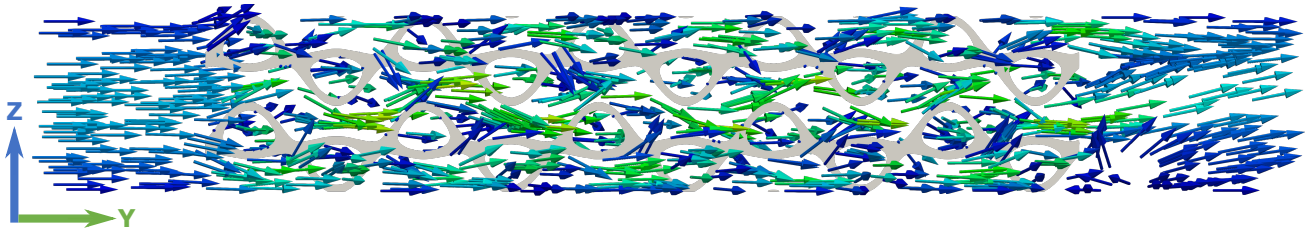

(e) Split-p matrix lattice.

Figure 5.10: Fluid velocity vectors across the $x = 0.005$ m plane for structures with a volume fraction of 0.25 and a superficial fluid velocity of 5×10^{-3} m s^{-1}.

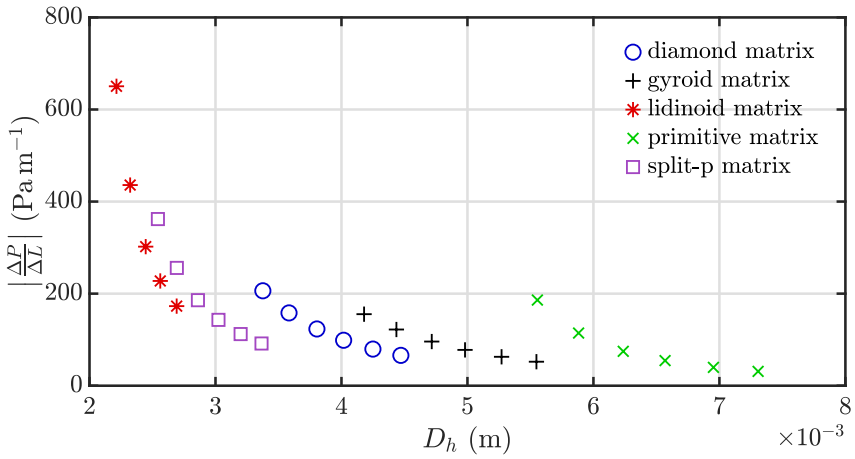

Figure 5.11: Pressure drop against hydraulic diameter for structures with a superficial fluid velocity of 5×10^{-3} m s^{-1}.

describes the surfaces shown in figure 5.14, which gives the hydraulic performance of each of the examined lattice cell types, and figure 5.15, which gives the hydraulic performance of all of the examined lattice structures. Fit values for the parameters are given in table 5.4, which can henceforth be used to specify the volume fraction for the examined TPMS-based lattice structures to provide a pressure drop per unit length for a known flow rate. The above figures and table can be used to decide which TPMS-based lattice structure should be used within a heat sink, based on hydraulic performance.

5.3.2 Thermal performance

Volumetric Nusselt numbers are presented in figure 5.16. Correlations of the form

$$Nu_{\mathrm{vol}} = F\, Re^{n} \tag{5.24}$$

were sought, where Fu *et al* [62] stated that the parameters n and F are related to the geometrical features of the structure, with F also containing the Prandtl number. Figure 5.16 shows that this relationship describes the data accurately. Equations 5.20 and 5.24 are then combined to provide

$$h_{\mathrm{m,vol}} = \frac{F\, k\, Re^{n}}{{D_{\mathrm{h}}}^{2}}\,, \tag{5.25}$$

which is valuable because this can be expressed in terms of superficial fluid velocity and volume fraction. This is done using equations 5.14 and 5.15, while the hydraulic diameter can also be defined as

$$D_{\mathrm{h}} = 4\frac{V_{\mathrm{w}}}{A_{\mathrm{w,s}}} = 4\frac{(V_{\mathrm{w}}/V_{\mathrm{T}})}{(A_{\mathrm{w,s}}/V_{\mathrm{T}})} = \frac{4}{A_{\nu}}\,(1-\gamma)\,, \tag{5.26}$$

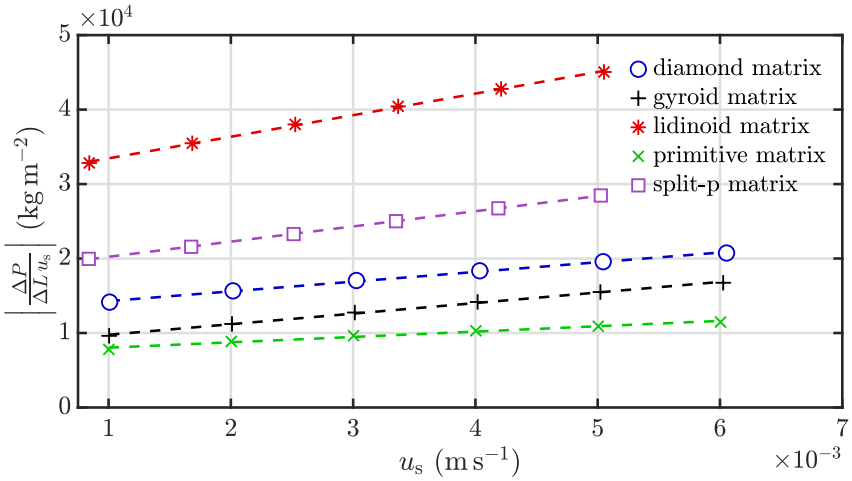

Figure 5.12: Pressure drop per unit length per unit velocity against superficial fluid velocity for structures with a volume fraction of 0.25. The (−−) lines represent equation 5.13.

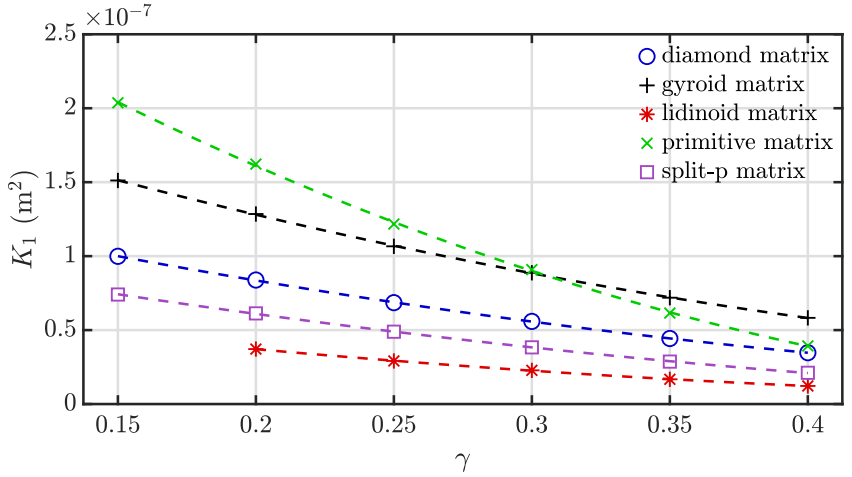

(a) Forchheimer permeability constant. The (−−) lines represent equation 5.21.

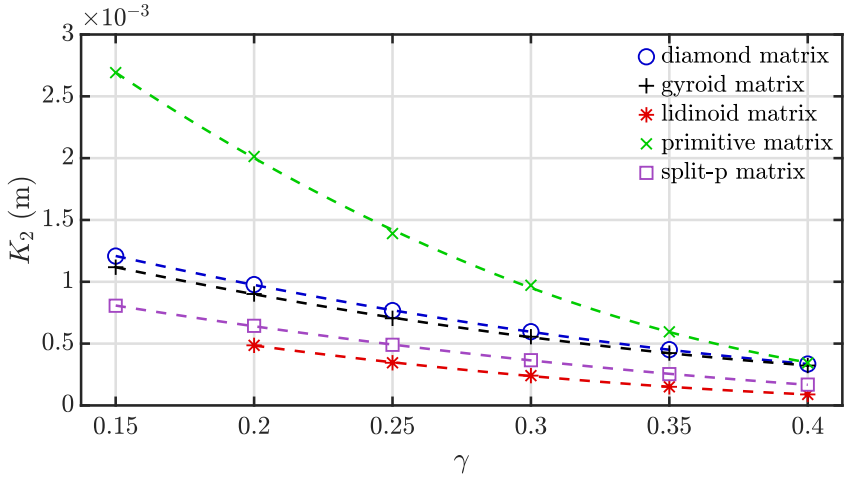

(b) Inertial permeability constant. The (−−) lines represent equation 5.22.

Figure 5.13: Permeability constants as a function of volume fraction for different lattice geometries.

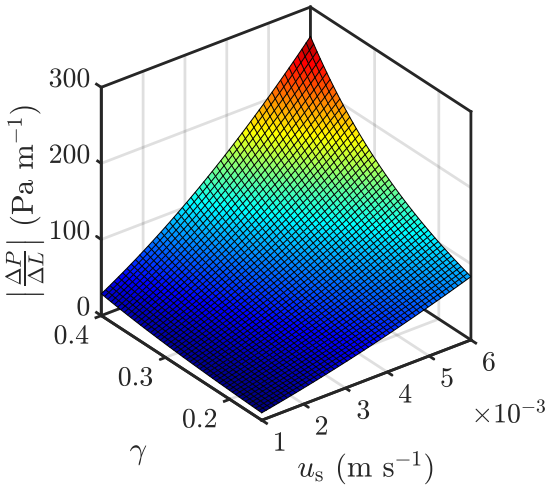

(a) Diamond matrix lattice. These fluid velocities correspond to Reynolds numbers of $6.0 - 38.4$.

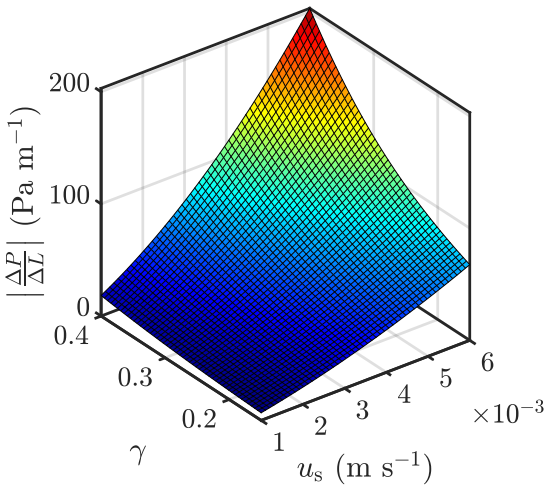

(b) Gyroid matrix lattice. These fluid velocities correspond to Reynolds numbers of $7.4 - 47.2$.

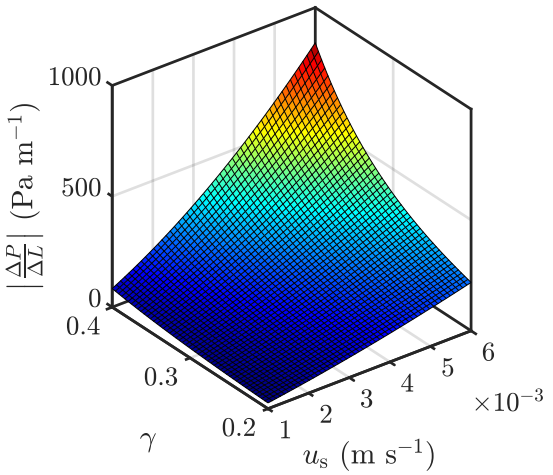

(c) Lidinoid matrix lattice. These fluid velocities correspond to Reynolds numbers of $3.2 - 21.0$.

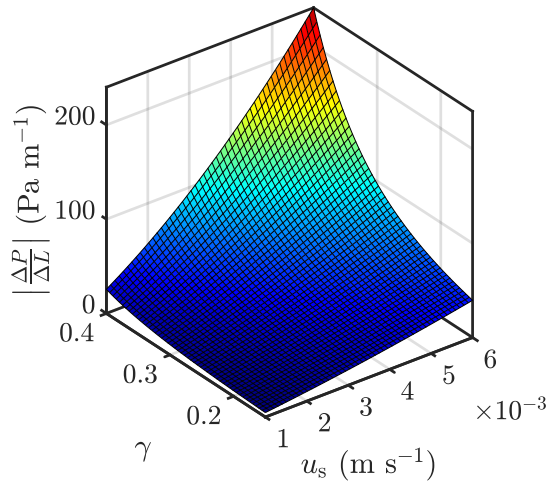

(d) Primitive matrix lattice. These fluid velocities correspond to Reynolds numbers of $9.7 - 62.4$.

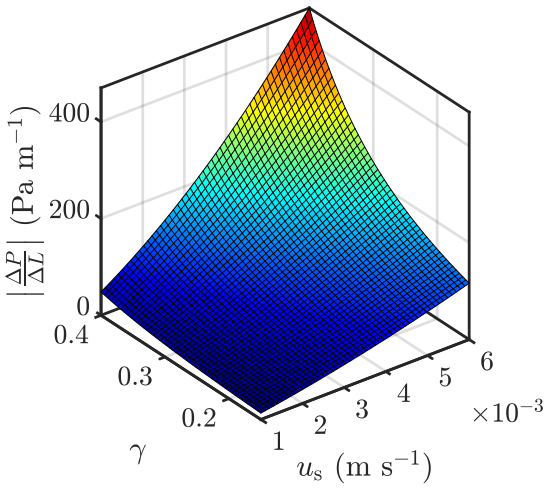

(e) Split-p matrix lattice. These fluid velocities correspond to Reynolds numbers of $3.7 - 24.0$.

Figure 5.14: Pressure drop as a function of superficial fluid velocity and volume fraction for the examined TPMS-based lattice structures.

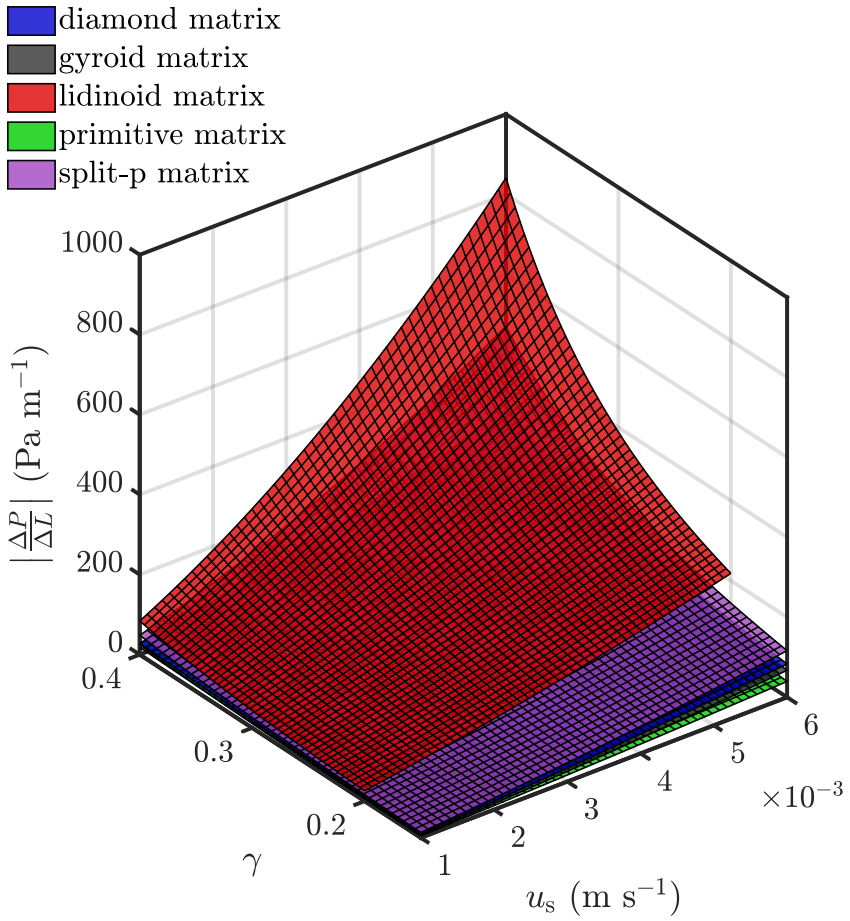

Figure 5.15: Comparison of pressure drop as a function of superficial fluid velocity and volume fraction for the examined TPMS-based lattice structures. These fluid velocities correspond to Reynolds numbers of $3.2 - 62.4$.

	Fit parameter $\times 10^{-7}$ (m^2)				Fit parameter $\times$ 10^{-3} (m)			
Lattice type	A_1	B_1	C_1	Adjusted R^2	A_2	B_2	C_2	Adjusted R^2
Diamond matrix	3.4	-4.5	1.59	0.9999	5.9	-6.8	2.09	0.9999
Gyroid matrix	4.7	-6.3	2.35	0.9998	6.0	-6.5	1.95	0.9998
Lidinoid matrix	2.1	-2.5	0.79	0.9995	4.9	-4.9	1.27	0.9994
Primitive matrix	10.1	-12.1	3.63	0.9997	22.3	-21.6	5.44	0.9994
Split-p matrix	2.6	-3.6	1.22	0.9998	3.9	-4.7	1.42	0.9998

Table 5.4: Determined fit parameters for equation 5.23.

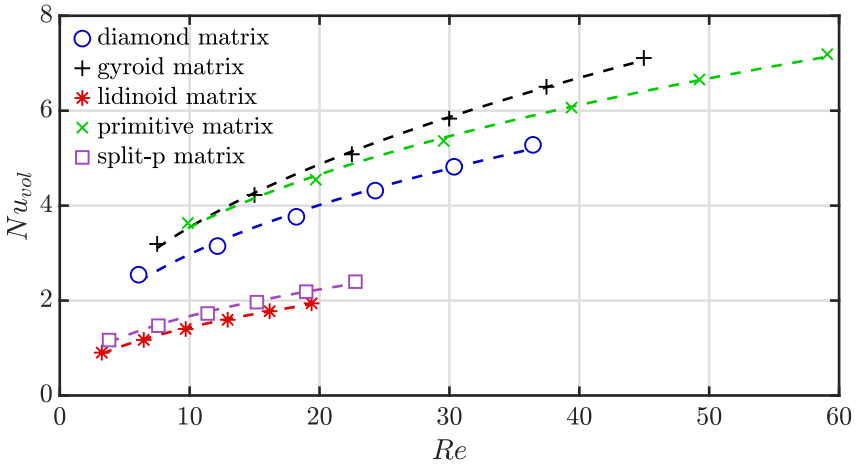

Figure 5.16: Volumetric Nusselt numbers for lattice structures with a volume fraction of 0.25. The (−−) lines represent equation 5.24.

where V_T is the total volume of the design space. Equation 5.25 can therefore be expressed as

$$\begin{aligned} h_{\mathrm{m,vol}} &= F\,k\,{D_\mathrm{h}}^{n-2}\left(\frac{u_\mathrm{s}}{\nu\,(1-\gamma)}\right)^n, \\ &= F\,k\left(\frac{4}{A_\nu}\right)^{n-2}(1-\gamma)^{n-2}\left(\frac{u_\mathrm{s}}{\nu\,(1-\gamma)}\right)^n, \\ &= F\,k\left(\frac{4}{A_\nu}\right)^{n-2}\left(\frac{u_\mathrm{s}}{\nu}\right)^n(1-\gamma)^{-2}. \end{aligned} \tag{5.27}$$

To use equation 5.27 as a predictive model for $h_{\mathrm{m,vol}}$ over a range of fluid velocities and volume fractions, the dependence of A_ν, n and F on volume fraction must be known. It was found that A_ν could be described by $A_\nu = p_1\gamma^{p_2} + p_3$, shown in figure 5.17, where it decreased as volume fraction increased. This indicated that surface area must exhibit a sharper negative gradient for varying volume fraction than the fluid volume. This equation was not able to explain how A_ν behaves as volume fraction tends to zero (where surface area is zero) or as it tends to one (where the fluid volume is zero). It was also found that n decreased with volume fraction and was well described by $n = n_1\gamma + n_2$, shown in figure 5.18. This indicates that the Reynolds number has a weaker impact on the volumetric Nusselt number as volume fraction increases and implies that conduction has a larger impact on heat transfer than convection. All of the parameters discussed here exhibited adjusted R^2 values greater than 0.87, indicating a good level of accuracy. No discernible relationship was observed between F and volume fraction, as can be seen in figure 5.19, but the full range of F values fell within $\overline{F}\ \pm\ 8\%$ for each lattice type. This was expected as F contains the Prandtl number, which would not vary with volume fraction or fluid velocity. F was therefore treated as a constant by calculating its mean value. Wu *et al* [63] followed a similar method and found that, for ceramic foams with volume fractions of $0.07 - 0.34$ and air with Reynolds numbers of $70 - 800$ flowing through them, n was 0.438 and F ranged from $1.77 - 2.01$. This is within the same order of magnitude as the values calculated for the examined TPMS-based lattice structures.

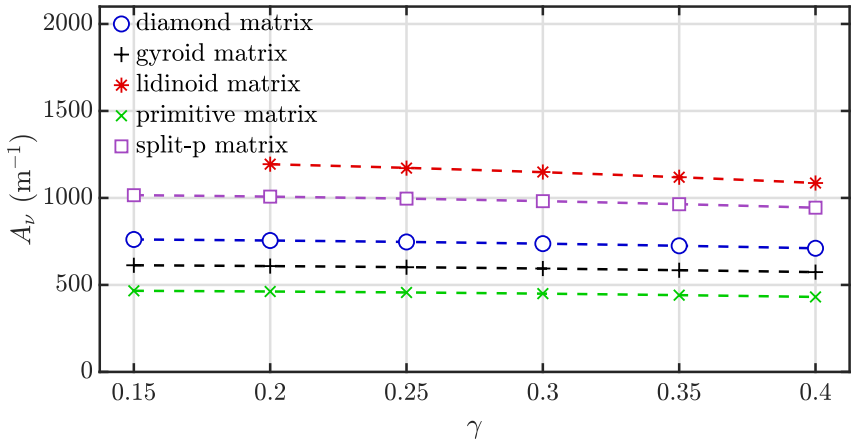

Figure 5.17: Specific surface area against volume fraction. The (−−) lines represent a power law.

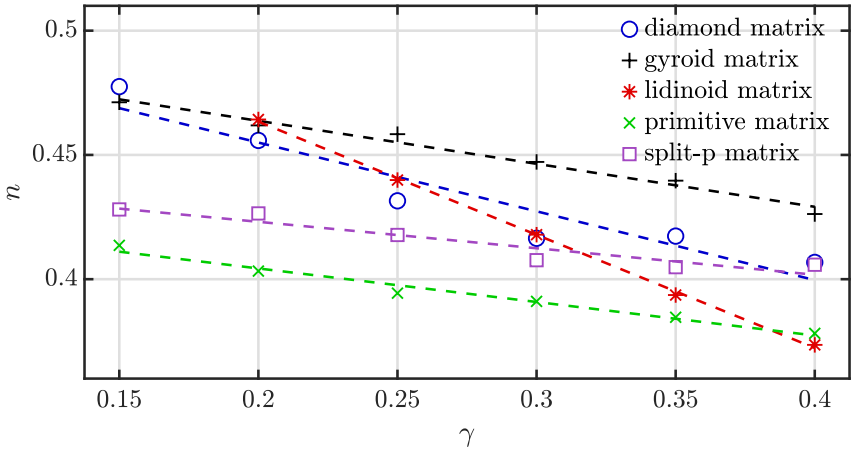

Figure 5.18: n against volume fraction. The (−−) lines represent a first order polynomial.

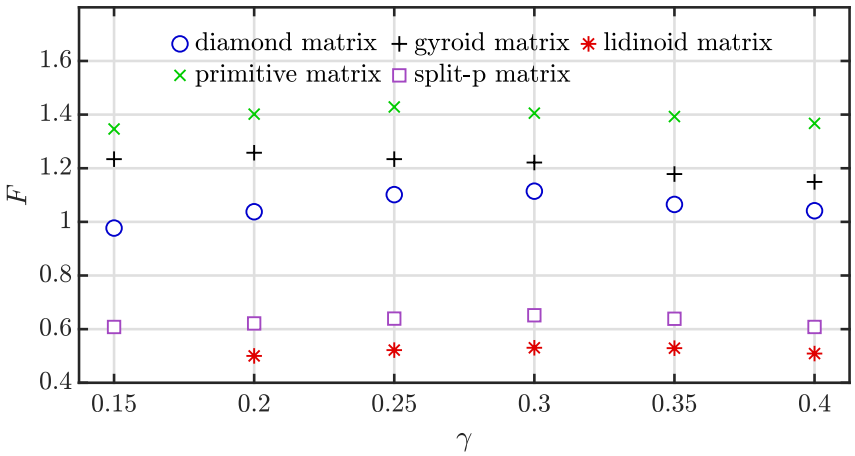

Figure 5.19: F against volume fraction.

Lattice type	p_1 (m^{-1})	p_2	p_3 (m^{-1})	Adjusted R^2	n_1	n_2	Adjusted R^2	$\overline{F}$
Diamond matrix	-405	2.13	768	0.9999	-0.277	0.510	0.8812	1.06
Gyroid matrix	-308	2.09	619	0.9998	-0.173	0.499	0.9738	1.21
Lidinoid matrix	-847	1.92	1232	0.9990	-0.455	0.554	0.9987	0.52
Primitive matrix	-305	2.23	471	0.9998	-0.135	0.431	0.9709	1.39
Split-p matrix	-580	2.13	1026	0.9999	-0.106	0.444	0.8733	0.63

Table 5.5: Determined fit parameters for equation 5.28.

The volumetric heat transfer coefficient can then be obtained from

$$h_{\mathrm{m,vol}} = \frac{\overline{F}\, k \left(\dfrac{4}{p_1 \gamma^{p_2} + p_3}\right)^{n_1\gamma+n_2-2} \left(\dfrac{u_\mathrm{s}}{\nu}\right)^{n_1\gamma+n_2}}{(1-\gamma)^2}, \tag{5.28}$$

with $p_{1,2,3}$, $\overline{F}$ and $n_{1,2}$ given in table 5.5. This equation describes a surface and can be used to predict the volumetric heat transfer coefficient over a range of volume fractions and superficial fluid velocities. This model accurately predicts the volumetric heat transfer coefficient from equation 5.19, with a maximum deviation less than 10% over the examined ranges of volume fraction and flow rate.

Figure 5.20 displays the volumetric heat transfer coefficient exhibited by each examined structure and figure 5.21 compares the volumetric heat transfer coefficient for all of the examined structures, predicted by equation 5.28. It was found that the lidinoid matrix lattice exhibited the greatest volumetric heat transfer coefficient at low volume fractions and the diamond matrix lattice exhibited the highest volumetric heat transfer coefficient at high volume fractions. The primitive matrix exhibited the lowest volumetric heat transfer coefficient in this study.

Local effects are important in determining how the lattice geometry affects heat transfer. Local wall heat transfer coefficients were calculated across 70 equally spaced cross-sections along the flow direction and are shown in figure 5.22. All of the TPMS-based lattice structures exhibited periodically fluctuating local wall heat transfer coefficients, with the primitive matrix lattice showing the greatest variation in local wall heat transfer coefficient, from $2,100 - 44,000$ W m^{-2} K^{-1}. The primitive matrix lattice structure exhibited the lowest volumetric heat transfer coefficient because it exhibited lower local wall heat transfer coefficients across the majority of its surface than the other examined structures. This was despite it also having the greatest peak local wall heat transfer coefficient. The other examined lattice structures exhibited much smaller variance in local wall heat transfer coefficient.

The distribution of local heat transfer coefficient on the lattice surface further explains the differences observed in figure 5.22. The distribution of the local wall heat transfer coefficient for the primitive matrix lattice is displayed in figure 5.23, and was chosen due to the large variation in local wall heat transfer coefficient. Peak local wall heat transfer coefficients were seen in regions where the channel diameter was narrowest in the central channel. Other high local wall heat transfer coefficients were observed outside the central channel, where the channel was at a local minima. The fluid moves faster in these sections, as shown in figure 5.10(d), and can

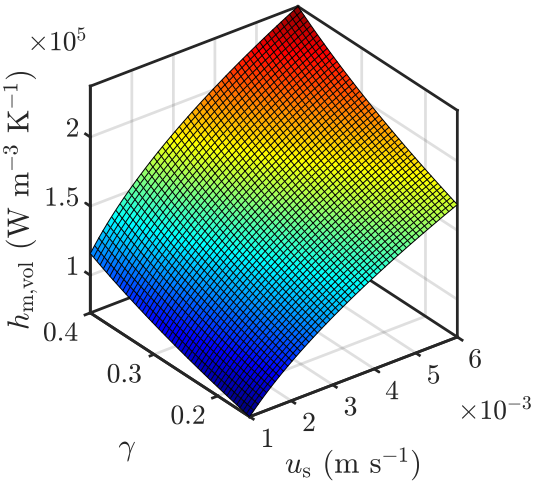

(a) Diamond matrix lattice. These fluid velocities correspond to Reynolds numbers of $6.0 - 38.4$.

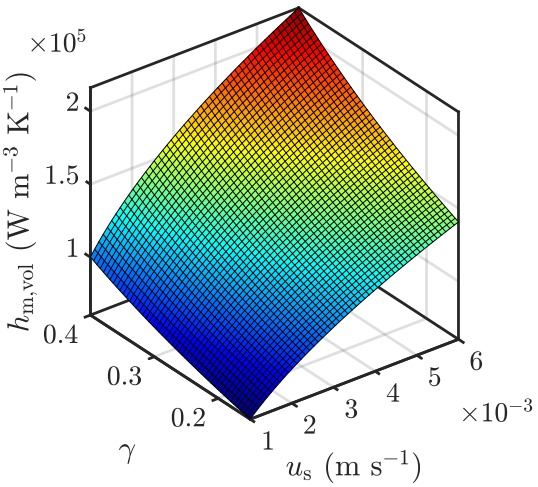

(b) Gyroid matrix lattice. These fluid velocities correspond to Reynolds numbers of $7.4 - 47.2$.

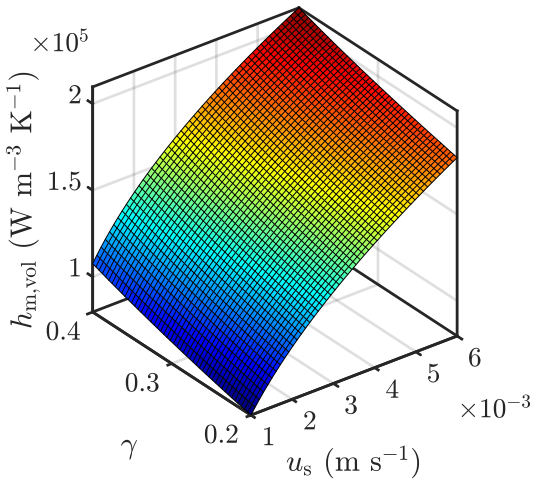

(c) Lidinoid matrix lattice. These fluid velocities correspond to Reynolds numbers of $3.2 - 21.0$.

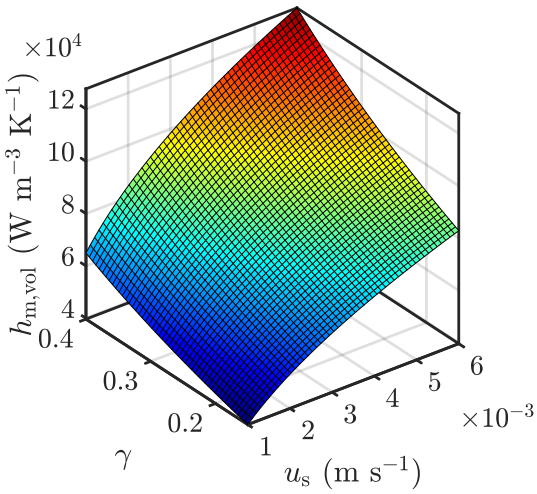

(d) Primitive matrix lattice. These fluid velocities correspond to Reynolds numbers of $9.7 - 62.4$.

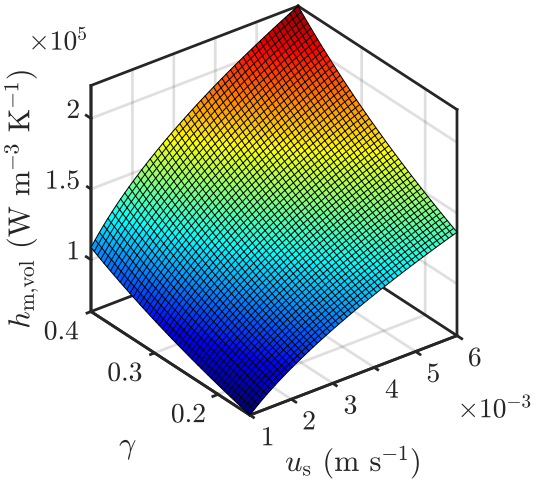

(e) Split-p matrix lattice. These fluid velocities correspond to Reynolds numbers of $3.7 - 24.0$.

Figure 5.20: Volumetric heat transfer coefficient as a function of superficial fluid velocity and volume fraction for the examined TPMS-based lattice structures.

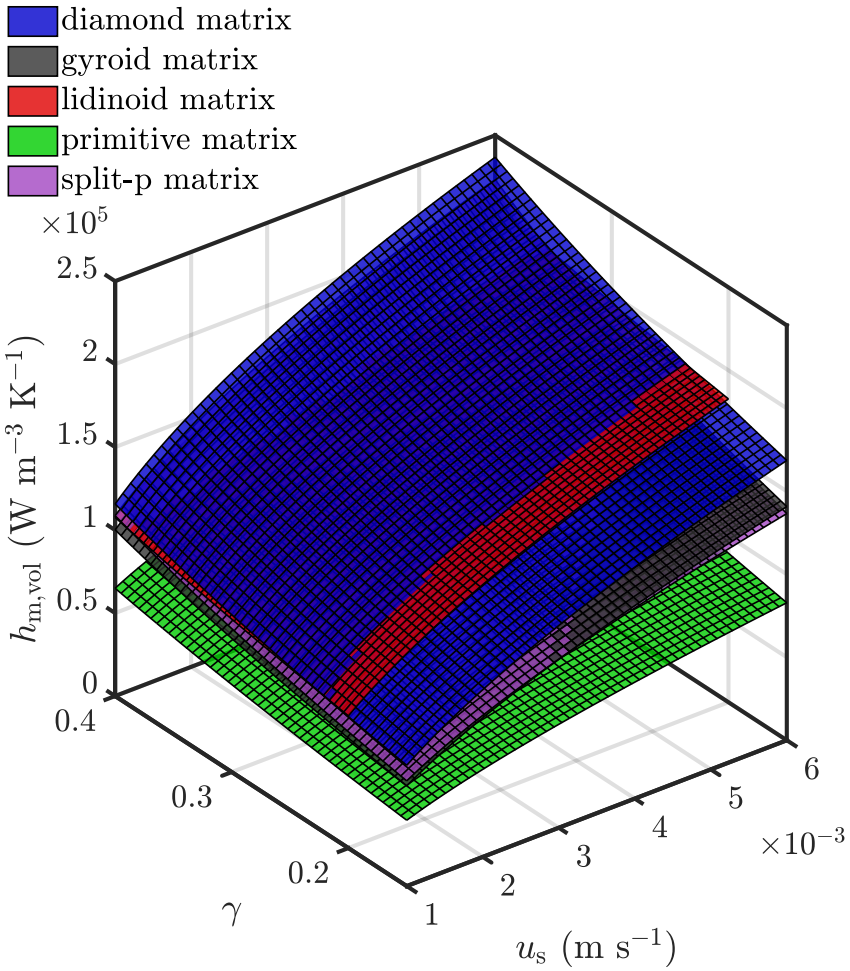

Figure 5.21: Comparison of volumetric heat transfer coefficient as a function of superficial fluid velocity and volume fraction for the examined TPMS-based lattice structures. These fluid velocities correspond to Reynolds numbers of $3.2 - 62.4$.

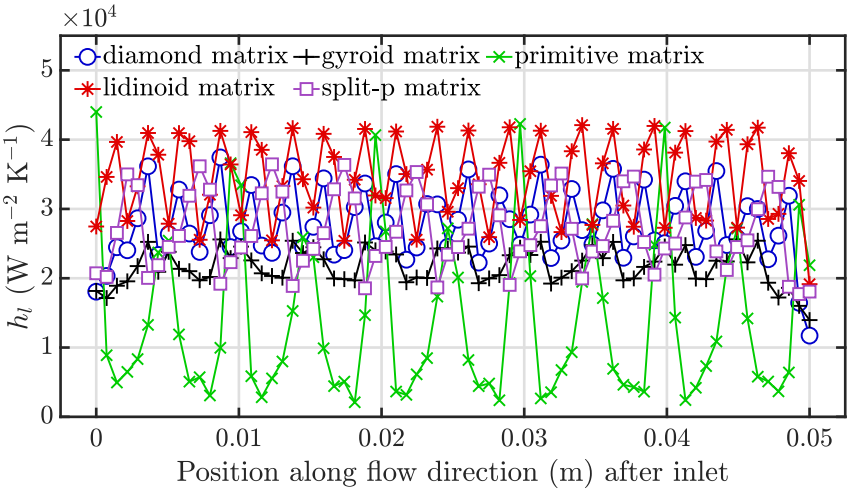

Figure 5.22: Evolution of local wall heat transfer coefficient within the examined structures (superficial fluid velocity $= 5 \times 10^{-3}$ m s^{-1}, volume fraction $= 0.25$).

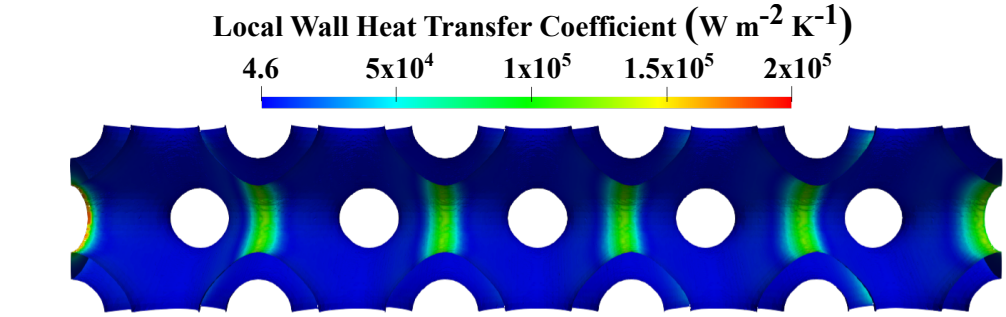

(a) Inside the central channel.

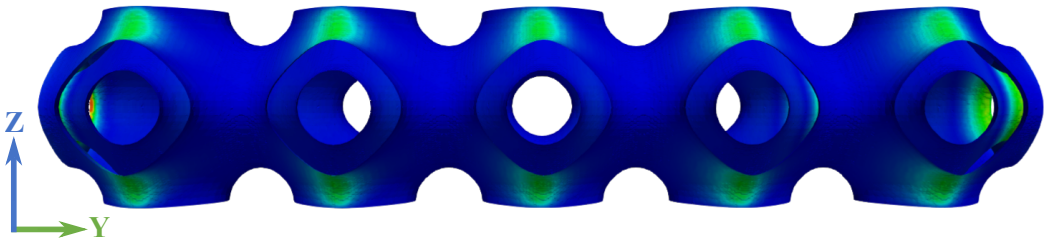

(b) Outside the central channel.

Figure 5.23: Distribution of local wall heat transfer coefficient in the primitive matrix lattice (superficial fluid velocity = 5×10^{-3} m s^{-1}, volume fraction = 0.25).

therefore transport more heat away from the walls there. The same effect was also observed, but to a lesser extent due to the smaller changes in the channel diameter, in the other examined TPMS-based lattice structures. For example, the local wall heat transfer coefficient for the gyroid matrix lattice ranged from $14,000 - 25,000$ W m^{-2} K^{-1}, which was a much narrower range than that exhibited by the primitive matrix lattice ($2,100 - 44,000$ W m^{-2} K^{-1}). From figure 5.10, we deduce that the local wall heat transfer coefficient is driven mainly by local fluid velocity, which itself is largely determined by channel diameter.

5.4 Discussion

5.4.1 Hydraulic performance

Santos *et al* [83] calculated the permeability constants for different lattice structures consisting of $4 \times 4 \times 4$ cells in a $13 \times 13 \times 13$ mm volume over a range of different flow regimes. Compared to the structures presented here, those lattices have greater surface area and more cells per unit volume, and we can therefore expect the structures of Santos *et al* [83] to be less permeable than the lattice structures examined here within the Forchheimer flow region. This is confirmed in figure 5.24, where the permeability constants, K_1 and K_2, for the gyroid and primitive matrix lattice structures in this study were up to two orders of magnitude greater than those of Santos *et al* [83]. This highlights the challenge of developing general and practicable analytical relationships for the flow in these structures, as a range of geometrical properties, such as the number of cells and design space volume, clearly have a large impact on the permeability. The work of Santos *et al* [83] confirms, that the primitive matrix lattice is more permeable at lower volume fractions and the gyroid matrix is more permeable at larger volume fractions. This finding was further elaborated here by examining the fluid dynamics (see figure 5.10) and evolution of pressure drop (see figure 5.9) within the structures, where sharp pressure drops were found in the

primitive matrix lattice at the cell boundaries but not in the gyroid matrix lattice.

Dietrich *et al* [61] calculated the permeability constants for foams of different materials with varying pore sizes and volume fractions. A selection of those results were compared to this study in figure 5.24. The gyroid and primitive matrix lattices possessed permeabilities similar to manufactured foam. Additively manufactured TPMS-based lattices can therefore be a valid substitute for conventional foams in fluid flow applications, as they are hydraulically no less efficient and also possess a greater degree of tailorability due to their computer-based design method.

The Forchheimer and inertial permeabilities of lattice structures are dependent on the internal geometry, and therefore the volume fraction. The fits used here (equations 5.21 and 5.22) are empirical, and do not account for such factors as surface area or channel tortuosity, either of which may be found to have a predominant effect on fluid flow. A robust, general model will incorporate these, and other, geometrical factors into structure-performance relationships capable of accurately predicting fluid through any lattice type. Equation 5.23 and the parameters

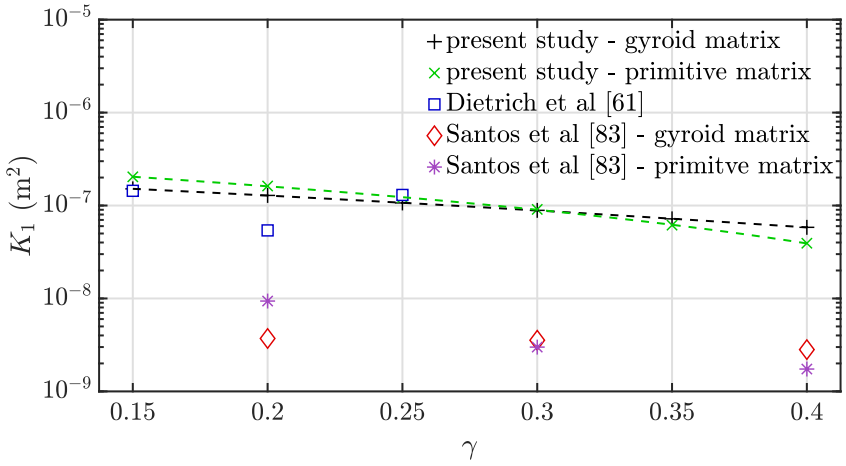

(a) Forchheimer permeability constant. The (−−) lines represent equation 5.21.

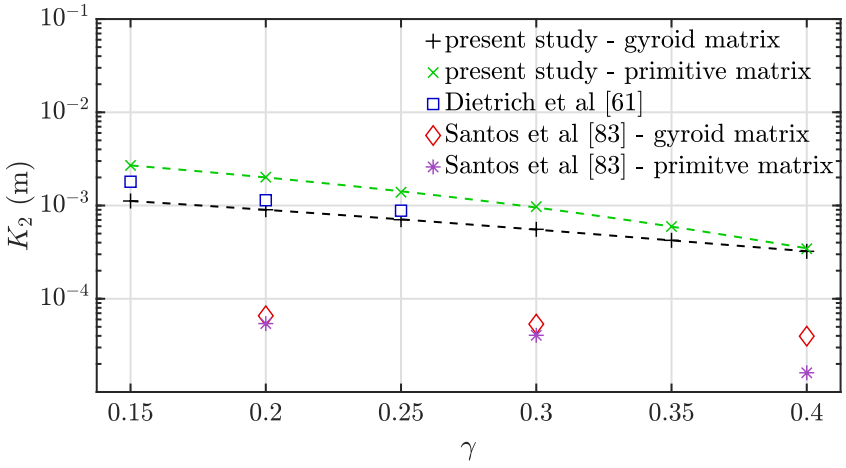

(b) Inertial permeability constant. The (−−) lines represent equation 5.22.

Figure 5.24: Permeability constants of the gyroid matrix and primitive matrix structures of the current study, gyroid and primitive matrix structures [83] and a foam structure [61].

quoted in table 5.4 contribute towards this goal. They can be used to predict pressure drop over a range of volume fractions and fluid velocities for the examined lattice structures. This will enable designers to make informed decisions on lattice design for fluid flow applications. These fit parameters are only valid for structures with $1 \times 5 \times 1$ cells and dimensions of $10 \times 50 \times 10$ mm. These results are still valuable since flow in larger lattice structures (i.e., $N_x \times N_y \times N_z$ cells) is determined to a large extent by the characteristic fluid dynamics in individual cells.

5.4.2 Thermal performance

As discussed previously, the local wall heat transfer coefficient is ultimately dependent on the channel diameter. It is therefore expected that TPMS-based lattice structures exhibit volumetric heat transfer coefficients which mirror their pressure drop behaviour in figure 5.11, where structures with smaller hydraulic diameters have larger pressure drops. This is not the case however, as the diamond matrix lattice exhibits relatively small pressure drops but high volumetric heat transfer coefficients, for example.

By examining the distribution of fluid temperature in the primitive matrix lattice in figure 5.25, minimal thermal mixing was observed within the structure due to the high-velocity central flow channel (shown in figure 5.10(d)) which prevented the fluid from moving across it. It was also observed that there was minimal heat transfer taking place in the upper regions where the local wall heat transfer coefficient peaks (see figure 5.23). This was because the heat was only applied to the structure from one direction (below). Therefore, structures which (i) conduct more heat through the lattice walls far away from the heat input, and (ii) maximise thermal mixing, should boast greater volumetric heat transfer coefficients.

This theory is corroborated by the distribution of fluid outlet temperatures in figure 5.26. Here, it was observed that the primitive matrix lattice, which had the lowest volumetric heat transfer coefficient, had the least well distributed fluid outlet temperature and that the top half was rendered relatively ineffective for heat transfer. Following on from this, the gyroid matrix and split-p matrix lattices had the next highest volumetric heat transfer coefficients and more evenly distributed fluid outlet temperatures, though a discontinuity was still observed between the bottom and top halves of those structures. Finally, the diamond and lidinoid matrix lattices had the highest volumetric heat transfer coefficients in this study and their fluid outlet temperatures were relatively well distributed, indicating better fluid mixing.

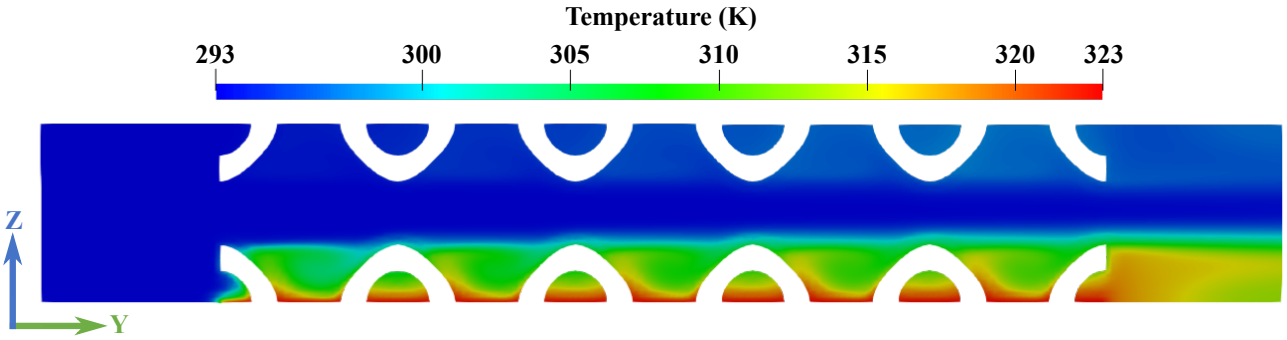

Figure 5.25: Fluid temperature across the $x = 0.005$ m plane for the primitive matrix lattice (superficial fluid velocity $= 5 \times 10^{-3}$ m s^{-1}, volume fraction $= 0.25$).

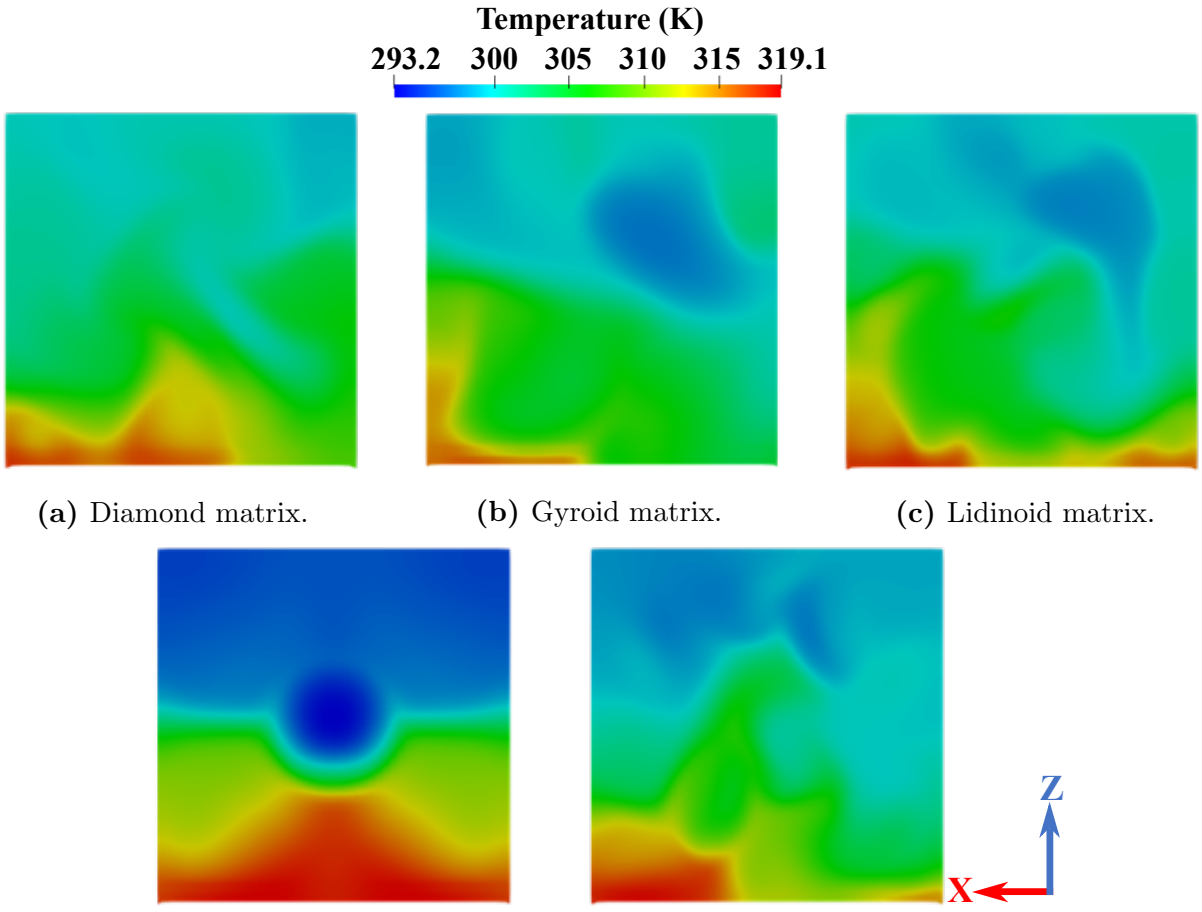

(a) Diamond matrix. **(b)** Gyroid matrix. **(c)** Lidinoid matrix.

(d) Primitive matrix. **(e)** Split-p matrix.

Figure 5.26: Distribution of outlet fluid temperature (superficial fluid velocity = 5×10^{-3} m s^{-1}, volume fraction = 0.25).

The thermal performance of TPMS-based lattice structures is therefore heavily dependent on the internal geometry of the structure in the case of a directional heat input, where lattices that can distribute heat across the entire fluid volume exhibit greater performance. In the case of a non-directional heat input (e.g., fixed wall temperatures) the thermal performance will be largely determined by the diameters of the channels within the structure. This is in keeping with the emerging picture from investigation of TPMS-based lattices as heat sinks; their thermal performance is heavily dependent on lattice cell geometry [75].

Nusselt numbers for foams were previously examined by Wu *et al* [63] and Fu *et al* [62], who employed the relationship given in equation 5.24. The excellent agreement with this model for the lattice structures examined here (figure 5.16) confirms that these TPMS-based lattices can be characterised by volumetric Nusselt numbers in the same way as conventional foams. A robust, general model will be able to predict the thermal performance of TPMS-based lattices across a range of superficial fluid velocities and volume fractions. Equation 5.28 and the parameters quoted in table 5.5 contribute to this and can accurately predict the volumetric heat transfer coefficient for the examined TPMS-based lattice structures with 1× 5 × 1 cells and dimensions of 10 × 50 × 10 mm. This model can be improved, and generalised to other lattice structures, by incorporating more complete descriptions of how the Nusselt parameters F and n are affected by the internal lattice geometry.

Combined with the model discussed above for hydraulic performance, TPMS-based lattice structures can henceforth be designed in a way which minimises their pressure drop for a given flow rate whilst achieving a specified heat transfer coefficient for one-sided heating applications. This can be achieved via a simple search-based algorithm applied to their pressure drop and heat transfer relationships (i.e., the surfaces given by equations 5.23 and 5.28). The practical implication of reduced pressure drop for a given flow rate is reduced power consumption for the pumps which drive the coolant through the heat sink. Being able to design TPMS-based heat sinks which reduce or maintain power consumption compared to traditional designs, whilst improving heat transfer capabilities, will be important for various applications requiring enhanced cooling.

5.5 Summary

Permeability constants for the examined TPMS-based lattice structures were calculated and used to create a predictive model for pressure drop over a range of fluid velocities and volume fractions. Relationships between volumetric Nusselt number and Reynolds number were also found and can be used to predict volumetric heat transfer coefficients for the examined structures across a range of fluid velocities and volume fractions. With these models, heat sinks based on the examined lattice structures can be designed to meet pre-defined performance requirements. It is unsuitable to extrapolate these relationships outside of the examined ranges of fluid velocity and volume fraction as they could yield erroneous results. For example, turbulent flow may have a large impact on the hydraulic and thermal performance at high Reynolds numbers. This investigative method can be applied across the large, and ever-increasing, family of lattice structures for heat sinks without expensive manufacturing and testing.

The complex internal geometries of TPMS-based lattice structures cause mixing and eddy formation within the channels. These flow features can increase heat transfer. Analysis of fluid flow and temperature distributions indicated that the examined primitive matrix lattice, which exhibited a volumetric heat transfer coefficient 37% lower than the gyroid matrix lattice (at the largest examined volume fraction and fluid velocity), is a poorer candidate for heat management than the other examined TPMS-based lattice structures. This is despite the formation of eddies in the central channel, as fluid mixing across the entire structure is impeded by the formation of a high-velocity central flow channel. This shows that not all TPMS-based lattice structures are suitable for heat transfer problems and decisions on the inclusion of such lattice structures within heat sinks need to be based off quantitative evidence. It was also found that TPMS-based lattice structures which are able to distribute heat across the entire fluid volume, such as the diamond matrix lattice, are better candidates for heat management as they maximise the fluid-solid thermal interactions and fluid mixing.

Structure-performance relationships of the kind determined here can be used in conjunction with other such rules, like the Gibson-Ashby scaling laws for stiffness or thermal conductivity [45], to design multifunctional components which, for example, provide maximal stiffness and thermal transport within a given weight restriction. New lattice structures for efficient heat sinks can be identified, or even designed from first-principles, with greater understanding of their flow and heat transfer mechanisms. Such optimised TPMS-based heat sinks can only be manufactured via additive manufacturing and can therefore be embedded in components of arbitrary geometry without the need for subsequent joining or assembly processes.

Chapter 6

Impact of Geometry on Fluid Flow and Heat Transfer

6.1 Introduction

In the previous chapter, relationships which correlate the fluid flow and heat transfer of TPMS-based lattice structures and their principal design parameters (i.e., volume fraction) were found. Modifying the volume fraction has wider implications for the geometry of the structures, as an increasing volume fraction leads to smaller channel radii, for example. This also impacts tortuosity as the potential flow paths within the structure change.

As discussed in chapter 5, the hydraulic diameter has an impact on the pressure drop across a structure. For TPMS-based lattice structures with non-consistent channel radii, the hydraulic diameter does not give information on the range of channel radii or its maximum and minimum values. These properties may provide more useful information in determining hydraulic and thermal performance. Tortuosity is also important as it can be considered a measure of the complexity of the channels within a structure. Tortuosity, if found to be a good indicator of fluid flow or heat transfer, could be used to downselect TPMS-based lattice structures for heat sinks from a broad range of candidate designs. This would remove the need for costly and time-intensive CFD modelling.

Here, the performance of the five examined TPMS-based lattice structures from the previous study, see figure 5.1, are correlated against tortuosity and channel radius for varying volume fraction. Either of these may have a predominant impact on the hydraulic and thermal performance of TPMS-based lattice structures and are therefore compared to the results found in chapter 5. If this is the case, then a relationship between the volume fraction and these geometric variables should be established, or these variables should be used as a design parameter when designing TPMS-based lattice structures for heat transfer applications. These properties have not been examined in great detail in regards to TPMS-based lattice heat sinks and may provide key insight in to the fluid dynamics and thermal transport within these structures.

6.2 Method

6.2.1 Tortuosity

Tortuosity, τ, is defined as the ratio between the length of a path and the shortest distance between its start and end point. When a path has a tortuosity equal to one, that path is a straight line connecting the start and end points. This is depicted in figure 6.1.

Tortuosity here was calculated by importing a voxelised model of the examined lattice structures into MATLAB. The *Tort3D* [136] and *dijkstra* [137] open-source functions were used to find the shortest path from every discretised void inlet position to the void outlet, both of which were in the xz-plane. This gives a tortuosity distribution for each structure. The solid domain and paths were visualised using the user-created *PATCH_3Darray* [138] function, which uses the Marching Cubes algorithm [139], to generate surface meshes.

Due to the non-uniform distribution of tortuosity values for a given structure, it is not appropriate to calculate and use a mean tortuosity. The distribution of the tortuosity data must be taken in to account. This was achieved by using whisker plots, which display the median, lower and upper quartiles and minimum and maximum values.

For each examined lattice type, the tortuosity was determined from a single cell rather than a lattice structure with $1 \times 5 \times 1$ cells. The calculated paths are typically repeated within every cell and, hence, modelling five cells significantly increases the computational resources whilst not providing more information. Modelling a single cell minimises computational costs and allows a greater spatial resolution. This is important as straight paths (i.e., a path with no curvature from its start to end point) may not be considered straight when examining a discretised low-resolution array, shown in figure 6.2. This has a large impact on the tortuosity distribution. A single, high resolution cell was therefore used for this study.

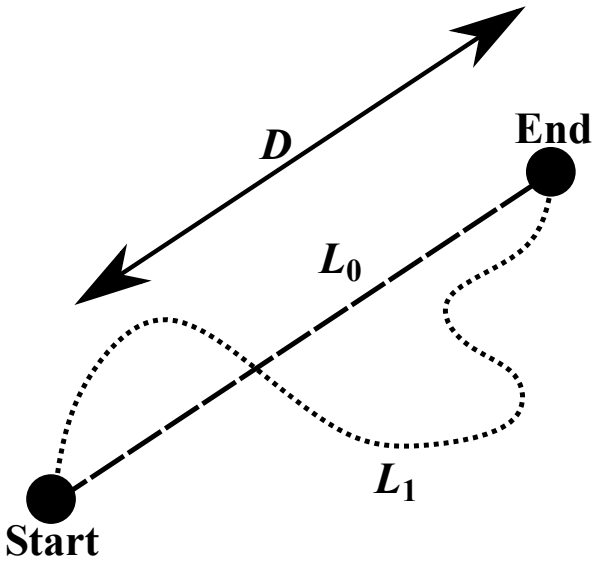

Figure 6.1: Depiction of a straight path, with length L_0, and a curved path, with length L_1, between a start and end point. The shortest distance between the two points is D. The straight path will have a tortuosity equal to 1 as $L_0 = D$ whereas the curved path will have a tortuosity greater than 1 as $L_1 > D$.

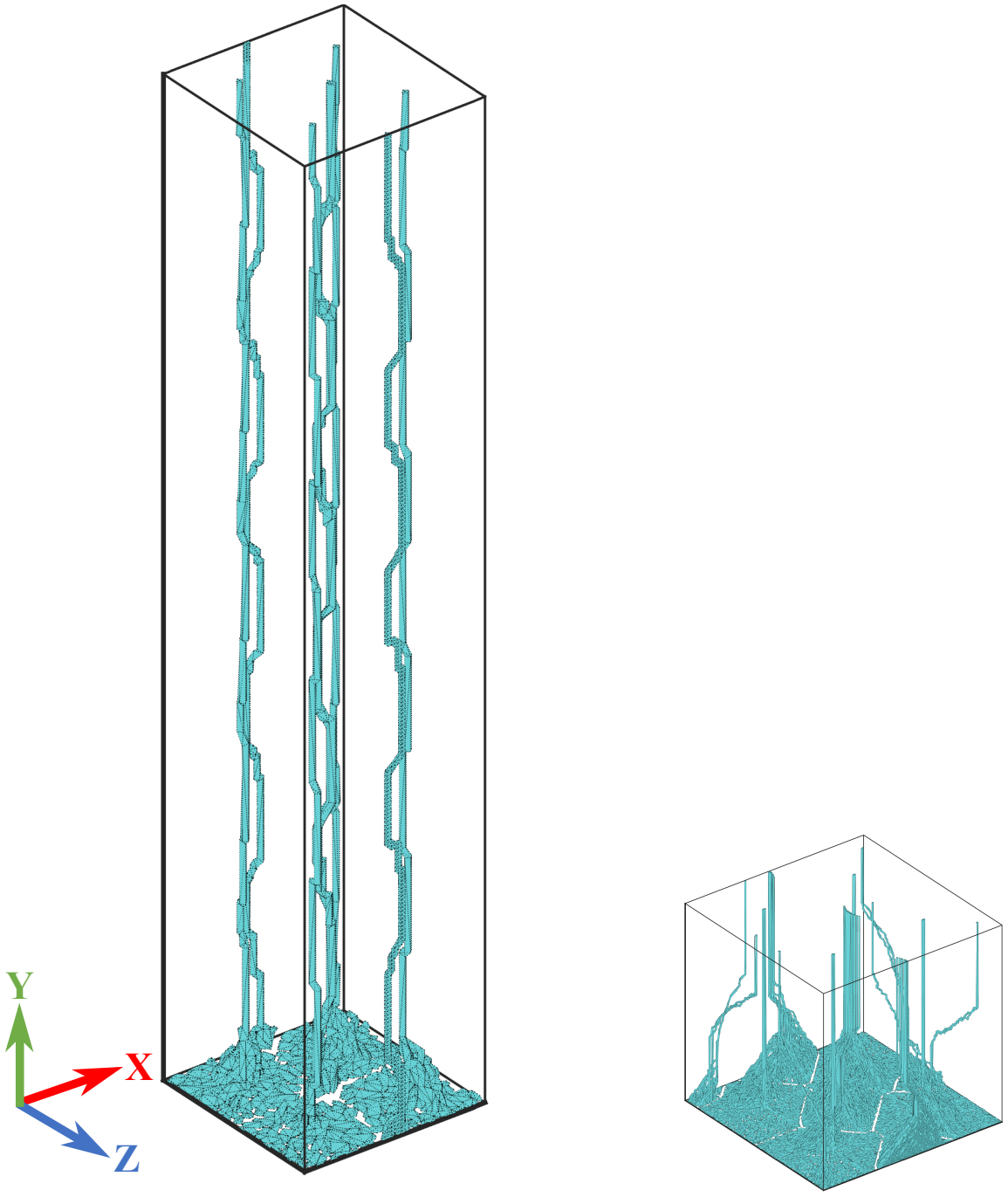

(a) 1 × 5 × 1 cells with array dimensions of 54 × 266 × 54.

(b) 1 × 1 × 1 cell with array dimensions of 201 × 201 × 201.

Figure 6.2: Calculated shortest paths for the split-p matrix lattice structure with a volume fraction of 0.4 for a low cell-resolution array (left) and a high cell-resolution array (right).

It is important to note that while fluids tend to take the path of least resistance, which can often be the shortest path, the paths calculated here do not necessarily correspond to fluid flow paths. Care must therefore be taken when discussing tortuosity here, as this refers to the tortuosity of the channels and not the tortuosity of the flow paths.

6.2.2 Channel radius

The channel radius, r, was calculated by importing a voxelised model of the examined lattice structures into MATLAB. An algorithm was used to skeletonise the channels, see figure 6.3 for a two-dimensional example, of the examined structures. The channel radii was isolated by finding the closest neighbouring solid domain voxel from each point on the skeleton. Figure 6.4 depicts a two dimensional representation of this method. The distances were calculated in units of voxels and converted into metres by multiplying it by the physical length of one voxel, which was found by dividing the length of the examined lattice structure in a given direction by the number of voxels in that direction. The solid domain and channel skeletons were visualised using the *PATCH_3Darray* [138] function, as discussed in section 6.2.1.

A single lattice cell was initially used to find the channel radii, rather than a lattice structure with $1 \times 5 \times 1$ cells. Since the geometry repeats every cell, only a singular cell needs to be examined to determine channel radii for an arbitrary number of cells. Higher resolution arrays could then be used, whilst minimising the impact on computational resources.

From preliminary studies, it was found that the skeleton was inaccurate along the edges of the array. This was solved by examining lattices with $1.4 \times 1.4 \times 1.4$ cells (i.e., an additional 0.2 cells either side of the lattice in the x, y and z directions) and finding the channel skeletons for this array. This produced accurate channel skeletons within the central cell. The additional structures outside this region were then removed from the array and only the central cell was examined further. Walls on the plane perpendicular to the inlet (the xz-plane) were not included as they also impacted the accuracy of the skeletonised channels at the edge of the array.

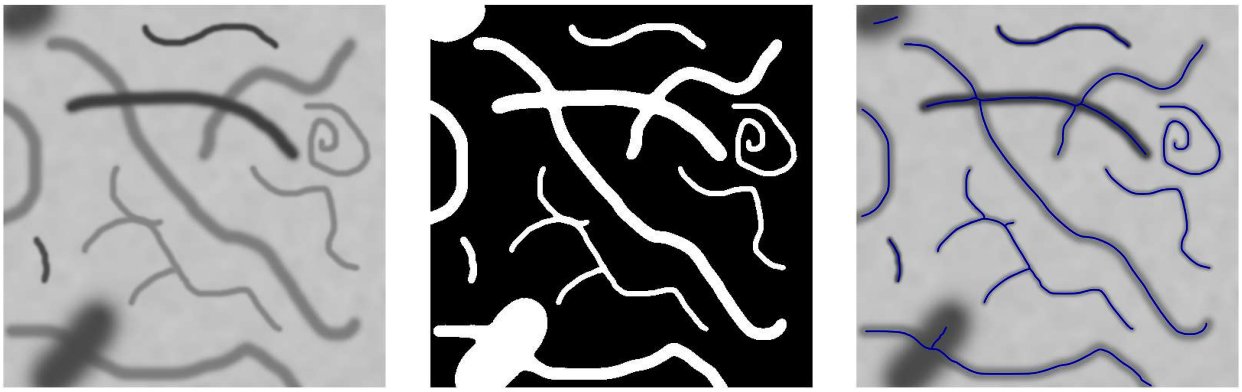

Figure 6.3: Two-dimensional example of an image (left) being binarised (centre), skeletonised and overlaid over the original image (right). Modified from [140].

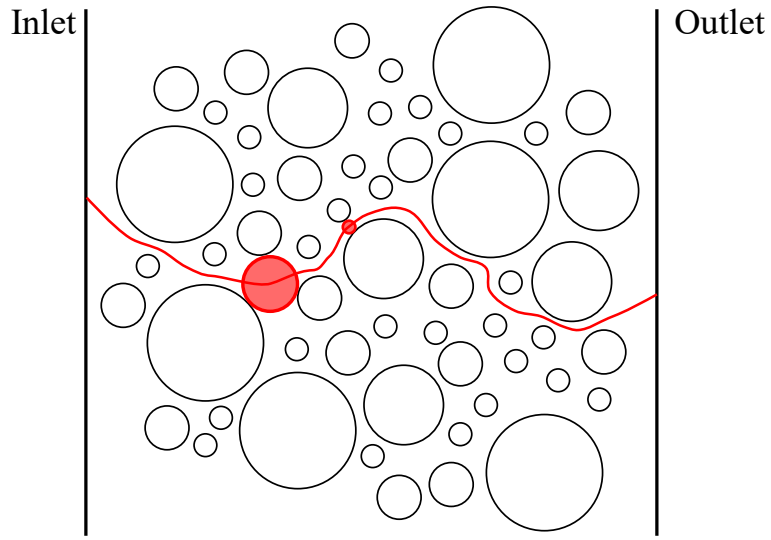

Figure 6.4: How channel radii is calculated from a skeleton (red path). The red circle shows the channel radius and is found by finding the smallest circle in contact with a solid wall.

6.3 Results

6.3.1 Tortuosity

The shortest paths calculated from the tortuosity analysis are displayed in figure 6.5, where only structures with a volume fraction of 0.25 are shown for brevity. From a visual examination of the shortest paths, all structures had paths that could travel straight through the cell, apart from the diamond matrix lattice. This was true throughout the entire range of examined volume fractions, shown in figure 6.6, where the red line denotes the median tortuosity, the bars denote the lower and upper tortuosity quartiles and the whiskers denote the minimum and maximum tortuosities. The diamond matrix lattice was the only examined structure that had a minimum tortuosity greater than 1, which indicates that there are no direct paths from the inlet to the outlet.

Figure 6.6 shows that the median tortuosity and the maximum tortuosity for the examined TPMS-based lattice structures increased with volume fraction. This is expected as increasing volume fraction thickens the walls of a given structure, limiting the possible paths through it. The minimum tortuosity only increased in the diamond matrix lattice structure as there were no possible straight paths through the structure within the examined range of volume fractions, which was not the case for the remaining structures.

It was observed that the diamond matrix lattice exhibited the largest tortuosity values of all the examined structures. Its median tortuosity, which ranged between $1.30 - 1.52$, also exhibited a higher rate of change with respect to volume fraction. This was due to the lack of straight paths from the inlet to the outlet, such that this structure had a minimum tortuosity larger than 1, which increased the median tortuosity significantly. The remaining structures exhibited comparable median tortuosities, ranging from $1.10 - 1.21$, but displayed greater variation for their maximum tortuosity values.

As tortuosity is a measure of the complexity of the channels, examining the spread of the tortuosity distribution may provide some key insight in to the variation of channel complexity within

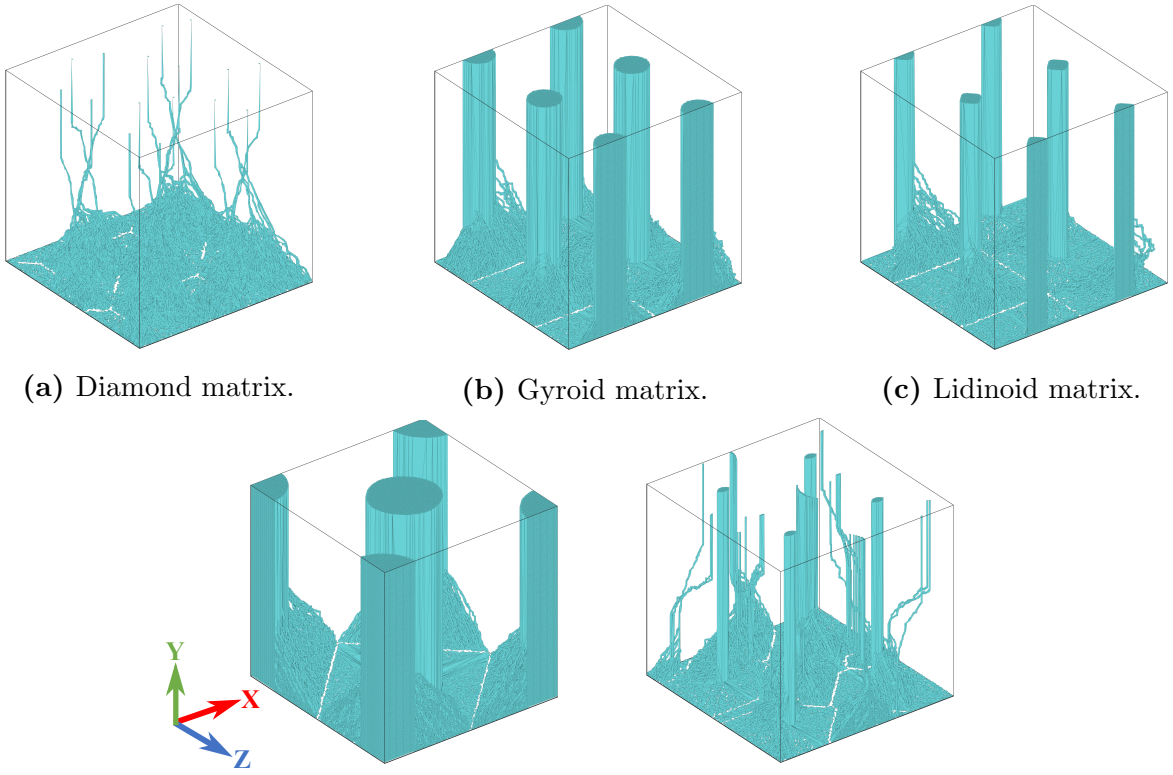

(a) Diamond matrix. **(b)** Gyroid matrix. **(c)** Lidinoid matrix.

(d) Primitive matrix. **(e)** Split-p matrix.

Figure 6.5: Shortest calculated paths in the examined TPMS-based lattice structures with a volume fraction of 0.25 for the tortuosity analysis

each examined lattice structure. This is shown in figure 6.7, where the tortuosity range, $\Delta\tau$, is examined against volume fraction. For the majority of the examined structures, the tortuosity range increased with volume fraction as the minimum tortuosity remained at 1 whilst the maximum tortuosity increased. This was not the case for the diamond matrix lattice, where the range decreased due to the minimum tortuosity increasing with volume fraction. It was therefore expected that structures will experience a growing tortuosity range whilst there exists a direct path from the inlet to the outlet, with the range then decreasing once a channel is blocked due to the increased volume fraction. This needs to be confirmed by examining these structures in various orientations.

The tortuosity range may not be an appropriate parameter to examine however as it only takes into account the minimum and maximum values, which may not be representative of the structures as the tortuosity distribution is non-uniform. The tortuosity interquartile range, τ_{IQR}, shown in figure 6.8, was therefore examined as it takes into account the distribution of the tortuous paths. The interquartile range for the majority of the examined lattice structures in the examined volume fraction range increased with volume fraction, albeit only by 10% for the split-p matrix lattice and approximately 3.4% for the gyroid, lidinoid and primitive matrix lattices. The interquartile range for the diamond matrix lattice varied within $\pm$ 5% of the mean value. The small changes observed for the interquartile range indicate that each TPMS-based lattice structure, in a given orientation, may have a pre-defined interquartile range that is not dependent on volume fraction. Despite the tortuosity of the structures increasing with volume fraction, the small changes to the interquartile range indicates that the variation in their tortuosity (or channel complexity) remains relatively consistent.

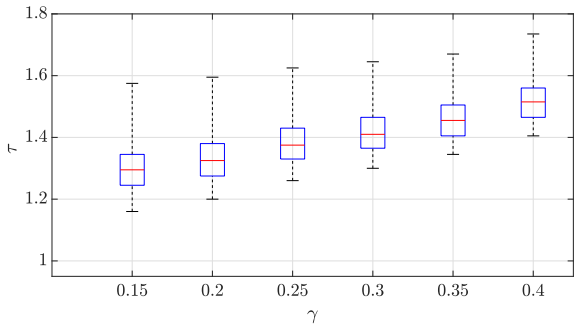

(a) Diamond matrix lattice.

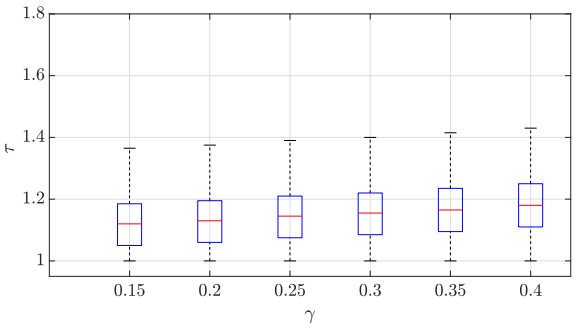

(b) Gyroid matrix lattice.

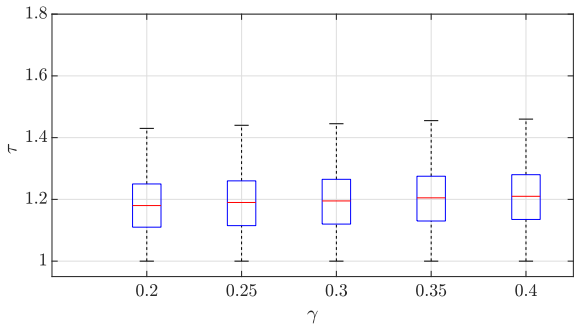

(c) Lidinoid matrix lattice.

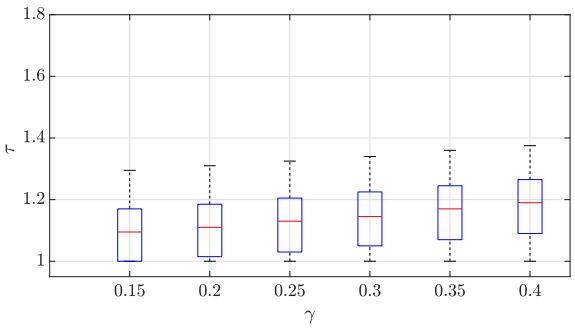

(d) Primitive matrix lattice.

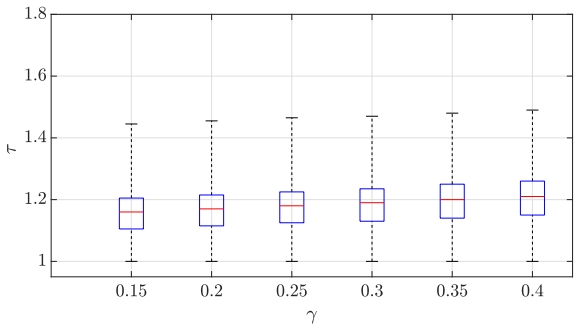

(e) Split-p matrix lattice.

Figure 6.6: Tortuosity distribution for the examined TPMS-based lattice structures. The median, lower and upper quartiles, and minimum and maximum tortuosity values are displayed.

6.3.2 Channel radius

The skeletonised channels, and their respective lattice structures, are shown below in figure 6.9. Two skeletons were observed for each structure, which corresponded to the two fluid domains present in a TPMS-based matrix lattice structure (as discussed in section 2.3).

Figure 6.10 shows the minimum channel radius, r_{min}, for each of the examined lattice structures. The uncertainty shown here is ± 2 voxel lengths, as there is an uncertainty of ± 1 voxel associated with the position of the channel skeleton and an uncertainty of ± 1 voxel associated with the distance from the channel skeleton to the nearest wall. The voxels for the split-p matrix had a length of 25.0 µm while the voxels for the remaining examined lattice structures had a length of 49.8 µm. It was observed that the minimum channel radius decreased with increasing volume fraction, as expected due to the walls thickening. The lidinoid matrix structure had the smallest minimum channel radius. The primitive matrix and gyroid matrix lattice structures

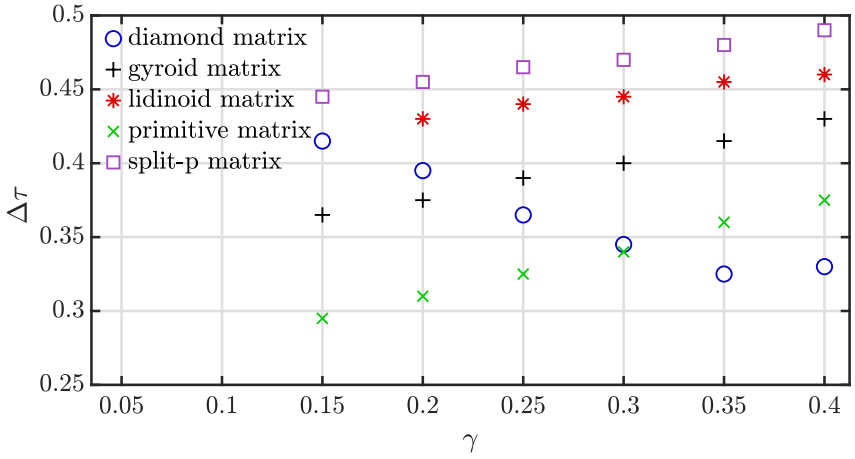

Figure 6.7: Tortuosity range for the examined TPMS-based lattice structures with varying volume fraction.

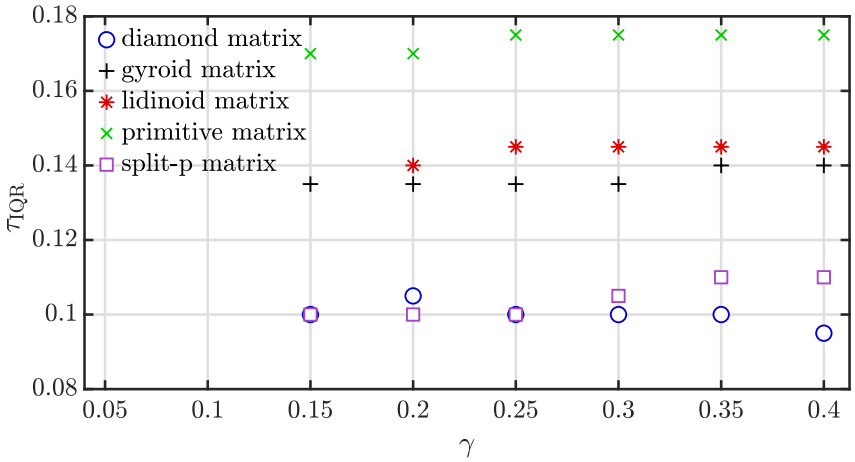

Figure 6.8: Tortuosity interquartile range for the examined TPMS-based lattice structures with varying volume fraction.

had the largest minimum channel radii at low and high volume fractions, respectively, where they intersect at a volume fraction of approximately 0.25.

The maximum channel radius, $r_{\max}$, is shown in figure 6.11 for each of the examined lattice structures. The maximum channel radius decreased with increasing volume fraction. The primitive matrix lattice presented the largest maximum channel radius, where it was consistently larger by a factor of approximately 2 than the next largest maximum channel radius for a given volume fraction. The lidinoid matrix had the smallest maximum channel radius.

As discussed in section 5.3.1, changes in the channel diameter lead to localised pressure drops. This effect was significant for larger changes in the channel diameter. The range of channel radii, Δr, within the structures is presented in figure 6.12 to examine this effect. It was observed that the channel radii range increased with volume fraction for all of the examined TPMS-based lattice structures. The primitive matrix lattice exhibited the largest channel radii range, which was larger than the next largest channel radii range by a factor greater than 2. The gyroid matrix lattice exhibited the smallest channel radii range.

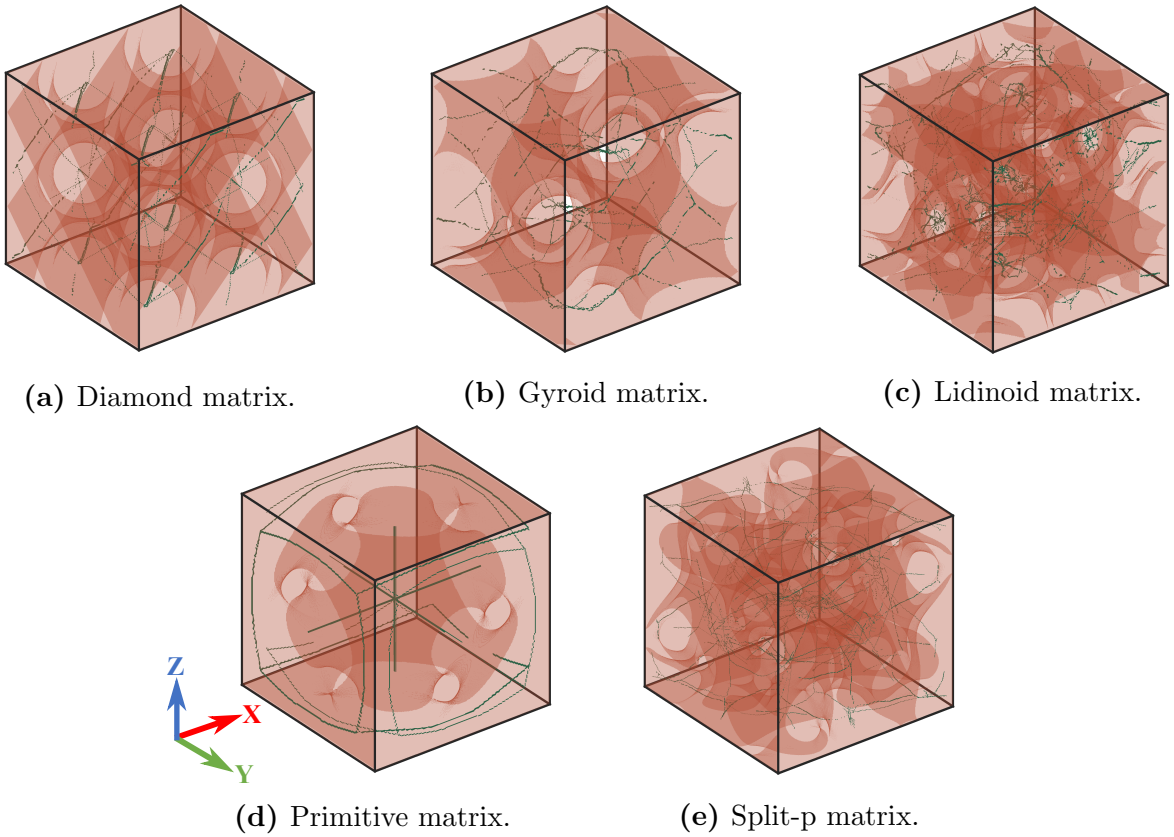

(a) Diamond matrix. **(b)** Gyroid matrix. **(c)** Lidinoid matrix.

(d) Primitive matrix. **(e)** Split-p matrix.

Figure 6.9: Skeletonised channels in the examined TPMS-based lattice structures with a volume fraction of 0.25

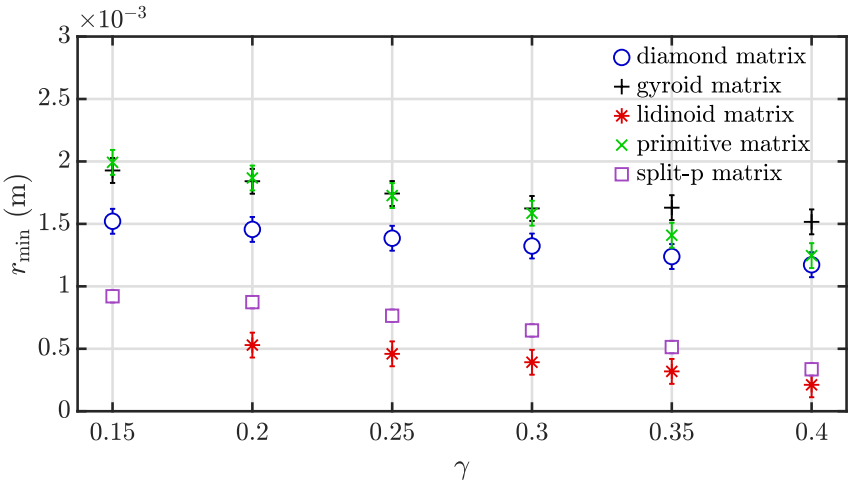

Figure 6.10: Minimum channel radius for the examined TPMS-based lattice structures with varying volume fraction.

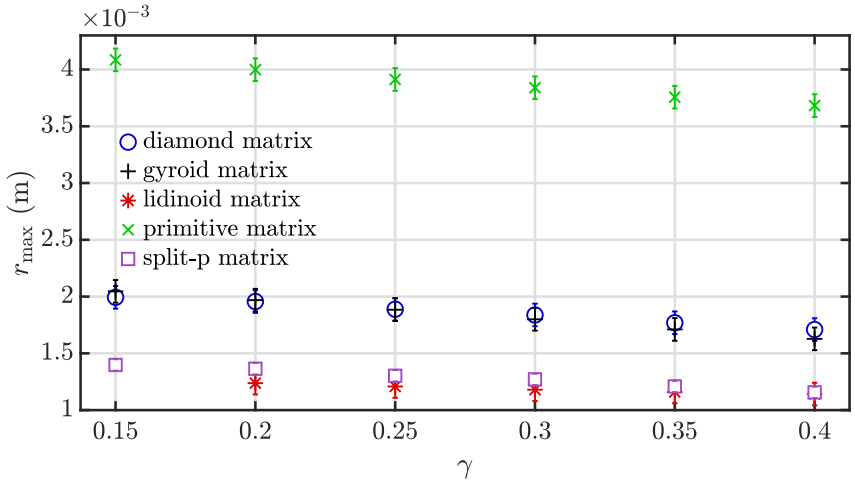

Figure 6.11: Maximum channel radius for the examined TPMS-based lattice structures with varying volume fraction.

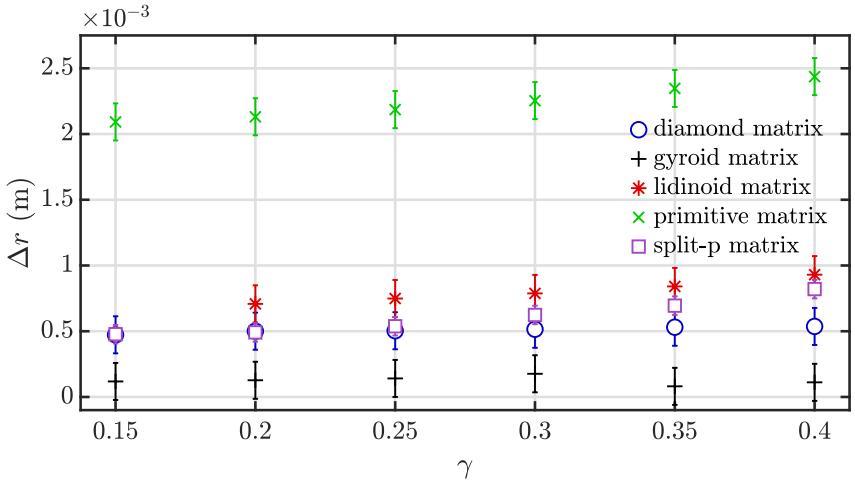

Figure 6.12: Channel radii range for the examined TPMS-based lattice structures with varying volume fraction.

6.4 Discussion

6.4.1 Hydraulic performance

Here, the impact of tortuosity on the hydraulic performance was determined, where the hydraulic performance was specified as the pressure drop per unit length exhibited by the examined structures. Figure 6.13 presents the pressure drop per unit length against the tortuosity distribution for increasing volume fraction, where the markers denote the median tortuosity and the bars denote the minimum and maximum tortuosities. It was observed that the exhibited pressure drop per unit length increased with tortuosity, with all but one of the examined structures following the same general trend for the median tortuosity (the diamond matrix lattice does not follow this trend as it has a minimum tortuosity greater than 1). This implies that tortuosity may be a good indicator of the hydraulic performance for a set of TPMS-based lattice structures. However, it was found that very small changes in median tortuosity lead to significant changes in the exhibited pressure drop per unit length of the examined structures. The median tortuosity, and its minimum and maximum values, therefore cannot be used to distinguish the hydraulic

performance between different TPMS-based lattices structures.

The same conclusion was also reached when examining the spread of the tortuosity data. Figure 6.14 shows how the pressure drop per unit length varies with the tortuosity range for the examined TPMS-based lattice structures. Here, the pressure drop increased with tortuosity range for the majority of the examined structures. This was not the case for the diamond matrix lattice, where the pressure drop per unit length decreased. This was because the tortuosity range decreased with volume fraction, as shown in figure 6.7, due to its increasing minimum tortuosity. The primitive matrix lattice also exhibited higher pressure drops than the gyroid matrix structure despite having lower tortuosity ranges, and the same behaviour was also seen between the lidinoid and split-p matrix lattice structures. The tortuosity interquartile range is not discussed here as no discernible trend exists.

From these results we can conclude that tortuosity is not the principal driver behind the hydraulic performance of the examined TPMS-based lattice structures, though the median tortuosity can be used to determine the hydraulic performance for a given lattice cell type. The tortuosity distribution for a given TPMS-based lattice structure and volume fraction is dependent on its

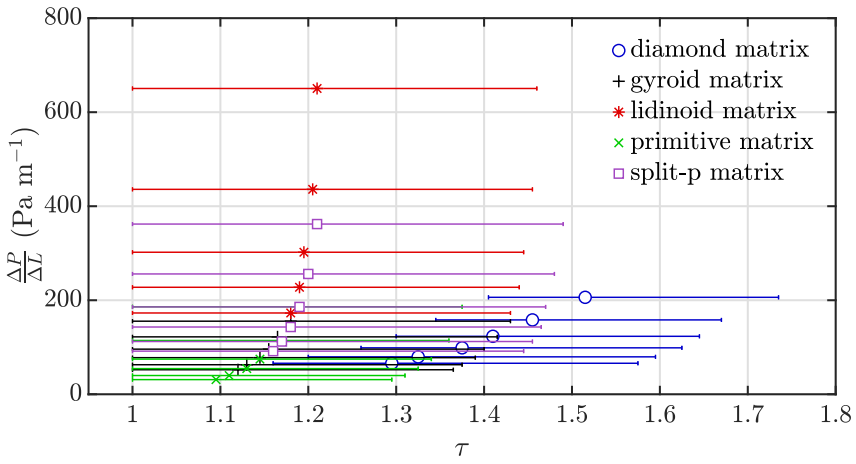

Figure 6.13: Pressure drop per unit length for the examined TPMS-based lattice structures with varying tortuosity distribution (superficial fluid velocity = 5×10^{-3} m s^{-1}).

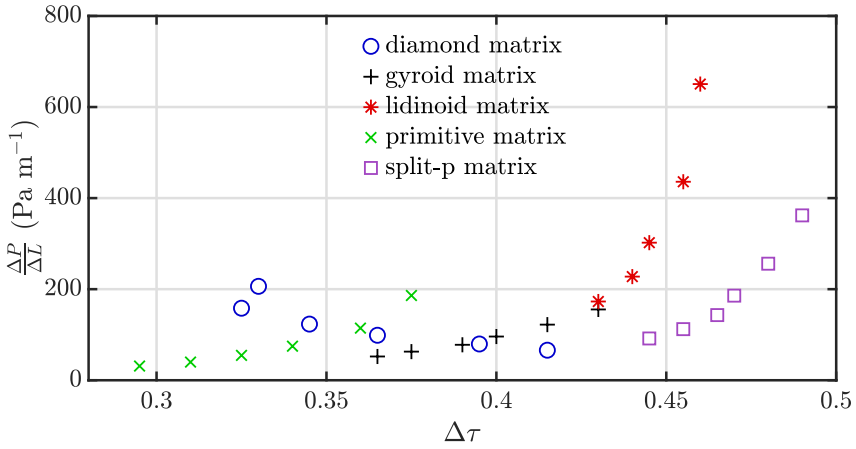

Figure 6.14: Pressure drop per unit length for the examined TPMS-based lattice structures with varying tortuosity range (superficial fluid velocity = 5×10^{-3} m s^{-1}).

orientation, however. This can be seen in figure 6.15, where straight paths from the inlet to the outlet through the diamond matrix lattice structure exist when it is rotated by 45° around its z-axis. This will have a large impact on the hydraulic performance for a given cell type as the channel walls no longer obstructs the fluid from travelling straight through the structure. This needs to be confirmed by studying the hydraulic performance for a selection of TPMS-based lattice structures with varying orientations.

The impact of the channel radius on the hydraulic performance was also examined. Figure 6.16 presents the pressure drop per unit length against the minimum channel radius. It was observed that the pressure drop per unit length increased when the minimum channel radius decreased, as expected from the discussion in section 5.3.1. The minimum channel radius does not solely determine the hydraulic performance however, as there are multiple examples of the gyroid matrix lattice structure having a larger minimum channel radius than the primitive matrix lattice structure while exhibiting a larger pressure drop per unit length. The examined TPMS-based lattice structures were also separated into two distinct groups, one which encompassed the lidinoid and split-p matrix lattice structures and another which encompassed the diamond, gyroid and primitive matrix lattice structures. The geometry of TPMS-based lattice structures therefore plays a key role in determining their hydraulic performance, despite the minimum channel radius having a large impact on exhibited pressure drop per unit length. The maximum channel diameter had

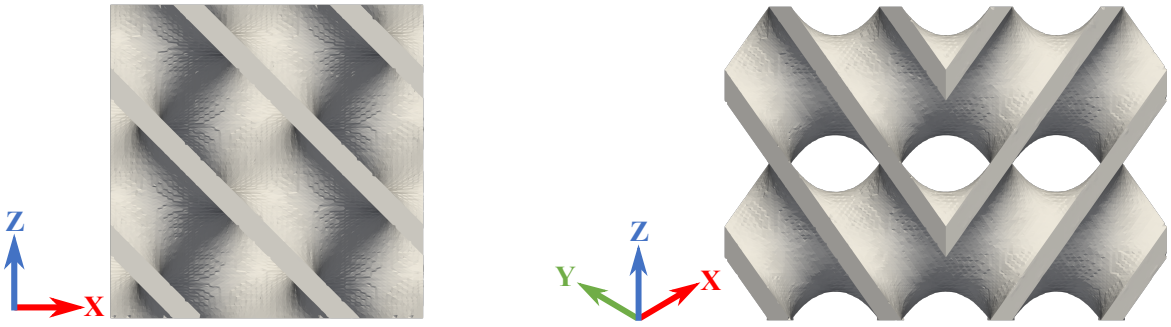

(a) No rotation. **(b)** 45° rotation.

Figure 6.15: Two-dimensional projection of the diamond matrix lattice cell rotated in the z-axis.

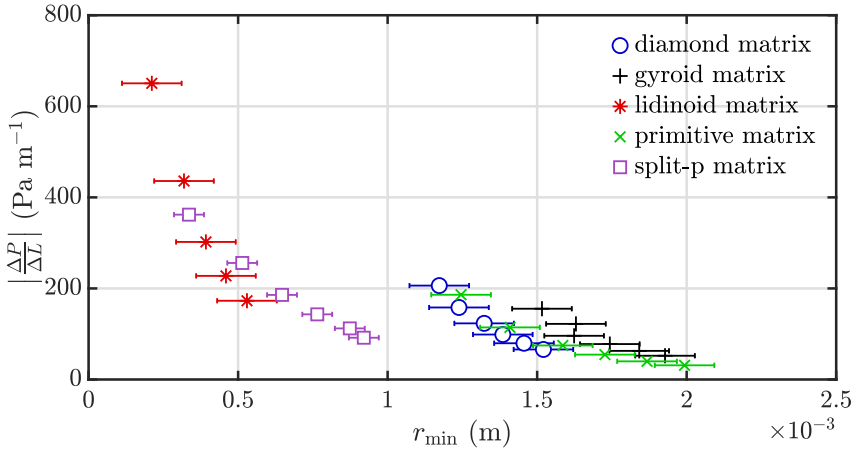

Figure 6.16: Pressure drop per unit length for the examined TPMS-based lattice structures with varying minimum channel radius (superficial fluid velocity = 5×10^{-3} m s^{-1}).

less impact on the hydraulic performance and is therefore not an ideal parameter to use when determining the hydraulic performance across a range of different TPMS-based lattice cell types.

Figure 6.17 shows how the pressure drop per unit length varies with the range of channel radii for the examined TPMS-based lattice structure. It was observed that the exhibited pressure drop per unit length increases as the difference between the minimum and maximum channel radius increased for the majority of the examined structures. The channel radii range does not appear to be a key geometrical feature which can determine the hydraulic performance across a variety of different cell types however, as the gyroid and primitive matrix lattices exhibited comparable pressure drop per unit length despite having the smallest and largest channel radii range respectively. The lidinoid matrix structure also exhibited the highest pressure drop per unit lengths despite not possessing a relatively large channel radii range.

The pressure drop behaviour exhibited by the examined lattice structures can be explained by finding how changes in the channel radius affect the local evolution of pressure within the examined structures, where in section 5.3.1 it was theorised that changes in the channel radius lead to localised pressure drops. Figure 6.18 presents the evolution of pressure and minimum channel radius within the channels with the smallest radius of the examined structures. The primitive matrix lattice exhibited periodic, discontinuous pressure drops when the channel radius was at a local minimum. Sharper drops were seen at the interface between cells (i.e., at a position of 0.01 m), which corresponded to the central channel. This showed that the central channel had a larger impact on the pressure within the structure than the outer channels. Similar features were also observed in the split-p matrix lattice structure. This effect was less pronounced however, possibly due to it having a smaller channel radii range than the primitive matrix lattice. The diamond and lidinoid matrix lattice structures had comparable channel radii range to the split-p matrix structure but did not exhibit local pressure drops as expected. This was because the channels in these two structures reach their minimum radius more frequently than the channels in the split-p matrix, where the fluid flow was bottlenecked, such that the pressure drop could not stabilise. The gyroid matrix lattice structure also did not exhibit local discontinuous pressure drops but this was due to it having the smallest channel radii range of the examined structures. Discontinuous pressure drops within a TPMS-based lattice structure are therefore dependent on both the channel radii range and the frequency of the channels reaching their minimum radius.

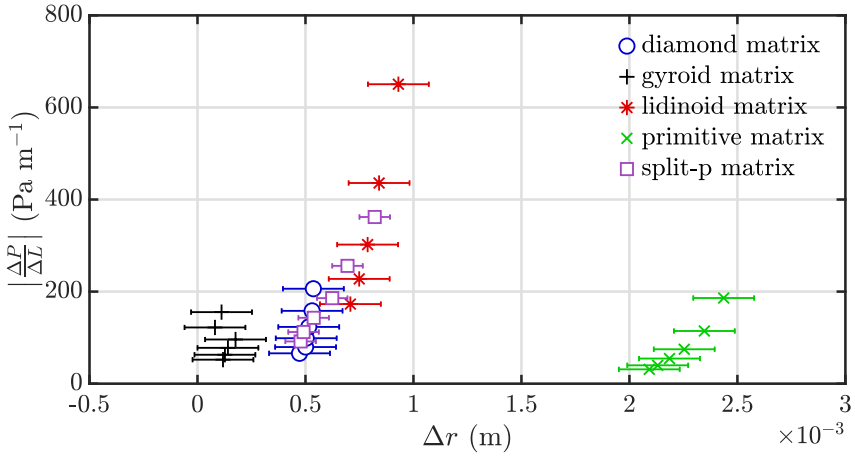

Figure 6.17: Pressure drop per unit length for the examined TPMS-based lattice structures with varying channel radii range (superficial fluid velocity = 5×10^{-3} m s^{-1}).

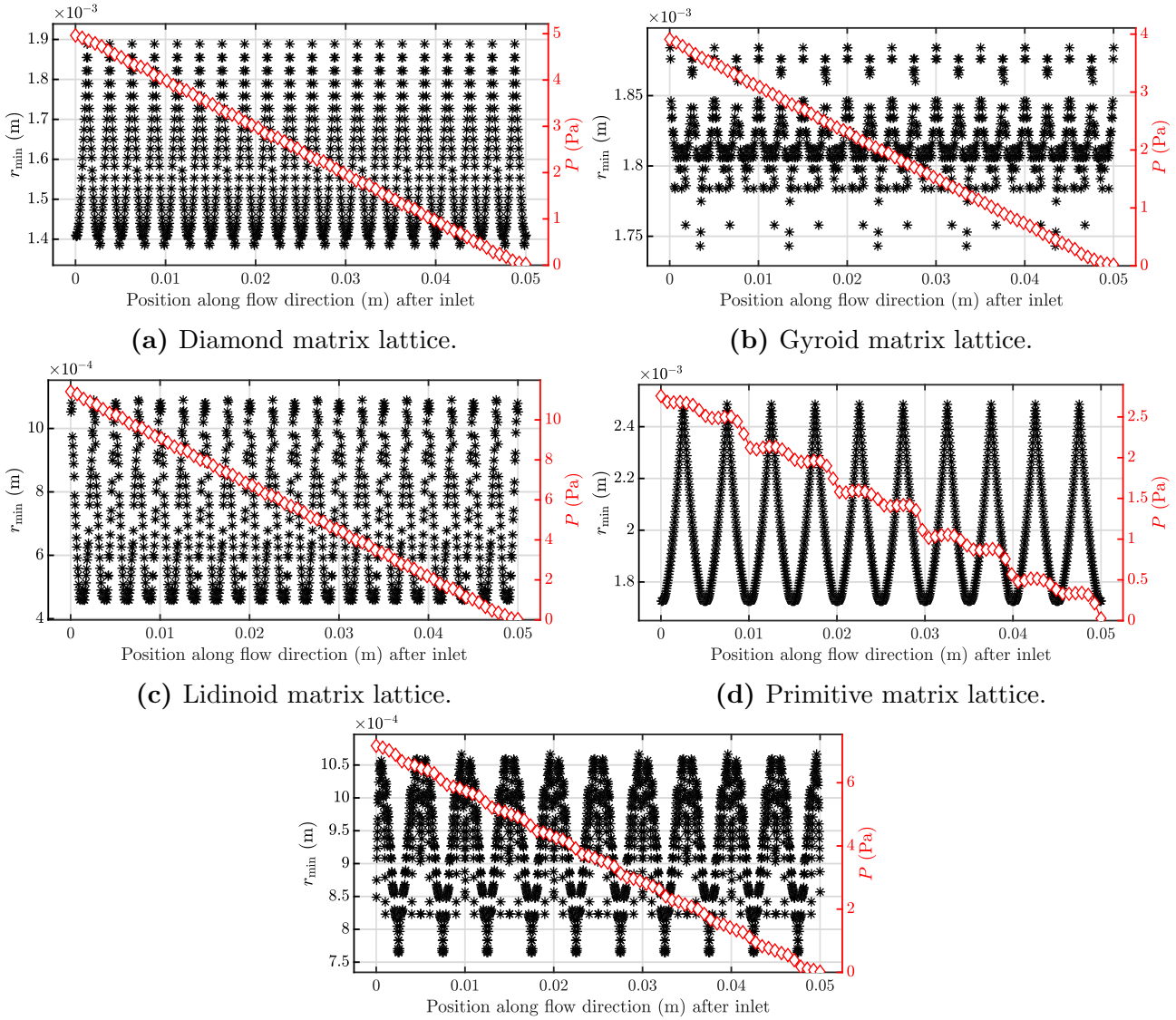

(a) Diamond matrix lattice.

(b) Gyroid matrix lattice.

(c) Lidinoid matrix lattice.

(d) Primitive matrix lattice.

(e) Split-p matrix lattice.

Figure 6.18: Evolution of pressure and minimum channel radius within the examined structures (superficial fluid velocity = 5×10^{-3} m s^{-1}, volume fraction = 0.25).

A variety of tortuosity and channel radius properties can be used to determine the hydraulic performance and the evolution of pressure within a structure for a given lattice cell type. This is not the case when examining multiple different TPMS-based lattice structures however, as the geometry of the structure has a large impact on performance. This is because these properties only represent an aspect of the geometry of the structures and are not able to capture all of the complex dynamics of the fluid flowing through them. Additional geometrical properties, such as surface area, need to be considered or a combination of the examined properties need to be examined (using methods such as machine learning) in tandem to better understand the effect that these have on their hydraulic performance.

6.4.2 Thermal performance

The impact that the geometrical features identified in this chapter have on the thermal performance of the examined TPMS-based lattice structures, defined as the volumetric heat transfer coefficient, is discussed here. It can be seen in figure 6.19 that the primitive matrix lattice structure had comparable median tortuosities to the gyroid, lidinoid and split-p matrix lattices yet exhibited significantly smaller volumetric heat transfer coefficients. The diamond matrix lattice also had significantly higher median tortuosities than the lidinoid matrix structure but exhibited comparable volumetric heat transfer coefficients. The median tortuosity does not therefore have a large impact on the volumetric heat transfer coefficient exhibited by the examined structures, despite it increasing with median tortuosity for a given lattice cell type.

Figure 6.20 shows how the tortuosity range impacts the volumetric heat transfer coefficient. For the majority of the examined structures, the volumetric heat transfer coefficient increased with tortuosity range. This indicates that structures with a larger range of tortuous paths through the channels would exhibit increased volumetric heat transfer coefficients. These structures have a minimum tortuosity of 1, which means that the property being examined here is the maximum tortuosity. This does not apply to the diamond matrix lattice, as this has a minimum tortuosity greater than 1, and it was observed that the exhibited volumetric heat transfer coefficient decreased with an increasing tortuosity range. The tortuosity range is therefore not an appropriate property to use to determine thermal performance.

It was observed in figure 6.21 that the volumetric heat transfer coefficient decreased with an increasing tortuosity interquartile range, as the diamond matrix and split-p matrix exhibited the greatest volumetric heat transfer coefficients whilst also having the smallest tortuosity interquartile range. The primitive matrix exhibited the lowest volumetric heat transfer coefficient and the largest interquartile range. This indicates that lattice cell types which minimise the distribution of its tortuous paths may have improved thermal performance. There are cases examined here where a structure with a smaller tortuosity interquartile range also exhibited a smaller volumetric heat transfer coefficient however, so this may not be true for all cases.

The impact that the channel radius has on thermal performance was also examined. The volu-

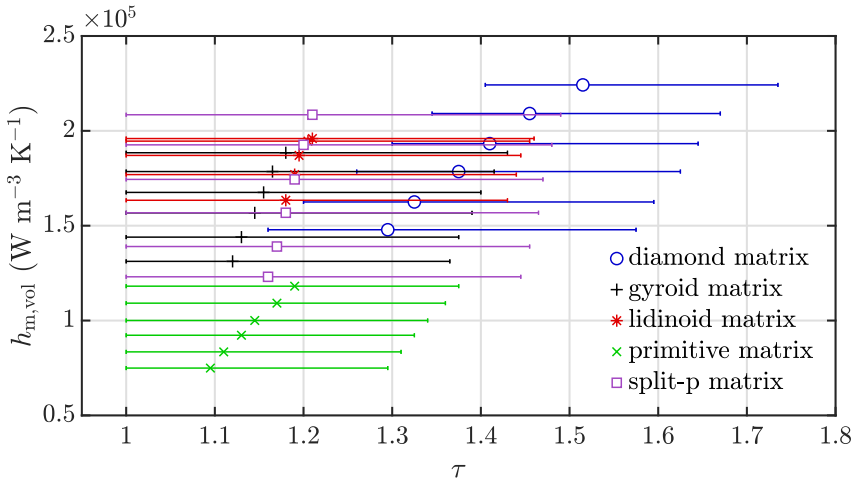

Figure 6.19: Volumetric heat transfer coefficient for the examined TPMS-based lattice structures with varying tortuosity distribution (superficial fluid velocity = 5×10^{-3} m s^{-1}).

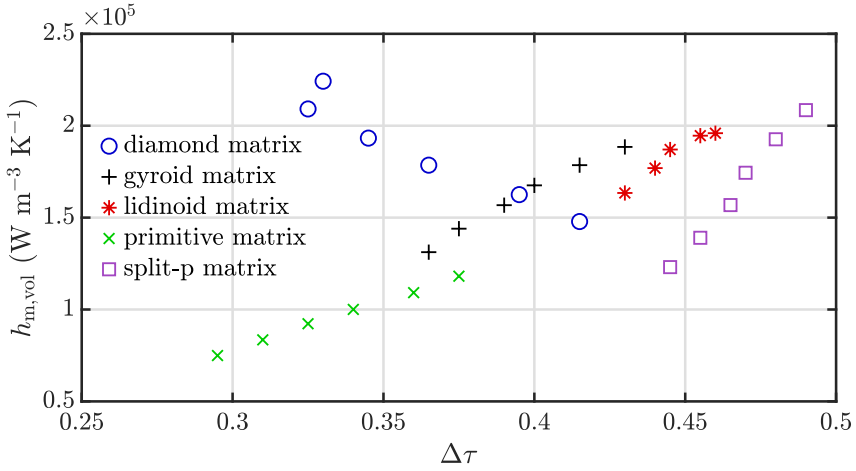

Figure 6.20: Volumetric heat transfer coefficient for the examined TPMS-based lattice structures with varying tortuosity range (superficial fluid velocity = 5×10^{-3} m s^{-1}).

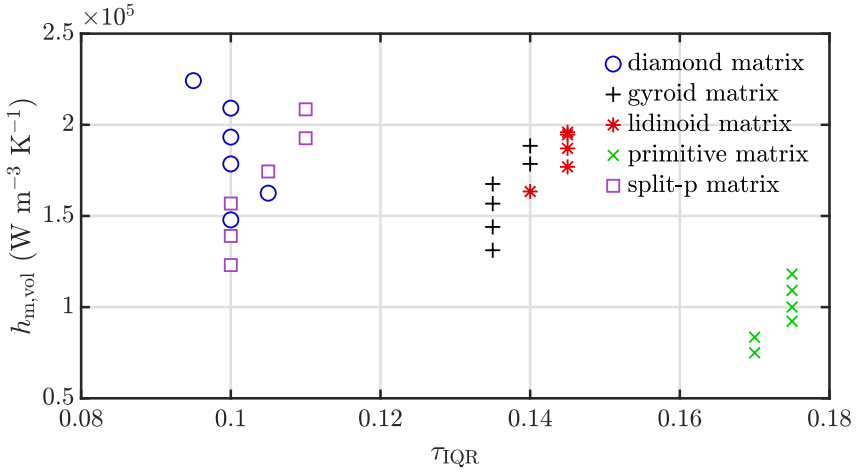

Figure 6.21: Volumetric heat transfer coefficient for the examined TPMS-based lattice structures with varying tortuosity interquartile range (superficial fluid velocity = 5×10^{-3} m s^{-1}).

metric heat transfer coefficient, for a given lattice cell type, was seen to decrease with an increasing minimum channel radius, shown in figure 6.22. This did not apply across different TPMS-based lattice structures as the diamond matrix lattice structure exhibited the greatest volumetric heat transfer coefficient despite consistently having larger minimum channel radii then both the lidinoid and split-p matrix lattice structures. The same effect was also observed when examining the maximum channel radius.

The channel radii range, presented in figure 6.23, does not have a strong impact on thermal performance. While the exhibited volumetric heat transfer coefficient increased with channel radii range for the lidinoid, primitive and split-p matrix lattice structures, this was not the case for the diamond matrix lattice structure, which experienced marginal increases to its channel radii range, and the gyroid matrix lattice structure. Additionally, the diamond matrix lattice structure exhibited the greatest volumetric heat transfer coefficient despite consistently having larger channel radii than the gyroid matrix lattice structure and smaller channel radii range than the primitive matrix lattice structure.

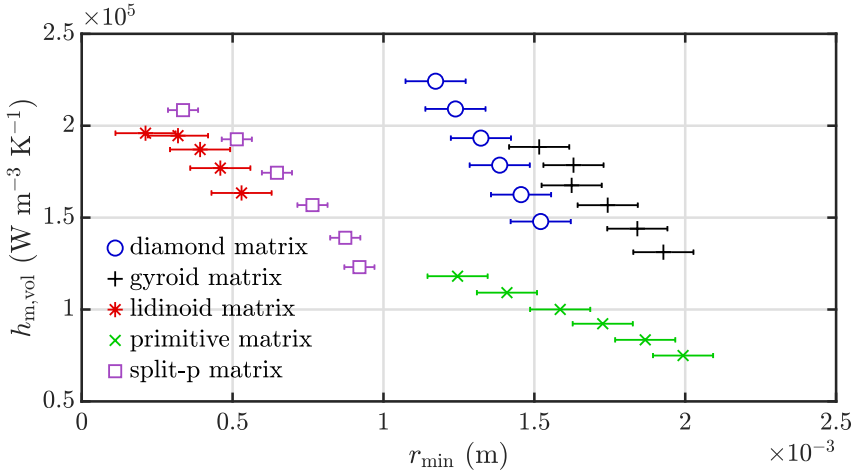

Figure 6.22: Volumetric heat transfer coefficient for the examined TPMS-based lattice structures with varying minimum channel radius (superficial fluid velocity = 5×10^{-3} m s^{-1}).

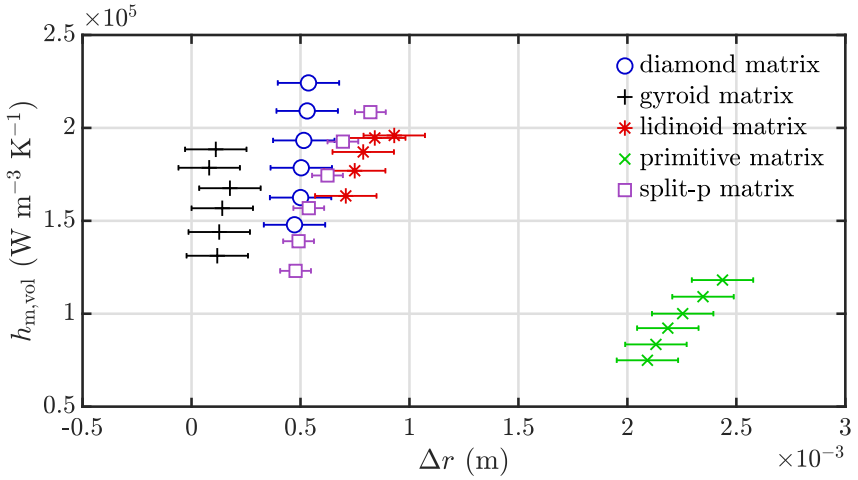

Figure 6.23: Volumetric heat transfer coefficient for the examined TPMS-based lattice structures with varying channel radii range (superficial fluid velocity = 5×10^{-3} m s^{-1}).

The volumetric heat transfer coefficients exhibited by the examined TPMS-based lattice structures can be further explained by finding how changes in the channel radius affect the local wall heat transfer coefficients. It was theorised in section 5.3.2 that smaller channel radii would cause the local fluid velocity to increase, which would lead to a peak local wall heat transfer coefficient. Figure 6.24 shows how the channel radius and local wall heat transfer coefficient vary throughout the examined structures, with the channels presented in this figure being the channels with the smallest radius. It was observed that peak local wall heat transfer coefficients were obtained where the channel radius was at a local minimum for the lidinoid, primitive and split-p matrix lattice structures. The diamond and gyroid matrix lattice structures do not follow this theory, however. The diamond matrix lattice structure exhibited peak local wall heat transfer coefficients when the channel radius was largest, as shown in figure 6.25. This happened because the fluid exhibited greater velocities when it travelled in the direction of the inlet flow, which was regularly prevented in this structure due to the orientation of its channels. The channels which allowed the fluid to travel completely in this direction in the diamond matrix lattice were regions where the channel radius was also largest. In cases such as these, the orientation of the channels has a large impact on the local wall heat transfer coefficient. The gyroid matrix

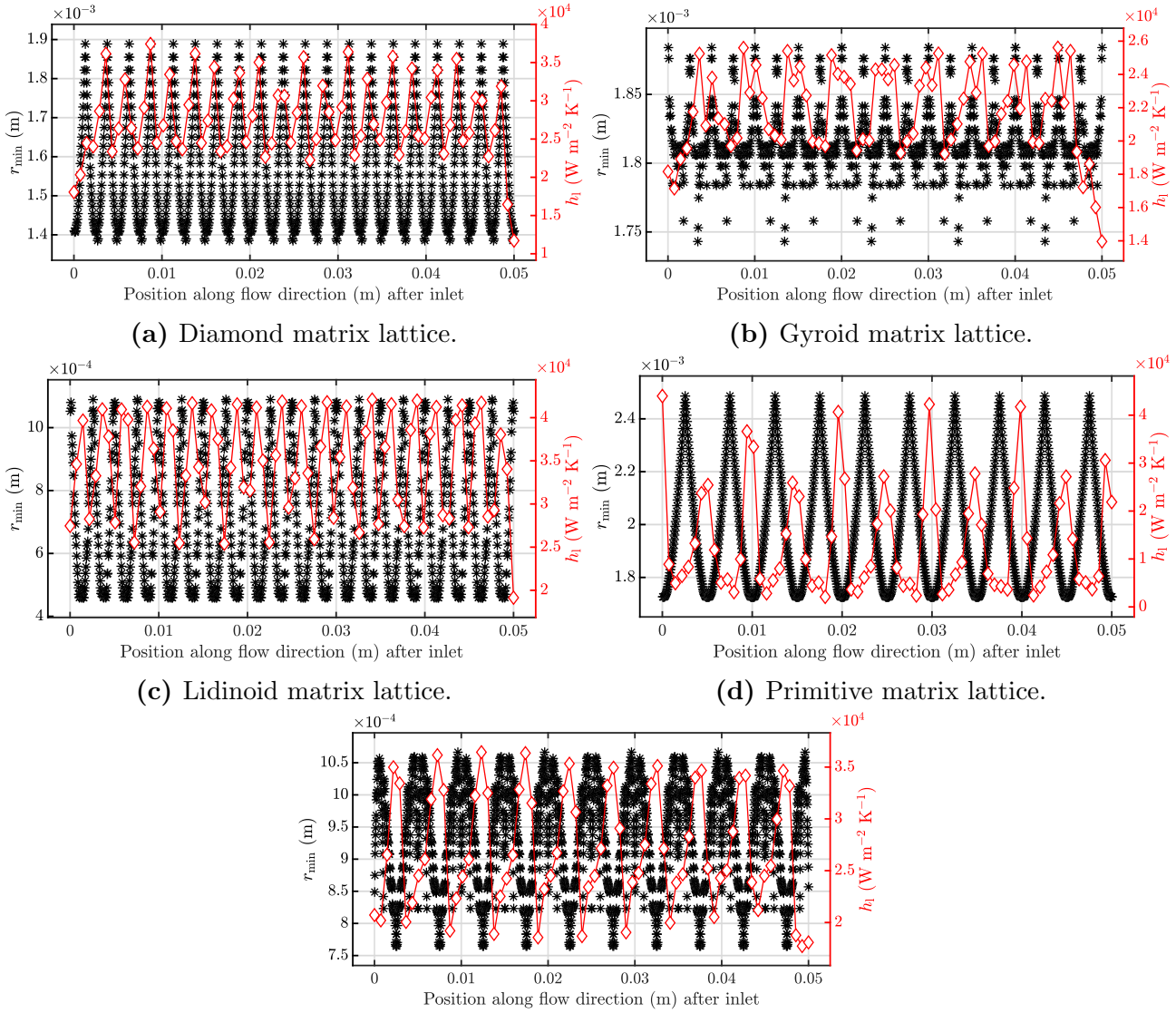

(a) Diamond matrix lattice.

(b) Gyroid matrix lattice.

(c) Lidinoid matrix lattice.

(d) Primitive matrix lattice.

(e) Split-p matrix lattice.

Figure 6.24: Evolution of local wall heat transfer coefficient and minimum channel radius within the examined structures (superficial fluid velocity = 5×10^{-3} m s^{-1}, volume fraction = 0.25).

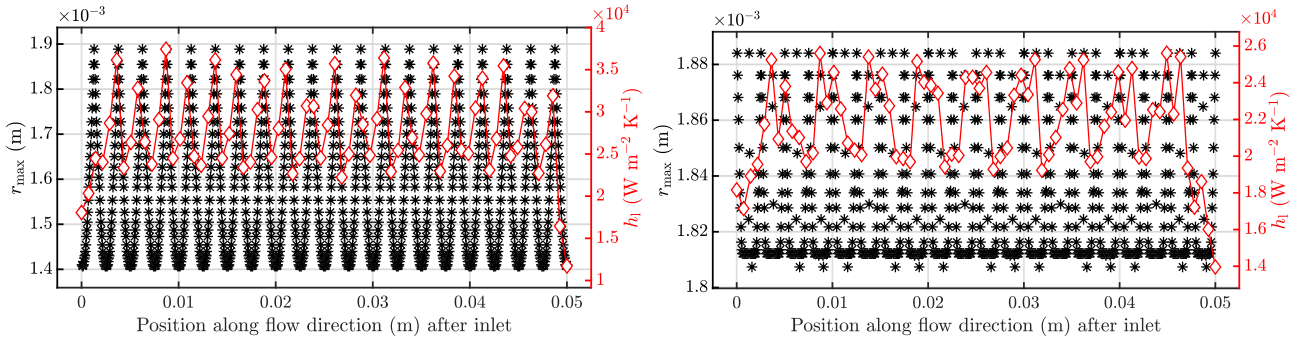

(a) Diamond matrix lattice.

(b) Gyroid matrix lattice.

Figure 6.25: Evolution of local wall heat transfer coefficient and maximum channel radius for selected TPMS-based lattice structures (superficial fluid velocity = 5×10^{-3} m s^{-1}, volume fraction = 0.25).

lattice structure exhibited peak local wall heat transfer coefficients when the channel was both at its largest and smallest. This may be because the geometry of a structure has a larger impact on the peak local wall heat transfer coefficient in cases where there is a small channel radii range.

Figure 6.26 presents the local average fluid velocity, u_l, and how the radius of the smallest channels evolves within the structure. It was observed that the local average fluid velocity in the gyroid, lidinoid and split-p matrix lattice structures tended to be larger at smaller channel radii and that the reverse was true for the diamond matrix lattice structure. One noticeable exception to this was the primitive matrix lattice structure which exhibited peak local wall heat transfer coefficients when the channel radius was relatively small, but peak local average fluid velocities when the channel radius was large. This was because, as the central channel expanded into the chamber, the volume of slow-moving fluid within it increased, shown in figure 5.10(d), and as it shrunk in to a small channel, the volume of slow-moving fluid outside the central channel increased. This significantly decreased the local average fluid velocity in these regions,

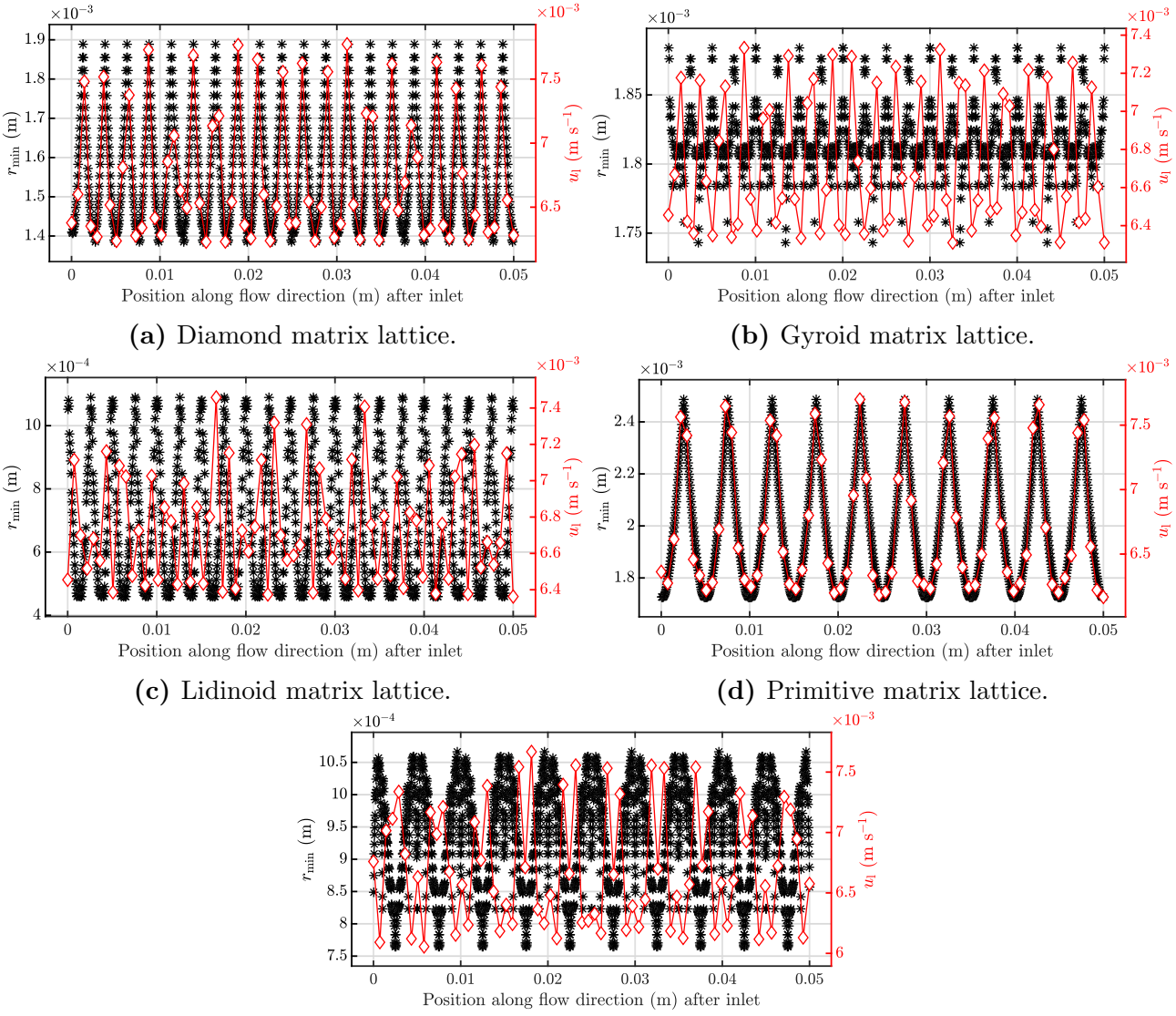

(a) Diamond matrix lattice.

(b) Gyroid matrix lattice.

(c) Lidinoid matrix lattice.

(d) Primitive matrix lattice.

(e) Split-p matrix lattice.

Figure 6.26: Evolution of local average fluid velocity and minimum channel radius within the examined structures (superficial fluid velocity = 5×10^{-3} m s^{-1}, volume fraction = 0.25).

meaning that the local average fluid velocity is not an accurate parameter to use in this case for the primitive matrix lattice structure. These results confirms our theory from section 5.3.2, where higher fluid velocities increases the local wall heat transfer coefficient and this is driven by smaller channel radii, in most cases, for the examined TPMS-based lattice structures.

Whilst a variety of tortuosity and channel radius properties can be used to determine either the thermal performance or local heat transfer coefficients for a given lattice cell type, they are not appropriate to determine the thermal performance across a range of different TPMS-based lattice structures as the geometry has a much larger impact on performance. This is because, while tortuosity and channel radii may be able to inform some of the fluid dynamics within a TPMS-based lattice structure, they can not be used to determine key fluid dynamics for thermal transport, such as vortices, or fluid-solid interactions.

6.5 Summary

Both tortuosity and channel radius exhibited a strong correlation with the hydraulic and thermal performance for a given lattice cell type, where lattices that were more tortuous and had smaller channel radii exhibited poorer hydraulic performances but better thermal performances. Locally varying channel radii also impacted the local fluid pressure and local wall heat transfer coefficient for a given TPMS-based lattice structure. Structures which had a large range of channel radii exhibited local discontinuous pressure drops if the channels reached their minimum radius infrequently. It was also found that the local fluid velocity inside the examined TPMS-based lattice structures increased when its channel radius was at a minimum, which lead to higher local wall heat transfer coefficients. There was an exception for the diamond matrix lattice however, as its tortuous paths impeded the fluid from travelling in the inlet plane normal direction. Here, the local wall heat transfer coefficient peaked when the channel radius was at a local maximum instead, where the fluid could travel in the inlet plane normal direction. In this case, the fluid velocity, and hence the local wall heat transfer coefficient, was determined by the orientation of the channels.

Tortuosity and channel radius are less significant when examining multiple different lattice cell types, however, and cannot be solely used to predict or characterise their performance. This was because the examined geometrical properties only represent an aspect of the geometry of TPMS-based lattice structures and, individually, do not provide sufficient information to determine the fluid dynamics which affect the hydraulic and thermal performance of the examined structures.

Chapter 7

TPMS-based Lattices in Fusion Relevant Conditions

7.1 Introduction

The fluid dynamics and thermal transport within TPMS-based lattice structures, at relatively low Reynolds numbers and temperatures, were examined in chapters 5 and 6. This work characterised the hydraulic and thermal performance of TPMS-based lattice structures in terms of their principal design parameters and determined the impact that different geometrical features have on their performance at relatively low heat fluxes and Reynolds numbers. These structures would be expected to perform under fusion-relevant conditions, such as higher Reynolds numbers and heat fluxes, if implemented into the divertor target geometry, however. These conditions may impact the fluid dynamics within TPMS-based lattice structures (e.g., turbulence) and have a large effect on their hydraulic and thermal performance.

Here, a selection of TPMS-based lattice structures were incorporated into structures exemplar of the geometries used in AMAZE, where their hydraulic and thermal performances were examined both numerically and experimentally under fusion-relevant conditions. Experimental parameters within HIVE's, a high heat flux testing facility, operational regime were determined numerically such that the examined structures would not suffer damage from high heat fluxes and fluid pressures. HIVE provided data which could quantify the behaviour of the examined structures under different fluid flow and heating conditions. This was also used to validate the numerical model and identify areas of improvement. Figure 7.1 shows the general work flow for the work presented in this chapter. This preliminary study will determine whether TPMS-based lattice structures should be considered as alternatives to conventional channels for thermal management

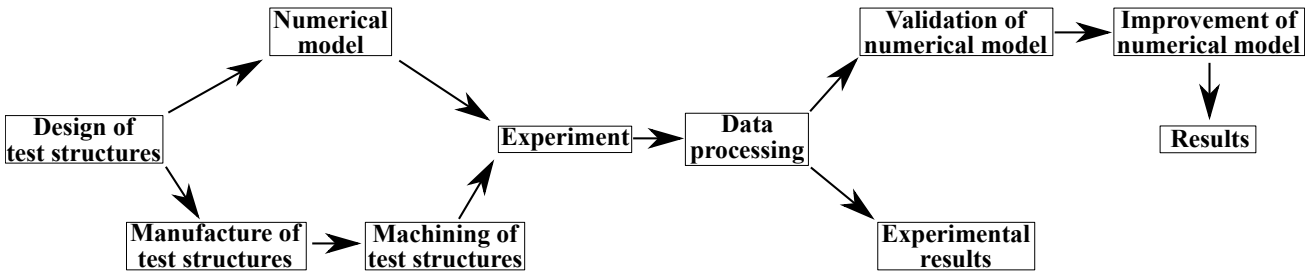

Figure 7.1: General work flow for the study of TPMS-based lattice structures in fusion relevant conditions.

in PFUs under fusion relevant conditions.

7.2 HIVE

7.2.1 Background

As discussed in section 3.4, novel concepts for the divertor target structure have been proposed to improve the performance of the divertor. These concepts must go through a qualification process, typically involving high heat flux testing using electron beam and ion beam facilities [141–144]. These facilities provide detailed data, but the scale of these experiments do not allow for a large number of experiments to be performed [145] and an alternative testing facility for early verification of concepts could prove useful.

HIVE [145] is a bespoke high heat flux testing facility, operated by UKAEA, and is used for early verification of mechanical, hydraulic and thermal performances of high heat flux components in a cost and time-effective manner. This facility consists of a vacuum vessel, an induction heating system, a coolant supply and a control computer, shown in figure 7.2. A schematic of the HIVE vacuum vessel is also shown in figure 7.3.

7.2.2 Equipment

The vacuum vessel has a diameter and height of 500 mm. The vessel is depressurised by a 240 l s^{-1} turbomolecular pump and can operate at a $2{\times}10^{-7}$ mbar. It has been designed and tested to a leak rate of less than 10^{-9} mbar l s^{-1} and rated for an absolute pressure of 2 bar, in the event of a sample failure or coolant leak. The interior of the vacuum vessel can be viewed through the available ports, which have optical and infrared (IR) transparent windows.

The lid of the vacuum vessel can be lifted and rested on to a support structure, shown in figure 7.4, where maintenance and assembly takes place. The cooling pipes, induction coil and test

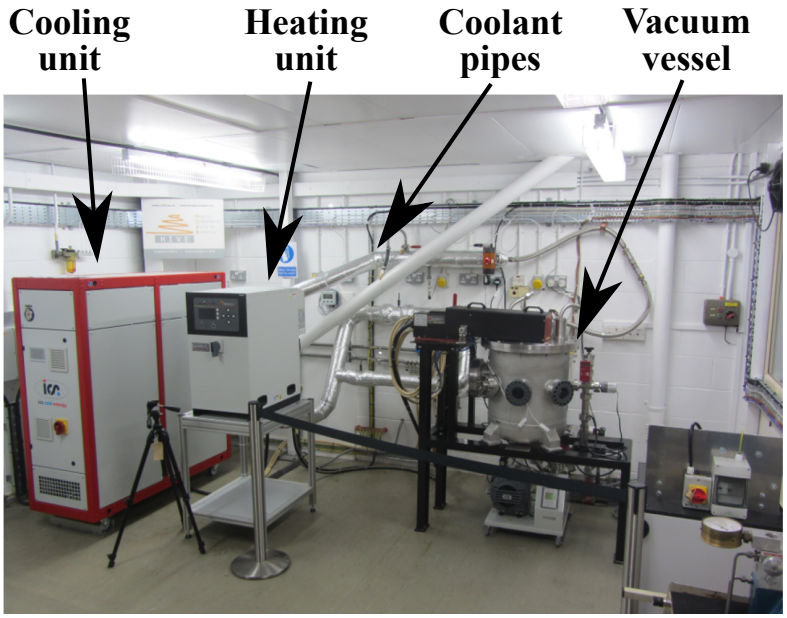

Figure 7.2: The HIVE facility. Modified from [145].

structures (via the cooling pipes) are attached to the vacuum vessel lid.

A 45 kW, 50−150 kHz induction heating system is used to heat the test structures. If a pancake coil arrangement is used, pictured in figure 7.4, a maximum power of approximately 8 kW is supplied to a test part through direct coupling, though the coupling efficiency for this coil arrangement is expected to be between 25%−30% due to the electromagnetic phenomena described below [146].

For induction heating, a time-varying magnetic field is generated by passing an alternating current through an induction coil. This field penetrates the test structure and, if it is a conductor, creates eddy currents inside of it. The eddy currents flow through the test structure and heat it via Joule heating.

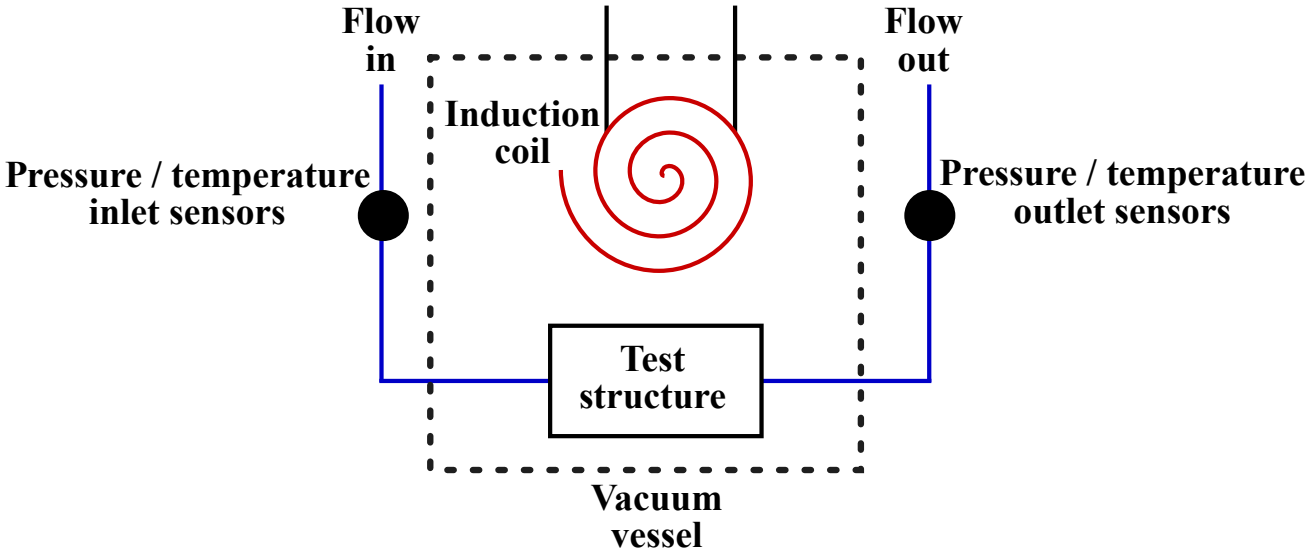

Figure 7.3: Schematic of the HIVE vacuum vessel.

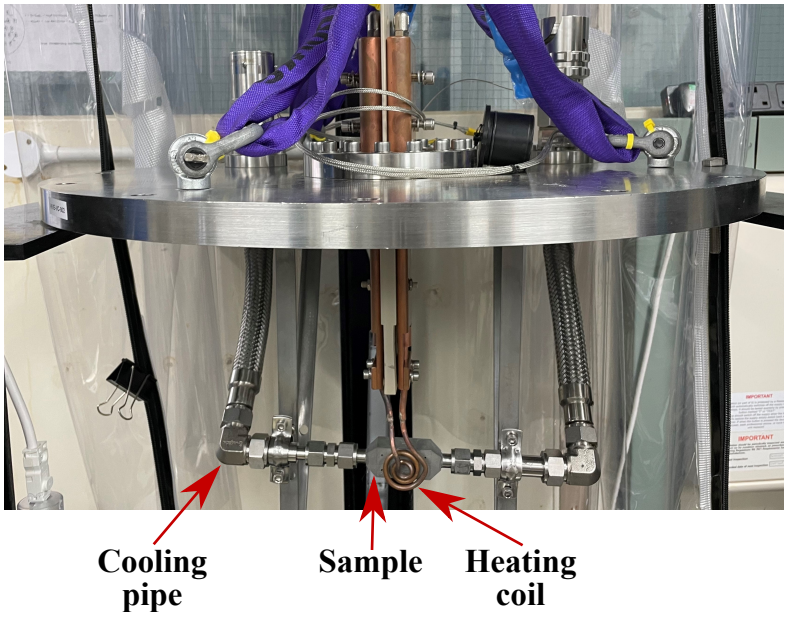

Figure 7.4: HIVE vacuum vessel lid.

There are multiple electromagnetic phenomena which significantly impact the induction heating of test structures within HIVE. Flinders *et al* [147] identified three key phenomena: edge effects, the skin effect and the proximity effect, which are described below.

The edge effect describes the distortions in the magnetic field at the edges of the test structure. This affects the current density distribution by tending the eddy currents towards the edges of the structure. This leads to greater heat fluxes at the edges and lower heat fluxes at the centre of the structure, where there is often a dead-spot. This is illustrated in figure 7.5.

Eddy currents generated on the surface of the test structure can also penetrate into the body. This provides a volumetric heat flux, instead of a surface heat flux, and is known as the skin effect.

Finally, the distance between the induction coil and the test structure affects the transfer of current density and is known as the proximity effect. This distance needs to be accurately set as it has an impact on both the coupling efficiency and the surface heat flux distribution of the test structure.

Water can be pumped into the system to cool the test structures at up to 80 l min^{-1}, with pressures ranging from ambient conditions to 20 bar, and is controlled manually using a combination of in-line and bypass valves. The temperature of the coolant, controlled by a closed-loop temperature control unit and an external 20 kW chiller, can range from ambient conditions to 200 °C.

HIVE is operated through a custom LabView graphical user interface on a nearby computer. This interface controls all of the digital and analogue inputs and control signals in a local cubicle, which has control over the heating, cooling and vacuum systems.

Transducers are placed in-line and outside of the vacuum vessel lid to measure coolant inlet and outlet flow rate, pressure and temperature. K-type thermocouples are percussion welded into drilled holes in the test structures to find the temperature of the structure. This is supplemented by IR thermography of the heated surface using a FLIR SC7000 camera and the FLIR Research Studio software to analyse the data. The power and frequency supplied to the induction coil is recorded by the induction heating system itself. A combination of pirani and inverted magnetron wide range gauges, for pressure measurement, and an external residual gas analyser, to determine the elemental makeup of the gas inside the vessel.

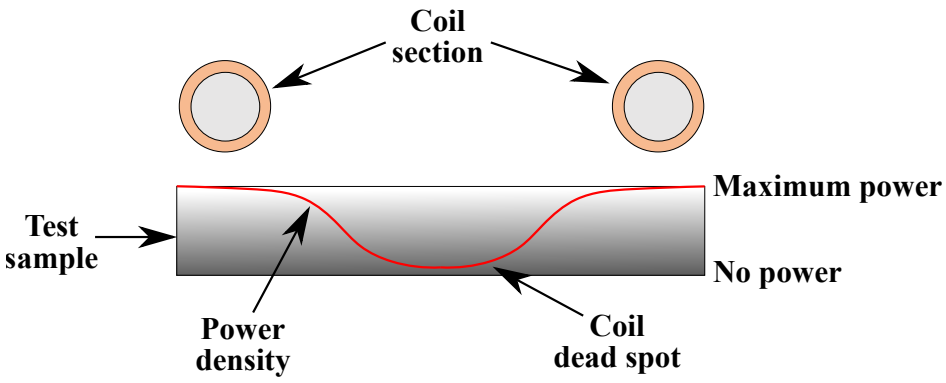

Figure 7.5: Illustration of the edge effect in induction heating.

7.3 Test structures

7.3.1 Design

The test structures used in this study were initially based on structures used for HIVE commissioning and AMAZE testing [145], which consisted of a copper block brazed to a tungsten tile and a copper pipe. This ensured that the examined structures were compatible with HIVE. The CAD model and dimensions for a conventional HIVE test structure is given in figure 7.6.

Four different structures were designed, manufactured and tested. They were identified as E-029-01, E-029-02, E-029-03 and E-029-04. These structures possessed similar external geometries, where the CAD model for the E-029-02 structure is shown in figure 7.7, with a total dimensions of 30 × 130 × 25 mm.

The different geometries used for the internal structures are shown in figure 7.8. The E-029-01

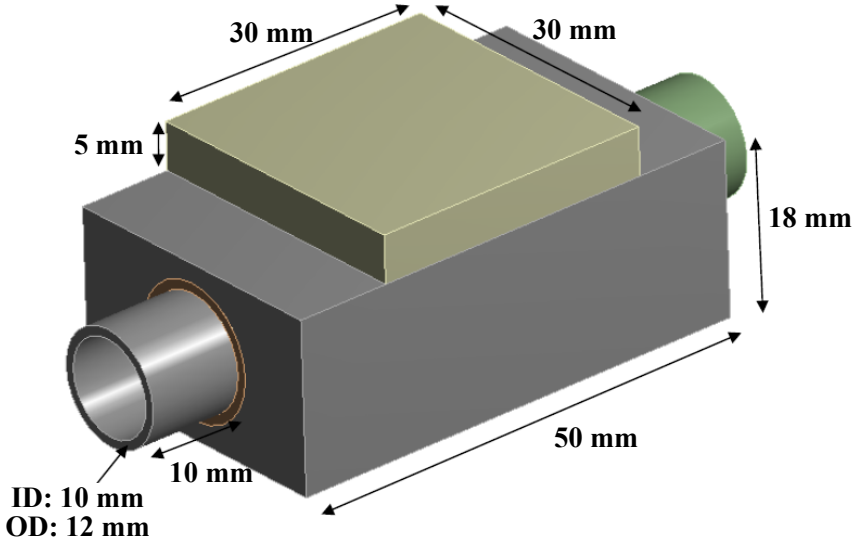

Figure 7.6: An example HIVE structure.

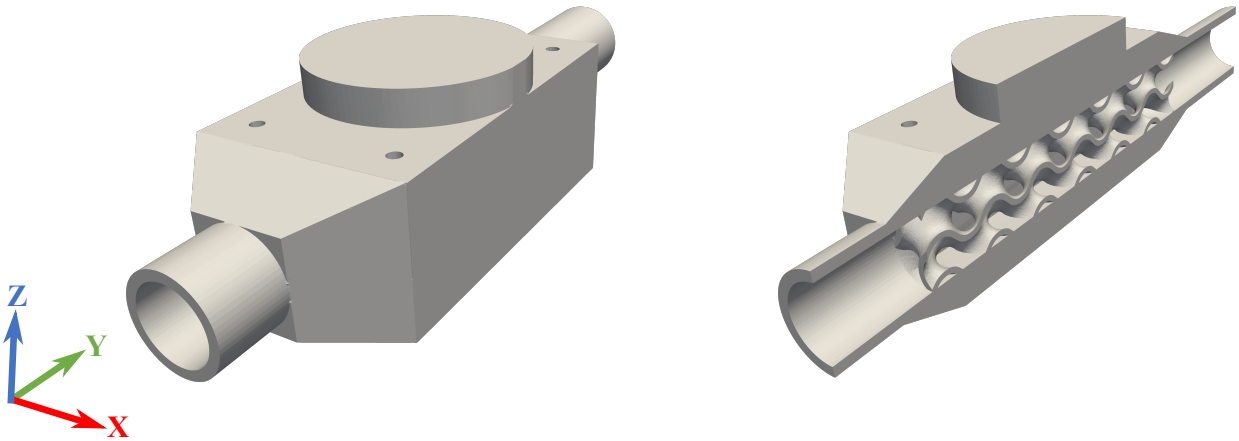

(a) External structure. **(b)** Internal structure.

Figure 7.7: HIVE E-029-02 CAD model.

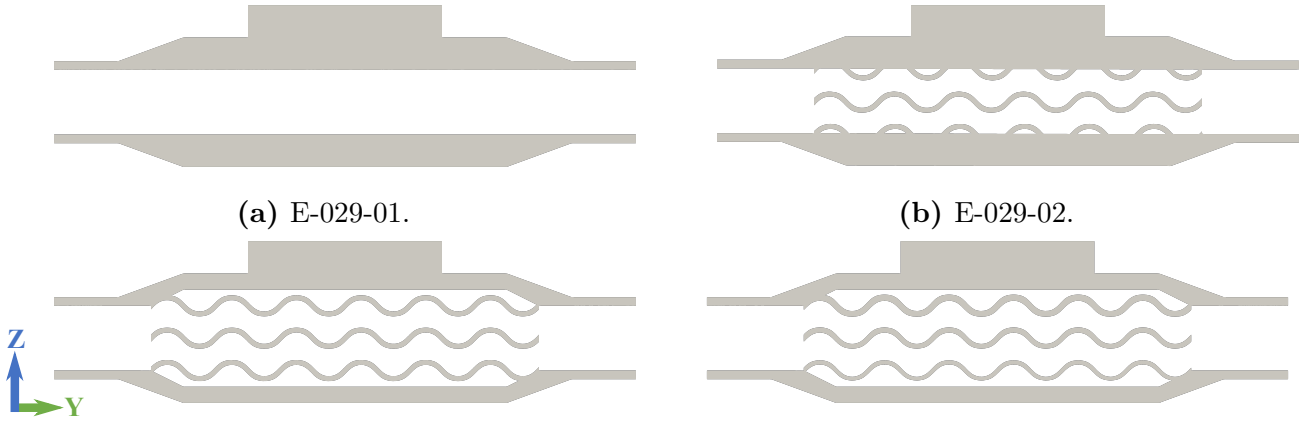

(a) E-029-01. **(b)** E-029-02.

(c) E-029-03. **(d)** E-029-04.

Figure 7.8: Internal geometry of HIVE E-029 structures, cross-sectioned at x=0.015 m.

structure featured a circular channel with an inner diameter of 10 mm. This is equivalent to a volume fraction of 0.215 when considering a design volume of 10 × 60 × 10 mm. The E-029-02 structure featured a 10 × 60 × 10 mm gyroid matrix lattice, an example of this lattice cell type is shown in figure 5.1(b), with 1 × 6 × 1 cells, with a volume fraction of 0.215. This ensured that both the E-029-01 and E-029-02 structures had the same fluid volume. The E-029-03 structure featured a 25 × 60 × 15 mm gyroid matrix lattice with 2.5 × 6 × 1.5 cells and a volume fraction of 0.215. The E-029-04 structure featured a similar geometry, but with a linear-graded volume fraction increasing in the z-direction from 0.15 to 0.28 so that the average volume fraction of the lattice was 0.215. The circular channel was designed using AutoCAD and the TPMS-based lattice structures were designed using FLatt Pack. The gyroid matrix lattice structures were used here because they had adequate hydraulic and thermal performances, discussed in chapter 5, from the examined selection of TPMS-based lattice structures.

The E-029-01 and E-029-02 structures were designed to have equivalent fluid volumes and design spaces so that their performances could be compared against each other. The gyroid matrix lattice occupied a larger design space within the E-029-03 structure to determine how this would impact the performance of high heat flux components. The same cell aspect ratios and volume fractions were used in E-029-02 and E-029-03 so that they could be examined against each other. E-029-04 featured a linear-graded volume fraction such that its impact on performance could be determined via a direct comparison with E-029-03, which has a constant volume fraction.

Externally, these test structures featured 30 mm long inlet and outlet pipes, with inner and outer diameters of 10 mm and 12.7 mm respectively. The main body had cuboid dimensions of 30 × 70 × 20 mm with a 5 mm tall, 30 mm diameter circular tile on top of the main body. Due to the different internal geometries present within the E-029 structures, the CAD models of the external structures were slightly different to each other. The schematics of the CAD models are given in figures 7.9 and 7.10. The CAD models of the pipes and main body were produced separately on AutoCAD and then merged together to form the external structure, before being exported into an STL file format. The interior geometries (i.e., channel and lattice structures) were then incorporated into the external geometry using Materialise Magics.

There were significant differences between the structures designed here and the example HIVE test structure shown in figure 7.6. The most prominent being the use of a circular tile instead

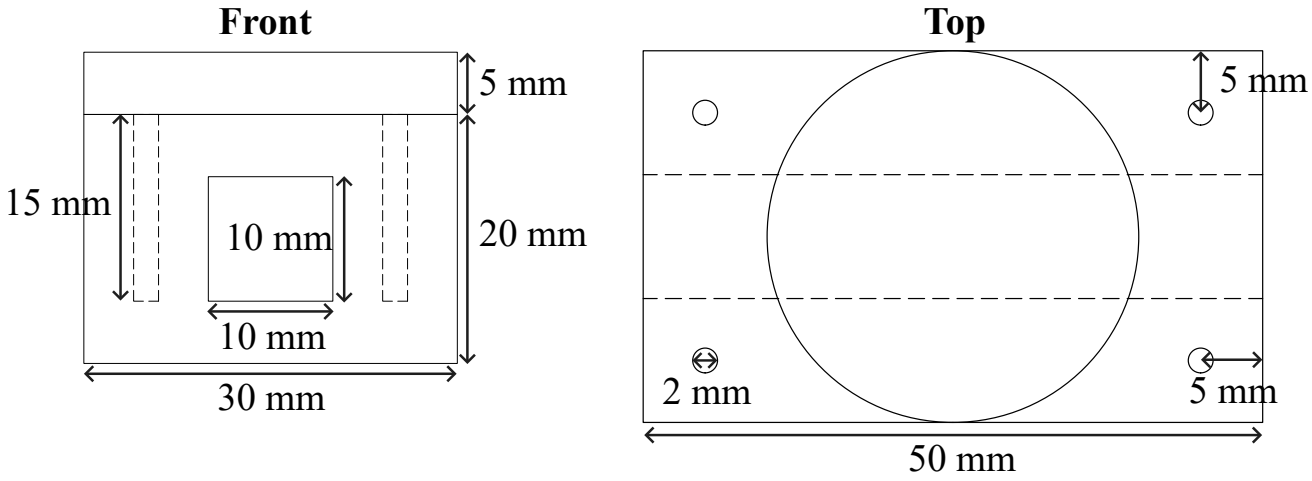

(a) E-029-01 and E-029-02.

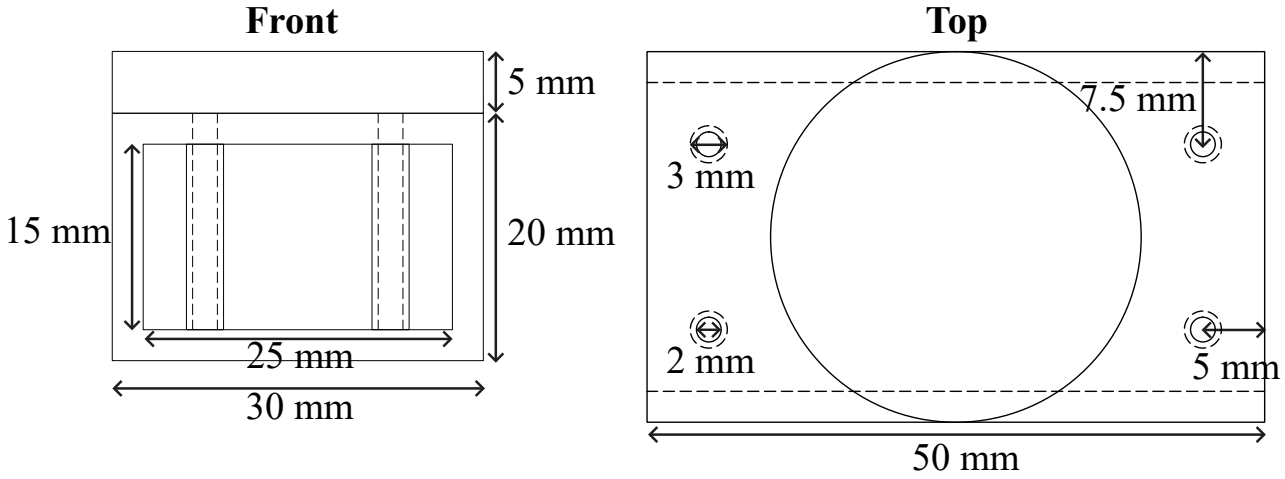

(b) E-029-03 and E-029-04.

Figure 7.9: Engineering drawings of the CAD model of the main body of the E-029 structures.

of a rectangular tile. Due to the electromagnetic edge effect, the induction coil will provide a higher heat flux to the edge of the tile. This effect is more pronounced on the corners of the rectangular tile, where two edges meet. Implementing a circular tile therefore improves the uniformity of the incident heat flux due to there being only a single, constant edge. An additional length of 20 mm was added to the pipes such that they could be compression fitted to Swagelok fittings. Four 2 mm diameter holes were also designed into each test structure, where K-type thermocouples could be percussion welded to the bottom of the structures. Finally, where the example HIVE test structure featured multiple parts and different materials brazed together, the test structures designed here will all be manufactured as a single part. This simplifies the manufacturing process, keeps the thermal conductivity (and other properties) within the test structures consistent and removes the need for metal-joining processes.

7.3.2 Manufacture and machining

These structures were additively manufactured at the University of Nottingham using the Renishaw AM 250 LPBF machine, where the process parameters were provided by Renishaw, and Inconel-718 powder. This material was chosen because it has been used in heat sinks in the aerospace industry [20] and extensively researched at the University of Nottingham [148–151].

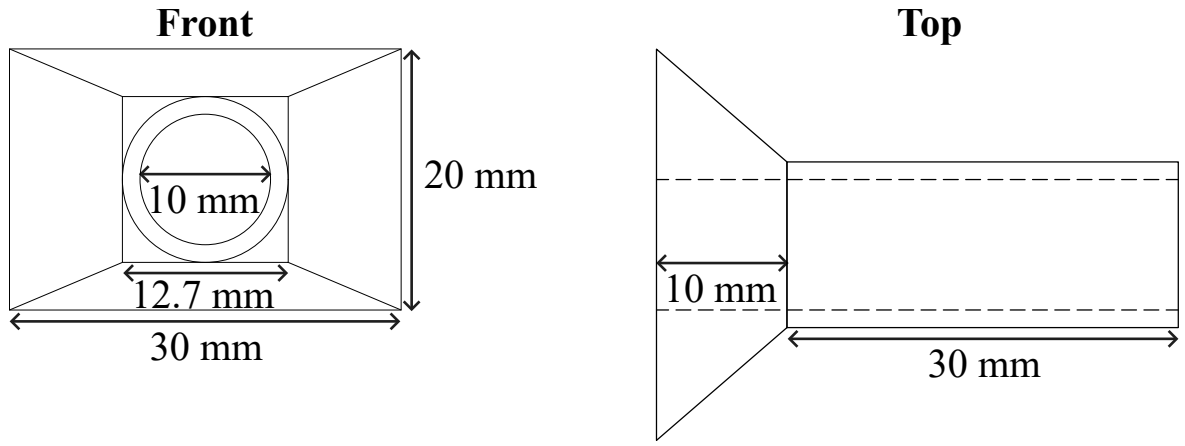

(a) E-029-01.

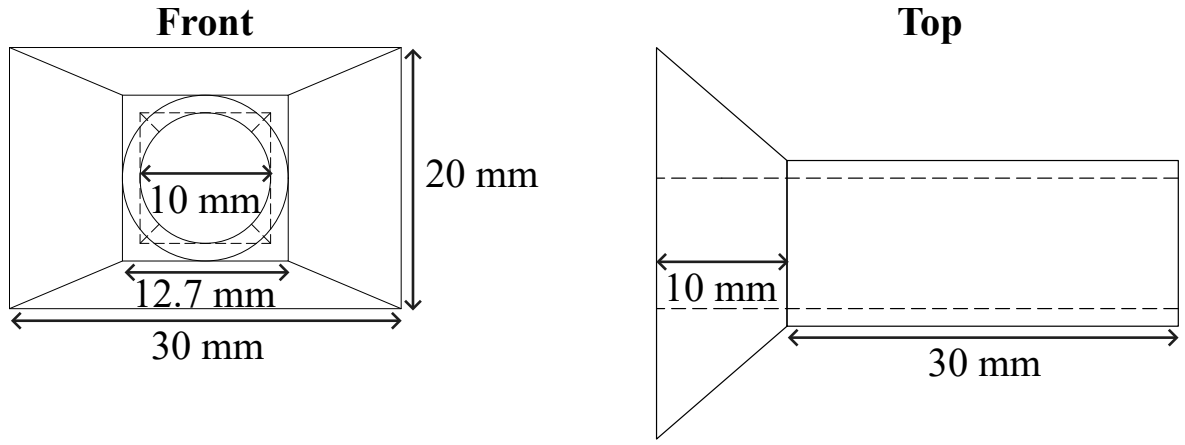

(b) E-029-02.

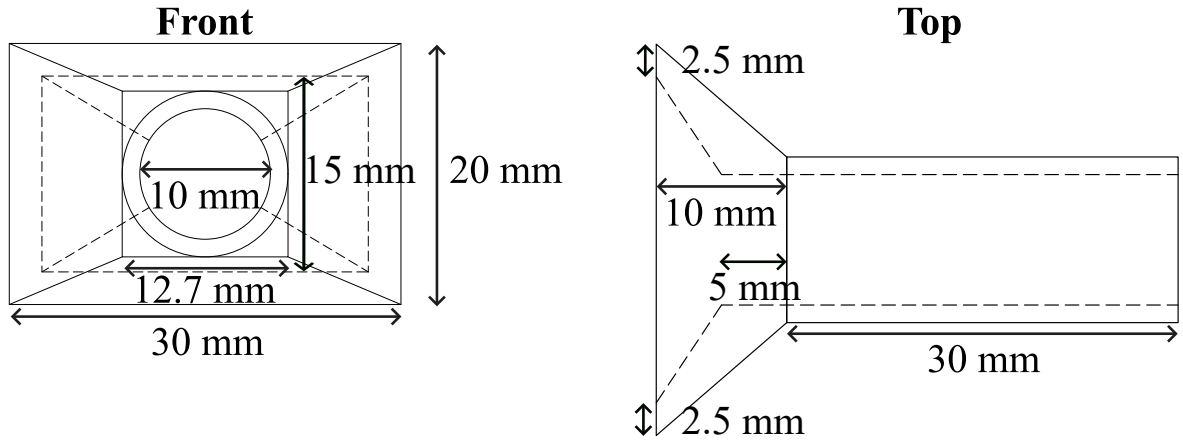

(c) E-029-03 and E-029-04.

Figure 7.10: Engineering drawings of the CAD model of the pipes of the E-029 structures.

An initial test build was first performed to ensure that the test structures were manufacturable and fully-dense (i.e., free of significant porosity). This was done by manufacturing representative sub-volumes of the four test structures, with different orientations and support structures, and $10 \times 10 \times 10$ mm sample cubes. The test structures were successfully manufactured and are shown in figure 7.11. The circled lattice structures in figure 7.11 experienced some deformation at the bottom of the structure due to the lack of support structures. There was also discolouration in the vertically manufactured pipes, possibly due to overheating from the laser (which leads to oxygen pickup). The density of the material was determined by sectioning, mounting and polishing the sample cube. A Nikon optical microscope was used to examine the surface of the polished cube, shown in figure 7.12, and to calculate the area of porous holes. It was found that the sample cube possessed a density of 99.6%.

The pipe CAD models were modified, shown in figure 7.13, because the compression fitting required that

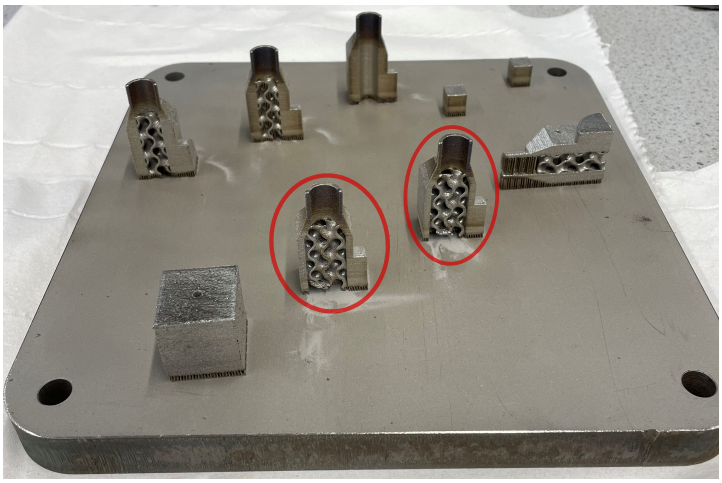

Figure 7.11: Test build for the E-029 structures. The circled parts experienced deformation.

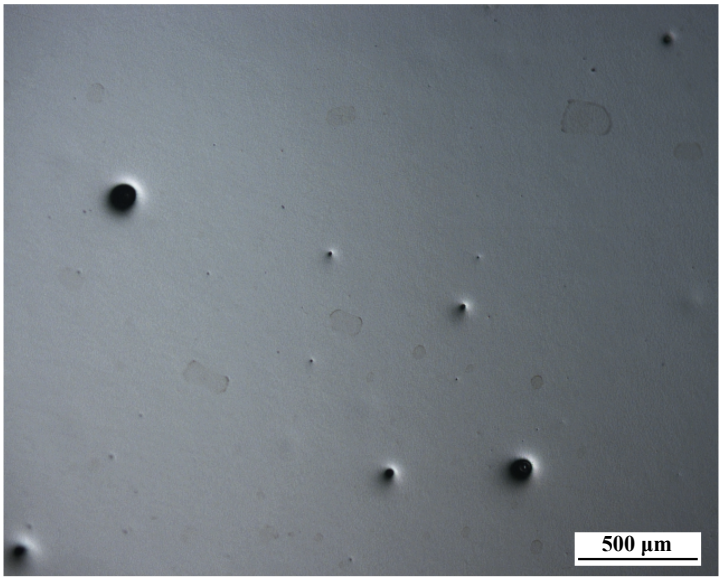

Figure 7.12: Optical microscopy of the polished sample cube from the initial test build.

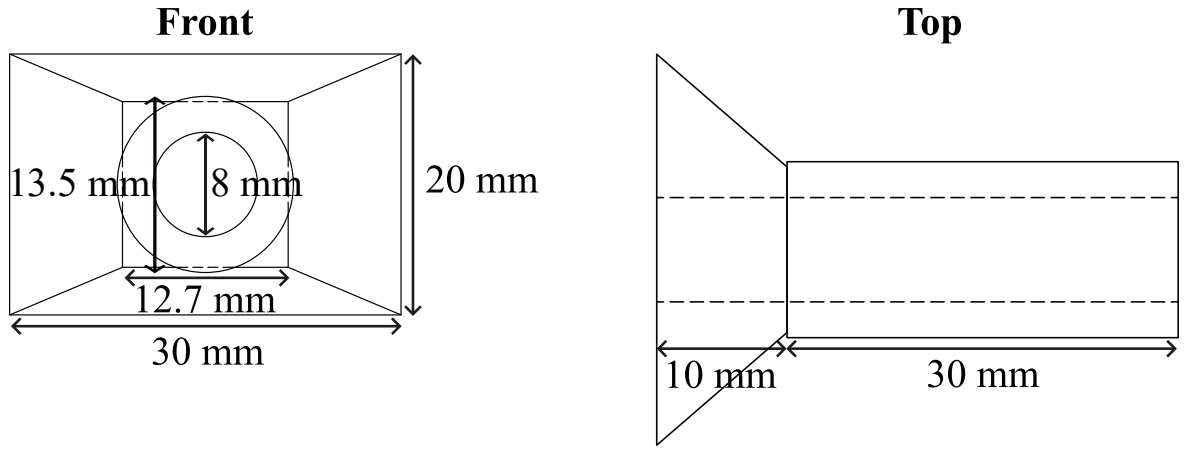

(a) E-029-01.

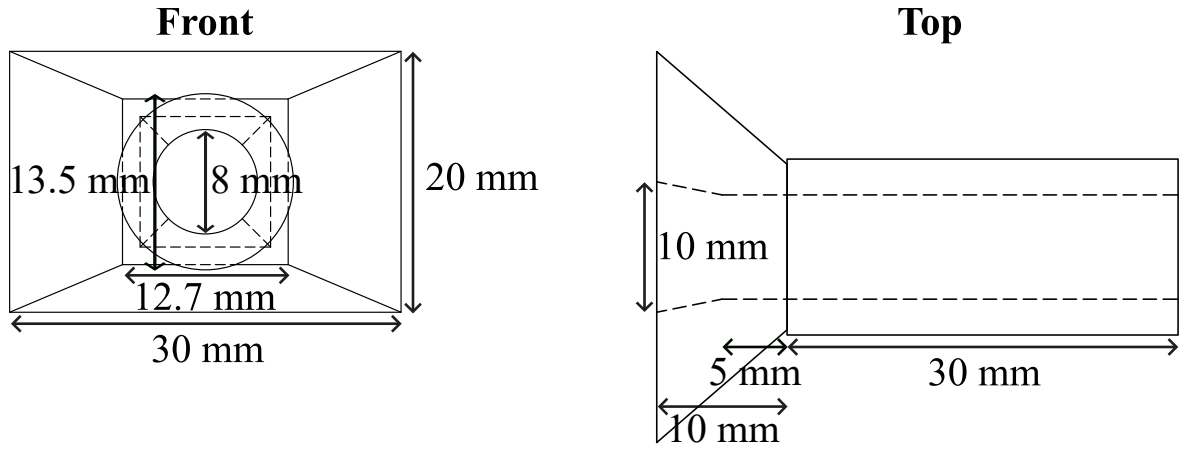

(b) E-029-02.

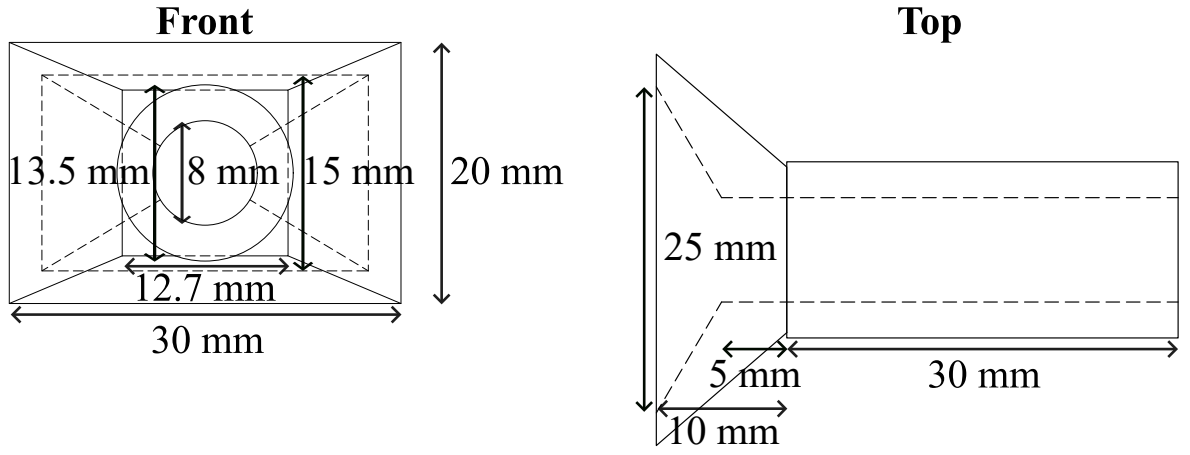

(c) E-029-03 and E-029-04.

Figure 7.13: Engineering drawings of the modified CAD model of the pipes of the E-029 structures.

- the pipes have an outer diameter of 12.7 ± 0.08 mm and a wall thickness of at least 1.3 mm.
- the pipe outer surface is circular.
- there are no scratches on the pipe surface.

The wall thickness of the pipes was therefore increased. The pipes could then be machined to the above specifications to negate the effect that surface roughness and warping could have on the fitting process. The structures were successfully manufactured, shown in figure 7.14. Warping in the pipes, particularly near the ends, is shown in figure 7.15 as the support structures detached from the pipe due to build up of stress.

The structures on the build plate were post-processed to prevent potential further warping when removing them from the build plate due to the high residual stresses. The structures were heat treated via solution annealing, using a process guided by the existing literature on the LPBF of Inconel [152–155], to reduce the residual stresses in the structures. The build plate was placed in a furnace and heated to 1,050 °C for 6 hours in air, cooled to 500 °C over a period of 1.4 hours and then air quenched at room temperature.

The structures were removed from the build plate using wire-cut electrical discharge machining. The pipes were then milled in accordance with the original CAD models, see figure 7.10, and

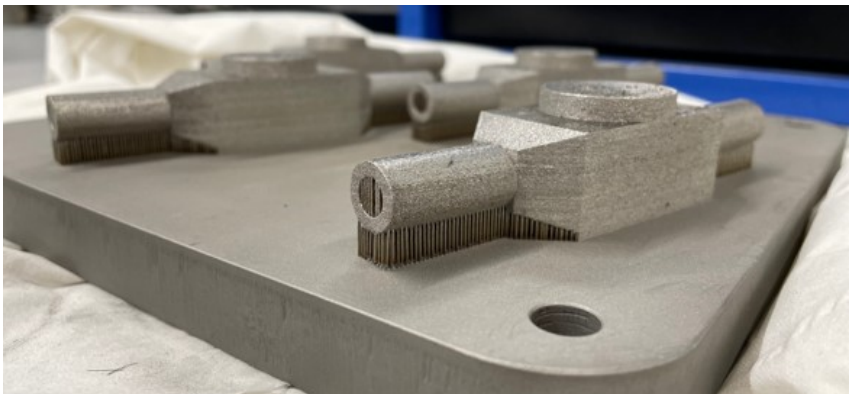

Figure 7.14: The manufactured E-029 structures.

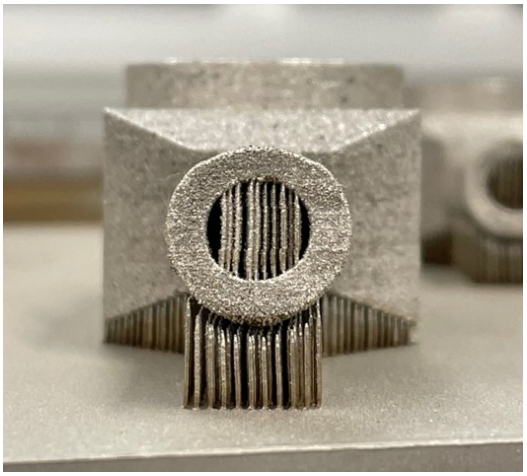

Figure 7.15: Warping and detached support structures near the end of the pipe.

the aforementioned compression fitting specifications. Due to warping in the pipes, the outer surface was prioritised during the machining process to ensure that it would meet the fitting specifications. This lead to the inner pipe surface not being circular, walls with relatively small thicknesses and, in some cases, rough surface features near the end of the pipe. An example of this is shown in figure 7.16. The structures were sandblasted to remove contaminants from the machining process and to smooth the surfaces of the structures. The post-machined and sandblasted structures are shown in figure 7.17.

These structures were fitted with Swagelok fittings by UKAEA, successfully pressure tested up to 10 bar and deemed suitable for testing in HIVE. K-type thermocouples were not used in this study due to practical difficulties with the welding process. All of the thermal data for the structures examined in HIVE will therefore come from the IR camera.

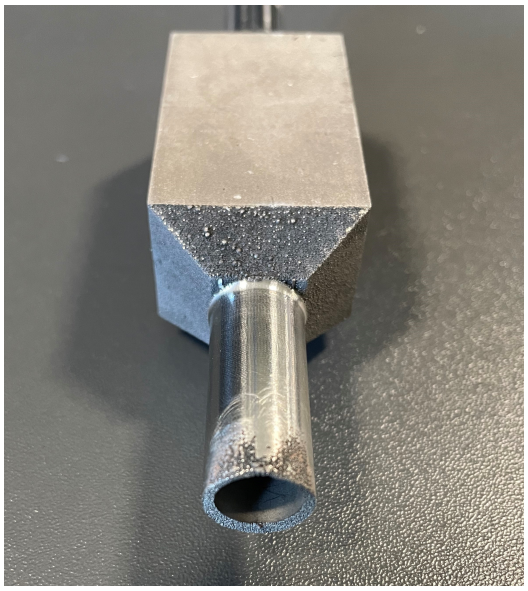

Figure 7.16: Example of non-circular inner pipe walls, small pipe wall thicknesses and rough outer pipe walls for a post-machined E-029 structure.

Figure 7.17: Post-machined E-029 structures.

7.4 Numerical model

7.4.1 Method

The structures discussed in section 7.3 were modelled in OpenFOAM to determine both their performance and the initial experimental parameters (e.g., flow rate and incident power) so that they would not suffer damage due to high fluid pressures or temperatures. Hydraulic performance was determined by examining pressure drop, as in chapter 5, whereas the thermal performance was determined by examining the tile surface temperature (i.e., the surface being heated) instead of outlet fluid temperature. This is because the power incident surface of divertor target components can be significantly damaged (i.e., melting) from high heat fluxes and it was deemed important to understand this effect. The structures used here were based from the original CAD models (see figures 7.9 and 7.10), but with an inlet and outlet pipe length of 10 mm and 20 mm, respectively, to improve computational performance.

The computational domain had cuboid dimensions of 30 × 100 × 25 mm. The schematics of the computational model for the E-029-01 structure are provided in figure 7.18. The properties of the computational domains can be seen in table 7.1. The *chtMultiRegionSimpleFoam* solver

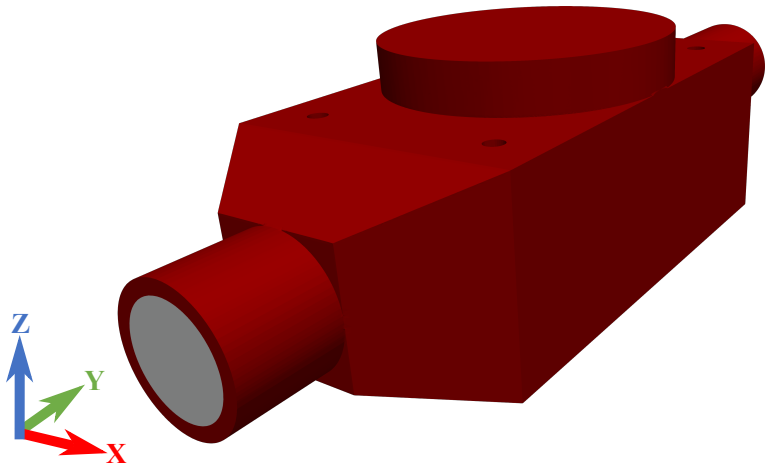

(a) Three-dimensional view of the computational solid domain (red) and fluid domain (grey).

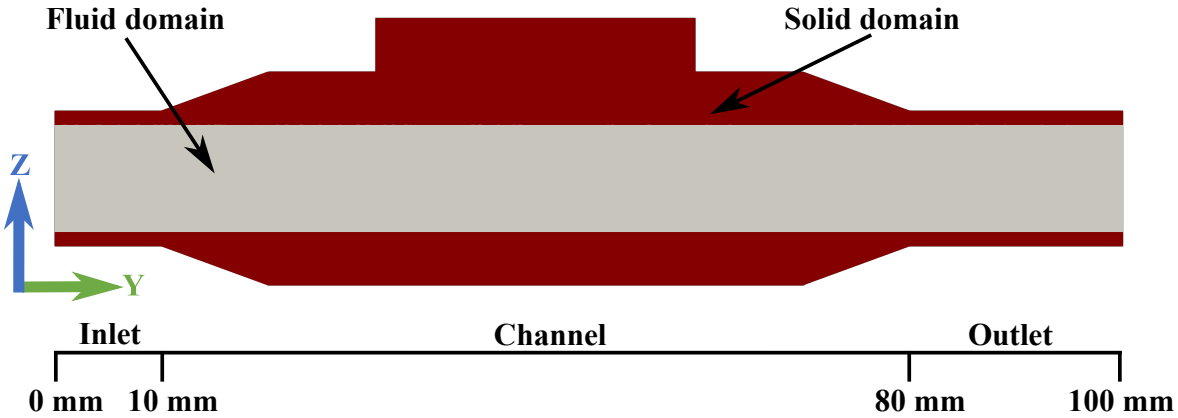

(b) Cross-sectional view of the fluid domain (grey) and solid domain (red).

Figure 7.18: Schematics for the computational domain of the E-029-01 structure.

Computational domain	Medium	Density (kg m^{-3})	Kinematic viscosity (m^2 s^{-1})	Specific heat capacity (J kg^{-1} K^{-1})	Thermal conductivity (W m^{-1} K^{-1})
Solid	Inconel-718	8,190		435	11.4
Fluid	Water (incompressible)	1,000	8.9×10^{-7}	4,180	0.532

Table 7.1: Material properties for the computational domains in the HIVE model.

	Boundary conditions			
Boundary	Velocity, u (m s^{-1})	Pressure, P (Pa)	Fluid temperature, T_f (K)	Lattice temperature, T_l (K)
Inlet	$u = u_\mathrm{ref}$	Adjust $\boldsymbol{\nabla} P$ to match flux with velocity	$T_\mathrm{f} = 293$	
Outlet	$\boldsymbol{\nabla} u = 0$	$P = 0$	$\boldsymbol{\nabla} T_\mathrm{f} = 0$	
Fluid-solid boundary	$u = 0$	Adjust $\boldsymbol{\nabla} P$ to match flux with velocity	$T_\mathrm{f} = T_\mathrm{l,adj}$, $\boldsymbol{\nabla} T_\mathrm{f} = 0$	$T_\mathrm{l} = T_\mathrm{f,adj}$, $\boldsymbol{\nabla} T_\mathrm{l} = 0$
Tile surface				Adjusts T_l by a user specified heat flux

Table 7.2: Boundary conditions for the non-turbulence parameters in the HIVE model. Here, the subscript 'ref' refers to a user-specified value and the subscript 'adj' refers to an adjacent face in a different domain.

was used to model the heat transfer between the two domains.

The boundary conditions used in this study are given in table 7.2. The fluid was modelled travelling in the y-direction with inlet fluid velocities of $0.21 - 8.49$ m s^{-1}, corresponding to inlet Reynolds numbers of $2{,}362 - 94{,}942$, and an inlet temperature of 293 K. A fully-developed inlet fluid velocity profile was implemented using C++. The inlet turbulent fluid velocity profile was of the form [156]

$$u_i = u_\mathrm{max} \left(1 - \frac{{r_i}^2}{r^2}\right)^{\frac{1}{n}} , \tag{7.1}$$

where u_i was the fluid velocity on the mesh element i, u_max was the maximum fluid velocity of the profile, r_i was the radial distance from the centre of the channel to the mesh element i, r was the radius of the channel and n was an exponent which was calculated from

$$n = 0.77 \ln (Re) - 3.47 . \tag{7.2}$$

The effective fluid velocity of this profile, u_eff, can be used instead of the maximum fluid velocity and was calculated from

$$u_\mathrm{eff} = \frac{n}{n+1} u_\mathrm{max} . \tag{7.3}$$

The solid domain was modelled with uniform effective powers of $250 - 1{,}000$ W incident on the

Boundary	Boundary conditions		
	Kinetic energy, k (m^2 s^{-2})	Specific dissipation rate, ω (s^{-1})	Viscosity, ν (m^2 s^{-1})
Inlet	$\nabla k = 0$	$\nabla \omega = 0$	
Outlet	$\nabla k = 0$	$\nabla \omega = 0$	
Fluid-solid boundary	Constrains k for low-Re and high-Re turbulence models	Constrains ω for low-Re and high-Re turbulence models	Constrains ν based on k and modifies the wall roughness parameter

Table 7.3: Boundary conditions for the turbulence parameters in the HIVE model.

tile surface. The thermal energy would then transfer across the solid and fluid domains from the tile.

The transition region between laminar and turbulent flow exists between $2{,}000 < Re < 4{,}000$ for circular channels [123] and $10 < Re < 2{,}000$ for porous structures [124]. This indicated that, for the examined velocity range in this study, the fluid was turbulent and that a turbulence model was needed. RANS was used instead of DNS and LES to reduce computational costs.

Multiple RANS turbulence models exist, such as the k-ϵ model which is well-researched and validated for external flows [157]. It is not accurate for internal flows, however. The k-ω model has improved accuracy for internal flows compared to the k-ϵ model, but is very sensitive to the inlet free-stream conditions [157]. The k-ω-SST model adopts a k-ω treatment inside the boundary layer (or near-wall region) and a k-ϵ treatment in the free-stream region [158]. This model is generally used for internal flows and minimises the problems found in both the k-ϵ and k-ω turbulence models [85]. The boundary conditions used for the RANS turbulence model are given in table 7.3.

The fluid-solid boundary was modelled as a smooth interface (i.e., sand-grain roughness = 0). Whilst the inner pipe walls in the E-029-01 structure were smooth from the machining process, the walls of the TPMS-based lattice structures within the E-029-02, E-029-03 and E-029-04 structures were expected to be rough due to the manufacturing process. The arithmetic average roughness of the walls was unknown for these structures and a smooth wall was assumed for the numerical model instead.

7.4.2 Validation of the numerical model

The analytical friction factor was compared against the results from the k-ω-SST and k-ϵ turbulence models via a mesh convergence study to confirm whether the k-ω-SST turbulence model was appropriate for this case. The friction factor is a parameter that relates the pressure drop due to friction along a channel and can be calculated experimentally for incompressible fluids from the Darcy-Weisbach equation [134]

$$f_{\mathrm{D}} = \frac{\Delta P}{\Delta L} \frac{2}{\rho} \frac{D_{\mathrm{h}}}{{u_{\mathrm{in}}}^2}, \tag{7.4}$$

where f_D is the Darcy friction factor and u_{in} is the inlet fluid velocity. For laminar flow through a circular channel, the friction factor is given analytically by [134]

$$f_D = \frac{64}{Re}\,. \tag{7.5}$$

The analytical friction factor for turbulent flow through a circular channel is given by the Colebrooke-White equation [159, 160]

$$\frac{1}{\sqrt{f_D}} = -2\log\left(\frac{\epsilon}{3.7\,D_h} + \frac{2.51}{Re\sqrt{f_D}}\right)\,, \tag{7.6}$$

where ϵ/D_h is the wall relative roughness. The mesh convergence study was only performed for the E-029-01 structure, with an inlet fluid velocity of 14.8 m s^{-1}, as analytical relationships for the friction factor do not exist for TPMS-based lattice structures. It was also assumed that the fluid-solid boundary was smooth (i.e., $\epsilon/D_h = 0$ in equation 7.6). Figure 7.19 showed that, once a suitable mesh element density was reached, the k-ϵ model gave a friction factor that was 128% larger than the analytical value while the k-ω-SST model gave a friction factor that was equal to the analytical value. The k-ω-SST turbulence model was therefore used throughout this study. Information regarding the mesh in the near wall region is provided in figure 7.19, which gives the relevant mean n^+ (discussed in appendix B.5) for each of the examined turbulence models.

A mesh convergence study was also performed to determine a suitable mesh element density for both accurate fluid flow and conjugate heat transfer calculations in the examined structures and is shown in figure 7.20. Convergence, for this study, was defined as when the recorded values varied by a maximum of 5% when the mesh was doubled. It was observed that the pressure drop and maximum tile surface temperature were well converged at 1.9×10^6 elements for the E-029-01 structure with an inlet fluid velocity of 14.8 m s^{-1} and incident effective power of 707 W. Similar results were also seen for the E-029-02 and E-029-03 structures, where the pressure drop and maximum tile surface temperature were well converged at 1.7×10^6 and 2.1×10^6 elements respectively. Figure 7.21 also gives the relevant mean n^+ for each of the examined turbulence models. Similar meshes were therefore used for each structure in this study. Figure 7.22 shows an unstructured mesh with refined polyhedral elements at the fluid-solid boundary and hexahedral elements elsewhere for the E-029-01 and E-029-02 structures, with the former also featuring prism layers at the fluid-solid boundary.

The E-029-01 structure was further validated by comparing the friction factor calculated from the numerical model to the analytical results, calculated from equations 7.5 and 7.6, over a range of Reynolds numbers. Figure 7.23 shows that the numerical model gave friction factors within 14% of the analytical values when ignoring the data point in the laminar-turbulent transition region. An interesting effect is observed where the numerical friction factor reaches a local minima and then increases with increasing Reynolds number. This is likely due to changes in the viscous sublayer of the fluid (discussed in appendix B.5), which could not be fully resolved by a mesh optimised for an inlet fluid velocity of 14.8 m s^{-1}. For future work, care must be taken in generating optimised meshes when a large range of turbulent flow rates are examined.

7.4.3 Results

Pressure drop across the examined structures are shown in figure 7.24. It was observed that the pressure drop exhibited by the modelled structures increased non-linearly in accordance with

$$|\Delta P| = G\,u_{in} + H\,{u_{in}}^2\,, \tag{7.7}$$

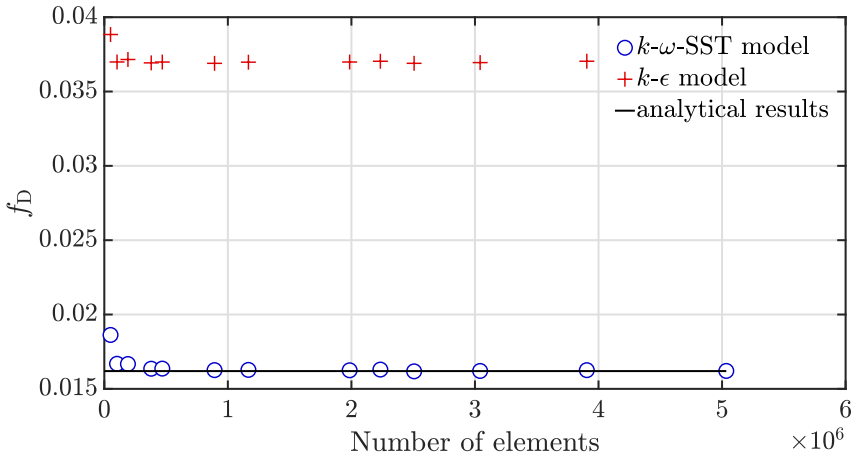

(a) Friction factor against the number of mesh elements.

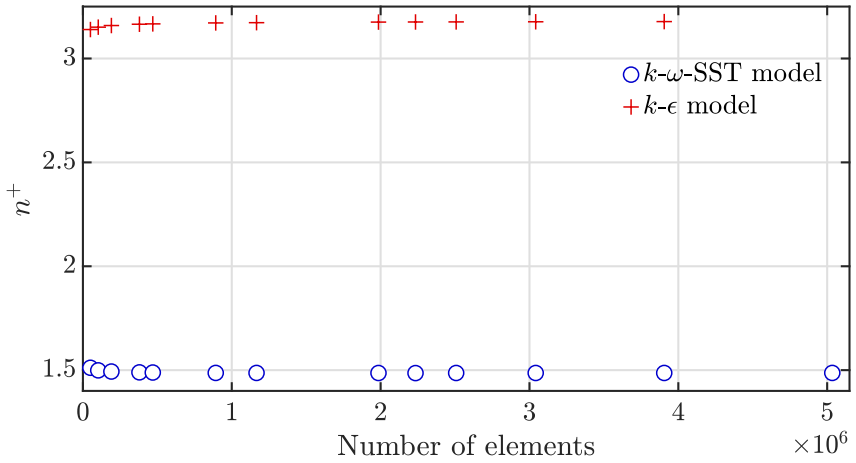

(b) Number of mesh elements against mean n^+.

Figure 7.19: Friction factor mesh convergence analysis for the E-029-01 structure using analytical results and the RANS k-ω-SST and k-ϵ turbulence models (inlet fluid velocity = 14.8 m s^{-1}).

where the constants G and H were fit parameters. This was analogous to equation 5.12. The pressure drops exhibited by the structures did not exceed $2{\times}10^6$ Pa (i.e., 20 bar), where the greatest and smallest observed pressure drops for an inlet fluid velocity of 8.49 m s^{-1} were $7.2{\times}10^5$ Pa and $5.7{\times}10^3$ Pa by the E-029-02 and E-029-01 structures, respectively. It was expected that the E-029-02 structure would exhibit the greatest pressure drop as it had (alongside the E-029-01 structure) the lowest fluid volume and because its internal structure would obstruct fluid flow. In addition, the E-029-03 and E-029-04 structures exhibited similar pressure drops. The examined fluid velocity range therefore fell within HIVE's operational regime.

The maximum tile surface temperature, $T_{t,max}$, for the examined structures are presented in figure 7.25 for a range of inlet fluid velocities and incident power on the tile surface. This was examined to determine the potential damage that can occur to the structure from overheating. The greatest and lowest observed maximum tile surface temperatures for an effective incident power of 1,000 W and inlet fluid velocity of 0.21 m s^{-1} were 2,262 K and 1,446 K by the E-029-01 and E-029-03 structures, respectively. Inconel-718 has a melting point of 1,533 – 1,609 K [155]. The maximum tile surface temperatures calculated here exceeded the melting point in the E-029-01 structure, at 750 W for low fluid velocities and 1,000 W within the examined fluid velocity

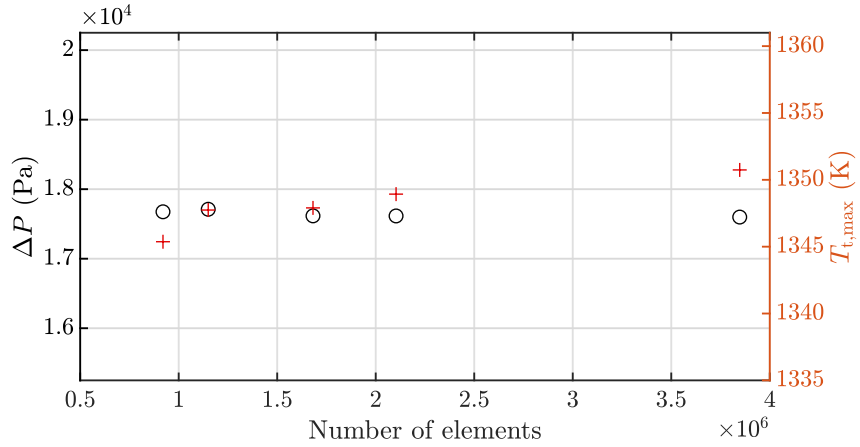

(a) E-029-01.

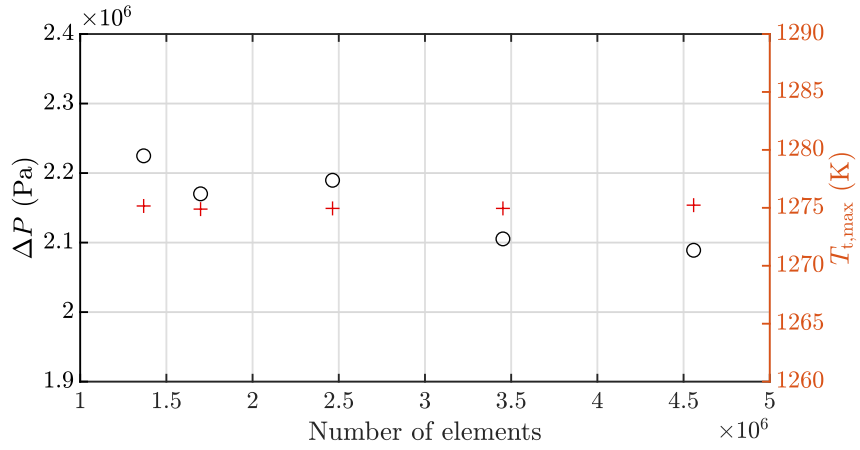

(b) E-029-02.

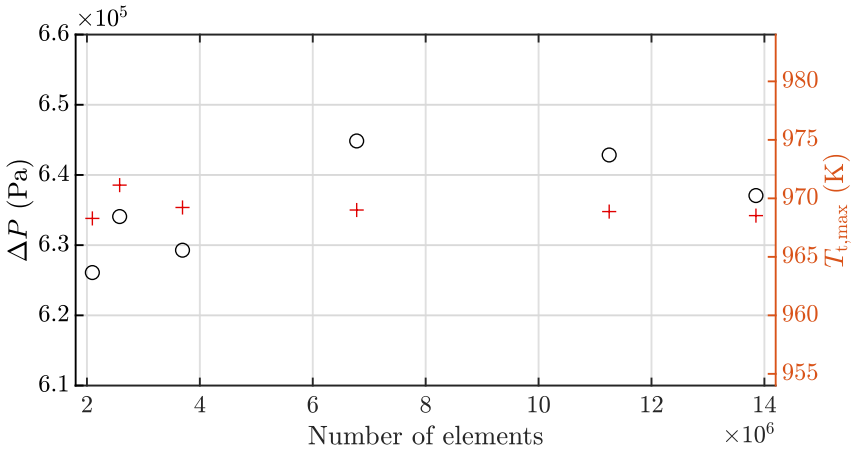

(c) E-029-03.

Figure 7.20: Pressure drop (black circle) and maximum tile surface temperature (red plus) mesh convergence study for the examined structures (inlet fluid velocity = 14.8 m s^{-1}, incident effective power = 707 W).

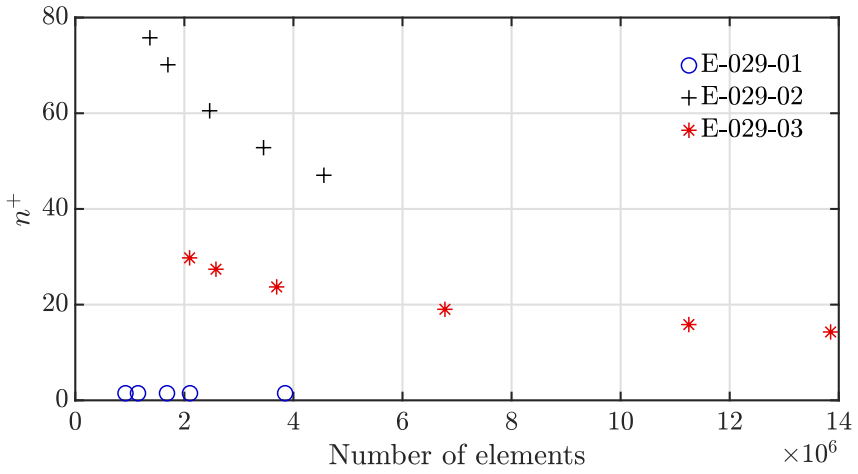

Figure 7.21: Number of mesh elements against mean n^+ for the E-029-01, E-029-02 and E-029-03 structures.

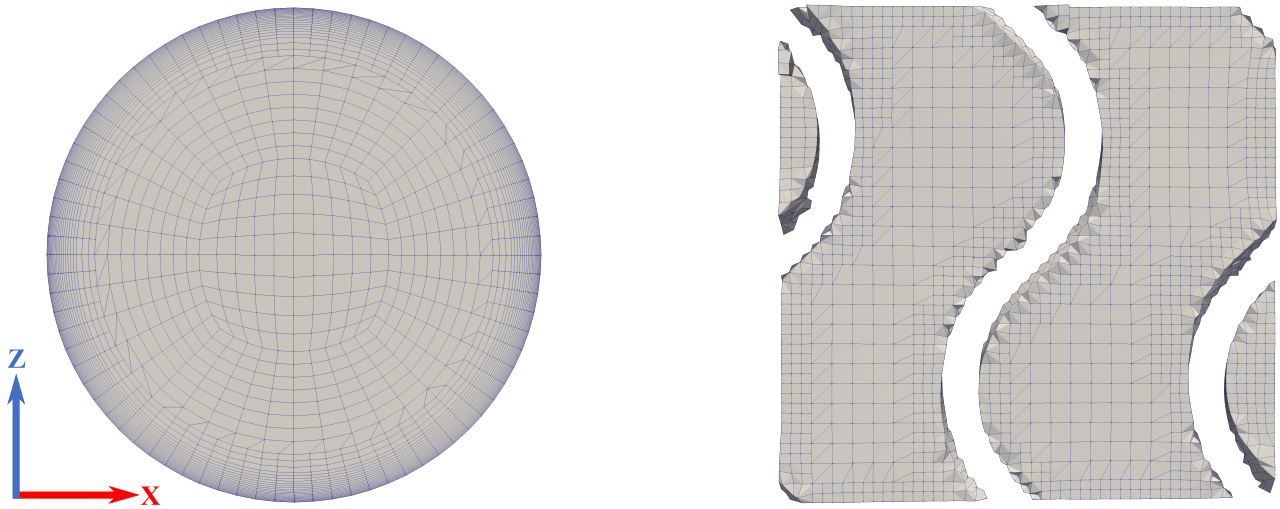

(a) E-029-01. **(b)** E-029-02.

Figure 7.22: Mesh structure in the fluid domain for the E-029 structures at a position $y = 0.025$ m after the inlet plane.

range, and the E-029-02 structure, at 1,000 W. This corresponds to heat fluxes of 1.06 MW m^{-2} and 1.41 MW m^{-2} on the tile surface, respectively. These heat fluxes are an order of magnitude lower than what a divertor target is expected to experience within DEMO (discussed in section 3.3). This is not surprising, given that Inconel-718 is not an ideal material for plasma-facing components. For a brief comparison, tungsten (a material often used in plasma-facing components) has a greater melting point (by a factor of 2) and thermal conductivity (by an order of magnitude) than Inconel-718. Regardless, care must be taken when examining the structures within HIVE as there is the possibility of damaging them at large heat fluxes.

The mean tile surface temperature, $T_{\mathrm{t,m}}$, for the examined structures are presented in figures 7.26 and 7.27. This was used to determine the thermal performance of the structures. It was observed in figure 7.26 that the mean tile surface temperature decreased asymptotically with increasing fluid velocity. A power law model was selected to explore the impact of inlet fluid

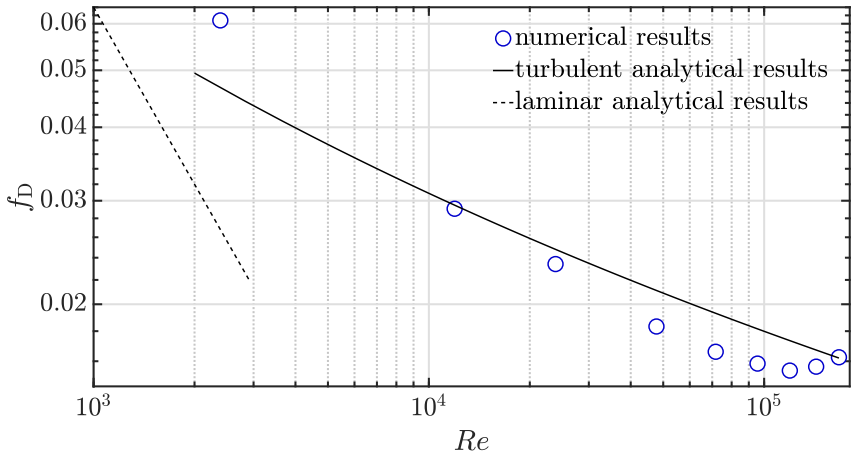

Figure 7.23: Comparison between the numerical results and the analytical solution for friction factor for the E-029-01 structure.

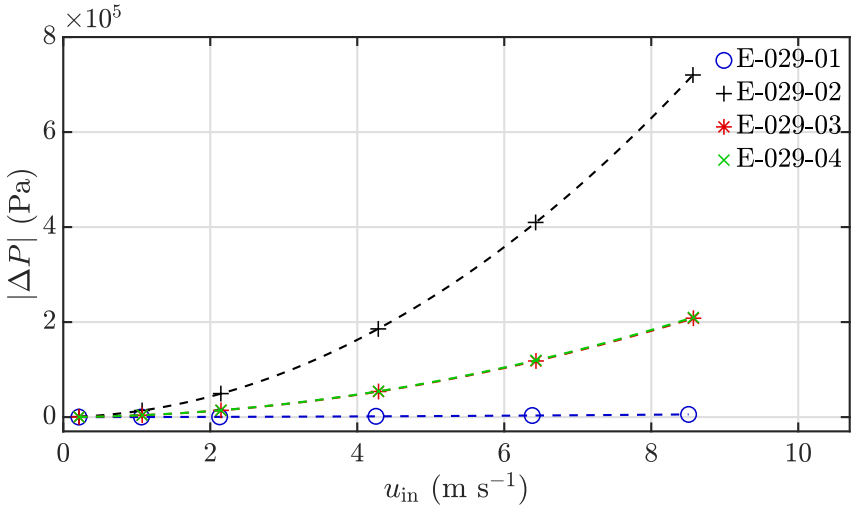

Figure 7.24: Pressure drop for the examined E-029 structures calculated from the numerical model. The (−−) lines represent equation 7.7.

velocity on the mean tile surface temperature. This model was of the form

$$T_{t,m} = M_1 \, {u_{in}}^{-O_1} + R_1 \,, \tag{7.8}$$

where M_1, O_1 and R_1 were positive fit parameters, with R_1 denoting the asymptotic temperature, and described the data well. This indicated that the cooling power of the fluid will not increase with fluid velocity once a large enough velocity is reached. Any increase in fluid velocity past this point will only lower the cooling efficiency of the structure due to the greater power required to drive the fluid through the structure.

It was also observed that the maximum tile surface temperature in figure 7.27 was linearly proportional to the incident effective power. This behaviour was well described by

$$T_{t,m} = S_1 \, Q_{eff} + W_1 \,, \tag{7.9}$$

where W_1 was a positive fit parameter which gives the initial steady temperature of the tile and S_1 was a positive fit parameter which gives the product of a heat transfer coefficient and

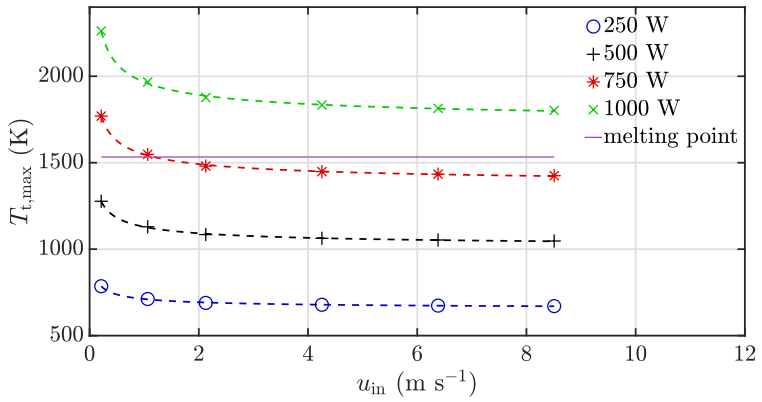

(a) E-029-01.

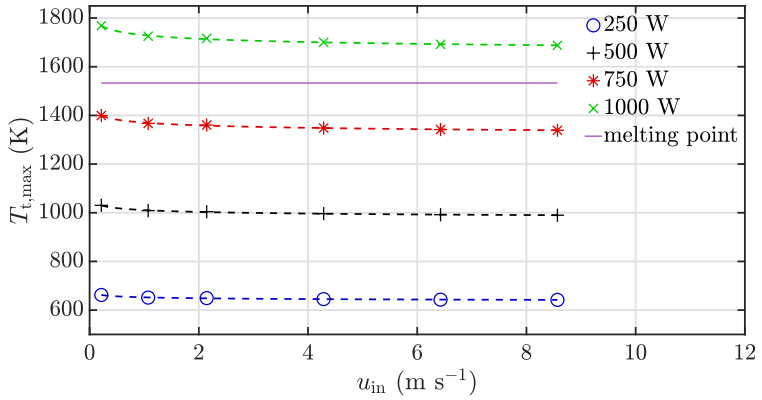

(b) E-029-02.

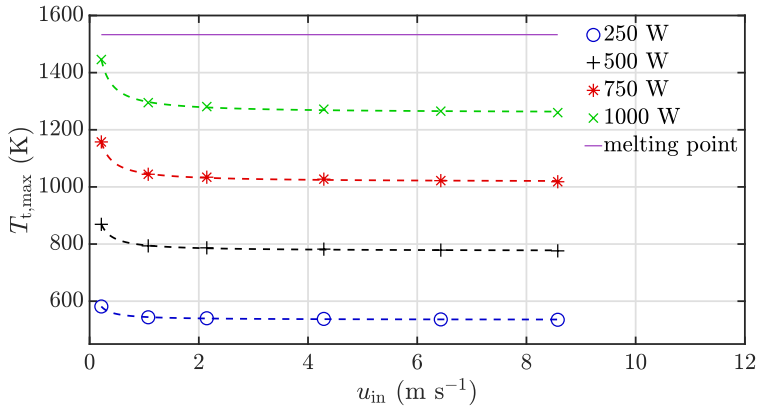

(c) E-029-03.

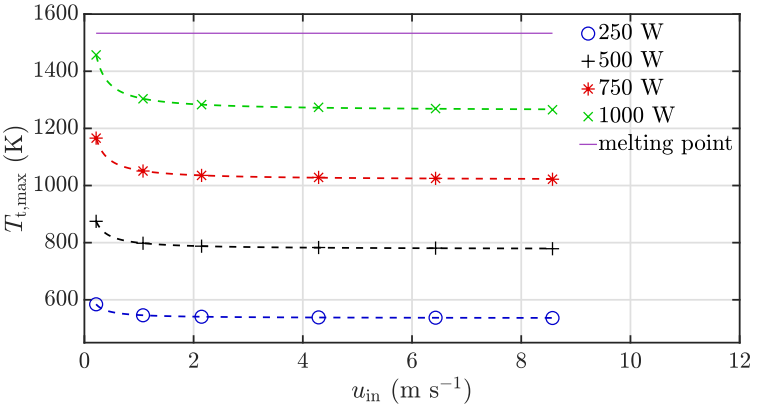

(d) E-029-04.

Figure 7.25: Maximum tile surface temperature for the examined E-029 structures calculated numerically with varying inlet fluid velocity. The (−−) lines represent a power law.

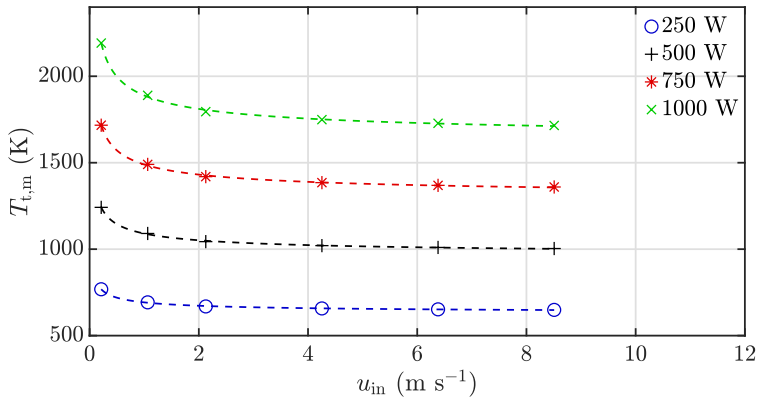

(a) E-029-01.

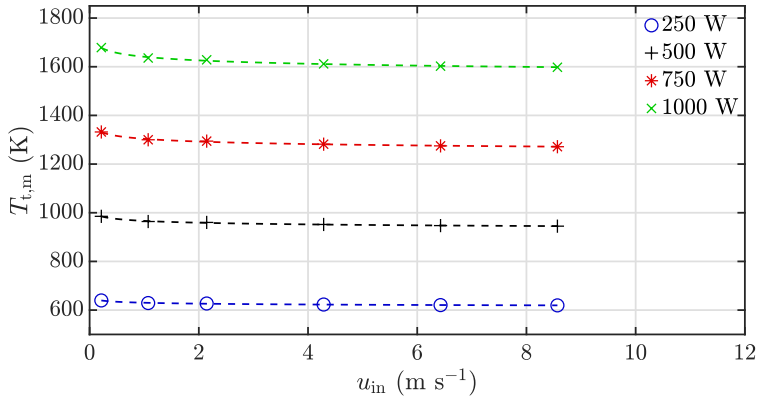

(b) E-029-02.

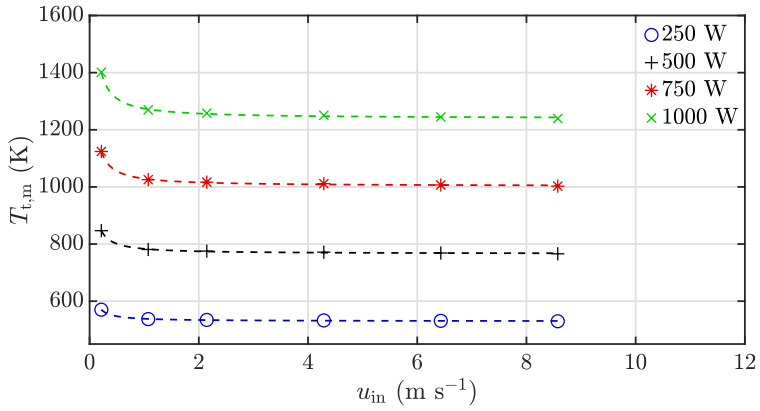

(c) E-029-03.

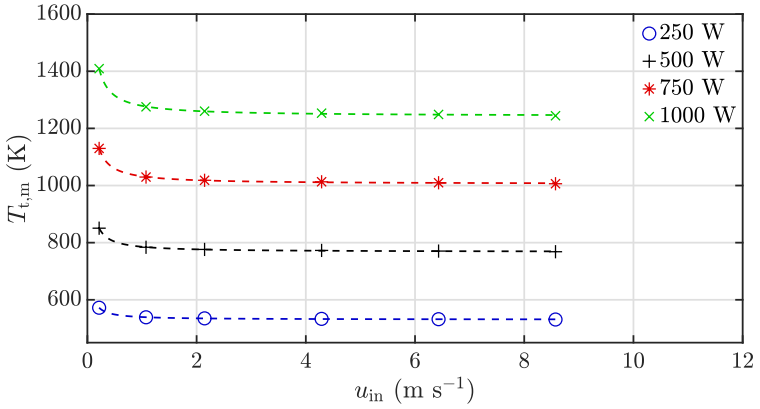

(d) E-029-04.

Figure 7.26: Mean tile surface temperature for the examined E-029 structures calculated numerically with varying inlet fluid velocity. The (−−) lines represent equation 7.8.

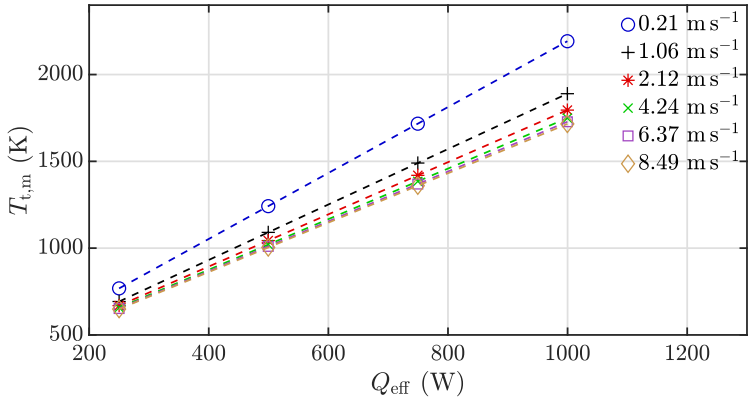

(a) E-029-01.

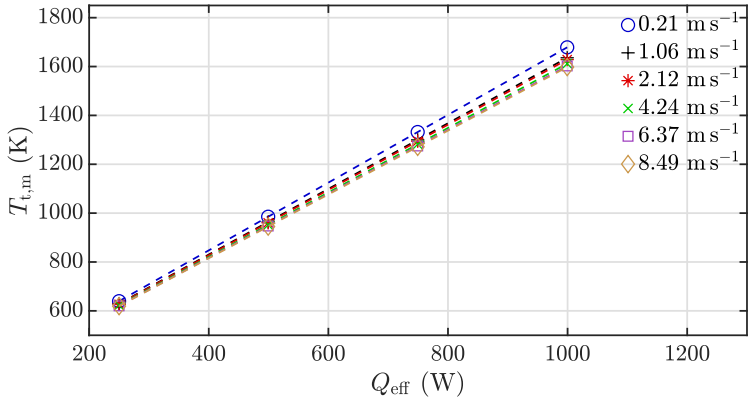

(b) E-029-02.

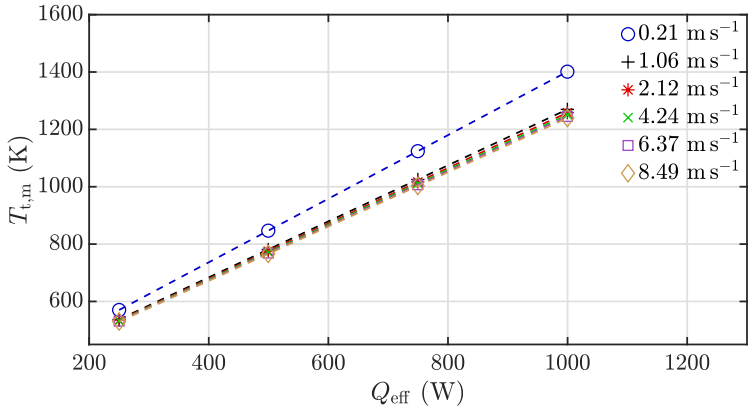

(c) E-029-03.

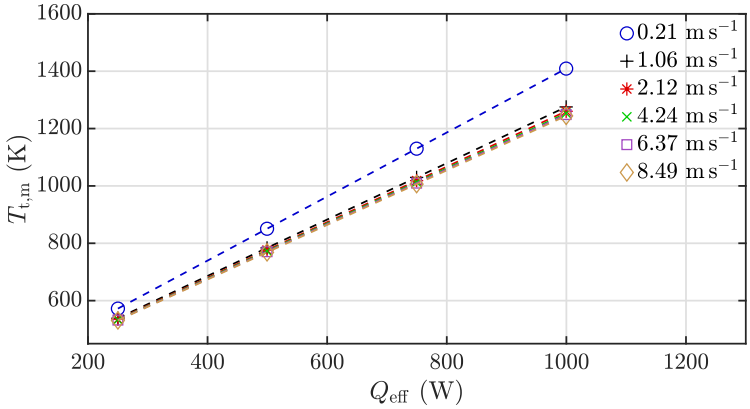

(d) E-029-04.

Figure 7.27: Mean tile surface temperature for the examined E-029 structures calculated numerically with varying incident power. The (−−) lines represent equation 7.9.

the surface area of the tile. This indicated that the maximum tile surface temperature of the examined structures would increase with heat flux until a phase transition is approached, which was not accounted for in this model.

The lowest mean tile surface temperature exhibited by a given structure and incident power occurs when an increasing fluid velocity (if a sufficiently powerful pump is used) does not remove more energy from the system. This can be calculated when the inlet fluid velocity approaches infinity in equation 7.8. This gives

$$T_{\mathrm{t,m}}\left(u_{\mathrm{in}} \to \infty\right) = R_1\,, \tag{7.10}$$

which represents the mean tile surface temperature at the maximum cooling power from the coolant with an inlet temperature of 293 K. This is shown in figure 7.28 for the examined structures with varying incident effective power. It was found that the E-029-01 structure exhibited the largest mean tile surface temperature and the E-029-03 and E-029-04 structures exhibited the lowest mean tile surface temperature at the maximum cooling power. The uncertainty observed in figure 7.28 is due to the uncertainty of R_1 from the fitting process of equation 7.8.

The improved thermal performance of the TPMS-based lattice structures (E-029-02, E-029-03 and E-029-04) can be quantified against a circular channel (E-029-01) by calculating the difference in thermal energy on the tile surface between the structures. This was done by using the specific heat capacity equation,

$$E = mc_{\mathrm{p}}\Delta T_{\mathrm{t,m}}\,, \tag{7.11}$$

where m was the mass of the object, where the examined structures shared the same mass, and $\Delta T_{\mathrm{t,m}}$ was the difference between the final and initial mean tile surface temperature, which gave the change in thermal energy of an object for a given temperature change, E. The percentage difference in change in thermal energy between the examined structures and E-029-01, ΔE, for

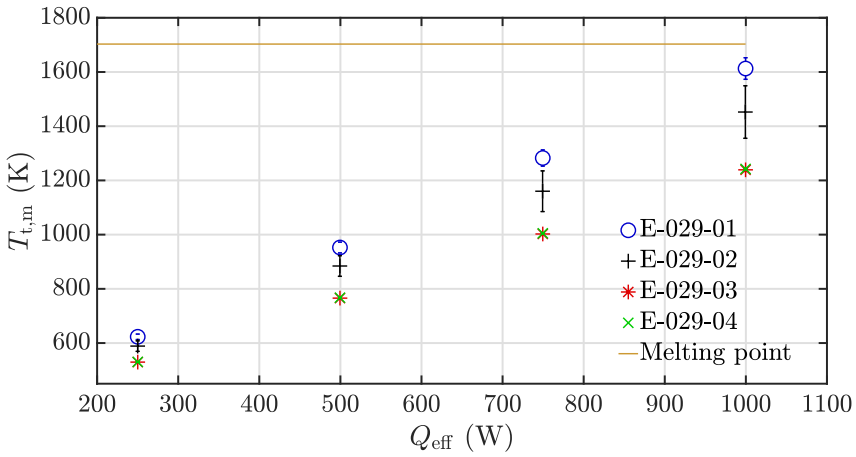

Figure 7.28: Mean tile surface temperature for the examined E-029 structures with varying incident effective power at maximum cooling power.

maximum cooling power (i.e., equation 7.10) was found by

$$\begin{aligned}\Delta E_{\text{E-029-0}x} &= \frac{E_{\text{E-029-0}x} - E_{\text{E-029-01}}}{E_{\text{E-029-01}}} \times 100\,, \\ &= \frac{mc_{\text{p}}\left(\Delta T_{\text{t,m,E-029-0}x} - \Delta T_{\text{t,m,E-029-01}}\right)}{mc_{\text{p}}\Delta T_{\text{t,m,E-029-01}}} \times 100\,, \\ &= \frac{\Delta T_{\text{t,m,E-029-0}x} - \Delta T_{\text{t,m,E-029-01}}}{\Delta T_{\text{t,m,E-029-01}}} \times 100\,, \end{aligned} \tag{7.12}$$

where the subscript E-029-0x denoted the examined structure and $x = 2$, 3 or 4. To determine how much energy was removed from the tile surface in comparison to the E-029-01 structure, ΔE_{t}, the final temperature was defined as the mean tile surface temperature at maximum cooling power and the initial temperature, T_{rtp}, was 293 K. Equation 7.12 was then simplified to

$$\begin{aligned}\Delta E_{\text{t,E-029-0}x} &= \frac{T_{\text{t,m,E-029-0}x} - T_{\text{rtp}} - T_{\text{t,m,E-029-01}} + T_{\text{rtp}}}{T_{\text{t,m,E-029-01}} - T_{\text{rtp}}} \times 100\,, \\ &= \frac{T_{\text{t,m,E-029-0}x} - T_{\text{t,m,E-029-01}}}{T_{\text{t,m,E-029-01}} - T_{\text{rtp}}} \times 100\,. \end{aligned} \tag{7.13}$$

It was observed in figure 7.29 that the E-029-02 structure removed approximately 11% more energy from the tile surface than the E-029-01 structure. The E-029-03 and E-029-04 structures removed significantly more energy from the tile surface than the E-029-01 structure, by approximately 28%. The percentage difference in change in thermal energy on the tile surface between the examined structures and the E-029-01 structure did not vary with the incident effective power as the data for the E-029-02, E-029-03 and E-029-04 structures were within ±2% of the mean value. The uncertainties shown were calculated using propagation of error theory and the uncertainty of R_1.

7.5 Experimental method

Two experiments were planned for HIVE. The hydraulic performance of the examined structures was determined in the first experiment by measuring the pressure drop across them over a range

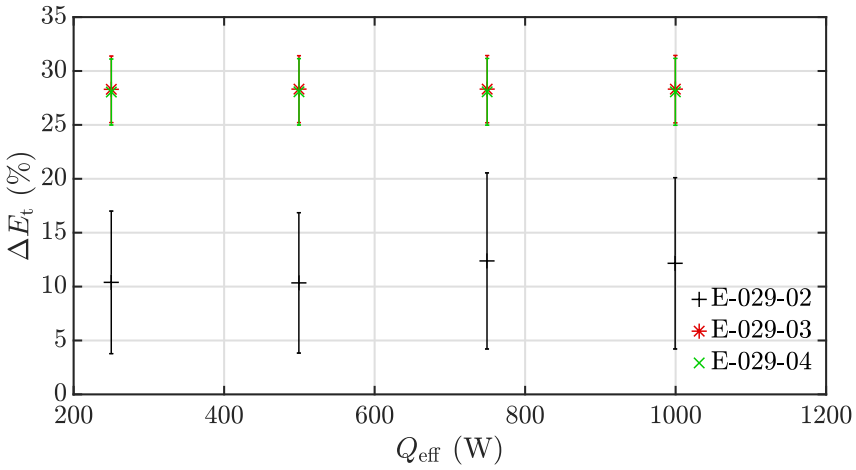

Figure 7.29: Percentage difference in change in thermal energy on the tile surface between the examined structures and the E-029-01 structure at maximum cooling power.

of inlet fluid velocities. There was no heat input in this experiment because the temperature-dependent properties of the coolant may vary significantly at high heat fluxes and because the incident heat flux profile may vary for different structures (due to the proximity effect). These effects can have a large impact on the exhibited pressure drop for the examined structures. The thermal performance of the examined structures was determined in the second experiment by using the IR camera to record the steady-state maximum tile surface temperature over a range of inlet fluid velocities and incident heat fluxes.

The hydraulic and thermal performance experiments were performed for a given structure before changing the test structure inside the vessel. This was due to the prolonged time taken for the vacuum within the vessel to stabilise and the difficulty associated with moving the lid and connecting the test structures to the coolant pipes.

The E-029 structures were first cleaned to remove surface impurities which could impact the vacuum quality from outgassing. The surface facing the IR camera was then coated in a graphite layer so that the surface emissivity of the examined structures was known. This was necessary to obtain accurate measurements from the IR camera. A pyrometer was also used to ensure the IR camera was calibrated correctly.

The HIVE vacuum vessel lid was lifted and placed on to the support structure, where the examined E-029 structure was attached to the coolant pipes. An induction coil with a pancake arrangement was inserted and used to heat the test structure. The lid was then moved back to the vessel and depressurised. Figure 7.30 shows the E-029-01 structure completely set-up within the vacuum vessel.

Coolant was pumped through the pipes and, once the target inlet fluid velocity was reached, the flow was allowed to develop and stabilise. The pressure drop exhibited by the examined structure was measured over a period of 1 minute for the hydraulic performance experiment

Figure 7.30: The E-029-01 structure set-up within the vacuum vessel.

and was calculated by finding the difference between the mean inlet and outlet pressure. The initial inlet fluid velocity was at 1 m s^{-1}. This was increased by increments of 1 m s^{-1} until the maximum inlet fluid velocity was reached for the examined structure.

For the thermal performance experiment, the induction coil power was specified by a user-input. To avoid damaging the test structure, a minimum induction coil power setting of 0.5 kW and the maximum inlet fluid velocity were initially specified. The induction coil was turned on once the fluid flow and vacuum quality stabilised. The pulse duration was determined by the vacuum quality, where the induction coil power would turn off once a vacuum pressure of 1×10^{-3} mbar was exceeded (for safety purposes). The flow rate was then reduced by increments of 1 m s^{-1} and the pulse repeated, whilst ensuring that the maximum tile surface temperature did not reach its melting point. The induction coil power was then increased by increments of $0.5 - 1$ kW and the inlet fluid velocity set to its maximum value before repeating the previous steps. The power was continuously raised until the maximum tile surface temperature approached the melting point.

The maximum tile surface temperature was found by specifying regions of interest in the FLIR Research Studio software, with an example shown in figure 7.31. The maximum, minimum and average recorded temperatures within these regions of interest were given and plotted against the recorded time to visualise their temporal evolution. The steady-state maximum tile surface temperature was taken when the maximum tile surface temperature no longer varied with time.

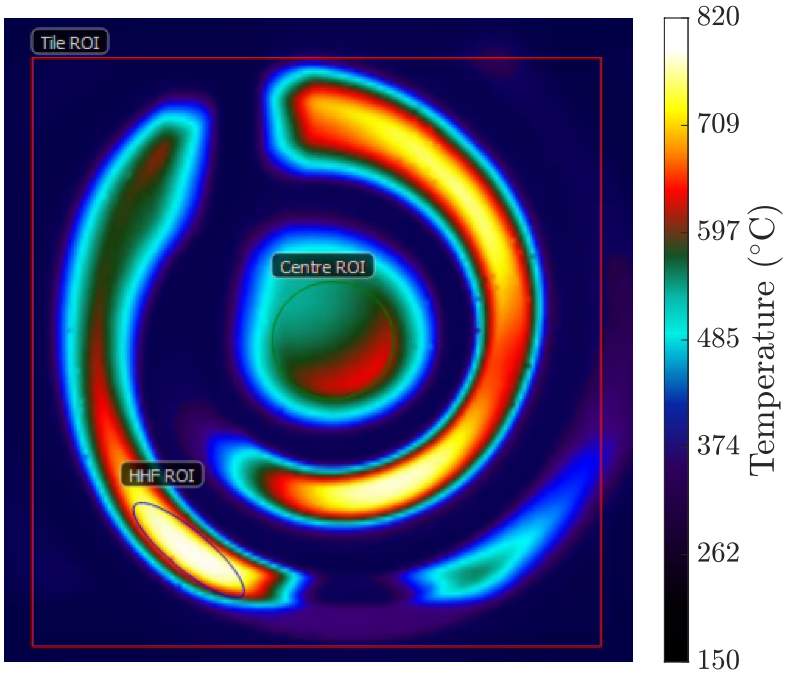

Figure 7.31: Image taken from FLIR Research Studio showing user-specified regions of interest and the surface temperature distribution for the E-029-01 structure (inlet fluid velocity = 2.17 m s^{-1} and induction coil power = 5 kW).

7.6 Experimental and numerical limitations

7.6.1 Hydraulic performance

Significant differences were observed between the numerical and experimental for both the hydraulic and thermal performance of the examined structures. For example, the experimental pressure drop was 15−21× larger than what was predicted numerically for the E-029-01 structure. This is likely due to the differences between the numerical model and the experiment, as the model is not a one-to-one recreation of HIVE. This section aims to (1) explain the limitations of the experimental method and facility, (2) explain how this leads to differences between the numerical and experimental results and (3) discuss whether the numerical model or experimental method can be modified to mitigate these issues.

Multiple reasons exist which could explain the discrepancy between the hydraulic performance given by the numerical models and the experimental results. The first being the geometrical differences of the structures used in the numerical model and in HIVE. For example, the modelled pipes had an inner diameter of 10 mm while the inner walls of the pipes used in HIVE were not circular and had varying wall thicknesses, as observed in figures 7.15 and 7.16. The geometry of the additively manufactured structures likely leads to increased pressure drops. The extent of this effect can only be quantified by either re-manufacturing these structures and machining them to the original specifications or by determining the exact internal geometry of the manufactured structures and designing equivalent CAD models, both of which were not possible in this study.

Figure 7.4 shows that the cooling pipe within the vessel experienced a 90° bend, which causes an additional pressure drop. The numerical model did not include the pipe bends and, hence, does not model the larger pressure drop associated with them. The pressure transducers within HIVE were able to measure this effect due to their positioning, which was not optimised for the numerical model. The pressure drop associated with the pipe bend could be accounted for numerically by modelling them, but this was deemed too computationally intensive.

The pipe bend also disrupts the fluid velocity profile and the fluid flow was not able to fully-develop before reaching the test structures due to the short length of the pipe. Both of these may impact the hydraulic performance of the examined structures. The true inlet fluid velocity profile could be found numerically by modelling the cooling pipes inside and outside the vessel, but this was computationally intensive. A uniform inlet fluid velocity boundary condition was instead implemented to determine whether the inlet fluid velocity profile has an impact on the pressure drop across a structure. Figure 7.32 shows the ratio between the pressure drop calculated from a uniform boundary condition, $\Delta P_{\text{num,uni}}$, and the pressure drop calculated from a fully-developed inlet velocity profile, $\Delta P_{\text{num,fD}}$, for the E-029-01 and E-029-02 structures. The E-029-01 structure exhibited pressure drops up to 1.5× greater when a uniform inlet boundary condition was used instead of a fully-developed inlet fluid velocity profile. This was likely due to the greater friction the fluid experienced on the pipe wall, caused by larger near-wall fluid velocities. The E-029-02 structure exhibited similar pressure drops when a uniform boundary condition was used compared to a fully-developed inlet profile. This was likely due to the internal structure, which obstructed the flow of fluid through the centre of the channel, as shown in figure 7.33, and was the key driver behind pressure drop.

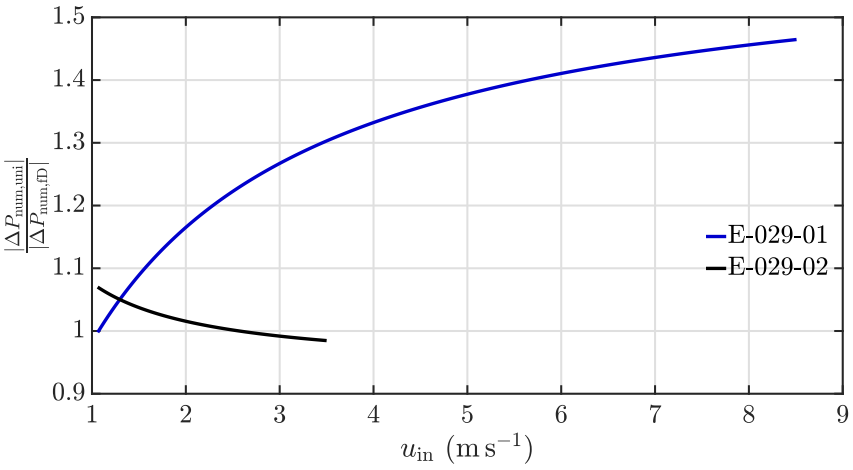

Figure 7.32: Ratio between the pressure drop calculated from a uniform boundary condition and a fully-developed inlet fluid velocity profile for the examined E-029 structures.

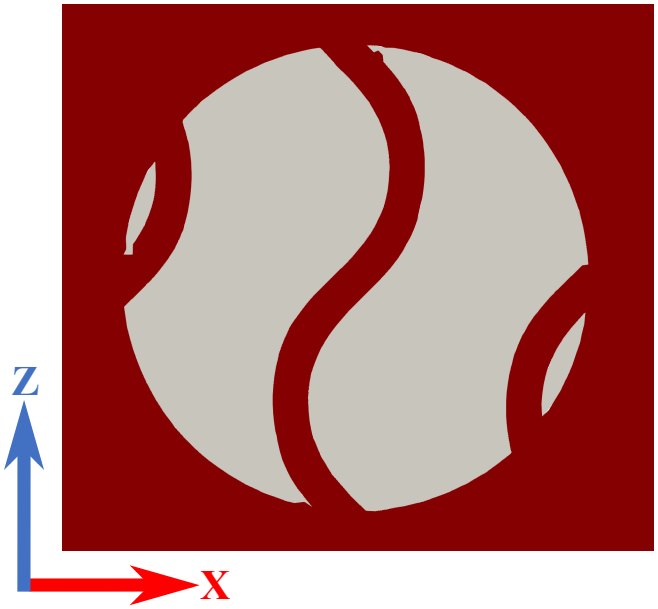

Figure 7.33: Cross-section of the E-029-02 solid domain (red) and fluid domain (grey) at a position of $y = 0.015$ m after the inlet plane.

Rough surfaces tend to lead to greater pressure drops due to the extra friction they provide. While smooth fluid-solid walls were implemented in the numerical model, the internal surfaces of the manufactured E-029-02, E-029-03 and E-029-04 structures were rough from the manufacturing process (the internal surface of the E-029-01 structure was smoothed from the machining process). A range of sand-grain roughnesses were implemented on the fluid-solid interface of the E-029-02 structure to determine the impact that surface roughness has on the hydraulic performance. Figure 7.34 shows the ratio of the pressure drop calculated with a non-zero sand-grain roughness, $\Delta P_{\mathrm{num,K_S}}$, and the pressure drop calculated with a sand-grain roughness of zero, $\Delta P_{\mathrm{num,S}}$. It was observed that the pressure drop exhibited by the E-029-02 structure increased significantly if the sand-grain roughness was greater than 10 µm. This was expected as, following the same method used in section 5.2.2, the sand-grain roughness needs to be greater than approximately 8.40 µm for the walls in the E-029-02 structure to be modelled as a rough interface when an inlet fluid velocity of 8.49 m s^{-1} was used. The pressure drop exhibited by

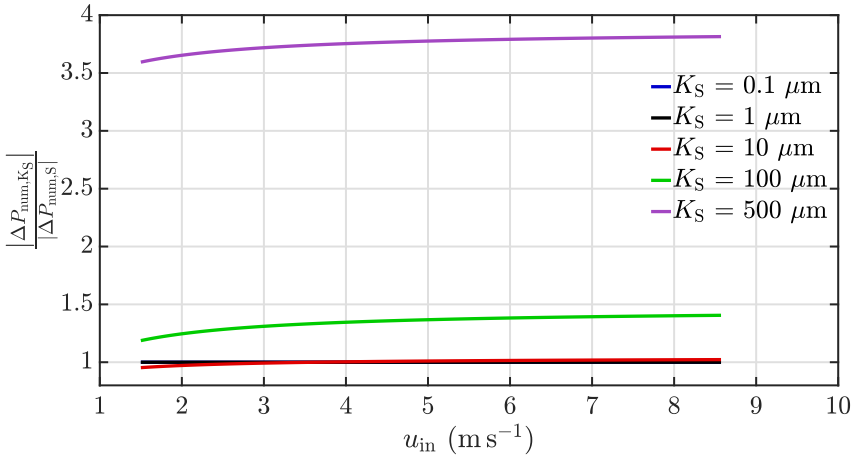

Figure 7.34: Ratio between the numerical pressure drop calculated from rough and smooth walls for the E-029-02 structure.

the E-029-02 structure was up to 3.8× greater when the walls were modelled with a sand-grain roughness of 500 µm, which can be converted into an arithmetic average roughness of 85.3 µm by equation 5.8. As discussed in section 5.2.2, the upward-facing surfaces of LPBF parts typically have arithmetic average roughnesses on the order of magnitude of 10 µm [128–131]. While an arithmetic average roughness of 85.3 µm is relatively large, this reflects that non-upward-facing surfaces in LPBF parts have a higher surface roughness than upward-facing surfaces. Surface roughness therefore has a large impact on the hydraulic performance of a manufactured specimen and this needs to be accounted for. To mitigate this issue, either the rough walls of the manufactured structures need to be smoothed (such that the smooth fluid-solid boundary assumption is correct) or the roughness of the manufactured walls need to be measured (such that they can be implemented within the numerical model). The first method is difficult to accomplish as the complex structures mean that machining cannot be used to smooth the walls and chemical polishing techniques can inadvertently modify the geometry in unexpected ways. The second method requires techniques such as CT scanning, as demonstrated by Stimpson *et al* [55], which was outside the scope of this study.

7.6.2 Thermal performance

The average tile surface temperature was not used here because it cannot be calculated due to the induction coil partially blocking the view from the IR camera, shown in figures 7.30 and 7.31. The maximum tile surface temperature was used instead to determine the thermal performance of the examined structures, which the numerical model can also output.

It was unclear whether the graphite layer (used to calibrate the IR camera with the emissivity of graphite) was applied uniformly across the surface of the manufactured structures and if this has a significant impact on the temperature given by the IR camera. Thermocouples would ideally be used to ensure that the IR camera was calibrated correctly but were not used as they would be damaged from the high heat flux. There is therefore an uncertainty regarding the recorded temperatures.

The vacuum pressure rapidly deteriorated when operating under high heat fluxes. This is likely due to outgassing from the manufactured structures and leakages from the vacuum vessel. This

meant that, for many cases, the pulse duration was too short for the temperature on the tile surface to reach equilibrium, as shown in figure 7.35. The temporal evolution of the maximum tile surface temperature was well described by

$$T_{\mathrm{t,max}}(t) = -a\, e^{-b\, t^{d}} + c\,, \tag{7.14}$$

where a, b, c and d were positive fit parameters and t was the elapsed time. The steady-state maximum tile surface temperature could therefore be predicted by tending the elapsed time to infinity, which reduced equation 7.14 to

$$T_{\mathrm{t,max}}(t \to \infty) = c\,, \tag{7.15}$$

where c gave the predicted steady-state maximum tile surface temperature. There are notable uncertainties in using a method such as this however. The first is that there is an additional uncertainty on the predicted steady-state maximum tile surface temperature from the fitting process. The second is that this assumes that there are no significant changes in the physics of the system which could affect heat transfer as the temperature increases (which would not be captured here).

The thermal performance of the examined structures determined experimentally cannot be accurately compared against each other, or to the numerical models, because each structure experiences different heat flux profiles due to the proximity and edge effects discussed in section 7.2. This has an impact on the power transferred from the coil to the test structure and on the temperature distribution of the tile surface. This is presented in figure 7.36, where two different tile surface temperature distributions (due to different incident heat flux profiles) are shown. Furthermore, a significant proportion of the power generated by the induction coil was lost to the environment and it was unknown how much power was supplied from the induction coil to the tile surface. The induction coil power in HIVE is therefore not equivalent to the incident power specified on the tile surface in the numerical model.

There were also three incorrect assumptions made for the numerical model when comparing it to the experiment. The first was that a uniform heat flux profile was assumed on the tile surface, though this is definitely not the case. This cannot be improved substantially however as it was

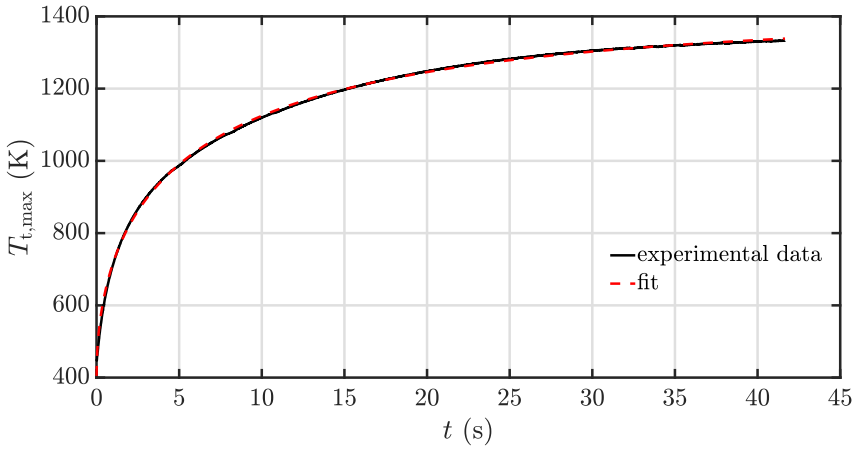

Figure 7.35: Extrapolation of the maximum tile surface temperature for the E-029-02 structure (inlet fluid velocity = 1.01 m s^{-1} and induction coil power = 4.5 kW). The (−−) lines represent equation 7.14.

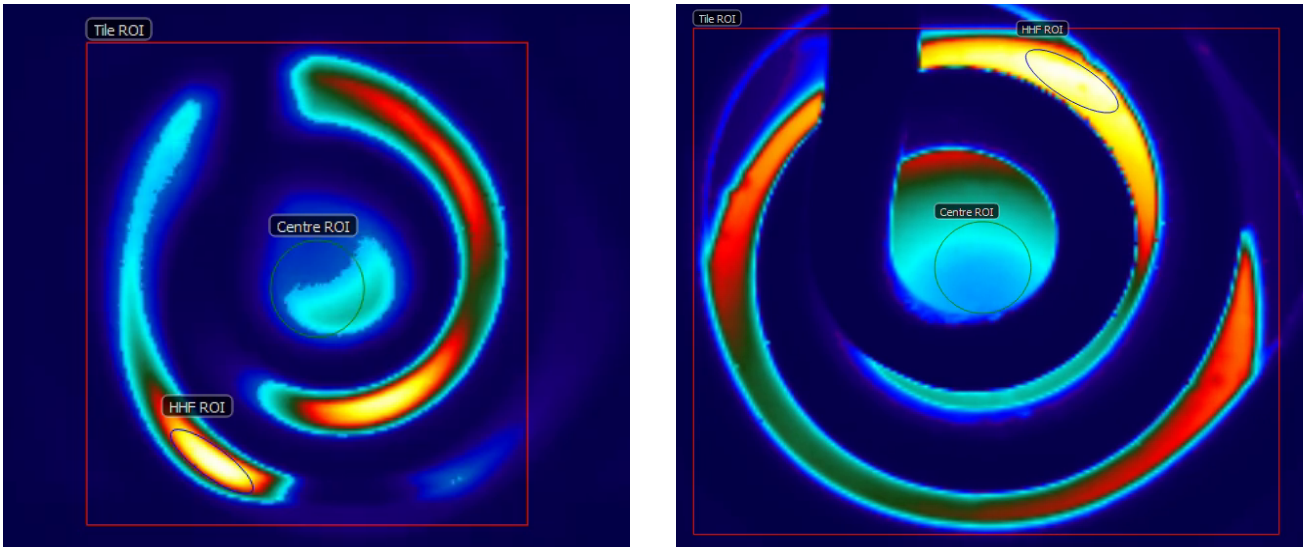

Figure 7.36: Surface temperature distributions for the E-029-01 structure (left) and the E-029-02 structure (right) indicating different incident heat flux profiles (inlet fluid velocity = 2.17 m s^{-1} and induction coil power = 3 kW).

not possible to determine what the heat flux profile for each structure was within HIVE (due to the induction coil blocking the view).

The second assumption was that the heat flux was only incident on the tile surface in the numerical model. This was not the case as induction heating occurs on all surfaces facing the induction coil, but to different degrees due to the proximity effect, and within the body of the structure, due to the skin effect. A numerical electromagnetic analysis technique could be used to determine the incident power generated from the induction coil for a given structure, which can then be implemented in the numerical model, but was outside the scope of this study. Both of these assumptions have a large effect on the energy supplied to the structures and improvements need to be made to allow the numerical model better approximate the experimental set-up.

The final assumption was that temperature-independent material properties were assumed for both the fluid and solid domain. This is not valid when examining parts with high thermal gradients, as is the case here. For example, the thermal conductivity of Inconel-718 can increase by a factor of two as temperature increases from room temperature up to 1,100 K, according to Agazhanov *et al* [161]. This can have a large impact on both the hydraulic and thermal performance determined numerically at greater temperatures. Temperature-dependent material properties must therefore be included in future work.

7.7 Summary

Figure 7.24 shows that structures featuring a TPMS-based lattice structure exhibited pressure drops $1-2$ orders of magnitude greater than a structure with a circular channel. The large pressure drops exhibited by the examined TPMS-based lattice structures are due to their internal structures, which obstructed fluid flow, and the high surface roughness on the internal walls, which leads to increased friction between the fluid and solid. This indicated that TPMS-based lattice structures may not be suitable for heat sinks in PFUs. Greater pressure drops are not

inherently problematic however, as long as the operational regime of the system is not exceeded, which is system-dependent. Additionally, if the TPMS-based lattice structures remove more thermal energy from the system than the additional energy that is needed to pump an equivalent volume of fluid through a larger pressure gradient, then the PFU exhibits a net-positive gain in energy management.

Figure 7.29 shows that TPMS-based lattices are more effective at removing heat from a structure than a simple circular channel, as the E-029-02 structure removed 11% more energy from the heated surface than the E-029-01 structure and the E-029-03 and E-029-04 structures removed 28% more energy from the heated surface, in theory. They also become more effective as a larger proportion of the structure is dedicated to the TPMS-based lattice. This increases the volume of fluid within the structure, improving the hydraulic performance, and the surface area of the lattice structure, improving the thermal performance. The E-029-03 and E-029-04 structures also exhibited very similar results which indicates that a graded volume fraction does not have a strong impact on the thermal performance, though a wider range of graded volume fractions need to be examined to determine this with certainty. The thermal performance of PFUs in a tokamak can therefore be improved through the implementation of TPMS-based lattices which incorporate a larger volume of the structure. Further research is needed to determine whether this can offset the increased energy demands from the poorer hydraulic performance, when compared to a circular channel, and if they can meet the performance requirements inside of a tokamak.

HIVE was also used to provide experimental data to validate the numerical model. The limitations associated with the experimental method and set-up resulted in significant differences between the experimental and numerical results, however. Different methods to improve or mitigate these limitations were discussed at length but, ultimately, could not be implemented here as this was outside the scope of this project.

The work undertaken within this chapter has shown that TPMS-based lattice structures show potential for use as heat sinks in high heat flux environments. A study focused on characterising their structure hydraulic and thermal performance based on their geometrical properties (similar to the work presented in chapters 5 and 6) at fusion relevant conditions (i.e., high heat flux and Reynolds numbers) is important to both determine whether the extreme environment changes the relationships found for low Reynolds numbers and temperatures, and to make informed decisions on which lattice structure should be used for a given application.

Chapter 8

Conclusion

This work examines additively manufactured TPMS-based lattice structures as candidates for high heat flux components in nuclear fusion, particularly for the divertor target. TPMS-based lattice structures have high surface-to-volume ratios, solid-fluid contact areas and enclosed channels which can promote heat transfer within heat sinks. The use of TPMS-based lattice structures for heat sink applications is novel and it is necessary to understand the fluid dynamics and heat transfer in such structures before implementing them in high heat flux components. Heat sinks featuring these structures can then be designed for specific applications to meet necessary performance requirements with this understanding.

The important results of this project are summarised in sections 5.5, 6.5 and 7.7. Rather than repeating these explanations, the key findings are given here instead:

- Structure-performance relationships were established for TPMS-based lattices heat sinks and can be used to optimise heat sink design.
- TPMS-based lattice structures which distribute heat across the entire fluid domain are better candidates for heat management than structures which mitigate heat distribution.
- Geometric properties, such as radius and tortuosity, can describe the hydraulic and thermal performance of individual TPMS-based lattice cell types.
- TPMS-based lattice structures are more effective at removing thermal energy in high heat flux environments than conventional structures, such as circular channels.

The aims of this research project, set out in section 1.3, were therefore met as the thermal and hydraulic performance of TPMS-based lattice structures were found to be dependent on different geometrical properties, though there is still scope to determine how these properties fundamentally impact fluid dynamics and heat transfer in these structures. It was also established that divertor target-like manifolds featuring TPMS-based lattice heat sinks can exhibit greater thermal performance than their conventional counterparts. This can be improved by further optimising their designs.

TPMS-based lattice structures therefore show great promise for high heat flux applications in nuclear fusion due to the additional cooling they provide from their complex geometries, reducing the risk that plasma-facing units melt or suffer a mechanical failure from the multiple load cycles and high temperatures. There are multiple facilities and experimental reactors that

are currently being designed and planned that could either benefit from implementing TPMS-based lattice structures into plasma-facing units or be used to test the suitability of TPMS-based lattice structures in a true fusion environment. If the additional work discussed in the following chapter is completed, TPMS-based lattice structures may see use in high heat flux applications within the nuclear fusion sector and other industries.

Chapter 9

Future Work

9.1 Short-term projects

The work presented in this study could be significantly improved by either expanding upon it or adjusting the methods used. This section proposes tasks and ideas which could be undertaken to achieve these improvements in a relatively short timescale.

The study presented in chapter 5 only considers structures with one lattice cell in the fluid normal directions. This is because the fluid dynamics within a large array of TPMS-based lattice cells will be predominately dependent on the fluid dynamics within one lattice cell. Many applications of TPMS-based lattices use multiple cells in all directions, however, and inter-cellular interactions may lead to different fluid dynamics which are not captured in this study. Hence, this study can be further improved by examining the effect that multiple lattice cells has on the fluid dynamics. A larger selection of TPMS-based lattice cell types can also be examined, as the structures examined here only cover a narrow range of the available TPMS-based lattice structures.

The only geometrical properties examined in chapter 6 are channel radius and tortuosity. It is unlikely that these two properties are able to fully describe structures as complex as TPMS-based lattice structures. Additional geometrical properties, such as surface area and roughness, need to be considered to better understand TPMS-based lattice structures and the impact that their different geometries have on the hydraulic and thermal performance. More sophisticated methods to analyse this data, such as machine learning and neural networks, may need to be adopted if datasets become too large (for example, when different geometrical parameters are examined and coupled together for multiple lattice cell types). Informed decisions on which TPMS-based lattice structures are appropriate for a given application can then be made with better understanding of their geometry.

The tortuosity of the examined TPMS-based lattice structures was also examined in only one direction. The tortuosity distribution of a given structure is heavily dependent on its orientation and, hence, a single TPMS-based lattice structure may have significantly different performances based on its orientations. The impact that tortuosity has on performance can be further understood by examining TPMS-based lattice cell types in different orientations.

The numerical model used in chapter 7 cannot be taken to be a digital replica of HIVE due to the assumptions made in the numerical model and HIVE's limitations. This is due to many reasons,

such as key pipe geometry being neglected in the model (e.g., the bends), assuming that all the induction coil power is supplied to the tile surface and that the power distribution on the tile surface is uniform. In order to develop a digital replica, the model needs to be developed further to account for the above issues. HIVE also needs to be modified in such a way to facilitate the creation of a digital replica. For example, different camera positions can be used to determine the distribution of power on the heated surface and a new method to set-up the test structures needs to be developed to ensure that the distance and angle between the induction coil and different parts is consistent.

Further research is needed to determine if the additional energy removed from the examined gyroid matrix lattices is greater than the additional energy associated with pumping the fluid through them. This will dictate whether they are more energy efficient than conventional structures.

Additionally, the CFD approach needs to be critiqued and modified. At high heat fluxes, it is expected that heat transfer mechanisms, such as nucleate boiling, will significantly increase heat transfer within the divertor targets. This phase change will need to be represented within the numerical model and can lead to significant development lead times. Alternatively, test structures can also be manufactured and experimental work can become more prominent. The CFD model would also benefit from robust experimental validation to build further confidence in the numerical model.

9.2 Long-term projects

Long-term research projects are needed in both the additive manufacturing and nuclear fusion sectors in order to take the promising results shown throughout this project and be able to develop optimised high heat flux components employing additively manufactured TPMS-based lattice structures. A selection of project ideas which would achieve this goal are discussed in this section.

This research project was largely focused on how the geometry of TPMS-based lattice structures impacted the fluid dynamics within their enclosed channels and how this affects both their hydraulic and thermal performance. The structural material was therefore largely neglected here. This, in reality, will have a large impact on the thermal performance of high heat flux components as materials can have different thermophysical properties, such as thermal conductivity. These properties will also affect the structural performance of a component as different materials will exhibit varying levels of embrittlement, activation, ductility, etc. It is therefore essential that additively manufactured materials are tested sufficiently in nuclear fusion relevant environments to ensure that an appropriate material is used to avoid the aforementioned issues.

Similarly, it is essential to improve the processability of additively manufactured refractory metals and alloys, particularly for nuclear fusion applications. Current designs and technology for tokamak-based high heat flux components prominently feature refractory metals such as tungsten and tantalum, but there are significant difficulties in additively manufacturing these materials consistently worldwide (more information is provided in appendix A). The implementation of TPMS-based lattice structures within high heat flux components is therefore dependent on the available selection of additively manufacturable materials as the improvements seen using

these structures can be negated by the lack of suitable materials for nuclear fusion applications.

TPMS-based lattice structures also need to be better understood in terms of their geometrical parameters. Currently, TPMS-based lattice structures are designed by selecting a lattice cell type, design volume, cell aspect ratio, volume fraction and transformations (e.g., rotation and translation). These 'design' parameters do not give an indication of the geometry of a given lattice cell type, however. Geometrical parameters, such as tortuosity and channel radius, may be able to describe the geometry of different lattice cell types. It may also be the case that any given lattice cell type has a specific configuration of geometrical parameters which act as the fingerprint of that lattice cell type. TPMS-based lattice structures could then be designed from geometrical parameters rather than design parameters.

Fluid dynamics and heat transfer within TPMS-based lattice structures across a range of different flow regimes and heat fluxes also need to be better understood. Different flow regimes (such as turbulence, Forchheimer and Darcian flow) can lead to significant changes in the fluid flow within these structures and varying levels of heat fluxes can lead to different heat transport mechanisms (such as convective cooling or nucleate boiling) becoming dominant. This impacts the hydraulic and thermal performance of TPMS-based lattice structures. A complete understanding of these phenomena will ensure that flow regimes and heat transport mechanisms which maximise heat transfer in TPMS-based lattice structures are selected for a given application.

With an in-depth understanding of both the geometry of TPMS-based lattices structures and of the fluid dynamics and heat transfer phenomena within them, structure-performance relationships can be developed from first principles. Optimised TPMS-based lattice structures could then be designed from these relationships for specific applications by engineers and lattice designers.

It is unlikely that TPMS-based lattice structures, as generated by the isosurface equations, are optimised for heat transport, however. Using knowledge of the fluid dynamics and heat transfer through these structures, their geometry can be significantly modified to improve and potentially optimise their performance (e.g., the inclusion of open channels in areas of low heat transfer to improve the hydraulic performance). This would require further research in finding an appropriate method of modifying TPMS-based lattice structures, which are hard to modify as they are typically outputted as triangulated surfaces, and how different modifications affect the thermal and hydraulic performance for a given structure. Other approaches, such as topology optimisation, can also be used to design heat exchange devices for specific applications and may be more suitable than the simple inclusion of TPMS-based lattice structures within heat sinks. This requires further study.

Finally, high heat flux components featuring TPMS-based lattice structures need to undergo extensive validation and testing in fusion relevant environments (e.g., at high heat fluxes and neutron irradiation doses). This is to ensure that these high heat flux components function as predicted by the fundamental research and that it can survive for their planned lifetime over numerous thermal cycles.

Bibliography

[1] Antonius Johannes Donné. "European Research Roadmap to the Realisation of Fusion Energy". In: *EUROfusion* (2018).

[2] Francesco Romanelli, Pietro Barabaschi, Duarte Borba et al. *Fusion Electricity: A roadmap to the realization of fusion energy*. 2012.

[3] J. H. You, E. Visca, Ch Bachmann et al. "European DEMO divertor target: Operational requirements and material-design interface". In: *Nuclear Materials and Energy* 9 (2016), pp. 171–176.

[4] Jeong-Ha You. "A review on two previous divertor target concepts for DEMO: mutual impact between structural design requirements and materials performance". In: *Nuclear Fusion* 55.11 (2015), p. 113026.

[5] J.H. You, G. Mazzone, E. Visca et al. "Divertor of the European DEMO: Engineering and technologies for power exhaust". In: *Fusion Engineering and Design* 175 (2022), p. 113010.

[6] Ian Gibson, David Rosen and Brent Stucker. *Additive manufacturing technologies: 3D printing, rapid prototyping, and direct digital manufacturing, second edition*. eng. Ed. by D. W. (David W.) Rosen and B. (Brent) Stucker. 2nd ed. New York: Springer, 2015, pp. 1–498.

[7] M. F. Ashby. *Metal foams : a design guide*. eng. Ed. by M. F Ashby. Oxford: Butterworth-Heinemann, 2000.

[8] T.J. Lu, H.A. Stone and M.F. Ashby. "Heat transfer in open-cell metal foams". In: *Acta Materialia* 46.10 (1998), pp. 3619–3635.

[9] J. Tian, T.J. Lu, H.P. Hodson et al. "Cross flow heat exchange of textile cellular metal core sandwich panels". In: *International Journal of Heat and Mass Transfer* 50.13-14 (2007), pp. 2521–2536.

[10] Haydn N.G. Wadley and Douglas T Queheillalt. "Thermal Applications of Cellular Lattice Structures". In: *Materials Science Forum* 539-543 (2007), pp. 242–247.

[11] Oraib Al-Ketan, Reza Rowshan and Rashid K. Abu Al-Rub. "Topology-mechanical property relationship of 3D printed strut, skeletal, and sheet based periodic metallic cellular materials". In: *Additive Manufacturing* 19 (2018), pp. 167–183.

[12] Wei Tang, Hua Zhou, Yun Zeng et al. "Analysis on the convective heat transfer process and performance evaluation of Triply Periodic Minimal Surface (TPMS) based on Diamond, Gyroid and Iwp". In: *International Journal of Heat and Mass Transfer* 201 (2023), p. 123642.

[13] Kirttayoth Yeranee and Yu Rao. "A Review of Recent Investigations on Flow and Heat Transfer Enhancement in Cooling Channels Embedded with Triply Periodic Minimal Surfaces (TPMS)". In: *Energies* 15.23 (2022), p. 8994.

[14] *OpenFOAM*. URL: https://www.openfoam.com/ (visited on 02/02/2022).

[15] ISO/ASTM 52900. "Additive manufacturing — General principles — Terminology". In: (2018).

[16] Mika Salmi. "Additive Manufacturing Processes in Medical Applications". In: *Materials* 14.1 (2021), p. 191.

[17] Amir A. Zadpoor and Jos Malda. "Additive Manufacturing of Biomaterials, Tissues, and Organs". In: *Annals of Biomedical Engineering* 45.1 (2017), pp. 1–11.

[18] A.B.V. Pettersson, M. Salmi, P. Vallittu et al. "Main Clinical Use of Additive Manufacturing (Three-Dimensional Printing) in Finland Restricted to the Head and Neck Area in 2016–2017". In: *Scandinavian Journal of Surgery* 109.2 (2020), pp. 166–173.

[19] Julia Jockusch and Mutlu Özcan. "Additive manufacturing of dental polymers: An overview on processes, materials and applications". In: *Dental Materials Journal* 39.3 (2020), pp. 345–354.

[20] Byron Blakey-Milner, Paul Gradl, Glen Snedden et al. "Metal additive manufacturing in aerospace: A review". In: *Materials & Design* 209 (2021), p. 110008.

[21] General Electric. *New manufacturing milestone: 30,000 additive fuel nozzles*. 2018. URL: https://www.ge.com/additive/stories/new-manufacturing-milestone-30000-additive-fuel-nozzles (visited on 25/01/2022).

[22] David Hancock, David Homfray, Michael Porton et al. "Refractory metals as structural materials for fusion high heat flux components". In: *Journal of Nuclear Materials* 512 (2018), pp. 169–183.

[23] Marco Grasso and Bianca Maria Colosimo. "Process defects and in situ monitoring methods in metal powder bed fusion: a review". In: *Measurement Science and Technology* 28.4 (2017), p. 044005.

[24] Fabrizia Caiazzo, Vittorio Alfieri and Giuseppe Casalino. "On the Relevance of Volumetric Energy Density in the Investigation of Inconel 718 Laser Powder Bed Fusion". In: *Materials* 13.3 (2020), p. 538.

[25] Tao Yang, Tingting Liu, Wenhe Liao et al. "Laser powder bed fusion of AlSi10Mg: Influence of energy intensities on spatter and porosity evolution, microstructure and mechanical properties". In: *Journal of Alloys and Compounds* 849 (2020), p. 156300.

[26] Liping Zheng, Qi Zhang, Hongzhong Cao et al. "Melt pool boundary extraction and its width prediction from infrared images in selective laser melting". In: *Materials & Design* 183 (2019), p. 108110.

[27] Dirk Herzog, Vanessa Seyda, Eric Wycisk et al. "Additive manufacturing of metals". In: *Acta Materialia* 117 (2016), pp. 371–392.

[28] Mike Ashby, Hugh Shercliff and David Cebon. *Materials : engineering, science, processing and design*. 3rd Editio. Oxford : Butterworth-Heinemann, 2014.

[29] Donald Askeland and Wendelin Wright. *Essentials of materials science and engineering*. 3rd Editio. Stamford, Conn. ; Andover : Cengage Learning, 2014.

[30] William F. (William Fortune) Smith. *Foundations of materials science and engineering*. eng. Ed. by Javad Hashemi and Francisco Presuel-Moreno. Sixth edit. McGraw-Hill Education, 2019.

[31] Shubhavardhan Ramadurga Narasimharaju, Wenhan Zeng, Tian Long See et al. "A comprehensive review on laser powder bed fusion of steels: Processing, microstructure, defects and control methods, mechanical properties, current challenges and future trends". In: *Journal of Manufacturing Processes* 75 (2022), pp. 375–414.

[32] Pavel Krakhmalev, Gunnel Fredriksson, Krister Svensson et al. "Microstructure, Solidification Texture, and Thermal Stability of 316 L Stainless Steel Manufactured by Laser Powder Bed Fusion". In: *Metals* 8.8 (2018), p. 643.

[33] Sindo Kou. *Welding metallurgy*. eng. Third edition. John Wiley & Sons, Inc., 2021.

[34] J.-P Kruth, M Badrossamay, E Yasa et al. "Part and material properties in selective laser melting of metals". In: *Proceedings of the 16th International Symposium on Electromachining (ISEM XVI)*. SHANGHAI JIAO TONG UNIV PRESS, 2010.

[35] Fuyao Yan, Wei Xiong and Eric Faierson. "Grain Structure Control of Additively Manufactured Metallic Materials". In: *Materials* 10.11 (2017), p. 1260.

[36] Yafei Wang, Chenfan Yu, Leilei Xing et al. "Grain structure and texture of the SLM single track". In: *Journal of Materials Processing Technology* 281 (2020), p. 116591.

[37] Q.B. Nguyen, Z Zhu, F.L. Ng et al. "High mechanical strengths and ductility of stainless steel 304L fabricated using selective laser melting". In: *Journal of Materials Science & Technology* 35.2 (2019), pp. 388–394.

[38] Raya Mertens, Stijn Clijsters, Karolien Kempen et al. "Optimization of Scan Strategies in Selective Laser Melting of Aluminum Parts With Downfacing Areas". In: *Journal of Manufacturing Science and Engineering* 136.6 (2014).

[39] Laura Cordova, Mónica Campos and Tiedo Tinga. "Revealing the Effects of Powder Reuse for Selective Laser Melting by Powder Characterization". In: *JOM* 71.3 (2019), pp. 1062–1072.

[40] Di Wang, Shibiao Wu, Fan Fu et al. "Mechanisms and characteristics of spatter generation in SLM processing and its effect on the properties". In: *Materials & Design* 117 (2017), pp. 121–130.

[41] Dirk Herzog, Vanessa Seyda, Eric Wycisk et al. "Additive manufacturing of metals". In: *Acta Materialia* 117 (2016), pp. 371–392.

[42] Aamer Nazir, Kalayu Mekonen Abate, Ajeet Kumar et al. "A state-of-the-art review on types, design, optimization, and additive manufacturing of cellular structures". In: *The International Journal of Advanced Manufacturing Technology* 104.9-12 (2019), pp. 3489–3510.

[43] I. Maskery, L. Sturm, A.O. Aremu et al. "Insights into the mechanical properties of several triply periodic minimal surface lattice structures made by polymer additive manufacturing". In: *Polymer* 152 (2018), pp. 62–71.

[44] Mauro Bracconi, Matteo Ambrosetti, Matteo Maestri et al. "A fundamental analysis of the influence of the geometrical properties on the effective thermal conductivity of open-cell foams". In: *Chemical Engineering and Processing - Process Intensification* 129 (2018), pp. 181–189.

[45] Lorna J Gibson. *Cellular solids : structure and properties*. eng. Ed. by M. F Ashby. 2nd ed. Cambridge solid state science series. Cambridge: Cambridge University Press, 1997.

[46] Anatolie Timercan, Vadim Sheremetyev and Vladimir Brailovski. "Mechanical properties and fluid permeability of gyroid and diamond lattice structures for intervertebral devices: functional requirements and comparative analysis". In: *Science and Technology of Advanced Materials* 22.1 (2021), pp. 285–300.

[47] I. Maskery, L.A. Parry, D. Padrão et al. "FLatt Pack: A research-focussed lattice design program". In: *Additive Manufacturing* 49 (2022), p. 102510.

[48] Meinhard Wohlgemuth, Nataliya Yufa, James Hoffman et al. "Triply Periodic Bicontinuous Cubic Microdomain Morphologies by Symmetries". In: *Macromolecules* 34.17 (2001), pp. 6083–6089.

[49] Paul J.F. Gandy, Sonny Bardhan, Alan L Mackay et al. "Nodal surface approximations to the P,G,D and I-WP triply periodic minimal surfaces". In: *Chemical Physics Letters* 336.3-4 (2001), pp. 187–195.

[50] I. Maskery, A.O. Aremu, L. Parry et al. "Effective design and simulation of surface-based lattice structures featuring volume fraction and cell type grading". In: *Materials & Design* 155 (2018), pp. 220–232.

[51] Oraib Al-Ketan, Dong-Wook Lee, Reza Rowshan et al. "Functionally graded and multi-morphology sheet TPMS lattices: Design, manufacturing, and mechanical properties". In: *Journal of the Mechanical Behavior of Biomedical Materials* 102 (2020), p. 103520.

[52] B.A. Jasperson, Yongho Jeon, K.T. Turner et al. "Comparison of Micro-Pin-Fin and Microchannel Heat Sinks Considering Thermal-Hydraulic Performance and Manufacturability". In: *IEEE Transactions on Components and Packaging Technologies* 33.1 (2010), pp. 148–160.

[53] David Hancock, David Homfray, Michael Porton et al. "Exploring complex high heat flux geometries for fusion applications enabled by additive manufacturing". In: *Fusion Engineering and Design* 136 (2018), pp. 454–460.

[54] Xiangjie Chen, Yuehong Su, David Reay et al. "Recent research developments in polymer heat exchangers – A review". In: *Renewable and Sustainable Energy Reviews* 60 (2016), pp. 1367–1386.

[55] Curtis K Stimpson, Jacob C Snyder, Karen A Thole et al. "Roughness Effects on Flow and Heat Transfer for Additively Manufactured Channels". In: *Journal of Turbomachinery* 138.5 (2016).

[56] Alexander J Wildgoose, Karen A Thole, Paul Sanders et al. "Impact of Additive Manufacturing on Internal Cooling Channels With Varying Diameters and Build Directions". In: *Journal of Turbomachinery* 143.7 (2021).

[57] Daniel Bacellar, Vikrant Aute, Zhiwei Huang et al. "Design optimization and validation of high-performance heat exchangers using approximation assisted optimization and additive manufacturing". In: *Science and Technology for the Built Environment* 23.6 (2017), pp. 896–911.

[58] Davoud Jafari and Wessel W. Wits. "The utilization of selective laser melting technology on heat transfer devices for thermal energy conversion applications: A review". In: *Renewable and Sustainable Energy Reviews* 91 (2018), pp. 420–442.

[59] Kathryn L Kirsch and Karen A Thole. "Pressure loss and heat transfer performance for additively and conventionally manufactured pin fin arrays". In: *International Journal of Heat and Mass Transfer* 108 (2017), pp. 2502–2513.

[60] Zhiyong Wu, Cyril Caliot, Fengwu Bai et al. "Experimental and numerical studies of the pressure drop in ceramic foams for volumetric solar receiver applications". In: *Applied Energy* 87.2 (2010), pp. 504–513.

[61] Benjamin Dietrich, Wilhelm Schabel, Matthias Kind et al. "Pressure drop measurements of ceramic sponges-Determining the hydraulic diameter". In: *Chemical Engineering Science* 64 (2009), pp. 3633–3640.

[62] R. Viskanta, X.Fu and J.P. Gore. "Measurement and correlation of volumetric heat transfer coefficients of cellular ceramics". In: *Experimental Thermal and Fluid Science* 17.4 (1998), pp. 285–293.

[63] Zhiyong Wu, Cyril Caliot, Gilles Flamant et al. "Numerical simulation of convective heat transfer between air flow and ceramic foams to optimise volumetric solar air receiver performances". In: *International Journal of Heat and Mass Transfer* 54.7-8 (2011), pp. 1527–1537.

[64] Kevin J. Maloney, Kathryn D. Fink, Tobias A. Schaedler et al. "Multifunctional heat exchangers derived from three-dimensional micro-lattice structures". In: *International Journal of Heat and Mass Transfer* 55.9-10 (2012), pp. 2486–2493.

[65] J.Y. Ho, K.C. Leong and T.N. Wong. "Additively-manufactured metallic porous lattice heat exchangers for air-side heat transfer enhancement". In: *International Journal of Heat and Mass Transfer* 150 (2020), p. 119262.

[66] Tisha Dixit, Perumal Nithiarasu and S. Kumar. "Numerical evaluation of additively manufactured lattice architectures for heat sink applications". In: *International Journal of Thermal Sciences* 159 (2021), p. 106607.

[67] Scott M Thompson, Zachary S Aspin, Nima Shamsaei et al. "Additive manufacturing of heat exchangers: A case study on a multi-layered Ti–6Al–4V oscillating heat pipe". In: *Additive Manufacturing* 8 (2015), pp. 163–174.

[68] Hadley Brooks and Kevin Brigden. "Design of conformal cooling layers with self-supporting lattices for additively manufactured tooling". In: *Additive Manufacturing* 11 (2016), pp. 16–22.

[69] M Wong, I Owen, C.J. Sutcliffe et al. "Convective heat transfer and pressure losses across novel heat sinks fabricated by Selective Laser Melting". In: *International Journal of Heat and Mass Transfer* 52.1-2 (2009), pp. 281–288.

[70] Seo-Hyeon Oh, Jong-Wook Ha and Keun Park. "Adaptive Conformal Cooling of Injection Molds Using Additively Manufactured TPMS Structures". In: *Polymers* 14.1 (2022), p. 181.

[71] Zahid Ahmed Qureshi, Salah Addin Burhan Al Omari, Emad Elnajjar et al. "Thermal characterization of 3D-Printed lattices based on triply periodic minimal surfaces embedded with organic phase change material". In: *Case Studies in Thermal Engineering* 27 (2021), p. 101315.

[72] Zahid Ahmed Qureshi, Emad Elnajjar, Oraib Al-Ketan et al. "Heat transfer performance of a finned metal foam-phase change material (FMF-PCM) system incorporating triply periodic minimal surfaces (TPMS)". In: *International Journal of Heat and Mass Transfer* 170 (2021), p. 121001.

[73] Zahid Ahmed Qureshi, Salah Addin Burhan Al-Omari, Emad Elnajjar et al. "Architected lattices embedded with phase change materials for thermal management of high-power electronics: A numerical study". In: *Applied Thermal Engineering* 219 (2023), p. 119420.

[74] Beatrice Pulvirenti, Michele Celli and Antonio Barletta. "Flow and Convection in Metal Foams: A Survey and New CFD Results". In: *Fluids* 5.3 (2020), p. 155.

[75] Oraib Al-Ketan, Mohamed Ali, Mohamad Khalil et al. "Forced Convection Computational Fluid Dynamics Analysis of Architected and Three-Dimensional Printable Heat Sinks Based on Triply Periodic Minimal Surfaces". In: *Journal of Thermal Science and Engineering Applications* 13.2 (2021).

[76] Zhilong Cheng, Ruina Xu and Pei-Xue Jiang. "Morphology, flow and heat transfer in triply periodic minimal surface based porous structures". In: *International Journal of Heat and Mass Transfer* 170 (2021), p. 120902.

[77] Reza Attarzadeh, Marc Rovira and Christophe Duwig. "Design analysis of the "Schwartz D" based heat exchanger: A numerical study". In: *International Journal of Heat and Mass Transfer* 177 (2021), p. 121415.

[78] Inderjot Kaur and Prashant Singh. "Flow and thermal transport characteristics of Triply-Periodic Minimal Surface (TPMS)-based gyroid and Schwarz-P cellular materials". In: *Numerical Heat Transfer, Part A: Applications* 79.8 (2021), pp. 553–569.

[79] Tim Femmer, Alexander J.C. Kuehne and Matthias Wessling. "Estimation of the structure dependent performance of 3-D rapid prototyped membranes". In: *Chemical Engineering Journal* 273 (2015), pp. 438–445.

[80] Wenguang Li, Weihong Li and Zhibin Yu. "Heat transfer enhancement of water-cooled triply periodic minimal surface heat exchangers". In: *Applied Thermal Engineering* 217 (2022), p. 119198.

[81] Reza Attarzadeh, Seyed-Hosein Attarzadeh-Niaki and Christophe Duwig. "Multi-objective optimization of TPMS-based heat exchangers for low-temperature waste heat recovery". In: *Applied Thermal Engineering* 212 (2022), p. 118448.

[82] Nihad Dukhan and Carel A. Minjeur. "A two-permeability approach for assessing flow properties in metal foam". In: *Journal of Porous Materials* 18.4 (2011), pp. 417–424.

[83] Jorge Santos, Tiago Pires, Bárbara P Gouveia et al. "On the permeability of TPMS scaffolds". In: *Journal of the Mechanical Behavior of Biomedical Materials* 110 (2020), p. 103932.

[84] A. Della Torre, G. Montenegro, G.R. Tabor et al. "CFD characterization of flow regimes inside open cell foam substrates". In: *International Journal of Heat and Fluid Flow* 50 (2014), pp. 72–82.

[85] Joel H. Ferziger, Milovan Perić and Robert L. Street. *Computational Methods for Fluid Dynamics*. 4th. Cham: Springer International Publishing, 2020.

[86] S. Li, H. Jiang, Z. Ren et al. "Optimal Tracking for a Divergent-Type Parabolic PDE System in Current Profile Control". In: *Abstract and Applied Analysis* 2014 (2014), pp. 1–8.

[87] R. Behrisch, J. Roth, G. Staudenmaier et al. "Sputtering in fusion devices". In: *Nuclear Instruments and Methods in Physics Research Section B: Beam Interactions with Materials and Atoms* 18.1-6 (1986), pp. 629–638.

[88] Jean Paul Allain and David N. Ruzic. "Fundamentals of Plasma-Material Interactions in Magnetic Fusion Devices". In: *Plasma Science and Technology - Basic Fundamentals and Modern Applications*. IntechOpen, 2019.

[89] D. Stork, R. Heidinger, T. Muroga et al. "Towards a programme of testing and qualification for structural and plasma-facing materials in 'fusion neutron' environments". In: *Nuclear Fusion* 57.9 (2017).

[90] European Commission and Directorate-General for Energy. "Foresight study on the worldwide developments in advancing fusion energy, including the small scale private initiatives." In: *Publications Office of the European Union* (2023).

[91] *JET: the Joint European Torus*. URL: https://ccfe.ukaea.uk/programmes/joint-european-torus/ (visited on 23/03/2023).

[92] Elizabeth Gibney. "Nuclear-fusion reactor smashes energy record". In: *Nature* 602.7897 (2022), pp. 371–371.

[93] *What will ITER do ?* URL: https://www.iter.org/sci/Goals (visited on 13/11/2019).

[94] *MAST Upgrade*. URL: https://ccfe.ukaea.uk/programmes/mast-upgrade/ (visited on 23/03/2023).

[95] *MAST Upgrade Research Plan*. 2019. URL: https://ccfe.ukaea.uk/wp-content/uploads/2019/12/MAST-U_RP_2019_v1.pdf (visited on 23/03/2023).

[96] *STEP*. URL: https://ccfe.ukaea.uk/programmes/step/ (visited on 23/03/2023).

[97] *STEP - Spherical Tokamak for Energy Production*. URL: https://step.ukaea.uk/ (visited on 23/03/2023).

[98] *ST40 achieves 15-million-degree target*. 2018. URL: https://world-nuclear-news.org/Articles/ST40-achieves-15-million-degree-target (visited on 23/03/2023).

[99] *Our technology*. URL: https://www.tokamakenergy.co.uk/technology/ (visited on 23/03/2023).

[100] *HTS magnet technology*. URL: https://www.tokamakenergy.co.uk/magnets/ (visited on 23/03/2023).

[101] T. Hirai, V. Barabash, F. Escourbiac et al. "ITER divertor materials and manufacturing challenges". In: *Fusion Engineering and Design* 125 (2017), pp. 250–255.

[102] *Limiters and Divertors — EFDA*. URL: https://web.archive.org/web/20140110094526/http://www.efda.org/fusion/focus-on/limiters-and-divertors/ (visited on 14/11/2019).

[103] R.A. Pitts, X. Bonnin, F. Escourbiac et al. "Physics basis for the first ITER tungsten divertor". In: *Nuclear Materials and Energy* 20 (2019), p. 100696.

[104] S.J Zinkle and N.M Ghoniem. "Operating temperature windows for fusion reactor structural materials". In: *Fusion Engineering and Design* 51-52 (2000), pp. 55–71.

[105] Kohei Tsuchida, Takeshi Miyazawa, Akira Hasegawa et al. "Recrystallization behavior of hot-rolled pure tungsten and its alloy plates during high-temperature annealing". In: *Nuclear Materials and Energy* 15 (2018), pp. 158–163.

[106] Fusion For Energy. *European prototypes for ITER Divertor Cassette completed - Fusion for Energy*. 2018. URL: https://fusionforenergy.europa.eu/news/european-prototypes-for-iter-divertor-cassette-completed/ (visited on 16/09/2023).

[107] T. Hirai, F. Escourbiac, S. Carpentier-Chouchana et al. "ITER tungsten divertor design development and qualification program". In: *Fusion Engineering and Design* 88.9-10 (2013), pp. 1798–1801.

[108] T. Hirai, F. Escourbiac, V. Barabash et al. "Status of technology R&D for the ITER tungsten divertor monoblock". In: *Journal of Nuclear Materials* 463 (2015), pp. 1248–1251.

[109] Hongyu Zhang, Jizhong Sun, Yingmin Wang et al. "Study of lattice thermal conductivity of tungsten containing bubbles by molecular dynamics simulation". In: *Fusion Engineering and Design* 161 (2020), p. 112004.

[110] Yingmei Ding, Xuebang Wu, Jie Zhan et al. "Simulation study of effects of grain boundary and helium bubble on lattice thermal resistance of tungsten". In: *Fusion Engineering and Design* 168 (2021), p. 112682.

[111] Ch. Linsmeier, M. Rieth, J. Aktaa et al. "Development of advanced high heat flux and plasma-facing materials". In: *Nuclear Fusion* 57.9 (2017), p. 092007.

[112] A.R. Raffray, R. Nygren, D.G. Whyte et al. "High heat flux components—Readiness to proceed from near term fusion systems to power plants". In: *Fusion Engineering and Design* 85.1 (2010), pp. 93–108.

[113] Jens Reiser and Michael Rieth. "Optimization and limitations of known DEMO divertor concepts". In: *Fusion Engineering and Design* 87.5-6 (2012), pp. 718–721.

[114] T Ihli, R Kruessmann, I Ovchinnikov et al. "An advanced He-cooled divertor concept: Design, cooling technology, and thermohydraulic analyses with CFD". In: *Fusion Engineering and Design* 75-79 (2005), pp. 371–375.

[115] M. Zhao, B. Ghidersa and R. Stieglitz. "CFD evaluation and optimization of the HEMJ divertor cooling design". In: *Fusion Engineering and Design* 158 (2020), p. 111669.

[116] J.R. Nicholas, P.T. Ireland, D. Hancock et al. "Development of a heat sink module for a near-term DEMO divertor". In: *Fusion Engineering and Design* 133 (2018), pp. 77–88.

[117] P. Rindt, J.L. van den Eijnden, T.W. Morgan et al. "Conceptual design of a liquid-metal divertor for the European DEMO". In: *Fusion Engineering and Design* 173 (2021), p. 112812.

[118] J.H. You, E Visca, T Barrett et al. "European divertor target concepts for DEMO: Design rationales and high heat flux performance". In: *Nuclear Materials and Energy* 16 (2018), pp. 1–11.

[119] THE MANUFACTURING TECHNOLOGY CENTRE LIMITED. *Final Report Summary - AMAZE (Additive Manufacturing Aiming Towards Zero Waste & Efficient Production of High-Tech Metal Products)*. URL: https://cordis.europa.eu/project/id/313781/reporting (visited on 28/04/2020).

[120] Nobuyoshi TSUZUKI, Yasuyoshi KATO, Konstantin NIKITIN et al. "Advanced Microchannel Heat Exchanger with S-shaped Fins". In: *Journal of Nuclear Science and Technology* 46.5 (2009), pp. 403–412.

[121] Bailey Curzadd, Alexander von Müller, Rudolf Neu et al. "Topology optimization of tungsten/copper structures for plasma-facing component applications". In: *Nuclear Fusion* 59.8 (2019).

[122] Kim Boldt. *Aerodynamic measurements: Boundary layer components - GRAS*. 2022. URL: https://www.grasacoustics.com/blog/aerodynamic-measurements-components-of-the-boundary-layer (visited on 09/01/2023).

[123] J.P. Holman. *Heat Transfer*. 10th. Boston, Mass. ; London : McGraw-Hill, 2010.

[124] M. J. (Martin J.) Rhodes. *Introduction to particle technology*. eng. Ed. by ProQuest (Firm). 2nd ed. Chichester, England ; Hoboken, NJ: Wiley, 2008.

[125] Chris Greenshields. *OpenFOAM v6 User Guide: 5.4 Meshing with snappyHexMesh*. 2018. URL: https://cfd.direct/openfoam/user-guide/v6-snappyhexmesh/ (visited on 12/05/2021).

[126] *QuickMesh - Feature Overview*. URL: https://quickmesh.co.jp/en/features_overview.html (visited on 29/03/2023).

[127] Thomas Adams, Christopher Grant and Heather Watson. "A Simple Algorithm to Relate Measured Surface Roughness to Equivalent Sand-grain Roughness". In: *International Journal of Mechanical Engineering and Mechatronics* 1.1 (2012).

[128] Bastien Vayssette, Nicolas Saintier, Charles Brugger et al. "Surface roughness effect of SLM and EBM Ti-6Al-4V on multiaxial high cycle fatigue". In: *Theoretical and Applied Fracture Mechanics* 108 (2020), p. 102581.

[129] P. Edwards and M. Ramulu. "Fatigue performance evaluation of selective laser melted Ti–6Al–4V". In: *Materials Science and Engineering: A* 598 (2014), pp. 327–337.

[130] Kwai S. Chan, Marie Koike, Robert L. Mason et al. "Fatigue Life of Titanium Alloys Fabricated by Additive Layer Manufacturing Techniques for Dental Implants". In: *Metallurgical and Materials Transactions A* 44.2 (2013), pp. 1010–1022.

[131] Chuan Guo, Sheng Li, Shi Shi et al. "Effect of processing parameters on surface roughness, porosity and cracking of as-built IN738LC parts fabricated by laser powder bed fusion". In: *Journal of Materials Processing Technology* 285 (2020), p. 116788.

[132] Salvatore P. Sutera and Richard Skalak. "The History of Poiseuille's Law". In: *Annual Review of Fluid Mechanics* 25.1 (1993), pp. 1–20.

[133] Sabri Ergun. "Fluid flow through packed columns". In: *Chem. Eng. Progress.* 48 (1952), pp. 89–94.

[134] Frank P Incropera and David P DeWitt. *Fundamentals of Heat and Mass Transfer*. 6th. Hoboken, N.J. : Wiley, 2007.

[135] S P Mahulikar and H Herwig. "Fluid friction in incompressible laminar convection: Reynolds' analogy revisited for variable fluid properties". In: *The European Physical Journal B* 62.1 (2008), pp. 77–86.

[136] Ahmet Cecen. *Tortuosity-MATLAB*. 2015. URL: https://github.com/ahmetcecen/Tortuosity-MATLAB (visited on 31/01/2023).

[137] Roman Casero. *vigente/gerardus*. 2010. URL: https://github.com/vigente/gerardus (visited on 31/01/2023).

[138] Adam Aitkenhead. *Plot a 3D array using patch - File Exchange - MATLAB Central*. 2012. URL: https://uk.mathworks.com/matlabcentral/fileexchange/28497-plot-a-3d-array-using-patch (visited on 31/01/2023).

[139] William E. Lorensen and Harvey E. Cline. "Marching cubes: A high resolution 3D surface construction algorithm". In: *Proceedings of the 14th annual conference on Computer graphics and interactive techniques - SIGGRAPH '87*. Vol. 21. 4. New York, New York, USA: ACM Press, 1987, pp. 163–169.

[140] *MATLAB: bwskel*. URL: https://uk.mathworks.com/help/images/ref/bwskel.html (visited on 09/02/2023).

[141] P Gavila, B Riccardi, S Constans et al. "High heat flux testing of mock-ups for a full tungsten ITER divertor". In: *Fusion Engineering and Design* 86.9-11 (2011), pp. 1652–1655.

[142] H. Greuner, H. Bolt, B. Böswirth et al. "Design, performance and construction of a 2MW ion beam test facility for plasma facing components". In: *Fusion Engineering and Design* 75-79.SUPPL. (2005), pp. 345–350.

[143] V. Kuznetsov, A. Gorbenko, V. Davydov et al. "Status of the IDTF high-heat-flux test facility". In: *Fusion Engineering and Design* 89.7-8 (2014), pp. 955–959.

[144] Gerald Pintsuk, Maja Bednarek, Pierre Gavila et al. "Characterization of ITER tungsten qualification mock-ups exposed to high cyclic thermal loads". In: *Fusion Engineering and Design* 98-99 (2015), pp. 1384–1388.

[145] David Hancock, David Homfray, Michael Porton et al. "Testing Advanced Divertor Concepts for Fusion Power Plants Using a Small High Heat Flux Facility". In: *Journal of Testing and Evaluation* (2018).

[146] S. (Stanley) Zinn and S. L. Semiatin. *Elements of induction heating design, control, and applications*. eng. Ed. by S. L Semiatin, Electric Power Research Institute, Battelle Memorial Institute. Columbus Laboratories et al. Polo Alto, CA : Metals Park, OH: Electric Power Research Institute ; ASM International, 1988.

[147] K Flinders, R Bamber, H Lewtas et al. "Characterising the Impact of First Wall Armor Castellations on Inductive High Heat Flux Testing in the HIVE Facility". In: *Eurofusion* 18 (2018).

[148] A.N.D. Gasper, B Szost, X Wang et al. "Spatter and oxide formation in laser powder bed fusion of Inconel 718". In: *Additive Manufacturing* 24 (2018), pp. 446–456.

[149] Zhengkai Xu, C.J. Hyde, A Thompson et al. "Staged thermomechanical testing of nickel superalloys produced by selective laser melting". In: *Materials & Design* 133 (2017), pp. 520–527.

[150] Zhengkai Xu, C.J. Hyde, C Tuck et al. "Creep behaviour of inconel 718 processed by laser powder bed fusion". In: *Journal of Materials Processing Technology* 256 (2018), pp. 13–24.

[151] S Catchpole-Smith, N Aboulkhair, L Parry et al. "Fractal scan strategies for selective laser melting of 'unweldable' nickel superalloys". In: *Additive Manufacturing* 15 (2017), pp. 113–122.

[152] N. Anbarasan, Bikash Kumar Gupta, S. Prakash et al. "Effect of Heat Treatment on the Microstructure and Mechanical Properties of Inconel 718". In: *Materials Today: Proceedings* 5.2 (2018), pp. 7716–7724.

[153] Saeede Ghorbanpour, Kaustubh Deshmukh, Saswat Sahu et al. "Additive manufacturing of functionally graded inconel 718: Effect of heat treatment and building orientation on microstructure and fatigue behaviour". In: *Journal of Materials Processing Technology* 306 (2022), p. 117573.

[154] Wenpu Huang, Jingjing Yang, Huihui Yang et al. "Heat treatment of Inconel 718 produced by selective laser melting: Microstructure and mechanical properties". In: *Materials Science and Engineering: A* 750 (2019), pp. 98–107.

[155] Special Metals Corporation. *INCONEL alloy 718 data sheet*. 2007. URL: https://www.specialmetals.com/documents/technical-bulletins/inconel/inconel-alloy-718.pdf (visited on 16/02/2023).

[156] Amgad Salama. "Velocity Profile Representation for Fully Developed Turbulent Flows in Pipes: A Modified Power Law". In: *Fluids* 6.10 (2021), p. 369.

[157] Serkan Solmaz. *Turbulence Models: Which Should I Select?* 2022. URL: https://www.simscale.com/blog/turbulence-cfd-analysis/ (visited on 17/02/2023).

[158] SimScale. *K-Omega and K-Omega SST — Global Settings — SimScale*. 2021. URL: https://www.simscale.com/docs/simulation-setup/global-settings/k-omega-sst/ (visited on 17/02/2023).

[159] C. F. Colebrook and C. M. White. "Experiments with fluid friction in roughened pipes". In: *Proceedings of the Royal Society of London. Series A - Mathematical and Physical Sciences* 161.906 (1937), pp. 367–381.

[160] C. F. Colebrook. "Turbulent Flow in Pipes, with particular reference to the Tansition Region Between the Smooth and Rough Pipe Laws". In: *Journal of the Institution of Civil Engineers* 11.4 (1939), pp. 133–156.

[161] A. Sh Agazhanov, D. A. Samoshkin and Yu M. Kozlovskii. "Thermophysical properties of Inconel 718 alloy". In: *Journal of Physics: Conference Series* 1382.1 (2019), p. 012175.

[162] E. M. Savitskii and G. S. Burkhanov. *Physical Metallurgy of Refractory Metals and Alloys*. Boston, MA: Springer US, 1995.

[163] J. Reiser, M. Rieth, B. Dafferner et al. "Charpy impact properties of pure tungsten plate material in as-received and recrystallized condition (1h at 2000 degrees Celsius (2273K))". In: *Journal of Nuclear Materials* 442.1-3 (2013), S204–S207.

[164] S. Gonderman, J.K. Tripathi, T.J. Novakowski et al. "Effect of dual ion beam irradiation (helium and deuterium) on tungsten–tantalum alloys under fusion relevant conditions". In: *Nuclear Materials and Energy* 12 (2017), pp. 346–352.

[165] Ravi K. Enneti, Rick Morgan and Sundar V. Atre. "Effect of process parameters on the Selective Laser Melting (SLM) of tungsten". In: *International Journal of Refractory Metals and Hard Materials* 71 (2018), pp. 315–319.

[166] D. Faidel, D. Jonas, G. Natour et al. "Investigation of the selective laser melting process with molybdenum powder". In: *Additive Manufacturing* 8 (2015), pp. 88–94.

[167] Andreas Gebhardt. *Understanding Additive Manufacturing: Rapid Prototyping – Rapid Tooling – Rapid Manufacturing*. Carl Hanser Verlag, 2011.

[168] Sohini Chowdhury, N. Yadaiah, Chander Prakash et al. "Laser powder bed fusion: a state-of-the-art review of the technology, materials, properties & defects, and numerical modelling". In: *Journal of Materials Research and Technology* 20 (2022), pp. 2109–2172.

[169] Chaolin Tan, Kesong Zhou, Wenyou Ma et al. "Selective laser melting of high-performance pure tungsten: parameter design, densification behavior and mechanical properties". In: *Science and Technology of Advanced Materials* 19.1 (2018), pp. 370–380.

[170] Shifeng Wen, Chong Wang, Yan Zhou et al. "High-density tungsten fabricated by selective laser melting: Densification, microstructure, mechanical and thermal performance". In: *Optics & Laser Technology* 116 (2019), pp. 128–138.

[171] A. V. Müller, G. Schlick, R. Neu et al. "Additive manufacturing of pure tungsten by means of selective laser beam melting with substrate preheating temperatures up to 1000 degrees Celsius". In: *Nuclear Materials and Energy* 19 (2019), pp. 184–188.

[172] Dianzheng Wang, Chenfan Yu, Jing Ma et al. "Densification and crack suppression in selective laser melting of pure molybdenum". In: *Materials & Design* 129 (2017), pp. 44–52.

[173] L. Kaserer, Jakob Braun, J. Stajkovic et al. "Fully dense and crack free molybdenum manufactured by Selective Laser Melting through alloying with carbon". In: *International Journal of Refractory Metals and Hard Materials* 84 (2019), p. 105000.

[174] J. Braun, L. Kaserer, J. Stajkovic et al. "Molybdenum and tungsten manufactured by selective laser melting: Analysis of defect structure and solidification mechanisms". In: *International Journal of Refractory Metals and Hard Materials* 84 (2019), p. 104999.

[175] Swee Leong Sing, Florencia Edith Wiria and Wai Yee Yeong. "Selective laser melting of titanium alloy with 50 wt% tantalum: Effect of laser process parameters on part quality". In: *International Journal of Refractory Metals and Hard Materials* 77 (2018), pp. 120–127.

[176] G T Gray, C M Knapp, D. R. Jones et al. "Structure/property characterization of spallation in wrought and additively manufactured tantalum". In: *Journal of Applied Physics*. Vol. 120. 2018, p. 060002.

[177] Libo Zhou, Tiechui Yuan, Ruidi Li et al. "Selective laser melting of pure tantalum: Densification, microstructure and mechanical behaviors". In: *Materials Science and Engineering: A* 707 (2017), pp. 443–451.

[178] Veronica Livescu, Cameron M. Knapp, George T. Gray et al. "Additively manufactured tantalum microstructures". In: *Materialia* 1 (2018), pp. 15–24.

[179] Jialin Yang. "Selective laser melting additive manufacturing of advanced nuclear materials V-6Cr-6Ti". In: *Materials Letters* 209 (2017), pp. 268–271.

[180] Jialin Yang and Jingfeng Li. "Fabrication and Analysis of Vanadium-Based Metal Powders for Selective Laser Melting". In: *Journal of Minerals and Materials Characterization and Engineering* 06.01 (2018), pp. 50–59.

[181] Leonhard Hitzler, Frank Alifui-Segbaya, Philipp Williams et al. "Additive Manufacturing of Cobalt-Based Dental Alloys: Analysis of Microstructure and Physicomechanical Properties". In: *Advances in Materials Science and Engineering* 2018 (2018), pp. 1–12.

[182] J. Thomas, J.E. Mogonye, S.A. Mantri et al. "Additive manufacturing of compositionally graded laser deposited titanium-chromium alloys". In: *Additive Manufacturing* 33 (2020), p. 101132.

[183] F Moukalled, L Mangani and M Darwish. *The Finite Volume Method in Computational Fluid Dynamics*. Vol. 113. Fluid Mechanics and Its Applications. Cham: Springer International Publishing, 2016.

[184] Michael A. Leschziner. “Reynolds-Averaged Navier-Stokes Methods”. In: *Encyclopedia of Aerospace Engineering*. Chichester, UK: John Wiley & Sons, Ltd, 2010.

[185] George K El Khoury, Philipp Schlatter, Azad Noorani et al. “Direct Numerical Simulation of Turbulent Pipe Flow at Moderately High Reynolds Numbers”. In: *Flow, Turbulence and Combustion* 91.3 (2013), pp. 475–495.

[186] Myoungkyu Lee and Robert D. Moser. “Direct numerical simulation of turbulent channel flow up to”. In: *Journal of Fluid Mechanics* 774 (2015), pp. 395–415.

[187] PHILIPP SCHLATTER and RAMIS ÖRLÜ. “Assessment of direct numerical simulation data of turbulent boundary layers”. In: *Journal of Fluid Mechanics* 659 (2010), pp. 116–126.

[188] Alexander J Smits and Ivan Marusic. “Wall-bounded turbulence”. In: *Physics Today* 66.9 (2013), pp. 25–30.

[189] Seyed Mostafa Ghiaasiaan. *Convective heat and mass transfer*. eng. Cambridge University Press, 2011.

[190] Donald A Nield and Adrian Bejan. *Convection in Porous Media*. eng. 5th ed. 20. Cham: Springer International Publishing, 2017.

Appendix A

Fusion relevant materials

As discussed in section 3.3, the substructure material will have a large impact on the thermal performance of the divertor. Ideal materials to be used in the substructure of a divertor component should therefore have the following general properties [4, 101]:

- High thermal conductivity.
- Adequate mechanical properties to sustain structural integrity under all operational conditions.
- High vacuum compatibility (e.g., low outgassing rate in a vacuum).
- High corrosion resistance.
- Sufficient manufacturability and joining (fabrication, brazing, re-welding, etc.).
- Industrial availability.

Finding materials that satisfy this extensive list has proven to be quite challenging, especially when there is a lack of material data from fusion specific neutron sources [22]. Hence, a selection of fusion relevant materials must be based on a comprehensive assessment of the various functional, operational and technological requirements for a specific application [101]. A particular focus is made on selecting materials that have high thermal conductivities, low sputtering yields and sufficient mechanical properties under neutron irradiation for DEMO [111].

Hancock *et al* [22] proposed that a parallel strengths, weaknesses, opportunities and threats analysis is needed to maintain a healthy selection of candidate materials in the absence of complete data. Employing this downselection method, shown in figure A.1, leads to the primary candidate materials being the refractory metals vanadium (V), chromium (Cr), tantalum (Ta), molybdenum (Mo), and tungsten (W). Despite molybdenum having a problematic activation (due to a long lived isotope), it is not discarded as it can be used as a minor alloying element to improve the performance of other candidate materials. It is interesting to note that the currently preferred structural materials, such as CuCrZr and steels, are not selected by this method.

Refractory metals typically have favourable thermophysical properties, such as high melting temperatures and thermal conductivities, making them good candidates for the structural material in the divertor target. They have been historically ignored when designing high heat flux components for fusion however, due to concerns regarding their activation and manufacturability, and a lack of data on their alloys [22]. They also have a very high DBTT, due to their

body-centered cubic crystal structure [162], which increases as they are activated. It is therefore important to continue research on the applications of refractory metals for high heat flux components in the absence of an ideal material [22].

There is more data available on tungsten for fusion relevant conditions than other refractory metals as it is the current standard for PFUs. Tungsten's high melting point (3,653 K), good thermal conductivity (128 W m^{-1} K^{-1} at 800 K), low sputtering yield, vacuum compatibility and reasonable neutron irradiation resistance make it one of the few candidates for the armour in the divertor [22, 162]. The main issue with tungsten is its brittleness at lower temperatures due to a high DBTT. This is heavily dependent on the condition of the material (e.g., microstructure) and on the strain-rate, which can be seen in the results of the Charpy tests performed in [163], where the DBTT of tungsten rose above 1,273 K. The DBTT of tungsten in the divertor therefore cannot be given with any certainty [111]. Alloying tungsten with tantalum can potentially improve ductility, but has also shown additional surface modification effects under ion radiation [164]. Additionally, parts in fusion relevant conditions will experience irradiation, which can adversely affect thermal conductivity as transmutation reactions causes helium to form on the grain boundaries. This was examined in tungsten by Zhang *et al* [109] and Ding *et al* [110] through molecular dynamics simulations, where they determined that tungsten's thermal conductivity would decrease as impurities within it increased.

Metallic AM development for LPBF has been mostly focused on titanium, nickel superalloys (e.g., Inconel), aluminium and steels (among others) [165–167]. This is because LPBF is typically used for biomedical and aerospace applications, where the above metals are commonly used, as it can manufacture lightweight and customisable parts [168]. Research on refractory metals has been a recent development in the AM community. For this reason, process parameters for refractory metals have not yet been completely optimised and fully-dense parts can not be manufactured consistently across different manufacturers.

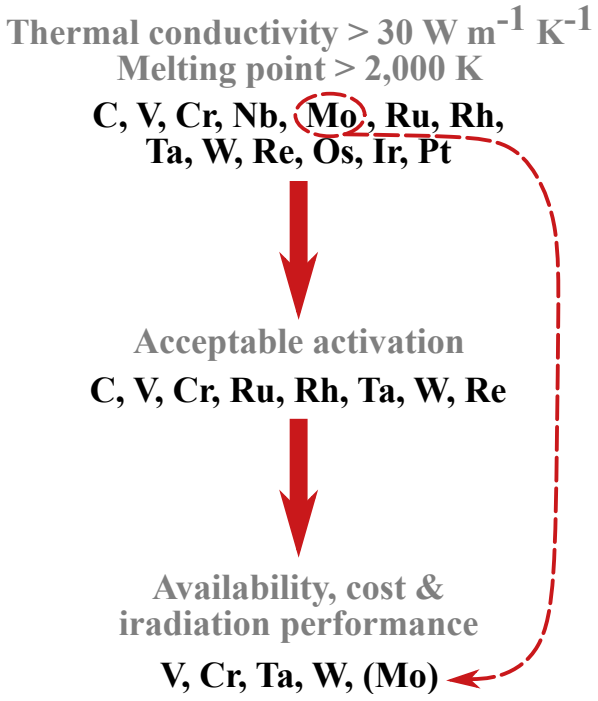

Figure A.1: Downselection flowchart for candidate fusion materials. Modified from [22].

The fusion relevant refractory metal most currently researched in AM is tungsten. The manufacture of pure tungsten with LPBF encounters almost all of the intractable difficulties of LPBF as it has an incredibly high melting point (large amounts of energy are needed to melt the powder), high thermal conductivity (rapid cooling and solidification of the melt pool), high surface tension of 2.361 N m^{-1} (promoting the balling phenomena), and a high viscosity of 8×10^{-3} Pa s (decreasing flowability) [165, 169]. Despite these issues, near fully-dense parts have been printed with LPBF by multiple researchers through careful control of the process parameters in recent years. Tan *et al* [169] reached a maximum density of 98.50 ± 0.12% with a micro hardness of 461 ± 18 $HV_{0.05}$ (exceeding the hardness of conventionally manufactured tungsten) and an ultimate compressive strength and compressive yield stress comparable to that of conventionally manufactured tungsten (1,015 MPa and 882 MPa respectively). Some of these properties were later improved upon by Wen *et al* [170] with LPBF produced tungsten samples reaching a density of 98.71%, micro hardness of 428 HV_3, compressive strength of 1523 MPa and a thermal conductivity of 148 W m^{-1} K^{-1}. Complex structures and composites produced with AM tungsten, W_{AM}, have also been successful. One example was a thin-walled tungsten honeycomb structure manufactured using LPBF, which was then fabricated using liquid copper, Cu, infiltration to form a W_{AM}/Cu composite [171]. Despite approaching LPBF-produced, fully-dense tungsten parts, Tan *et al* [169] argued that it is not possible to create a 100% dense part because the droplet spread time is almost double the solidification time. This leads to balling and difficulty in filling the inter-ball pores on the surface of previous layers.

Research and improvement in the printing of molybdenum [166, 172–174] and tantalum [175–178] has also been made in recent years. Although there has not been a widespread desire to additively manufacture vanadium or chromium, research in the AM of alloys containing these elements [179–182] is present.

The divertor target can also be improved through material property optimisation. This can be achieved using AM functionally graded material. For example, Curzadd *et al* [121] developed a methodology to optimise the material distribution of composite PFUs to reduce the thermal stress caused by high heat fluxes. Preliminary results showed that the thermal stress in a copper infiltrated AM tungsten divertor target could be reduced by up to 86% for nominal and off-nominal conditions compared to a solid tungsten block.

Appendix B

Computational Fluid Dynamics

B.1 Background

The Navier-Stokes equations are a set of partial-differential equations which describe the motion of viscous fluids. These equations are only analytically solvable for a limited range of flow types and conditions (typically fully-developed flows in simple geometries) due to their non-linear and coupled nature. One such example is Hagen-Poiseuille flow [132], which describes laminar flow through a uniform circular channel. This was derived from the Navier-Stokes equations by assuming that the fluid flow was steady, axisymmetric and fully-developed, and that the radial and azimuthal components of the fluid velocity were zero [85].

While existing solutions are important in understanding the fundamentals of fluid dynamics, they have limited applications in many scenarios due to the use of complex structures and the presence of non-fully-developed flows. This makes solving the Navier-Stokes equations difficult, though they can be simplified for engineering purposes. One method of simplifying these equations is by converting them to a dimensionless form (non-dimensionalisation of the Navier-Stokes equations). Many flow types require several dimensionless parameters and it may not be possible to scale an experiment correctly, however.

An alternative method to solving the Navier-Stokes equations is to use numerical techniques. Discretisation methods can be used to approximate the partial-differential equations through a system of algebraic equations, which can then be solved computationally. This is known as CFD. The Navier-Stokes equations can be solved relatively quickly for a wider range of flow types and conditions using CFD due to the power that modern technology provides. Differences between physical experiments and numerical results typically originate from the processes used to produce the numerical solutions, such as assumptions in boundary conditions and the discretisation process. CFD users must therefore analyse the results from a CFD simulation and determine whether they are accurate.

Obtaining feasible numerical solutions for many phenomena, such as turbulence and multi-phase flow, is not always possible. Models are therefore necessary in CFD to both remove the need to directly resolve the Navier-Stokes equations and to reduce computational costs. Experimental data is often needed to validate the models. An in-depth discussion regarding the numerical method is given in the following sections.

B.2 Numerical method

B.2.1 Mathematical model

The mathematical model is a set of partial differential or integro-differential equations and boundary conditions. An appropriate model must be selected for the target application (e.g., incompressible fluids, turbulence, multi-phase flows), which may include simplifications of the exact mass and momentum conservation laws. While many of the simplified models are not easier to solve analytically, they reduce computational costs. The general mass and momentum conservation equations are given below as an example.

$$\frac{\partial \rho}{\partial t} + \boldsymbol{\nabla} \cdot (\rho \boldsymbol{u}) = 0\,, \tag{B.1}$$

$$\frac{\partial (\rho \boldsymbol{u})}{\partial t} + \boldsymbol{\nabla} \cdot (\rho \boldsymbol{u} \otimes \boldsymbol{u}) = \boldsymbol{\nabla} \cdot \boldsymbol{\tau} + \rho \boldsymbol{b}\,, \tag{B.2}$$

where $\boldsymbol{\tau}$ is the stress tensor and $\boldsymbol{b}$ represents body forces (e.g., gravity). By assuming that fluid density is temporally and spatially invariant, these equations are reduced to

$$\boldsymbol{\nabla} \cdot \boldsymbol{u} = 0\,, \tag{B.3}$$

$$\frac{\partial \boldsymbol{u}}{\partial t} + (\boldsymbol{u} \cdot \boldsymbol{\nabla})\, \boldsymbol{u} = \nu \boldsymbol{\nabla}^2 \boldsymbol{u} - \frac{1}{\rho} \boldsymbol{\nabla} P + \boldsymbol{b}\,. \tag{B.4}$$

This gives the mass and momentum conservation equations for incompressible and isothermal fluids.

B.2.2 Coordinate systems and numerical grids

The conservation equations can be written using different coordinate systems and basis vectors. This choice depends on the form of the target flow and can influence the choice of discretisation method and grid type used.

The solution domain is divided in to a finite number of subdomains. This is known as the numerical grid and it defines the locations where the variables will be calculated. There are multiple different grid types, such as structured, block-structured and unstructured grids.

Structured grids consist of grid lines, with the property that members of a single family do not cross each other and only cross members of other families once. The position of any control volume can therefore be defined by a set of indexes. In block-structured grids, the domain is subdivided in to two or more levels. The coarse level contains blocks which are large segments of the domain and may be irregular. The fine level contains a locally structured grid, however. Unstructured grids are often used for complex geometries as they are flexible and can fit any arbitrary solution domain boundary. For three-dimensional cases, the control volumes are typically made of tetrahedral, hexahedral or arbitrary polyhedral shapes. Examples of the above grid types are depicted in figure B.1.

B.2.3 Discretisation method

A method to approximate the partial differential equations in the mathematical model by a system of algebraic equations at some set of discrete locations in space and time need to be

selected. This is known as the discretisation method. The main discretisation methods are the finite difference, finite volume and finite element methods. Each of these methods would yield the same solution if the grid was fine enough.

The solution domain for the finite difference method is covered by a grid, where each grid point denotes a computational node. The differential form of the mathematical model are applied to each computational node and the partial derivatives are replaced by approximations of the examined variable at the node. This results in one algebraic equation per grid node, where the variable at the node and a number of adjacent nodes are unknown.

In the finite volume method, the solution domain is divided into a finite number of control volumes by a grid. This grid dictates the boundaries of the control volume and the computational nodes are found within the control volume, depicted in figure B.2. The finite volume method also uses the integral form of the mathematical model, such as

$$\frac{\partial}{\partial t}\int_V \rho \, \mathrm{d}V + \int_S \rho \boldsymbol{u} \cdot \boldsymbol{n} \, \mathrm{d}\boldsymbol{S} = 0\,, \tag{B.5}$$

which is the integral form of the mass conservation equation, where the volume integrals contain source terms and the surface integrals contain either convection or diffusion terms. This is

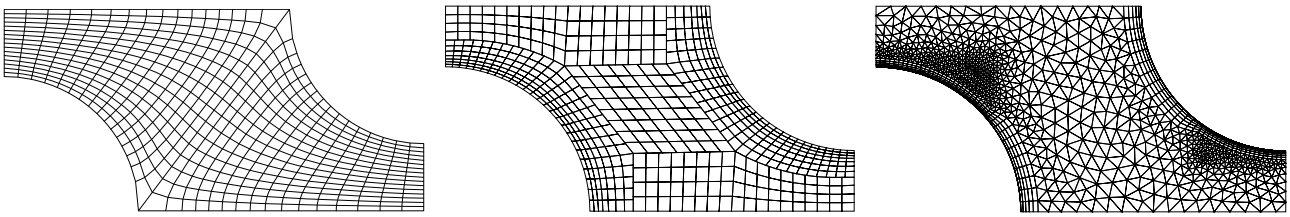

Figure B.1: Example of a structured, non-orthogonal grid (left), a block-structured, non-conformal grid (centre), and an unstructured grid with tetrahedral elements (right). Modified from [85].

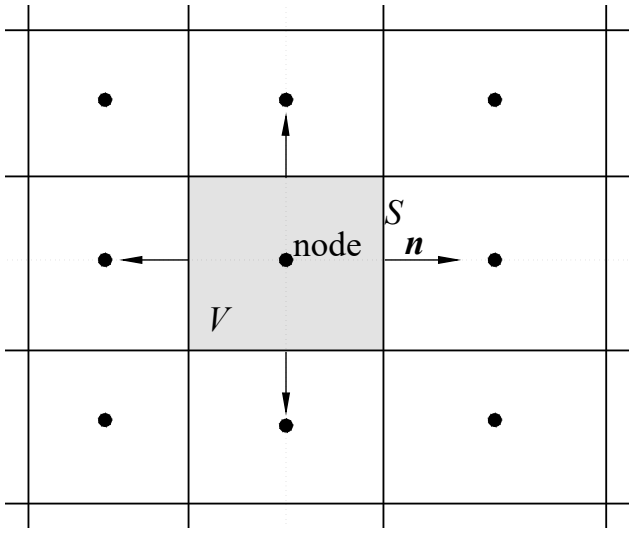

Figure B.2: A typical two-dimensional control volume used in the finite volume method, where V is the volume of the control volume, S is the surface of the control volume and $\boldsymbol{n}$ is the vector direction normal to the control volume surface. Modified from [85].

represented in figure B.3. These equations are applied to each control volume and the variables (e.g., fluid velocity in equation B.5) are calculated at the computational node. The value of the calculated variables are interpolated to express them on the surface of the control volume. This method is also suitable for complex geometries and polyhedral mesh elements as the control volumes are defined by vertexes connected by straight lines. The shape of the control volume surface therefore does not matter as it is bounded by straight line segments.

The finite element method discretises the solution domain in a similar manner to the finite volume method and uses the integral forms of the partial differential equations. The key feature of the finite element method is that the Navier-Stokes equations from the mathematical model are multiplied by a weight function prior to being integrated across the domain.

B.2.4 Finite approximations

The approximations used in the discretisation method also needs to be selected. This selection affects the accuracy of the approximation and the computational speed of the code so a compromise must be made between the two. In the finite volume method, the surface and volume integrals are approximated by quadrature formulas. This gives an algebraic equation for each control volume.

For the surface integrals, the net flux through the control volume boundary is given by

$$\int_S \boldsymbol{f}\, \mathrm{d}\boldsymbol{S} = \sum_i \int_{S_{a_i}} \boldsymbol{f}\, \mathrm{d}\boldsymbol{S}\,, \tag{B.6}$$

where $\boldsymbol{f}$ is a convection or diffusion flux vector component in the direction normal to the face a. This is shown in figure B.3. To maintain conservation, the control volumes do not overlap and each face is unique to the two adjacent control volumes.

To calculate the surface integral on an arbitrary face, the integrand would need to be known everywhere on the specified surface. This is not the case as only the nodal values are calculated

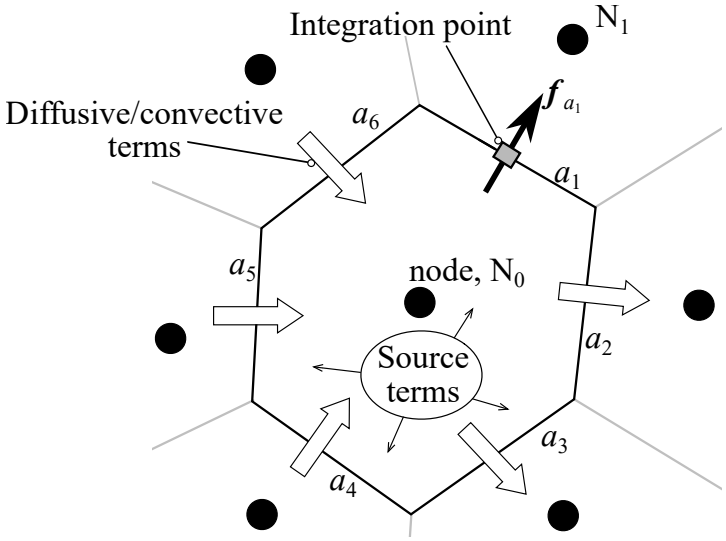

Figure B.3: Depiction of the diffusive and convective flux through a control volume in the finite volume method. One integration point is depicted on the surface a_1. Modified from [183].

and an approximation must therefore be introduced. The surface integral can be approximated by first approximating the integral in terms of the variables at one or more locations on the surface and then by approximating the surface values in terms of the nodal values.

The midpoint rule is the simplest approximation for the surface integral, where it is approximated as the product of the integrand at the centre of the surface (i.e., one integration point) and the surface area. This is given as

$$\int_{S_{a_1}} \boldsymbol{f} \, \mathrm{d}\boldsymbol{S} = \overline{\boldsymbol{f}}_{a_1} A_{a_1} \approx \boldsymbol{f}_{a_1} A_{a_1} \,, \tag{B.7}$$

for a control volume surface a_1 where $\overline{\boldsymbol{f}}_{a_1}$ is the mean value of the convection or diffusion term across a_1, A_{a_1} is the surface area of a_1 and $\boldsymbol{f}_{a_1}$ is the convection or diffusion term at the centre a_1. Figure B.3 was used as the reference grid. Another approximation for the surface integral is the trapezoid rule, where the convection or diffusion flux vectors at the corners of a control volume surface are evaluated instead of the vector at the centre of the surface.

The value of $\boldsymbol{f}_{a_1}$ is obtained through interpolation as only its nodal values are available. Convection terms are given as $\boldsymbol{f}^{\mathrm{c}} = \rho\phi\boldsymbol{u} \cdot \boldsymbol{n}$ and diffusion terms are given as $\boldsymbol{f}^{\mathrm{d}} = \Gamma\boldsymbol{\nabla}\phi \cdot \boldsymbol{n}$, where ϕ is a field variable and Γ is a diffusion constant. Assuming that fluid velocity, density and the diffusion constant are known everywhere, only the field variable ϕ needs to be interpolated on to the control volume surface. There are many common interpolation schemes, such as the upward-differencing scheme, where

$$\begin{aligned} \phi_{a_1} &= \phi_{N_0} \quad \text{if} \quad \boldsymbol{u} \cdot \boldsymbol{n} > 0 \quad \text{or} \\ \phi_{a_1} &= \phi_{N_1} \quad \text{if} \quad \boldsymbol{u} \cdot \boldsymbol{n} < 0 \,, \end{aligned} \tag{B.8}$$

or the central-difference scheme, where

$$\phi_{a_1} = \phi_{N_1}\gamma_{a_1} + \phi_{N_0}\left(1 - \gamma_{a_1}\right) . \tag{B.9}$$

Figure B.3 was used here as a reference grid, where ϕ_{a_1} is the interpolated field variable on the surface a_1, ϕ_{N_0} is the field variable at the node N_0, ϕ_{N_1} is the field variable at the node N_1 and γ_{a_1} is a linear interpolation factor.

Volume integrals are typically given as

$$\int_V q \, \mathrm{d}V \,, \tag{B.10}$$

where q is a source or sink term. Volume integrals can be approximated in terms of the variables at one or more locations inside the control volume.

The simplest second-order accurate approximation for volume integrals is to replace it with the product of the mean of the source or sink term and the volume of the control volume. The mean of the source or sink term is then approximated as the nodal value. This is given as

$$\int_V q \, \mathrm{d}V = \overline{q}\Delta V \approx q_{N_0}\Delta V \,, \tag{B.11}$$

where $\overline{q}$ is the mean of the source or sink term across the control volume, ΔV is volume of the control volume and q_{N_0} is the source or sink term at the node N_0. Figure B.3 was used as the

reference grid. q_{N_0} does not need to be interpolated as it is the nodal value. The approximation between the second and third term in equation B.11 also becomes exact if q is either constant or varies linearly within the control volume. Approximations of higher order require more points within the control volume and the interpolation of q at these points is necessary as only the nodal value exists.

B.2.5 Solution method

The discretisation results in a large system of linear or non-linear algebraic equations, where there is one equation for each node, which needs to be solved. This system can be written in matrix notation as

$$\boldsymbol{A}\boldsymbol{\phi} = \mathbf{Q}\,, \tag{B.12}$$

where $\boldsymbol{A}$ is a square sparse (i.e., most of the matrix elements are zero) coefficient matrix, $\boldsymbol{\phi}$ is a column vector containing the nodal variable values and $\boldsymbol{Q}$ is the vector of known terms.

Direct methods can be used to solve a system of linear equations, where the basic method used is Gauss elimination. For a system of non-linear equations, an iterative method needs to be used to solve them instead. This is done by guessing a solution, linearising the equations and then improving the solution. This process is repeated until a converged result is obtained. For CFD problems, the iterative method is generally less computationally intensive than the direct method, as typically each iteration is cheap and there are a small number of them. This method can also used for linear cases.

Considering a matrix of the form in equation B.12, the following non-exact solution is obtained after n iterations

$$A\boldsymbol{\phi}^n = \mathbf{Q} - \boldsymbol{\rho}^n\,, \tag{B.13}$$

where $\boldsymbol{\rho}^n$ is a residual. By subtracting equation B.13 from equation B.12 (i.e., $A\boldsymbol{\phi} - A\boldsymbol{\phi}^n$), a relation for the residual is found:

$$A\boldsymbol{\epsilon}^n = \boldsymbol{\rho}^n\,, \tag{B.14}$$

where $\boldsymbol{\epsilon}^n = \boldsymbol{\phi} - \boldsymbol{\phi}^n$ and is the iteration error. The iteration procedure aims to bring the residual down to zero, which also reduces $\boldsymbol{\epsilon}$ to zero. Considering a scheme for a linear system, which can take the form of

$$M\boldsymbol{\phi}^{n+1} = N\boldsymbol{\phi}^n + \mathbf{B}\,, \tag{B.15}$$

convergence is defined when $\boldsymbol{\phi}^{n+1} = \boldsymbol{\phi}^n = \boldsymbol{\phi}$. This gives

$$M\boldsymbol{\phi} = N\boldsymbol{\phi} + \mathbf{B}\,. \tag{B.16}$$

By subtracting equation B.16 from equation B.15 and using the definition of the iteration error, it is found that

$$\boldsymbol{\epsilon}^{n+1} = M^{-1}N\boldsymbol{\epsilon}^n\,. \tag{B.17}$$

The iterative method converges if $\lim_{n\to\infty} \boldsymbol{\epsilon}^n = 0$. A critical role is played by the eigenvalues and eigenvectors of the iteration matrix $M^{-1}N$.

B.2.6 Convergence criteria

There are typically two levels of iterations which need to be stopped, lest they continue indefinitely. A convergence criteria therefore needs to be defined to stop the iteration procedure, to minimise computational costs, whilst obtaining accurate results.

The first level are the inner iterations, where the linear equations are solved, as discussed in the previous section. The iteration error needs to be estimated (through the calculation of the eigenvalues of the iteration matrix) to determine whether it has reduced past a user-defined tolerance, at which point convergence has been reached.

The second level are the outer iterations, where each field equation, such as those for momentum and pressure, is solved sequentially (treating the other variables as known). This repeats until the equations are satisfied, hence the need for a convergence criteria. Changes in one variable can also change the coefficients of another variable, which may impact convergence. Under-relaxation values are therefore used to limit this change and aid in convergence.

B.3 Properties of the numerical method

The CFD solution method should contain certain properties (which are *italicised* in this section) to ensure that the numerical model outputs accurate results. The most important ones are explained below.

The truncation error is defined as the difference between the discretised and exact Navier-Stokes equations. As the grid spacing becomes infinitesimally small, the discretisation theoretically approaches the exact Navier-Stokes equations and, hence, the truncation error tends to zero. In this case, the approximations are *consistent*. This does not mean that the solution of the discretised Navier-Stokes equations becomes exact in the limit of a small step size (convergence). For this to be the case, the solution needs to be stable as well.

For a numerical solution to be *stable*, it must not magnify errors that appear throughout the numerical process. For temporal problems, stability ensures that the solution for a bounded (discussed below) exact equation is always bounded and for iterative methods, it ensures that the solution does not diverge. Small time steps and under-relaxation are typically used to keep a solution stable.

The numerical solution must also *converge*. Convergence is reached when the solution of the discretised Navier-Stokes equations tends to the solution of the exact Navier-Stokes equations as the grid spacing becomes infinitesimally small.

The numerical method needs to follow the conservation laws set by the Navier-Stokes equations on both a local and global scale. If the strong conservative form of the equations and the finite volume method are used, *conservation* is then guaranteed for each individual control volume and the entirety of the domain. Non-conservative schemes can be used and lead to consistent and stable solutions for fine grids (where the error is negligible), but it is difficult to know on which grids this is applicable. Hence, conservative schemes are preferred.

Numerical solutions should be physically plausible. For example, negative absolute temperatures

should be prohibited as they are a non-physical quantity. In other words, the numerical solution needs to be *bounded*. This can be difficult to guarantee for second-order schemes (and above) as they can produce unbounded solutions, though this typically happens when the grid is too coarse.

Models for phenomena that are too complex to be treated directly (e.g., turbulence) need to ensure that they give physically realistic solutions, otherwise the results will be inaccurate or the numerical method can diverge. This is known as a *realizable* model.

Numerical solutions are only approximate and therefore always include multiple separate types of systematic errors, which affect the *accuracy* of the solution. It is important to be aware of them and to be able to distinguish between them as they may cancel each other out, leading to solutions on a coarse mesh sometimes agreeing better with experimental results than with a fine mesh. These errors are as follows [85]:

- **Modelling errors -** defined as the difference between the actual flow and exact solution of the mathematical model. These can be neglected for laminar flows as the Navier-Stokes equations are extremely accurate. These errors can be quite large for more complex flows, however. These errors can only be examined when the discretisation and iteration errors are negligible.
- **Discretisation errors -** defined as the difference between the exact solution of the conservation equations and the exact solution of the discretised conservation equations. These errors decrease as the mesh is refined and the time step is reduced.
- **Iteration errors -** defined as the difference between the iterative solutions and the exact solutions of the algebraic equations systems.
- **Numerical errors -** which include losses due to numerical truncation.

There are many solution schemes and these need to be chosen to ensure that the desired accuracy is reached with minimal computational effort.

B.4 Boundary conditions

Information regarding the domain boundary has to be given to render a unique solution. When considering the finite volume method for example, each control volume provides an algebraic equation, similar to equation B.5. While the volume integral is calculated the same way for every control volume, the surface integral through the control volume faces coinciding with the domain boundary need to be known or expressed as a combination of interior and boundary data.

This is satisfied through the implementation of boundary conditions. The most common of these being Dirichlet boundary conditions, which specifies the value of the variable at the boundary, and Neumann boundary conditions, which specifies the gradient of the value in a particular direction from the boundary.

Boundary conditions can be used to find the value at the boundary in different ways. If a Dirichlet boundary condition is used, then there is no need to solve for it since the boundary value is already known. If a Neumann boundary condition (where the gradient of the value is

provided) is used instead, interior grid points can be used to calculate the value at the boundary. For example, if a boundary condition of the form

$$\left(\frac{\partial \phi}{\partial x}\right)_1 = 0\,, \tag{B.18}$$

where ϕ is a field variable, x is a Cartesian co-ordinate and the subscript 1 denotes the boundary, is applied to the finite difference method (for simplicity), a simple approximation leads to the following equation

$$\frac{\phi_2 - \phi_1}{x_2 - x_1} = 0\,, \tag{B.19}$$

where the subscript 2 denotes the interior grid point closest to the boundary. This gives $\phi_1 = \phi_2$ and specifies the boundary value. This is a first-order approximation and higher-order approximations can be obtained by using polynomial fits of higher degrees.

An alternative strategy is to use ghost points (points outside of the computational domain) to center the derivative term at the boundary between the ghost point and the interior grid point closest to the boundary, as seen in figure B.4. A similar methodology to the above is used to calculate the boundary value.

The boundary conditions that are implemented are dependent on where they are in relation to the flow and what is physically known about the system there. At an fluid inlet boundary, for example, all flow conditions need to be specified. If assumptions to the inlet profile are made, then the inlet should be far away from the region of interest to minimise the impact of poorly chosen boundary conditions. Little is usually known about the flow at the outlet and, hence, it should be located far away from the regions of interest to avoid propagation of errors upstream. At impermeable walls, a no-slip condition is typically applied as viscous fluids stick to solid boundaries and convections fluxes are all zero, while diffusion fluxes for scalars such as thermal energy require more attention.

B.5 Fluid dynamics

The conservation equations for mass and momentum assume that all fluid properties vary in space and time. A fluid is incompressible when its density is constant, however. This is assumed to be true for liquids, in most cases, and gasses, when the Mach number is below 0.3 [85]. In these cases, the mass and momentum conservation equations are simplified to equations B.3 and B.4.

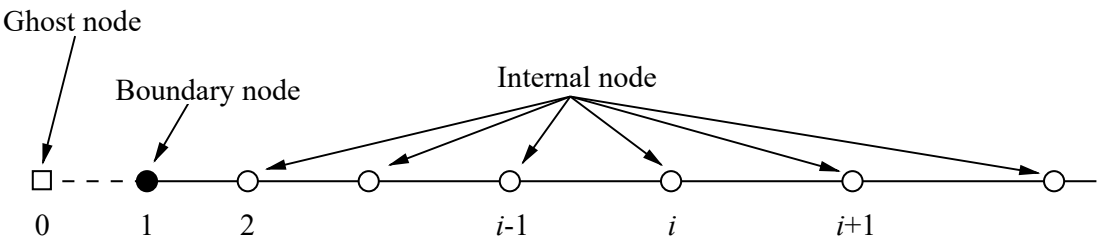

Figure B.4: Example of a one-dimensional grid with a ghost node at $i = 0$, outside the computational domain. Modified from [85].

Fluid flow can be described as either laminar or turbulent. Laminar flow can be solved directly from the Navier-Stokes equations due to its simplicity. Turbulent flow is far more complex and different methods can be used to solve this type of flow instead. These are [85]:

- **Direct numerical simulation (DNS) -** where the Navier-Stokes equations are solved without averaging or making any approximations (outside of the numerical discretisation).
- **Large-eddy simulation (LES) -** where the equations of motion for small length scales are decomposed into their mean and fluctuating components via low-pass filtering. The mean is calculated via time and spatial averaging. This method is able to solve large-scale motions while approximating small-scale motions.
- **Reynolds-averaged Navier-Stokes (RANS) -** where the equations of motions are decomposed into their mean and fluctuating components over all length scales. The equations obtained can either represent steady or unsteady flow.

Each of the presented methods above uses more approximations than the previous one. DNS is therefore the most exact method but is far more computationally intensive (as a very fine grid is needed to capture the turbulence), while RANS is the least accurate but is more computationally efficient.

A key point to note is that in LES and RANS, the decomposed equations do not form closed sets because of the non-linear convection terms. Turbulence models are therefore used to approximate equations for the unknowns in the above methods. These models should be [184]:

- Based on physical concepts instead of intuition.
- Constructed from appropriate mathematical principles.
- Constrained to yield physically realizable data.
- Widely applicable.
- Mathematically simple.
- Built from variables with accessible boundary conditions.
- Computationally stable.

Examples of these models are the k-ϵ and k-ω-SST models in RANS and the k-ω-SST-DES and Smagorinsky SGS models in LES. They should be treated as engineering approximations instead of scientific laws.

In the near-wall region, turbulence effects are negligible and the fluid flow is laminar due to the viscosity of the fluid and skin friction. The region where this happens is defined as the viscous sublayer. The velocity component parallel to the wall here varies linearly with wall distance. The boundary conditions for the momentum equations are the same as in laminar flows if the numerical grid solves this region. The mesh elements near the walls need to be thin for three-dimensional flows at high Reynolds numbers (a dimensionless ratio of the inertial and viscous forces acting on a fluid). On top of this, elements next to a curved wall may become misshapen if the mesh is not sufficiently refined in the tangential direction. Therefore, the viscous sublayer is typically only solved at moderate Reynolds numbers and an alternative method needs to be

used for higher Reynolds numbers.

The velocity profile across a boundary layer at different Reynolds numbers can be scaled if the shear velocity is used. This results in a dimensionless fluid velocity at the first mesh element node from the wall, u^+, and the dimensionless distance of the first mesh element node from the wall, n^+, given by the equations

$$u^+ = \frac{u_\mathrm{w}}{u^*}\,, \tag{B.20}$$

$$n^+ = \frac{u^* n}{\nu_\mathrm{w}}\,, \tag{B.21}$$

where u_w is the near-wall fluid velocity, u^* is the shear velocity, n is the distance of the first mesh element node from the wall and ν_w is the near-wall kinematic viscosity. n^+ is also traditionally labelled as y^+ because early computations were two-dimensional and y was typically the direction normal to the wall. By plotting u^+ against n^+, as shown in figure B.5, it is apparent that there are three identifiable regions; the viscous sublayer, the log-law region and an intermediate region known as the buffer layer. The dimensionless fluid velocity obeys the following relationship in the viscous sublayer

$$u^+ = n^+\,, \tag{B.22}$$

whereas it obeys the following relationship in the log-law region

$$u^+ = \frac{1}{k_\mathrm{C}} \ln\!\left(R_\mathrm{P}\, n^+\right)\,, \tag{B.23}$$

where k_C is the Von Kármán constant (typically given as 0.41) and R_P is a wall roughness parameter (which is approximately 9 for a smooth wall).

The existence of these regions have been confirmed both experimentally and through DNS. Smits *et al* [188] suggested that there are variations which may depend on both the Reynolds numbers

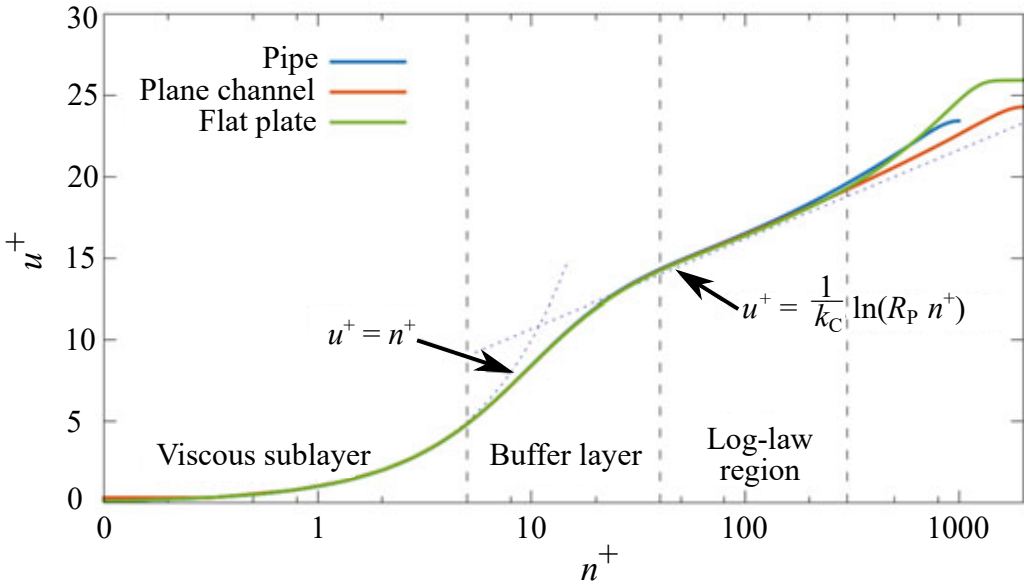

Figure B.5: Dimensionless velocity against dimensionless distance from the wall for a circular pipe [185], plane channel [186] and flat plate [187]. Three distinct boundary layer regions are visible. Modified from [85].

and the geometry of the fluid domain and, hence, this law may not be universal.

Computational resources can be reduced by ensuring that the first node (i.e., the closest mesh element to the wall) lies within the log-law region. A relationship can then be derived between the wall shear stress and the velocity in the log-law region by using equation B.23 and the following assumptions [85]:

1. The flow is in local equilibrium.
2. The total shear stress is constant between the wall and first node and also equal to the wall shear stress.

These are known as wall functions, where high-Re wall functions are used when the first node is located in the log-law region while low-Re wall functions are used when the first node is located in the viscous sublayer region.

It is very difficult to ensure that all computational nodes across an entire domain reside within the desired region at all times. Fluid dynamics such as flow separation, stagnation and reattachment zones can drastically change the wall shear stress. This impacts both u^+ and n^+ and hence, affects the physical length of the viscous sublayer, log-law and buffer layer regions. Computational nodes may therefore be found across all regions for a given CFD simulation, despite the nodes themselves not changing position. A common method used to combat this is to use the all-n^+ wall treatment where if the node is within the viscous sublayer then a linear velocity profile is assumed, if the node is within the log-law region then standard wall functions are applied, and if the node is within the buffer layer then a blended approach is used.

B.6 Heat transfer

B.6.1 Mechanisms

Fluid flow may include a wide range of phenomena that is not described by the Navier-Stokes equations. One such example is heat and mass transfer, where a scalar quantity, such as temperature, is included and can affect the fluid properties, such as density and viscosity. This section discusses how CFD solves heat transport problems.

Fluids must satisfy the conservation of energy, which is described by the following equation

$$\frac{\partial\left(\rho E_{\text{num}}\right)}{\partial t}+\boldsymbol{\nabla}\cdot\left(\rho\boldsymbol{u}E_{\text{num}}\right)=-\boldsymbol{\nabla}\cdot\boldsymbol{\Phi}+S_{\text{e}}+\boldsymbol{\nabla}\cdot\left(\sigma\cdot\boldsymbol{u}\right)+\rho\boldsymbol{g}\cdot\boldsymbol{u}\,, \tag{B.24}$$

where E_{num} is the specific total energy of the system, $\boldsymbol{\Phi}$ is a heat flux, S_{e} is a source or sink term (e.g., an exothermic reaction or energy losses due to friction) and each term in the above equation is a measure of the rate of change of energy density in the system. The specific total energy can be separated in to components of specific internal energy, e_{num}, and specific kinetic energy, K_{num}, by $E_{\text{num}}=e_{\text{num}}+K_{\text{num}}$. This gives

$$\begin{aligned}\overbrace{\frac{\partial\left(\rho e_{\text{num}}\right)}{\partial t}+\boldsymbol{\nabla}\cdot\left(\rho\boldsymbol{u}e_{\text{num}}\right)}^{\text{thermal}}+\overbrace{\frac{\partial\left(\rho K_{\text{num}}\right)}{\partial t}+\boldsymbol{\nabla}\cdot\left(\rho\boldsymbol{u}K_{\text{num}}\right)}^{\text{mechanical}}=\\ \underbrace{-\boldsymbol{\nabla}\cdot\boldsymbol{\Phi}+S_{\text{e}}}_{\text{thermal}}+\underbrace{\boldsymbol{\nabla}\cdot\left(\sigma\cdot\boldsymbol{u}\right)+\rho\boldsymbol{g}\cdot\boldsymbol{u}}_{\text{mechanical}}\,,\end{aligned} \tag{B.25}$$

with the terms corresponding to thermal and mechanical energy noted above. The mechanical energy terms can be neglected without loss of energy conservation in many cases [189], such as in incompressible flows, which simplifies equation B.25 to

$$\underbrace{\frac{\partial\left(\rho e_{\text{num}}\right)}{\partial t}}_{\text{time-dependent}} + \underbrace{\boldsymbol{\nabla}\cdot\left(\rho\boldsymbol{u}e_{\text{num}}\right)}_{\text{convection}} = \underbrace{-\boldsymbol{\nabla}\cdot\boldsymbol{\Phi}}_{\text{diffusion}} + S_{\text{e}}\,. \tag{B.26}$$

This equation describes the transport of thermal energy in the system.

For an incompressible fluid, equation B.26 can be manipulated in to the following form

$$\frac{\partial\left(\rho c_{\text{p}}T\right)}{\partial t} + \boldsymbol{u}\cdot\boldsymbol{\nabla}\left(\rho c_{\text{p}}T\right) = \boldsymbol{\nabla}\cdot\left(k\boldsymbol{\nabla}T\right) + S_{\text{e}}\,, \tag{B.27}$$

where T is temperature, c_{p} is the specific heat capacity and k is thermal conductivity. This is achieved by using $\boldsymbol{\Phi} = -k\boldsymbol{\nabla}T$ (Fourier's law), $e_{\text{num}} = c_{\text{p}}T$ (definition of internal energy for an incompressible fluid) and equation B.3 (mass conservation). Specific heat capacity, density and thermal conductivity can be neglected from the partial derivative operators if they are isotropic (and if buoyancy is neglected).

The mechanisms which drive thermal transport are radiation, conduction and convection. Radiation is not discussed here as it has little relevance throughout this research project. Convection is the heat transfer process most closely linked with fluid mechanics and is given as the second term in equation B.26. Steady (time-independent) heat conduction is described by equations similar to

$$\boldsymbol{\nabla}\cdot\left(\boldsymbol{\nabla}\phi\right) = 0 \tag{B.28}$$

and unsteady (time-dependent) conduction is described by equations similar to

$$k\boldsymbol{\nabla}\cdot\left(\boldsymbol{\nabla}\phi\right) = \rho c_{\text{p}}\frac{\partial\phi}{\partial t}\,, \tag{B.29}$$

which are Laplace's equation and the heat equation respectively, where ϕ is an arbitrary field variable [85]. These terms can be observed in equation B.26. When an iterative scheme (discussed in section B.2.5) is used, temperature-dependent properties are first calculated using the temperature in the current iteration, which is then updated. This process is repeated.

B.6.2 Conjugate heat transfer

Conjugate heat transfer refers to problems where heat transfer through coupled solid and fluid regions need to be assessed. The equation for thermal transport in a solid is

$$\frac{\partial\left(\rho e_{\text{num}}\right)}{\partial t} = -\boldsymbol{\nabla}\cdot\boldsymbol{\Phi} + S_{\text{e}}\,, \tag{B.30}$$

which is equivalent to equation B.26 when $\boldsymbol{u} = 0$ and $\boldsymbol{\nabla}\cdot\boldsymbol{u} = 0$.

In the case where two computational domains are present, one fluid and one solid, two thermal transport equations are present, equations B.26 and B.30. These are typically solved sequentially,

where the solution for a previously solved equation is inserted in to the subsequent equation, before moving on to the next iteration.

If heat is transported across a fluid-solid boundary, then the coupling between the two domains needs to be described mathematically to allow interactions between them. There are two methods that can be used to describe this coupling. The first method assumes that the temperature at the boundary of the two domains is equal. This is achieved by setting the temperature in the adjacent element centres in the fluid and solid domain to be equal to each other and by ensuring that the heat flux entering one domain at one side of the interface is equal to the heat flux leaving the other domain on the other side of the interface.

The second method assumes that the temperature at the boundary between the two domains is not equal. This is typically the case for fast-moving fluids or for mediums that have vastly different thermal conductivities [190]. The heat flux at the solid-fluid interface therefore needs to be expressed as a function of temperatures in the adjacent element centres in the fluid and solid domains without knowing the temperature at the interface. A visual representation is shown in figure B.6, where the element k separates the nearest element in the fluid domain, C′, and the nearest element in the solid domain, N′. The heat flux through the element face k is similar to the expression for the heat transfer from a wall to the environment:

$$\Phi_{\mathrm{Q,wall}} = h\left(T_{\mathrm{wall}} - T_{\infty}\right) , \tag{B.31}$$

where $\Phi_{\mathrm{Q,wall}}$ is the wall heat flux, T_{wall} is the wall temperature, T_{∞} is the temperature of the fluid domain in the element closest to the wall and h is the heat transfer coefficient [85].

Many CFD users wish to visualize and calculate the heat transfer coefficient along the walls of

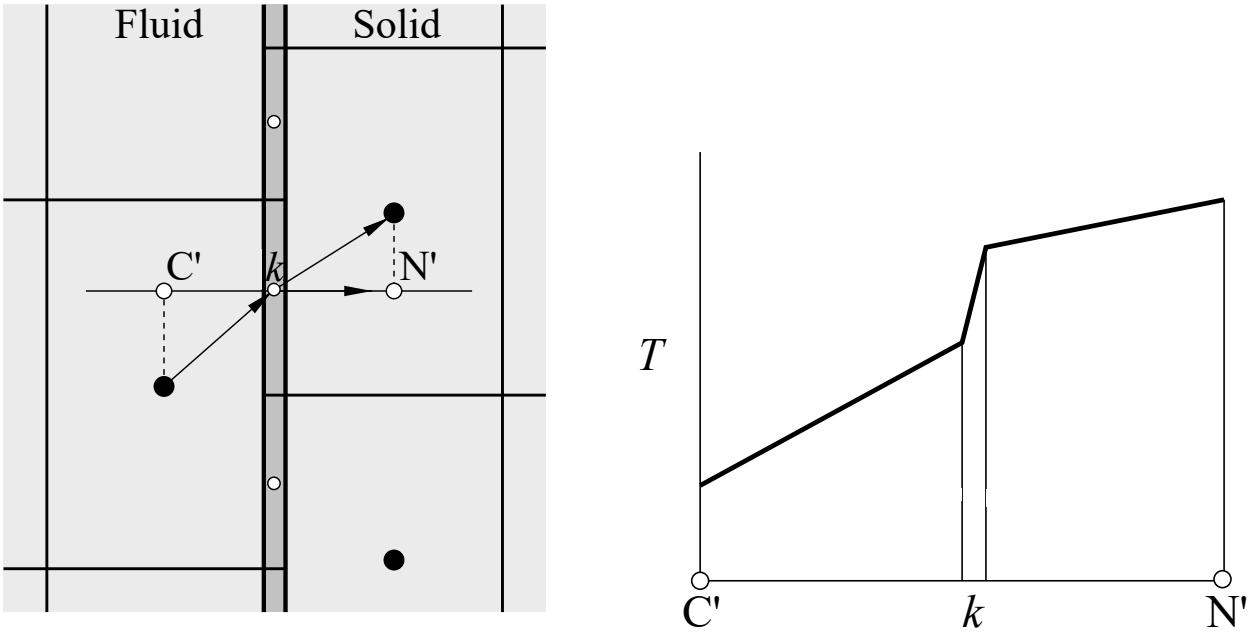

(a) An example mesh demonstrating a fluid and solid domain, separated by a coating layer.

(b) Graph demonstrating the difference in temperature between the two domains.

Figure B.6: Visual representation of the local thermal non-equilibrium model for conjugate heat transfer. Modified from [85].

the solid-fluid interface. Heat transfer coefficient is not a uniquely defined quantity, however, because it is not apparent what the reference environmental temperature should be for internal flows and complex geometries. Heat transfer coefficients and environment temperatures should therefore be expressed together [85]. There are also different ways to extract heat transfer coefficient depending on the solvers used.